Stochastic and Numerical Models for Tropical Convection and Hadley–Monsoon Dynamics

by

Michèle De La Chevrotière
B.Sc., Université de Montréal, 2002
M.Sc., University of Victoria, 2008

A Dissertation Submitted in Partial Fulfillment of the
Requirements for the Degree of

DOCTOR OF PHILOSOPHY

in the Department of Mathematics and Statistics

Stochastic and Numerical Models for Tropical Convection and Hadley–Monsoon Dynamics

by

Michèle De La Chevrotière
B.Sc., Université de Montréal, 2002
M.Sc., University of Victoria, 2008

Supervisory Committee

Dr. Boualem Khouider, Supervisor
(Mathematics and Statistics)

Dr. Reinhard Illner, Departmental Member
(Mathematics and Statistics)

Dr. Julie Zhou, Departmental Member
(Mathematics and Statistics)

Dr. Norman McFarlane, Outside Member
(School of Earth and Ocean Sciences)

University of Victoria

Stochastic and Numerical Models for Tropical Convection and
Hadley–Monsoon Dynamics

Michèle De La Chevrotière

Department of Mathematics and Statistics

ABSTRACT

The poor representation of cloud processes in general circulation models (GMCs) has been recognized for decades as one of the major sources of uncertainties in weather and climate predictions. Because of the coarse spatial resolution of GCMs, subgrid-scale cloud and convection processes are modelled by parameterization schemes that provide a statistical representation of the subgrid-scale processes in terms of the large-scale, gridbox fields. This thesis focuses on the stochastic multicloud parameterization of Khouider et al. (2010), which is based on the three cloud types (congestus, deep, and stratiform) that are most observed in tropical convective systems. A rigorous parameter estimation model based on the Bayesian paradigm is developed to infer from data a set of seven convective timescales that determine the transition rates from one cloud type to another in the multicloud framework. The Bayesian posterior is given in terms of a costly model likelihood function that must be approximated numerically using high-performance linear algebra routines for parallel distributed computing. The Bayesian procedure is applied to the Giga-LES dataset of Khairoutdinov et al. (2009), a large-eddy simulation of tropical deep convection that covers a physical domain comparable to that of a typical horizontal grid cell in a GCM. The stochastic multicloud model and its deterministic version are then coupled to a zonally symmetric atmospheric model to study the meridional Hadley circulation and monsoon dynamics. The main model is based on the hydrostatic Boussinesq equations on a rotating sphere, and is composed of a deep convective troposphere and a dynamical planetary boundary layer to sustain shallow convection. The resulting equations form a system of nonconservative partial different equations, which is solved numerically using high order non-oscillatory finite volume methods. Results from deterministic and stochastic simulations reveal a mean local Hadley cell structure with some features of organized convection. In the stochastic case, the Giga-LES parameter regime best captures the Hadley-type circulation and monsoon trough features, compared to a parameter regime used in a different study.

Contents

List of Tables

List of Figures

ACKNOWLEDGEMENTS

I wish to thank my advisor, Boualem Khouider, for providing continual support and guidance through the course of this dissertation, and especially for allowing me to research in avenues that I found most captivating. This work would not have been possible without his generous explanations and helpful suggestions, and the time he invested in our regular meetings and exchanges.

I am also extremely grateful to Belaid Moa, advanced research computing specialist at the University of Victoria Compute Canada/WestGrid office, for his remarkable assistance and useful advices regarding the high performance computing aspect of this work.

I would also like to thank Farouk Nathoo and Mike Waite, for useful exchanges, and the members of my Supervisory Committee, Reinhard Illner, Norm McFarlane, and Julie Zhou, for their feedbacks. A mention goes to the Department of Mathematics of the University of Victoria, which has given me with the most favorable environment to conduct my PhD and thrive as a graduate student.

Lastly, I wish to acknowledge the funding sources I received during my graduate studies, provided by the Department of Mathematics and Statistics of the University of Victoria, and the Monsoon Mission Grant of Boualem Khouider.

This research was enabled in part by support provided by WestGrid (www.westgrid.ca) and Compute Canada Calcul Canada (www.computecanada.ca).

À mes parents, Léo et Louise

To Marilyn

À Sébastien

Chapter 1

Introduction

Atmospheric convection plays a central role in redistributing thermal energy from the Sun. The Sun emits high energy, shortwave electromagnetic radiation that is transferred through the Earth's atmosphere to the Earth's surface. Part of the incoming solar radiation that is not absorbed or reflected off by the atmosphere and clouds reaches and penetrates the Earth's surface. The heated surface emits back low energy longwave radiation into the atmosphere and transfers heat to the air just above it through the process of convection. Warm air from the surface rises in the atmosphere in vertical columns, called *thermals*. Rising thermals cool as the result of adiabatic expansion, and if the air contains enough moisture, clouds are formed through condensation of water vapor. When water vapor condenses, it releases latent heat which helps to drive the convection even more. Rainfall from precipitating convective clouds cool down the lower atmosphere producing *cold pool* regions that contribute to the organization of convective clouds. Convective clouds directly affect their environment by modulating the vertical distribution of heating in the troposphere and radiation budget.

The interactions between moist convection and the large-scale atmosphere circulation are not well understood. Extreme mesoscale events such as flash flooding, gust fronts, or tornadoes are generated by intense moist convection. The collective effect of clouds are also an important component of large-scale monsoonal circulations, the Hadley and Walker circulations, and many synoptic and intraseasonal atmospheric disturbances which in turn affect global climatic phenomena such as the El Niño Southern Oscillation (ENSO), seen as a sea surface temperature oscillation pattern in the equatorial Pacific. Large-scale circulation in convecting atmosphere is a challenging problem that has attracted considerable interest in the last decades.

The treatment of clouds and convection processes in contemporary numerical models for weather and climate prediction is an equally important problem. *General circulation models* (GCM) used for global climate predictions discretize the primitive equations for the atmosphere on a three dimensional grid with a horizontal grid resolution of about 100 km. Subgrid-scale processes, such as convective clouds and radiation, are not resolved by the model and their effects must be accounted for using *parameterization* schemes. The poor representation of cloud processes is believed to be one of the main source of uncertainty in GCMs, and the formulation of new and improved convection parameterizations has been an area of intensive research for the last few decades.

Following the pioneering earlier work of Smagorinsky, Manabe and Smagorinsky (1967) introduced the idea of *moist convective adjustment* (MCA), which led to the first generation of cumulus parameterization schemes. MCA techniques were later replaced by more realistic parameterizations, like the Kuo-scheme in 1974 which is based on the observed correlation between large-scale moisture convergence and convection (Kuo, 1974). The same year, Arakawa and Schubert (Arakawa and Schubert, 1974) formulated a parameterization based on the quasi-equilibrium assumption, which assumes a large separation between the subgrid- and grid-scales processes. While these models constitute the benchmark of parameterizations used in GCMs today, their purely deterministic closures do not capture the highly intermittent dynamics and variability of organized tropical convection. Since then, many improvements in GCM came with the development of stochastic parameterizations (Lin and Neelin, 2003; Majda and Khouider, 2002), which encode model uncertainties as probability distributions and use convection statistics to represent the dynamics.

More recently, Khouider et al. (2010) introduced the stochastic multicloud model (SMCM) for organized tropical convection, a cumulus parameterization based on a birth–death stochastic process that evolves the populations of three cloud types (congestus, deep, and stratiform) that are observed to characterize tropical convection (Johnson et al., 1999; Kiladis et al., 2005; Lin and Johnson, 1996). Recent satellite observations have revealed that organized tropical convective systems have qualitatively a self-similar structure composed of three main building blocks: Congestus cloud decks, with a vertical extent that does not exceed the freezing level (5 or 6 km), are followed by deep convective towers that extend to the top of the troposphere, which in turn are lagged by stratiform anvils in their dissipation phase (see Figure 1.1). Congestus clouds heat the lower troposphere due to condensational heating and induce upper troposphere cooling because of detrainment at their tops and by blocking long wave radiation from the surface. Deep convective towers dominate the core of the storm and are believed to be responsible for most of the tropical rainfall and provide the bulk heating for the whole tropospheric column. Finally, stratiform anvil clouds heat the upper troposphere and cool the lower troposphere due to the evaporation of stratiform rain.

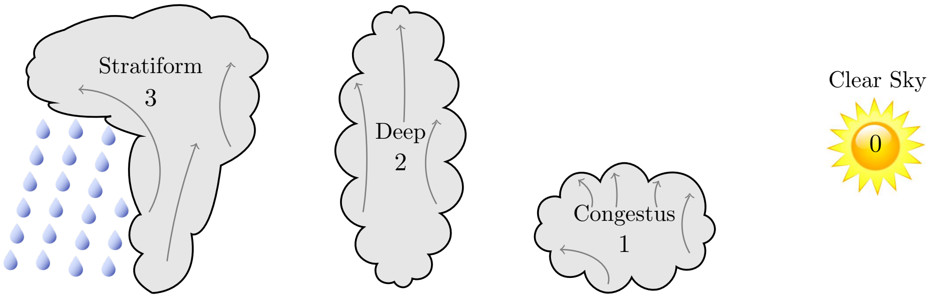

Figure 1.1: Recent analysis of observations have provided strong evidence that large-scale tropical convective systems involve three main cloud populations: shallow/congestus, deep penetrative cumulus clouds, and stratiform clouds. All three clouds are associated with trimodal distributions of heating profiles, divergence, cloud detrainment, and fractional cloudiness.

The SMCM has been shown in various idealized climate simulations to reasonably simulate tropical convection and improve the associated wave-like features, and intermittency of coherent structures that contribute to higher variability (Frenkel et al., 2012, 2013; Khouider et al., 2010). In Frenkel et al. (2012) and Khouider et al. (2013a), the authors study flows along the equator using the SMCM coupled with a toy GCM and obtain realistic mean Walker type circulations with wave like features that are analog to the convectively coupled waves observed in nature. More recently, Deng et al. (2015) coupled the SMCM to an aquaplanet GCM for simulations of the Madden-Julian oscillation (Madden and Julian, 1972).

1.1 Objectives

The central goal of this thesis is twofold. First, we study the organization of convection and its interaction with the large-scale circulation using a zonally symmetric atmospheric model coupled to the multicloud convective parameterization. The main model is based on the hydrostatic Boussinesq equations on a rotating sphere, and is composed of a deep convective troposphere and a dynamical atmospheric boundary layer (ABL) to sustain shallow convection. The free troposphere wave dynamics is truncated to the barotropic and first two baroclinic modes, and the free troposphere moist dynamics are represented through a vertically averaged large-scale moisture equation. The ABL dynamics are averaged over the mixed layer depth, below cloud base, and includes equations for velocity, potential and equivalent potential temperatures. The resulting system of nonconservative partial differential equations is solved numerically by combining some state-of-the art methods of hyperbolic systems, namely, the wave propagation method of LeVeque (1997) and the non-oscillatory central scheme of Nessyahu and Tadmor (1990), using the splitting strategy of Strang (1968). The impacts of different multicloud parameter regimes on the initiation and propagation of convection and mean meridional circulation are investigated in nonlinear simulations.

In the second part of the thesis, we focus on the SMCM and the important problem of using empirical data to inform our knowledge of model parameters. The SMCM dynamics is shown to be crucially linked to the choice of seven cloud timescale parameters that define transition rates from one cloud type to another. More precisely, the equilibrium distributions of cloud populations are primarily determined by the large-scale environment, and these seven cloud timescales. Our goal is to develop a rigorous statistical method to estimate the cloud timescales from atmospheric data. We formulate the parameter estimation problem within a Bayesian framework to derive the posterior distribution over the model parameters. The main challenge of this method is the calculation of the model likelihood function that involves the repeated evaluation of large matrix exponentials. To overcome this difficulty, we develop a parallel numerical technique that allows for fast and scalable approximations of large sparse matrix exponentials, without sacrificing accuracy. The high dimensional posterior distribution is sampled using the standard Markov Chain Monte Carlo (MCMC) method and the posterior simulator is validated against synthetic data. Finally, we conduct an inference study using the Giga-LES dataset (Khairoutdinov et al., 2009), a large-eddy simulation of deep convection over the tropical Atlantic that uses high enough resolution to realistically simulate clouds and some of the associated turbulent eddies.

The statistically inferred parameters from the Giga-LES dataset, which are obtained by way of the rigorous Bayesian methodology developed in Part II of the thesis, are used in Part I to simulate a mock Hadley circulation and monsoon-like dynamics. The Giga-LES parameter regime is compared with an ad hoc choice of parameters, used in Frenkel et al. (2012) to simulate zonally propagating convectively coupled waves and the Walker circulation. We show from the results of stochastic simulations that the Giga-LES parameter regime is much superior in terms of capturing some features of the Hadley circulation and monsoon trough dynamics.

1.2 Outline

The thesis is divided into two parts: Part I describes a zonally symmetric model for Hadley monsoon circulation and Part II looks at the parameter estimation problem for the SMCM. Part I is divided into Chapters 2, 3, and 4, while Part II comprises Chapters 5 and 6.

In Part I, the fluid dynamic model for meridional circulation is introduced in Chapter 2 and both the free troposphere and boundary layer dynamics are considered. In Chapter 3, the numerical scheme for the full model is explained, covering background theory and grid convergence error analysis. Chapter 4 presents simulations of mock Hadley-monsoon flow obtained with both the deterministic and stochastic multicloud models.

Chapter 5 introduces the Bayesian inference model and gives a detailed description of the parallel numerical method involved in the calculation of the model likelihood function. The second part of the chapter presents model validation results using synthetic experiments. The inference study using the simulated Giga-LES dataset is the topic of Chapter 6.

Part I

Zonally Symmetric Model for Hadley Circulation and Monsoon Dynamics

In this first part of the thesis, we develop a zonally symmetric atmospheric model for the large-scale flow which incorporates both the small-scale effect of deep tropospheric convection and a dynamical boundary layer that sustains shallow convection. This axially symmetric model allows to study the propagation and initiation of convection and its interaction with the large-scale circulation without the effects of zonally propagating atmospheric waves.

Such axially symmetric models have been used by several authors to study meridional circulation features and Hadley-monsoon dynamics. Drbohlav and Wang (2005) emphasized the importance of the barotropic and baroclinic modes in the propagation and initiation of convection and studied monsoon intraseasonal oscillation using a 2D axially symmetric model. Pauluis (2004) used an axisymmetric model to investigate the role of the atmospheric boundary layer in the Hadley circulation.

Here the model describes the free tropospheric nonlinear wave dynamics using the barotropic and first two baroclinic modes, and incorporates the stochastic multicloud model of Khouider et al. (2010) to represent the unresolved features of organized tropical convection. It explicitly includes the effect of a bulk boundary layer dynamics which has been shown to enhance the instability of convectively coupled gravity waves and organization of convection at planetary scale in the form of a standing congestus mode (Waite and Khouider, 2009).

Results from nonlinear stochastic simulations are presented and demonstrate that the model reproduce well the mean local Hadley cell structure and some monsoon-like features such as the signature of the monsoon trough and convective mesoscale variability.

Chapter 2

Fluid Dynamics Model for Meridional Circulation

2.1 Primitive Equations for the Free Troposphere

The fluid mechanics of the atmosphere is governed by a set of nonlinear partial differential equations that describe the fundamental principles of conservation of momentum, mass, and energy of a fluid in motion. The atmospheric and other geophysical flows are characterized by the effects of stratification and rotation: The Earth's gravitational field leads to a stratified density distribution with height, and the Earth's rotation leads to the important Coriolis force (Majda, 2003; Stechmann, 2008; Vallis, 2006). Moreover, the atmosphere behaves much like a shallow layer of fluid, because its depth is much less then its horizontal extent. By making appropriate scaling arguments, the full Navier-Stokes equations can be reduced into simpler equations whose dynamics is dominated by the interaction of the Coriolis and buoyancy forces. These are the so-called *equatorial hydrostatic Boussinesq equations* (Emanuel, 1994; Majda, 2003; Vallis, 2006). To study the meridional structure of the flow and in an attempt to mitigate the influence of zonally propagating waves on the meridional dynamics, e.g. the Hadley cell and the monsoon circulation, we consider here a zonal average of these equations, leading to the *zonally averaged equatorial hydrostatic Boussinesq equations*:

$$\frac{\partial u}{\partial t} + v\frac{\partial u}{\partial y} + w\frac{\partial u}{\partial z} - \beta y v = 0 \qquad \text{(conservation of momentum in } x\text{)} \qquad (2.1.1a)$$

$$\frac{\partial v}{\partial t} + v\frac{\partial v}{\partial y} + w\frac{\partial v}{\partial z} + \beta y u = -\frac{\partial p}{\partial y} \qquad \text{(conservation of momentum in } y\text{)} \qquad (2.1.1b)$$

$$\frac{\partial p}{\partial z} = g\frac{\theta}{\theta_{ref}} \qquad \text{(hydrostatic balance)} \qquad (2.1.1c)$$

$$\frac{\partial \theta}{\partial t} + v\frac{\partial \theta}{\partial y} + w\frac{\partial \theta}{\partial z} + w\frac{d\theta_0}{dz} = 0 \qquad \text{(thermodynamic energy equation)} \qquad (2.1.1d)$$

$$\frac{\partial v}{\partial y} + \frac{\partial w}{\partial z} = 0 \qquad \text{(divergence free condition)} \qquad (2.1.1e)$$

Here x, y, z are, respectively, the zonal, meridional, and vertical coordinates with positive directions from West to East, South to North, and bottom to top, respectively; $t > 0$ is time. The horizontal velocity $\boldsymbol{u} = (u, v)$ has zonal (along the Equator) component u and meridional (North–South) component v. The vertical velocity is w. The scalars p and θ are the pressure and potential temperature (i.e. the temperature that a parcel of air would have if displaced adiabatically to a reference pressure) pertubations, respectively. A zero pressure differential at the endpoints is assumed in the (zonal) x-direction. The effective total potential temperature θ_{tot} is expressed as

$$\theta_{tot}(y, z, t) = \theta_{ref} + \theta_0(z) + \theta(y, z, t), \qquad (2.1.2)$$

where $\theta_{ref} = 300$ K is a reference potential temperature, θ_0 sets the background stratification, and θ is the deviation from this background. The background state θ_0

is related to the Brunt–Väisälä buoyancy frequency N_v according to

$$N_v^2 = \frac{g}{\theta_{ref}} \frac{d\theta_0}{dz} = 10^{-4}\,\mathrm{s}^{-2}, \tag{2.1.3}$$

where $g = 9.8$ ms^{-2} is the gravitational acceleration. β is the gradient of the Coriolis parameter $f(y) = 2\Omega \sin(y)$ (Ω is the Earth's rotational frequency) at the Equator:

$$\beta = \left.\frac{\partial f(y)}{\partial y}\right|_{y=0} = 2.28 \times 10^{-11}\mathrm{m}^{-1}\mathrm{s}^{-1}.$$

We next turn our attention to the scaling of the equations. We nondimensionalize the variables as

$$\begin{aligned} &(u,v) = c(\hat{u},\hat{v}), \qquad && w = \nu \hat{w}, \qquad && p = c^2 \hat{p}, \qquad && \theta = \alpha \hat{\theta}, \\ &(x,y) = L(\hat{x},\hat{y}), && z = \frac{H_T}{\pi}\hat{z}, && t = T\hat{t}, && \end{aligned} \tag{2.1.4}$$

where the caret variables are dimensionless and of order unity, and $H_T = 16$ km is the height of the troposphere. As referenced earlier, we need to use appropriate scalings to impose a regime where both the rotation and stratification are important. Such a regime is obtained with the following scaling relationships (Khouider et al., 2013b; Stechmann, 2008):

- the first baroclinic dry gravity wave speed $c = \dfrac{N_v H_T}{\pi} \approx 50$ ms^{-1} as the velocity scale;

- the equatorial Rossby deformation radius $L = \sqrt{c/\beta} \approx 1500$ km as a horizontal length scale;

- the equatorial timescale $T = L/c \approx 8$ hrs;

- the dry-static stratification $\alpha = \dfrac{H_T N_v^2 \theta_{ref}}{\pi g} \approx 15$ K as the temperature scale;

- the free troposphere vertical velocity and length scales $\nu = H_T/T\pi \approx 0.17$ m/s and H_T/π, respectively;

- and the pressure p scales as c^2.

Note that while the vertical velocity in the free troposphere scales as ν, its typical scale is smaller in the thin turbulent layer just above the surface and under the free troposphere (called the atmospheric boundary layer; See Section 2.2 and, in particular, the scalings 2.2.14).

The equatorial hydrostatic Boussinesq equations (2.1.1) are obtained from the incompressible Navier-Stokes equations (see Batchelor, 2000) by making important approximations which are based on these scalings. These approximations, described in Emanuel (1994) and Vallis (2006), are summarized next.

(i) *The equatorial β-plane approximation.* It is obtained by linearizing the Coriolis force $f(y) = 2\Omega\sin(y)$ about a latitude of reference $y = y_0$: $f(y) \approx f_0 + \beta(y - y_0)$. If $y_0 = 0$, the Equator, then $f_0 = 0$ and $f(y) \approx \beta y$. Since the Coriolis force acts perpendicular to the direction of motion, it enters in (2.1.1a-2.1.1b) as $\beta y \boldsymbol{u}^{\perp}$, where $\boldsymbol{u}^{\perp} = (-v, u)$. The vertical component of the Coriolis force is neglected.

(ii) *The hydrostatic approximation.* In the vertical momentum equation, the vertical pressure gradient force is assumed to be balanced by the gravity force, so that

$$\frac{\partial p}{\partial z} = g\frac{\theta}{\theta_{ref}}.$$

This approximation is valid when the vertical length scale is much smaller then the horizontal length scale (shallow fluid), i.e. $H_T/L << 1$. In such case, the inertial term in the vertical momentum equation is orders of magnitude less then the pressure and gravitational terms and may be neglected. Thus, in a hydrostatic atmosphere, large vertical accelerations of ascending parcels of air do not take form.

(iii) *The Boussinesq approximation.* In this approximation, density is replaced by a constant mean value everywhere, except in the buoyancy term in the vertical momentum equation. Hence density variations are only allowed when coupled with gravity. The Boussinesq approximation also implies that the flow of density ρ is incompressible, i.e. $D\rho/Dt = 0$ (D/Dt the material derivative), leading to the divergent-free equation (2.1.1e).

Parameter or Scaling Factors	Derivation	Approximate Value	Description
H_T		16 km	Tropopause height
θ_{ref}		300 K	Reference potential temperature
g		9.8 m/s	Gravitational acceleration
θ_0		function of height z	Background potential temperature, in K
N_v	$\sqrt{\frac{g}{\theta_{ref}}\frac{d\theta_0}{dz}}$	10^{-2} s^{-1}	Brent-Väisälä buoyancy frequency
c	$N_v H_T/\pi$	50 m/s	Horizontal velocity scale
β	$\left.\frac{\partial f(y)}{\partial y}\right\|_{y=0}$	2.28e–11m^{-1}s^{-1}	Variation of Coriolis parameter f at the Equator
L	$\sqrt{c/\beta}$	1500 km	Equatorial Rossby deformation radius/Horizontal length scale
T	L/c	8 hrs	Reference timescale
α	$\frac{H_T N_v^2 \theta_{ref}}{\pi g}$	15 K	Potential temperature scale
ν	$\frac{H_T}{\pi T}$	0.17 m/s	Free troposphere vertical velocity scale

Table 2.1: Troposphere model parameters and scaling factors

Using the scalings (2.1.4), we finally come to the scaled forms of the equatorial hydrostatic Boussinesq equations on the β-plane. These are, in the absence of viscous and body forces:

$$\frac{\partial \hat{u}}{\partial \hat{t}} + \hat{v}\frac{\partial \hat{u}}{\partial \hat{y}} + \hat{w}\frac{\partial \hat{u}}{\partial \hat{z}} - \hat{y}\hat{v} = 0, \tag{2.1.5a}$$

$$\frac{\partial \hat{v}}{\partial \hat{t}} + \hat{v}\frac{\partial \hat{v}}{\partial \hat{y}} + \hat{w}\frac{\partial \hat{v}}{\partial \hat{z}} + \hat{y}\hat{u} = -\frac{\partial \hat{p}}{\partial \hat{y}}, \tag{2.1.5b}$$

$$\frac{\partial \hat{p}}{\partial \hat{z}} = \hat{\theta}, \tag{2.1.5c}$$

$$\frac{\partial \hat{\theta}}{\partial \hat{t}} + \hat{v}\frac{\partial \hat{\theta}}{\partial \hat{y}} + \hat{w}\frac{\partial \hat{\theta}}{\partial \hat{z}} + \hat{w} = 0, \tag{2.1.5d}$$

$$\frac{\partial \hat{v}}{\partial \hat{y}} + \frac{\partial \hat{w}}{\partial \hat{z}} = 0. \tag{2.1.5e}$$

For the remainder of this thesis and unless specified otherwise, the carets will be dropped from the nondimensional variables for convenience, unless otherwise specified.

2.1.1 Decomposition Into Vertical Modes

It was noted in Section 2.1 that the atmosphere is generally not a homogeneous fluid. Instead it is composed of fluid parcels of various densities which, under gravity, tends to arrange itself so that heavier fluid parcels are found below lighter fluid parcels. When the stratification is mostly vertical (mean vertical gradient of density large compared with the horizontal gradient), gravity waves can be sustained internally. This can only happen when the atmosphere is *stably* stratified (higher densities below lower densities), so that a fluid parcel displaced vertically will undergo buoyancy oscillations, with frequency (in dimensional units)

$$N_v = \sqrt{\frac{g}{\theta_{ref}}\frac{d\theta_0}{dz}}. \tag{2.1.6}$$

Here we consider $N_v^2 > 0$ constant, or that the background stratification $\theta_0(z)$ is an increasing linear function of height z. A Boussinesq fluid with such stratification and well defined upper and lower boundaries (rigid or free) supports an infinite set $j = 1, 2, 3, \cdots$ of gravity waves with phase speeds c_j and sinusoid vertical profiles $\sin(jz)$, also called modes (see Majda, 2003). When the dynamics is linear, the waves are decoupled but in the nonlinear case, the waves are coupled and interact nonlinearly one with another.

In several recent models for organized tropical convection, the wave dynamics is truncated with the first two vertical modes $j = 1, 2$, as these account for most of the heating profile and cloud structure observed in the tropics (see Haertel and Kiladis, 2004; Khouider and Majda, 2006a,b,c, 2007; Majda et al., 2007; Mapes, 2000; Mapes and Houze, 1995; Stechmann, 2008).

Before looking at the nonlinear primitive equations, the vertical mode decomposition is illustrated for the linearized equations around a background at rest. In the linear case, the flow is shown to decompose into a spectrum of linear gravity waves each satisfying an independent set of equations.

Linearized rotating hydrostatic Boussinesq equations

Linearizing the zonally averaged dimensional primitive equations (2.1.1) with a zero basic state $\overline{\boldsymbol{u}} = \overline{w} = \overline{p} = \overline{\theta} = 0$ gives for the perturbation motion (in dimensional units):

$$\frac{\partial \boldsymbol{u}}{\partial t} + \beta y \boldsymbol{u}^{\perp} = -\nabla p, \tag{2.1.7a}$$

$$\frac{\partial p}{\partial z} = \frac{g}{\theta_{ref}} \theta, \tag{2.1.7b}$$

$$\frac{\partial \theta}{\partial t} + \frac{\theta_{ref}}{g} N_v^2 w = 0, \tag{2.1.7c}$$

$$\frac{\partial v}{\partial y} + \frac{\partial w}{\partial z} = 0, \tag{2.1.7d}$$

$$w\Big|_{z=0,H_T} = 0. \tag{2.1.7e}$$

The rigid lid condition is added in (2.1.7e): The fluid is assumed to come at rest perpendicular to the Earth's surface ($z = 0$), and to the tropopause ($z = H_T$). Immediately, we use (2.1.7b) and (2.1.7c) to find that

$$w = -\frac{1}{N_v^2} \frac{\partial^2 p}{\partial t \partial z}; \tag{2.1.8}$$

Viz. the stronger the stratification, i.e. larger N_v^2, the weaker the vertical velocity and vertical displacements. We assume that we can separate the variables and write the solution as

$$\begin{pmatrix} \boldsymbol{u} \\ p \end{pmatrix} (y, z, t) = \sum_{j=0}^{\infty} \begin{pmatrix} \boldsymbol{u}_j(y, t) \\ p_j(y, t) \end{pmatrix} C_j(z). \tag{2.1.9}$$

Substituting this ansatz into (2.1.8) and (2.1.7d) and combining gives the condition

$$\sum_{j=0}^{\infty} \left(C_j \frac{\partial v_j}{\partial y} - \frac{C_j''}{N_v^2} \frac{\partial p_j}{\partial t} \right) = 0, \qquad j = 0, 1, 2, \cdots. \tag{2.1.10}$$

This can naturally be satisfied if we have

$$N_v^2 \frac{\partial v_j}{\partial y} \left(\frac{\partial p_j}{\partial t} \right)^{-1} = \frac{C_j''}{C_j}, \qquad j = 0, 1, 2, \cdots.$$

Since the left and right-hand terms are functions of (y, t) and z, separately, they must be constants. In particular, for m_j constant, we can set

$$C_j'' + m_j^2 C_j = 0, \qquad j = 0, 1, 2, \cdots. \tag{2.1.11}$$

The rigid lid boundary conditions yield $C_j'|_{z=0,H_T} = 0$ (from (2.1.8) and the ansatz (2.1.9)) for $j = 0, 1, 2, \cdots$, and define the simplest possible solutions to the vertical structure equations (2.1.11):

$$C_j(z) = \cos(m_j z) \quad \text{with} \quad m_j = \frac{j\pi}{H_T}, \qquad j = 0, 1, 2, \cdots. \tag{2.1.12}$$

The cosines $C_j(z)$ form a complete orthogonal basis set of modes of vertical structure, whose discrete spectrum reconstitute the continuous pressure and horizontal winds as the infinite sums (2.1.9). To each mode j corresponds a local (for fixed y) standing wave of wind (pressure) amplitude $\boldsymbol{u}(y, t)$ ($p_j(y, t)$) and vertical structure $C_j(z)$, which arises through the reflection at the boundaries. While the atmosphere has no such fixed upper boundary (the tropopause) and that, strictly speaking, it is not composed of these normal modes of vertical structure, modal decomposition has been used by many authors (see Haertel and Kiladis, 2004; Khouider and Majda, 2006c, 2007; Mapes, 2000) as a relatively realistic model for the stratified tropical atmosphere.

Using the ansatz (2.1.9), we now find from the hydrostatic equation (2.1.7b) and incompressibility condition (2.1.7d) that the potential temperature and vertical wind are given by the expansions

$$\begin{pmatrix} \theta \\ w \end{pmatrix}(y,z,t) = \begin{pmatrix} 0 \\ w_0(y,t)z \end{pmatrix} + \sum_{j=1}^{\infty} \begin{pmatrix} \theta_j(y,t)j \\ w_j(y,t) \end{pmatrix} S_j(z), \tag{2.1.13}$$

with wave amplitudes

$$w_0 = \frac{\partial v_0}{\partial y}, \tag{2.1.14}$$

$$\theta_j = -\frac{\theta_{ref}}{g}\frac{\pi}{H_T}p_j, \qquad w_j = -\frac{1}{j}\frac{H_T}{\pi}\frac{\partial v_j}{\partial y}, \quad j = 1, 2, \cdots. \tag{2.1.15}$$

and vertical structure modes

$$S_j(z) = \sin\left(\frac{j\pi z}{H_T}\right), \quad j = 1, 2, \cdots. \tag{2.1.16}$$

Note that unlike $\boldsymbol{u}$ that has a mode $j = 0$ with no vertical structure, called the *barotropic* mode, θ has only z-dependent *baroclinic* modes, that is, modes with $j = 1, 2, 3, \cdots$. The first few modes of vertical structure are illustrated for $\boldsymbol{u}$ and θ in Figure 2.1. Moreover, the convention here is to expand θ in the basis jS_j but w in the basis S_j.

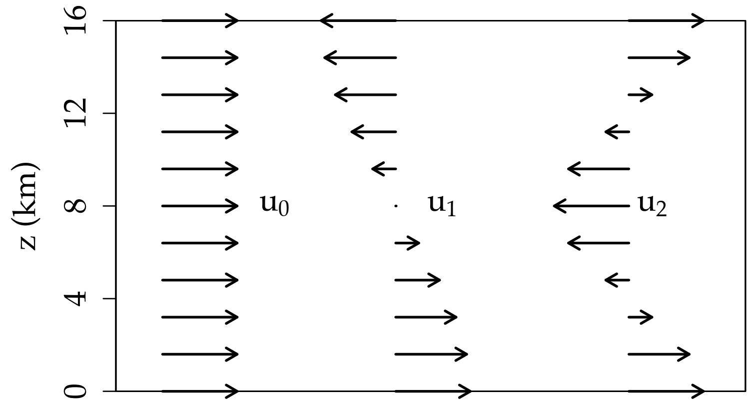

(a) Barotropic mode u_0 and first two baroclinic modes u_1 and u_2.

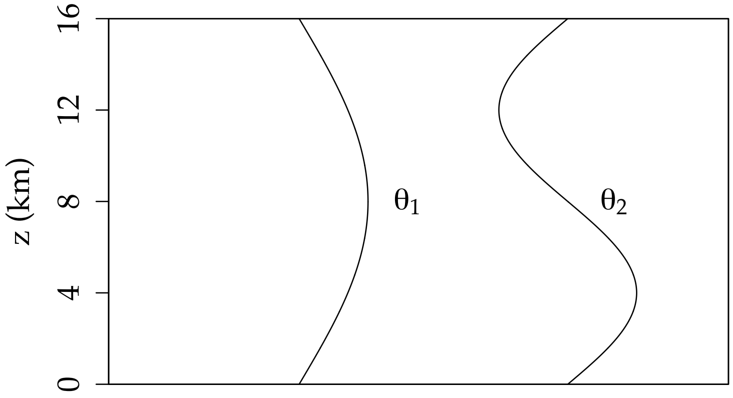

(b) First two baroclinic modes θ_1 and θ_2.

Figure 2.1: First few modes of vertical structure for the zonal wind u and potential temperature θ.

The equations for the wave mode j are obtained by projecting the linearized primitive equations (2.1.7) onto the basis functions C_j and S_j, following the standard Galerkin approach (see Evans, 1998). The resulting equations for the barotropic mode

$j = 0$ are the rotating linear 1D incompressible fluid equations:

$$\frac{\partial \boldsymbol{u}_0}{\partial t} + \beta y \boldsymbol{u}_0^{\perp} + \nabla p_0 = 0, \tag{2.1.17a}$$

$$\frac{\partial v_0}{\partial y} = 0. \tag{2.1.17b}$$

From this we learn that i) the barotropic mode carries only a horizontal velocity, that is,

$$w_0 = \frac{\partial v_0}{\partial y} = 0, \tag{2.1.17c}$$

and ii) the (1D) divergence of the horizontal barotropic flow is zero. However, as we will see in Section 2.3, this is no longer the case when a mechanical boundary layer is included. The barotropic pressure p_0 can be determined from v_0 by taking the divergence of (2.1.17a). For each other mode $j = 1, 2, 3, \cdots$, the equations that arise are the *rotating linear 1D shallow water equations* (see Majda, 2003, Section 4.1):

$$\frac{\partial \boldsymbol{u}_j}{\partial t} + \beta y \boldsymbol{u}_j^{\perp} - \frac{j^2 c_j^2}{\alpha} \nabla \theta_j = 0, \tag{2.1.17d}$$

$$\frac{\partial \theta_j}{\partial t} - \frac{\alpha}{j^2} \frac{\partial v_j}{\partial y} = 0, \qquad j = 1, 2, 3, \cdots, \tag{2.1.17e}$$

where $c_j = \frac{N_v H_T}{j\pi} = \frac{N_v}{m_j}$ is the wavespeed of the jth baroclinic mode, and α is the potential temperature scale (see Table 2.1). Moreover, the baroclinic modes $j = 1, 2, 3, \cdots$ carry the non-trivial vertical velocity and potential temperature components (2.1.15). The linear gravity waves supported by the equations (2.1.17) are decoupled: the waves of mode j evolve independently from the waves of mode k ($k \neq j$).

Nonlinear rotating hydrostatic Boussinesq equations: The barotropic – first two baroclinic mode system.

We return to the nonlinear (zonally averaged) primitive equations on the equatorial β-plane, equations (2.1.5), which we supplement for now with the rigid lid condition at the Earth's surface, and at the top of the troposphere:

$$\begin{aligned}
\frac{\partial u}{\partial t} + v\frac{\partial u}{\partial y} + w\frac{\partial u}{\partial z} - yv &= \mathcal{S}^u, && \text{(2.1.18a)}\\
\frac{\partial v}{\partial t} + v\frac{\partial v}{\partial y} + w\frac{\partial v}{\partial z} + yu &= -\frac{\partial p}{\partial y} + \mathcal{S}^v, && \text{(2.1.18b)}\\
\frac{\partial p}{\partial z} &= \theta, && \text{(2.1.18c)}\\
\frac{\partial \theta}{\partial t} + v\frac{\partial \theta}{\partial y} + w\frac{\partial \theta}{\partial z} + w &= \mathcal{H}^\theta + \mathcal{S}^\theta, && \text{(2.1.18d)}\\
\frac{\partial v}{\partial y} + \frac{\partial w}{\partial z} &= 0, && \text{(2.1.18e)}\\
w\Big|_{z=0,\pi} &= 0. && \text{(2.1.18f)}
\end{aligned}$$

Note that the troposphere has nondimensionalized vertical extent $0 \le z \le \pi$, and the stratification θ_0 is now absorbed in the nondimensionalization (see Table 2.1). The forcing terms $\mathcal{S}^u$, $\mathcal{S}^v$, $\mathcal{H}^\theta$ and $\mathcal{S}^\theta$ are added to represent the sources and sinks of zonal and meridional momentum, and potential temperature, respectively. Following Waite and Khouider (2009), we impose the following ansatz of truncating the wave dynamics to the first three modes of vertical structure:

$$\begin{pmatrix} \boldsymbol{u} \\ p \end{pmatrix}(y,z,t) = \begin{pmatrix} \boldsymbol{u}_0 \\ p_0 \end{pmatrix}(y,t) + \begin{pmatrix} \boldsymbol{u}_1 \\ p_1 \end{pmatrix}(y,t)C_1(z) + \begin{pmatrix} \boldsymbol{u}_2 \\ p_2 \end{pmatrix}(y,t)C_2(z), \qquad \text{(2.1.19)}$$

and

$$\begin{pmatrix} \theta \\ w \end{pmatrix}(y,z,t) = \begin{pmatrix} \theta_1 \\ w_1 \end{pmatrix}(y,t)S_1(z) + \begin{pmatrix} 2\theta_2 \\ w_2 \end{pmatrix}(y,t)S_2(z). \tag{2.1.20}$$

The basis functions take the form

$$\begin{aligned} S_1(z) &= \sqrt{2}\sin(z), \qquad S_2(z) = \sqrt{2}\sin(2z), \\ C_1(z) &= \sqrt{2}\cos(z), \qquad C_2(z) = \sqrt{2}\cos(2z). \end{aligned} \tag{2.1.21}$$

The factors $\sqrt{2}$ are added to obtain an orthonormal basis in the given L_2 inner product $\langle F, G\rangle = \frac{1}{\pi}\int_0^\pi F(z)G(z)dz$ that is, $\langle C_i, C_j\rangle = \delta_{ij}$ and $\langle S_i, S_j\rangle = \delta_{ij}$. As in the linear case, the vertical velocity and potential temperature have no barotropic mode. The potential temperature and vertical velocity baroclinic wave amplitudes are found by substituting (2.1.19) and (2.1.20) into the hydrostatic equation (2.1.18c) and incompressibility condition (2.1.18e):

$$\boxed{\theta_j = -p_j, \qquad w_j = -\frac{1}{j}\frac{\partial v_j}{\partial y}, \qquad j = 1, 2.} \tag{2.1.22}$$

Projecting equations (2.1.18) onto the barotropic mode gives:

$$\frac{D_0 u_0}{Dt} + \frac{\partial\left(u_1 v_1\right)}{\partial y} + \frac{\partial\left(u_2 v_2\right)}{\partial y} - y v_0 = \mathcal{S}_0^u, \tag{2.1.23a}$$

$$\frac{D_0 v_0}{Dt} + \frac{\partial (v_1^2)}{\partial y} + \frac{\partial (v_2^2)}{\partial y} + y u_0 = -\frac{\partial p_0}{\partial y} + \mathcal{S}_0^v, \tag{2.1.23b}$$

$$\frac{\partial v_0}{\partial y} = 0. \tag{2.1.23c}$$

Here $(D_0/Dt) = (\partial/\partial t) + v_0(\partial/\partial y)$ is the meridional barotropic transport operator. Projecting the equations (2.1.18) onto the first and second baroclinic modes gives

$$\boxed{\begin{aligned}
&\frac{D_0 u_1}{Dt} + v_1\frac{\partial u_0}{\partial y} + \frac{\sqrt{2}}{2}\left(v_1\frac{\partial u_2}{\partial y} + v_2\frac{\partial u_1}{\partial y} + 2u_2\frac{\partial v_1}{\partial y} + \frac{1}{2}u_1\frac{\partial v_2}{\partial y}\right) - yv_1 = \mathcal{S}_1^u,\\
&\frac{D_0 v_1}{Dt} + v_1\frac{\partial v_0}{\partial y} + \frac{\sqrt{2}}{2}\left(v_1\frac{\partial v_2}{\partial y} + v_2\frac{\partial v_1}{\partial y} + 2v_2\frac{\partial v_1}{\partial y} + \frac{1}{2}v_1\frac{\partial v_2}{\partial y}\right) + yu_1 = \frac{\partial \theta_1}{\partial y} + \mathcal{S}_1^v,\\
&\frac{D_0 \theta_1}{Dt} - \frac{\partial v_1}{\partial y} + \frac{\sqrt{2}}{2}\left(2v_1\frac{\partial \theta_2}{\partial y} - v_2\frac{\partial \theta_1}{\partial y} + 4\theta_2\frac{\partial v_1}{\partial y} - \frac{1}{2}\theta_1\frac{\partial v_2}{\partial y}\right) = \mathcal{H}_1^\theta + \mathcal{S}_1^\theta,
\end{aligned}}\qquad
\begin{aligned}&(2.1.24a)\\&(2.1.24b)\\&(2.1.24c)\end{aligned}$$

and

$$\boxed{\begin{aligned}
\frac{D_0 u_2}{Dt} + v_2\frac{\partial u_0}{\partial y} + \frac{\sqrt{2}}{2}\left(v_1\frac{\partial u_1}{\partial y} - u_1\frac{\partial v_1}{\partial y}\right) - yv_2 &= \mathcal{S}_2^u,\\
\frac{D_0 v_2}{Dt} + v_2\frac{\partial v_0}{\partial y} + yu_2 &= \frac{\partial \theta_2}{\partial y} + \mathcal{S}_2^v,\\
2\frac{D_0 \theta_2}{Dt} + \frac{\sqrt{2}}{2}\left(v_1\frac{\partial \theta_1}{\partial y} - \theta_1\frac{\partial v_1}{\partial y}\right) - \frac{1}{2}\frac{\partial v_2}{\partial y} &= \mathcal{H}_2^\theta + \mathcal{S}_2^\theta,
\end{aligned}}\qquad
\begin{aligned}&(2.1.25a)\\&(2.1.25b)\\&(2.1.25c)\end{aligned}$$

where the baroclinic relationships $p_j = -\theta_j$ and $w_j = -\frac{1}{j}\frac{\partial v_j}{\partial y}$ were used. Equations (2.1.22), (2.1.23), (2.1.24) and (2.1.25) will be termed *3-mode free troposphere model* (3MoFTM). In the remainder of this chapter, we will gradually modify the 3MoFTM through the addition of (1) a mechanical atmospheric boundary layer and (2) radiative/convective forcing terms $\mathcal{S}^u$, $\mathcal{S}^v$, $\mathcal{S}^\theta$, and $\mathcal{H}^\theta$.

2.2 Bulk Equation Model for the Atmospheric Boundary Layer

The atmospheric boundary layer (ABL) is that part of the troposphere which is influenced directly by the presence of the Earth's surface. Our approach here is to "lift the bottom" of the 3MoFTM and place a mixed layer representation of the ABL under it. The ABL has depth $h_b = 500$m, and spans $-h_b \le z < 0$, in dimensional units.

The Earth's surface is now located at $z = -h_b$, and the ABL top is located at $z = 0$. The free troposphere maintains a vertical extent $0 \leq z \leq H_T$, and is capped at $z = H_T$ by the tropopause.

The ABL has depth of $\mathcal{O}(1\,\text{km})$, and responds to surface forcing with a timescale of an hour or less (see Stull, 1988). Thus, the land surface, which has a depth of $\mathcal{O}(100\,\text{m})$, and the boundary layer interaction is non negligible. Processes within the ABL determine the exchange of mass, energy, and momentum between the free troposphere and the underlying surface and, as such, it is the source of energy for tropical convection.

The ABL is a region dominated by turbulence, the irregular fluctuations that occur in fluid motions. The energy from the Earth's heated surface is transferred to the ABL by the mechanism of dry convection, and turbulence causes eddies which tends to mix the thermodynamic quantities of the ABL, stabilizing temperature. The highly turbulent nature of the ABL justifies the following approximations:

1. *Absence of stratification:* The ABL is assumed to be *well mixed* at all times such that no stratification is allowed to settle, that is, $N_v = 0$;
2. *Bulk model:* Since the ABL is effectively homogenized by the turbulence, a bulk description, following the approach of Stevens (2006), is considered (see also Arakawa and Schubert, 1974; Bellon and Stevens, 2005; Betts, 1976). The bulk model consists of integrating out the vertical dependencies to represent the bulk thermodynamic structure of the ABL over the surface, but away from regions of deep convection (free troposphere);

The ABL is represented as a well-mixed hydrostatic Boussinesq fluid on the β-plane.

The zonally averaged, dimensionless equations are (see (2.1.5)):

$$
\begin{aligned}
\frac{\partial u}{\partial t} + \frac{\partial (uv)}{\partial y} + \frac{\partial (uw)}{\partial z} - yv &= 0, && \text{(2.2.1a)}\\
\frac{\partial v}{\partial t} + \frac{\partial (v^2)}{\partial y} + \frac{\partial (vw)}{\partial z} + yu &= -\frac{\partial p}{\partial y}, && \text{(2.2.1b)}\\
\frac{\partial \theta}{\partial t} + \frac{\partial (\theta v)}{\partial y} + \frac{\partial (\theta w)}{\partial z} &= \mathcal{S}^\theta, && \text{(2.2.1c)}\\
\frac{\partial p}{\partial z} &= \theta, && \text{(2.2.1d)}\\
\frac{\partial v}{\partial y} + \frac{\partial w}{\partial z} &= 0, && \text{(2.2.1e)}\\
w|_{z=-\delta\pi} &= 0, && \text{(2.2.1f)}\\
0 \le z \le -\delta\pi.
\end{aligned}
$$

Here we used the same scaling relationships as for the treatment of the primitive equations (2.1.1), and the divergence relation (2.2.1e) was used to write the equations in flux form. The rigid lid condition is conserved at the Earth's surface located at $z = -\delta\pi$ in nondimensional units, where $\delta = h_b/H_T$. Note that the well mixed fluid has a vertically homogeneous background state θ_0, and hence the term due to stratification is absent from (2.2.1c). A forcing term $\mathcal{S}^\theta$ is added to the potential temperature equation.

ABL Equivalent Potential Temperature Equation The moist thermodynamics in the ABL is represented using the *equivalent potential temperature* θ_e, defined as (Emanuel, 1994):

$$\theta_e \approx \theta \exp\left(\frac{L_v q_v}{c_p T}\right), \tag{2.2.2}$$

where T is the temperature, L_v is latent heat of vaporization at 0°C, c_p is the heat capacity at constant pressure, and $q_v = \rho_v/\rho_d$, the water vapor mixing ratio i.e., the density of water vapor divided by the density of dry air. We readily augment the system (2.2.1) with an advection equation for the ABL perturbation equivalent potential temperature θ_e, with forcing:

$$\frac{\partial \theta_e}{\partial t} + \frac{\partial(\theta_e v)}{\partial y} + \frac{\partial(\theta_e w)}{\partial z} = \mathcal{S}^{\theta_e}. \tag{2.2.3}$$

In the remaining of this section we describe the bulk ABL model developed by Stevens (2006) (see also Waite and Khouider, 2009). In Section 2.2 we review the traditional Reynolds decomposition of a turbulent fluid into large and small turbulent scale components, and derive the bulk, or vertically averaged, equation sets. The bulk equations are then closed in Section 2.2.2 by specifying turbulent flux closures in terms of the large scale quantities.

2.2.1 ABL Bulk Equations

The turbulent flow in the ABL contains a range of small scales fluctuations that cannot be resolved and represented in the model. Conceptually, we can think of decomposing the flow into the resolved scales (slowly evolving, large-scale) and the unresolved scales (quickly evolving, small-scale). For a generic scalar field ϕ, we then make what is called a *Reynolds decomposition* (see Holton and Hakim, 2012):

$$\phi = \langle \phi \rangle + \phi',$$

where $\langle \phi \rangle$ and ϕ' are respectively the resolved and unresolved scales. The resolved scales are interpreted as an ensemble average over the statistics of the turbulent processes (or eddies) and by construction, $\langle \phi' \rangle = 0$. Applying Reynolds decomposition to (2.2.1) and performing an ensemble (time) average yields equations for the average, or expected values:

$$\begin{aligned}
\frac{\partial\langle u\rangle}{\partial t}+\frac{\partial(\langle v\rangle\langle u\rangle)}{\partial y}+\frac{\partial(\langle w\rangle\langle u\rangle)}{\partial z}-y\langle v\rangle &= -\frac{\partial\langle u'w'\rangle}{\partial z}, \\
\frac{\partial\langle v\rangle}{\partial t}+\frac{\partial(\langle v\rangle\langle v\rangle)}{\partial y}+\frac{\partial(\langle w\rangle\langle v\rangle)}{\partial z}+y\langle u\rangle &= -\frac{\partial\langle p\rangle}{\partial y}-\frac{\partial\langle v'w'\rangle}{\partial z}, \\
\frac{\partial\langle\theta\rangle}{\partial t}+\frac{\partial(\langle v\rangle\langle\theta\rangle)}{\partial y}+\frac{\partial(\langle w\rangle\langle\theta\rangle)}{\partial z} &= -\frac{\partial\langle\theta'w'\rangle}{\partial z}+\langle\mathcal{S}^{\theta}\rangle, \\
\frac{\partial\langle\theta_e\rangle}{\partial t}+\frac{\partial(\langle v\rangle\langle\theta_e\rangle)}{\partial y}+\frac{\partial(\langle w\rangle\langle\theta_e\rangle)}{\partial z} &= -\frac{\partial\langle\theta_e'w'\rangle}{\partial z}+\langle\mathcal{S}^{\theta_e}\rangle, \\
\frac{\partial\langle p\rangle}{\partial z} &= \langle\theta\rangle, \qquad (2.2.4a) \\
\frac{\partial\langle v\rangle}{\partial y}+\frac{\partial\langle w\rangle}{\partial z} &= 0. \qquad (2.2.4b)
\end{aligned}$$

The new terms $\langle u'w'\rangle$ and $\langle v'w'\rangle$ are vertical turbulent fluxes of horizontal momentum, whereas $\langle\theta'w'\rangle$ and $\langle\theta_e'w'\rangle$ are vertical turbulent heat and moisture fluxes. Horizontal turbulent fluxes $\langle u'v'\rangle$, $\langle v'v'\rangle$ are neglected, together with eddy fluctuations to the forcings $\mathcal{S}^{\theta}$ and $\mathcal{S}^{\theta_e}$. Note that by taking the hydrostatic approximation earlier (see Section 2.1), we assumed no vertical acceleration and, accordingly, we also have neglected the effect of turbulent vertical motions in (2.2.4a).

Defining ϕ_b to be the vertical average of $\langle\phi\rangle$ over the ABL of nondimensional depth $\delta\pi$, for a scalar ϕ (u, v, θ, or θ_e), i.e.

$$\phi_b=\frac{1}{\delta\pi}\int_{-\delta\pi}^{0}\langle\phi\rangle dz,$$

it is straightforward to show that

$$\begin{aligned}
\frac{\partial u_b}{\partial t}+\frac{\partial\left(v_b u_b\right)}{\partial y}+\frac{1}{\delta\pi}\langle w\rangle_t\langle u\rangle_t-yv_b &= -\frac{1}{\delta\pi}\langle u'w'\rangle_t+\frac{1}{\delta\pi}\langle u'w'\rangle_s, && \text{(2.2.5a)}\\
\frac{\partial v_b}{\partial t}+\frac{\partial\left(v_b^2\right)}{\partial y}+\frac{1}{\delta\pi}\langle w\rangle_t\langle v\rangle_t+yu_b &= -\frac{\partial p_b}{\partial y}-\frac{1}{\delta\pi}\langle v'w'\rangle_t+\frac{1}{\delta\pi}\langle v'w'\rangle_s, && \text{(2.2.5b)}\\
\frac{\partial \theta_b}{\partial t}+\frac{\partial\left(v_b\theta_b\right)}{\partial y}+\frac{1}{\delta\pi}\langle w\rangle_t\langle \theta\rangle_t &= -\frac{1}{\delta\pi}\langle \theta'w'\rangle_t+\frac{1}{\delta\pi}\langle \theta'w'\rangle_s+\langle\mathcal{S}^{\theta}\rangle, && \text{(2.2.5c)}\\
\frac{\partial \theta_{eb}}{\partial t}+\frac{\partial\left(v_b\theta_{eb}\right)}{\partial y}+\frac{1}{\delta\pi}\langle w\rangle_t\langle \theta_e\rangle_t &= -\frac{1}{\delta\pi}\langle \theta_e'w'\rangle_t+\frac{1}{\delta\pi}\langle \theta_e'w'\rangle_s+\langle\mathcal{S}^{\theta_e}\rangle. && \text{(2.2.5d)}
\end{aligned}$$

Here we used the rigid lid condition, and the following approximation from Stevens (2006):

$$\frac{1}{\delta\pi}\int_{-\delta\pi}^{0}\langle v\rangle\langle\phi\rangle\,dz\approx v_b\phi_b,$$

which is justified when baroclinic circulations within the ABL influence negligibly the evolution of ϕ_b. The subscripts s and t in (2.2.5) denote evaluations at the Earth's surface $z=-\delta\pi$, and at the top $z=0$ of the ABL, approached from above, respectively. Taking a vertical average of the incompressibility equation (2.2.4b) and the hydrostatic equation (2.2.4a) over the ABL depth gives

$$\begin{aligned}
w_t &= -\delta\pi\frac{\partial v_b}{\partial y}, && \text{(2.2.6)}\\
p_t &= p_s+\delta\pi\theta_b. && \text{(2.2.7)}
\end{aligned}$$

The former was obtained using the rigid lid condition (2.2.1f). Here the notation w_t and p_t is not to be confounded with derivatives. Note that for this case and thereafter, the reference to ensemble averages is implicit.

ABL Vertical Velocity and Pressure

In the boundary layer, the vertical velocity is assumed to have the linear profile (see Figure 2.2)

$$w(z) = -(z + \delta\pi)\frac{\partial v_b}{\partial y}, \qquad -\delta\pi \le z \le 0, \tag{2.2.8}$$

which satisfies both boundary conditions (2.2.1f) and (2.2.6). The hydrostatic boundary layer is assumed to have the vertical linear pressure profile

$$p(z) = p_s + (z + \delta\pi)\theta_b, \qquad -\delta\pi \le z \le 0, \tag{2.2.9}$$

which is an appropriate approximation at the large horizontal scales of gravity waves we are considering (Waite and Khouider, 2009). A vertical average of (2.2.9) yields the bulk ABL pressure value

$$p_b = p_s + \frac{\delta\pi}{2}\theta_b, \qquad -\delta\pi \le z \le 0. \tag{2.2.10}$$

2.2.2 ABL Turbulent Flux Closures

The bulk boundary layer equations (2.2.5) are not a complete set of equations, as they contain unknown turbulent flux terms. Hence 8 auxiliary statements are required to approximate the unknown fluxes in terms of the state variables. We follow the approach of Waite and Khouider (2009) and Stevens (2006), and use the scalar (momentum) difference between the surface and mid-ABL heights to estimate the scalar (momentum) flux at the surface, that is,

$$\frac{1}{\delta\pi}\langle w'\phi'\rangle_s \equiv \frac{1}{\tau_e}(\phi_s - \phi_b), \quad (\phi = \theta, \theta_e) \qquad \frac{1}{\delta\pi}\langle w'\boldsymbol{u}'\rangle_s \equiv -C_d U \boldsymbol{u}_b. \tag{2.2.11a}$$

Here, the strengths of the fluxes are characterized by the evaporation timescale τ_e (≈ 8 hours in dimensional units), the surface drag coefficient C_d (0.001), and the turbulent velocity U (≈ 2 m/s in dimensional units). Similarly, the turbulent fluxes through the top of the ABL are estimated based on the scalar or momentum differences between the top the ABL, and the mid-ABL or mid-troposphere heights, denoted by the subscripts t, b, and m, respectively (Raymond, 1995; Waite and Khouider, 2009):

$$\frac{1}{\delta\pi}\langle w'\phi'\rangle_t \equiv M_u(\phi_b - \phi_t) - M_d(\phi_m - \phi_t), \quad (\phi = \theta, \theta_e), \tag{2.2.11b}$$

$$\frac{1}{\delta\pi}\langle w'\boldsymbol{u}'\rangle_t \equiv \frac{1}{\tau_T}(\boldsymbol{u}_b - \boldsymbol{u}_t). \tag{2.2.11c}$$

The momentum flux (2.2.11c) is described in terms of a timescale τ_T of turbulent mixing across the top of the ABL $z = 0$; The momentum effects of downdrafts from the free troposphere are neglected. The scalar flux (2.2.11b) has upward and downward contributions M_u and M_d (M_u and M_d are mass fluxes rescaled by density, and thus have units of velocity; See Table 2.2 for their typical dimensional values). We further define

$$M_d = \left\{D_c + \frac{\partial v_b}{\partial y}\right\}^+, \tag{2.2.12}$$

where D_c, the mass flux velocity from large-scale and convective downdraft, will be introduced in Section 2.4.2 (see Eqn. 2.4.20). The upward mass flux velocity at the top of the boundary layer M_u is assumed to be proportional to D_c with proportionality constant (see Waite and Khouider, 2009, and reference therein)

$$\alpha_m = \frac{D_c}{M_u}. \tag{2.2.13}$$

Note that the quantities U, M_u, M_d, τ_e and τ_T are associated with the following scalings:

$$U = \frac{T}{h_b}U^*, \quad M_u = \frac{T}{h_b}M_u^*, \quad M_d = \frac{T}{h_b}M_d^*, \quad \tau_e = \frac{\tau_e^*}{T}, \quad \text{and} \quad \tau_T = \frac{\tau_T^*}{T}, \tag{2.2.14}$$

where U^*, M_u^*, M_d^*, τ_e^* and τ_T^* are dimensional quantities given in the units of Table 2.2.

Combining the closure equations (2.2.11b) with the boundary layer equations (2.2.5), and using the vertical velocity at the top of the ABL (2.2.6) yields the closed bulk equations for the ABL:

$$\boxed{\begin{aligned}
\frac{\partial u_b}{\partial t} + v_b\frac{\partial u_b}{\partial y} - yv_b &= -E_u\Delta_t u - C_dUu_b, && (2.2.15a)\\
\frac{\partial v_b}{\partial t} + v_b\frac{\partial v_b}{\partial y} + yu_b &= -\frac{\partial p_b}{\partial y} - E_u\Delta_t v - C_dUv_b, && (2.2.15b)\\
\frac{\partial \theta_b}{\partial t} + v_b\frac{\partial \theta_b}{\partial y} &= \frac{1}{\tau_e}\Delta_s\theta - E\Delta_t\theta - M_d\Delta_m\theta - Q_{Rb}, && (2.2.15c)\\
\frac{\partial \theta_{e_b}}{\partial t} + v_b\frac{\partial \theta_{e_b}}{\partial y} &= \frac{1}{\tau_e}\Delta_s\theta_e - E\Delta_t\theta_e - M_d\Delta_m\theta_e - Q_{Rb}, && (2.2.15d)
\end{aligned}}$$

where

$$\boxed{\begin{aligned}
E &= \left(M_u - M_d + \frac{\partial v_b}{\partial y}\right)^+, && (2.2.15e)\\
E_u &= \left(\frac{1}{\tau_T} + \frac{\partial v_b}{\partial y}\right)^+, && (2.2.15f)
\end{aligned}}$$

are defined as momentum and scalar entrainment velocities, respectively. Here the thermodynamic forcing terms were replaced by

$$\langle \mathcal{S}^{(\theta,\theta_e)} \rangle = -Q_{Rb},$$

where $Q_{Rb} = \dfrac{T}{\alpha}Q_{Rb}^*$ is a (nondimensional) ABL radiative cooling rate. Also, the scalar and momentum differences between two heights were conveniently written as downward gradients. We have,

$$\Delta_s\phi \equiv \phi_s - \phi_b, \quad \Delta_t\phi \equiv \phi_b - \phi_t, \quad \Delta_m\phi \equiv \phi_b - \phi_m, \tag{2.2.16}$$

for a scalar ϕ. See Table 2.2 for all ABL parameters.

Parameter	Approximate Value	Description
h_b	500 m	ABL depth
τ_e^*	$\mathcal{O}$(7 hrs)	Surface evaporation timescale
U^*	2 m/s	Strength of turbulent velocity
C_d	0.001	Surface drag coefficient
τ_T^*	8 hrs	Momentum entrainment timescale
M_u^*	$\mathcal{O}$(2.5 cm/s)	Updraft velocity
M_d^*	$\mathcal{O}$(0.5 cm/s)	Downdraft velocity
$Q_{R_b}^*$	$\mathcal{O}$(5 K/day)	ABL radiative cooling rate
δ	0.03125	Ratio of boundary layer depth to height of the troposphere
α_m	0.2	Ratio of D_c to M_u

Table 2.2: ABL bulk model parameters

2.3 Mechanical Coupling of the ABL and Free Troposphere

We now consider the complete model for the atmosphere, which incorporates a free troposphere, whose vertical structure is truncated to the first three internal normal modes, sitting on top of a mixed ABL, described by a bulk dynamical model. The equations of the 3MoFTM are systematically coupled to the ABL equations (2.2.15) by assuming continuity of pressure and vertical velocity across the fixed interface, located at $z = 0$. As a consequence, the ABL vertical velocity is now the source of the divergence of the horizontal component of the barotropic flow in the troposphere. This nonzero divergence of the troposphere horizontal barotropic flow leads to (i) important vertical contributions to the 3MoFTM, which are described in Section 2.3.1, and (ii) a nontrivial Poisson pressure equation, derived in Section 2.3.2.

2.3.1 ABL Contributions in the Free Troposphere Model

In this section we examine how the barotropic – first two baroclinic mode system with no-flow bottom 3MoFTM presented in Section 2.1.1 is adjusted in the presence of a boundary layer. As mentioned before we must ensure continuity of vertical velocity at the top of the boundary layer, and therefore the free troposphere equations (2.1.18) are now equipped with the boundary conditions:

$$w\Big|_{z=\pi} = 0, \qquad \lim_{z\to 0^+} w = w_t, \tag{2.3.1}$$

where w_t is given in (2.2.6). Because the free troposphere vertical velocity no longer vanishes at the lower boundary, it has now a nonvanishing “barotropic” component. To see this, first integrate the divergence equation (2.1.18e) with the ansatz (2.1.19) and apply the boundary condition $w\big|_{z=\pi} = 0$ and (2.1.22) to obtain

$$w(y,z,t) = w_0(y,z,t) + w_1(y,t)S_1(z) + w_2(y,t)S_2(z),$$

where

$$w_0(y,z,t) = \frac{\partial v_0}{\partial y}(y,t)(\pi - z), \qquad 0 \le z \le \pi. \tag{2.3.2}$$

Projecting the divergence equation (2.1.18e) onto the barotropic mode gives now

$$\frac{\partial v_0}{\partial y} = \frac{1}{\pi}w_t = -\delta\frac{\partial v_b}{\partial y}, \tag{2.3.3}$$

which should be contrasted with (2.1.23c). The vertical structure of the coupled model including the barotropic vertical velocity profile, is depicted in Figure 2.2. Hence in the presence of an ABL, the barotropic horizontal velocity convergence in the free troposphere is no longer zero, and instead takes its source in the ABL horizontal velocity divergence. This nonzero horizontal divergence of the barotropic wind leads to the following linear and nonlinear vertical contributions to the basic state equations of the 3MoFTM, evidenced in shaded grey:

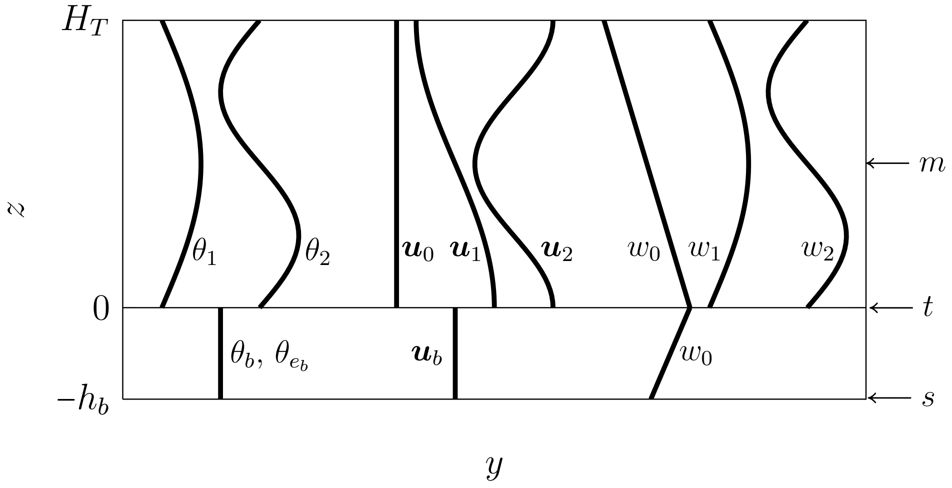

Figure 2.2: Vertical structure of the model. The subscripts s, t and m indicate vertical levels located at the *surface*, *top* of the ABL, and *middle* troposphere, respectively.

$$\frac{D_0 u_0}{Dt} + \frac{\partial\left(u_1 v_1\right)}{\partial y} + \frac{\partial\left(u_2 v_2\right)}{\partial y} - \sqrt{2}(u_1 + u_2)\frac{\partial v_0}{\partial y} - y v_0 = \mathcal{S}_0^u, \tag{2.3.4a}$$

$$\frac{D_0 v_0}{Dt} + \frac{\partial(v_1^2)}{\partial y} + \frac{\partial(v_2^2)}{\partial y} - \sqrt{2}(v_1 + v_2)\frac{\partial v_0}{\partial y} + y u_0 = -\frac{\partial p_0}{\partial y} + \mathcal{S}_0^v, \tag{2.3.4b}$$

$$\begin{aligned}\frac{D_0 u_1}{Dt} + v_1\frac{\partial u_0}{\partial y} + \frac{\sqrt{2}}{2}\left(v_1\frac{\partial u_2}{\partial y} + v_2\frac{\partial u_1}{\partial y} + 2u_2\frac{\partial v_1}{\partial y} + \frac{1}{2}u_1\frac{\partial v_2}{\partial y}\right)& \\ -\left(\frac{1}{2}u_1 + \frac{8}{3}u_2\right)\frac{\partial v_0}{\partial y} - y v_1 = \mathcal{S}_1^u,&\end{aligned} \tag{2.3.4c}$$

$$\begin{aligned}\frac{D_0 v_1}{Dt} + v_1\frac{\partial v_0}{\partial y} + \frac{\sqrt{2}}{2}\left(v_1\frac{\partial v_2}{\partial y} + v_2\frac{\partial v_1}{\partial y} + 2v_2\frac{\partial v_1}{\partial y} + \frac{1}{2}v_1\frac{\partial v_2}{\partial y}\right)& \\ -\left(\frac{1}{2}v_1 + \frac{8}{3}v_2\right)\frac{\partial v_0}{\partial y} + y u_1 = \frac{\partial \theta_1}{\partial y} + \mathcal{S}_1^v,&\end{aligned} \tag{2.3.4d}$$

$$\begin{aligned}\frac{D_0 \theta_1}{Dt} - \frac{\partial v_1}{\partial y} + \frac{\sqrt{2}}{2}\left(2v_1\frac{\partial \theta_2}{\partial y} - v_2\frac{\partial \theta_1}{\partial y} + 4\theta_2\frac{\partial v_1}{\partial y} - \frac{1}{2}\theta_1\frac{\partial v_2}{\partial y}\right)& \\ +\left(\frac{1}{2}\theta_1 - \frac{8}{3}\theta_2\right)\frac{\partial v_0}{\partial y} + \sqrt{2}\frac{\partial v_0}{\partial y} = \mathcal{H}_1^\theta + \mathcal{S}_1^\theta,&\end{aligned} \tag{2.3.4e}$$

$$\begin{aligned}\frac{D_0 u_2}{Dt} + v_2\frac{\partial u_0}{\partial y} + \frac{\sqrt{2}}{2}\left(v_1\frac{\partial u_1}{\partial y} - u_1\frac{\partial v_1}{\partial y}\right)& \\ +\left(\frac{2}{3}u_1 - \frac{1}{2}u_2\right)\frac{\partial v_0}{\partial y} - y v_2 = \mathcal{S}_2^u,&\end{aligned} \tag{2.3.4f}$$

$$\frac{D_0 v_2}{Dt} + v_2\frac{\partial v_0}{\partial y} + \left(\frac{2}{3}v_1 - \frac{1}{2}v_2\right)\frac{\partial v_0}{\partial y} + y u_2 = \frac{\partial \theta_2}{\partial y} + \mathcal{S}_2^v, \tag{2.3.4g}$$

$$\begin{aligned}2\frac{D_0 \theta_2}{Dt} + \frac{\sqrt{2}}{2}\left(v_1\frac{\partial \theta_1}{\partial y} - \theta_1\frac{\partial v_1}{\partial y}\right) - \frac{1}{2}\frac{\partial v_2}{\partial y}& \\ +\left(\frac{4}{3}\theta_1 + \theta_2\right)\frac{\partial v_0}{\partial y} + \frac{\sqrt{2}}{2}\frac{\partial v_0}{\partial y} = \mathcal{H}_2^\theta + \mathcal{S}_2^\theta,&\end{aligned} \tag{2.3.4h}$$

2.3.2 The Poisson Equation for Pressure

The pressure appears in the primitive equations (2.1.1) as a source term: the pressure gradient which acts as a force per unit of volume. There is no evolution equation for the pressure, and since the flow is incompressible, the pressure has no equation of state relating it to temperature, except for $\rho = const$ (Emanuel, 1994). The pressure remains a function of time and space, and must be determined from the momentum and continuity equations.

When normal mode decomposition is applied to the primitive equations and the dynamics is truncated to the first three mode of vertical structure, the pressure decomposes as $p = p_0 + p_1 C_1 + p_2 C_2$, where C_1 and C_2 are the cosine basis functions (2.1.21), and p_0, p_1 and p_2 are the pressure wave amplitudes of mode 0, 1, and 2. While the first and second baroclinic pressure components have been found to be related to the baroclinic potential temperatures according to (2.1.22), the barotropic pressure p_0 is left to be determined, along with boundary layer bulk pressure p_b.

Assuming continuity of pressure across the interface between the free troposphere and the ABL, we must require that $\lim_{z\to 0^+} p(y,z,t) \equiv p_t$, where $p_t = p_b + \frac{\delta\pi}{2}\theta_b$ is found by evaluating (2.2.9) at $z = 0$ and using the surface pressure value in (2.2.10). This yields the following relation between the barotropic and ABL pressures:

$$p_0 = p_b + \frac{\delta\pi}{2}\theta_b + \sqrt{2}\left(\theta_1 + \theta_2\right), \tag{2.3.5}$$

where the baroclinic hydrostatic relations (2.1.22) are used. This gives way to express p_0 in terms of p_b in the barotropic momentum equations (2.1.23), and reduces the problem to finding only the pressure in the boundary layer.

The Poisson Equation for the ABL Pressure

A governing equation for the ABL pressure is found by taking the divergence of both the barotropic meridional momentum equation (2.3.4b) and ABL meridional momentum equation (2.2.15b), and using the divergence relation (2.3.3) together with relation (2.3.5):

$$\boxed{\begin{aligned} &\frac{\partial^2 p_b}{\partial y^2} = \frac{1}{\delta+1}\left(\frac{\partial \Phi}{\partial y} - \frac{\partial^2 \phi}{\partial y^2}\right), && (2.3.6a)\\ &\text{where} && (2.3.6b)\\ &\Phi := \sqrt{2}(v_1+v_2)\frac{\partial v_0}{\partial y} - y(u_0+\delta u_b) - \delta E_u \Delta_t v - \delta C_d U v_b + \mathcal{S}_0^v, && (2.3.6c)\\ &\phi := \frac{\delta}{2}{v_b}^2 + \frac{1}{2}{v_0}^2 + {v_1}^2 + {v_2}^2 + \frac{\delta\pi}{2}\theta_b + \sqrt{2}(\theta_1+\theta_2). && (2.3.6d)\end{aligned}}$$

This 1D elliptic problem is easily solvable by double integration, with suitable boundary conditions on the pressure. Equation (2.3.6) gives the value of the gradient up to an additive constant (see Section 3.2 for a discussion on pressure boundary conditions). Numerically, the *Poisson pressure equation* (2.3.6) is solved iteratively with the free troposphere equations (2.3.4) and the ABL equations (2.2.15) to (1) calculate the pressure and (2) enforce the divergence relation (2.3.3).

2.4 Moist Dynamics

2.4.1 The Free Troposphere Moisture Equation

We consider the dimensional bulk water budget equations for the free troposphere flow (Frierson et al., 2004):

$$\frac{\partial q_v}{\partial t} + \frac{\partial (v q_v)}{\partial y} + \frac{\partial (w q_v)}{\partial z} = E_v - C, \tag{2.4.1a}$$

$$\frac{\partial q_c}{\partial t} + \frac{\partial (v q_c)}{\partial y} + \frac{\partial (w q_c)}{\partial z} = C - E_v - A_r, \tag{2.4.1b}$$

$$\frac{\partial q_r}{\partial t} + \frac{\partial (v q_r)}{\partial y} + \frac{\partial (w q_r)}{\partial z} - \frac{\partial (v_t^* q_r)}{\partial z} = A_r, \tag{2.4.1c}$$

(2.4.1d)

where q_v, q_c, and q_r are the mixing ratios of water vapor, cloud water, and rain, respectively (expressed in mass of water vapor, cloud water, or rain, per unit mass of air), E_v, C, A_r are the rates of evaporation, condensation, and conversion of cloud water into rain, respectively, and v_t^* is the fall speed of precipitation. The equations are zonally averaged and the incompressibility equation (2.1.1e) was used to write them in flux form.

At the synoptic timescale of $\mathcal{O}(T)$ and horizontal space scale of $\mathcal{O}(L)$, it is reasonable to assume that the dynamics of both cloud water and rain occur at smaller scales. Following the approach of Khouider and Majda (2006b), a "quasi-equilibrium" is considered so that on the synoptic scales, we have,

$$\overline{A_r} = -\frac{\partial(\overline{v_t^* q_r})}{\partial z} \qquad \text{and} \qquad \overline{C} = \overline{E_v} + \overline{A_r},$$

where the overbars represents the long time average; That is to say, the processes associated with cloud and rain formation are instantaneous at those scales. Using these time averaged condensation and evaporation rates in the water vapor equation in lieu of C and E_v gives the large scale equation for q_v:

$$\frac{\partial q_v}{\partial t} + \frac{\partial (v q_v)}{\partial y} + \frac{\partial (w q_v)}{\partial z} = \frac{\partial(\overline{v_t^* q_r})}{\partial z}. \tag{2.4.2}$$

We introduce the quantity

$$q = \frac{L_v}{c_p} q_v,$$

which satisfies

$$\frac{\partial q}{\partial t} + \frac{\partial (v q)}{\partial y} + \frac{\partial (w q)}{\partial z} = \frac{L_v}{c_p}\frac{\partial(\overline{v_t^* q_r})}{\partial z}, \tag{2.4.3}$$

where the constant L_v and c_p are the latent heat of vaporization at 0°C and the heat capacity at constant pressure, respectively. We decompose q further as a background moisture vertical profile Q^* (moisture stratification) plus a perturbation q':

$$q(y,z,t) = Q^*(z) + q'(y,z,t). \tag{2.4.4}$$

The moisture stratification is assumed to have the exponential profile

$$Q^*(z) = q_0^* \exp(-z/H_q), \quad 0 \le z \le H_T, \tag{2.4.5}$$

where H_q is the e-folding distance and $q_0^* = 37.3$ K is a constant reference value of background moisture at the top of the ABL (calculated based on a water vapor mixing ratio of $q_{v_0}^* = 0.015$ kg/kg estimated at 500 m). Substituting (2.4.4) into (2.4.3) and using the incompressibility condition (2.1.1e) gives:

$$\frac{\partial q'}{\partial t} + \frac{\partial(vq')}{\partial y} + \frac{\partial(wq')}{\partial z} + w\frac{dQ^*}{dz} = \frac{L_v}{c_p}\frac{\partial(\overline{v_t^* q_r})}{\partial z}, \tag{2.4.6}$$

At this point it is convenient to introduce the following scalings:

$$q' = \alpha\hat{q}' \quad \text{and} \quad Q^* = \alpha\hat{Q}, \tag{2.4.7}$$

where the carets indicate the nondimensional quantities, and α is given in Table 2.1. Inserting the scalings (2.4.7) and (2.1.4) into (2.4.6) gives the nondimensional equation:

$$\frac{\partial\hat{q}}{\partial\hat{t}} + \frac{\partial(\hat{v}\hat{q}')}{\partial\hat{y}} + \frac{\partial(\hat{w}\hat{q}')}{\partial\hat{z}} + \hat{w}\frac{d\hat{Q}}{d\hat{z}} = \frac{T\pi}{\alpha H_T}\frac{L_v}{c_p}\frac{\partial(\overline{v_t^* q_r})}{\partial\hat{z}}. \tag{2.4.8}$$

(with $\overline{v_t^* q_r}$ given in physical units). The carets are dropped below for readability.

We introduce the *bulk* free troposphere moisture perturbation, that is the vertical average of the moisture perturbation over the free troposphere nondimensional depth

π,

$$\langle q' \rangle := \frac{1}{\pi} \int_0^{\pi} q' dz. \tag{2.4.9}$$

Let $\mathcal{P}$ be the rate of precipitation which reaches the ground as the vertical average of the long time averaged precipitation flux (Khouider and Majda, 2006b; Khouider et al., 2013b; Neelin and Zeng, 2000):

$$\mathcal{P} = -\frac{\mu}{\pi} \int_0^{\pi} \frac{\partial(\overline{v_t^* q_r})}{\partial z} = \frac{\mu}{\pi} \overline{v_t^* q_r}\Big|_{z=0}, \qquad \mu = \frac{T\pi}{\alpha H_T} \frac{L_v}{c_p}.$$

assuming that on average q_r and v_t^* are zero at the top $z = \pi$ of the troposphere. The vertical average of (2.4.6) gives an equation for $\langle q' \rangle$, the bulk free troposphere moisture perturbation:

$$\frac{\partial \langle q' \rangle}{\partial t} + \frac{\partial \langle v q' \rangle}{\partial y} + \left\langle \frac{\partial (w q')}{\partial z} \right\rangle + \left\langle w \frac{dQ}{dz} \right\rangle = -\mathcal{P} + \mathcal{S}^q. \tag{2.4.10}$$

Here we added a source term $\mathcal{S}^q$ representing the collective effect of turbulence terms introduced from an implicit Reynolds averaging step (see Section 2.2). The third term on the left-hand side gives

$$\left\langle \frac{\partial (w q')}{\partial z} \right\rangle = -\frac{1}{\pi} w_t q'(y,0,t) = -\kappa \langle q' \rangle \frac{\partial v_0}{\partial y}, \qquad q'(y,0,t) = \kappa \langle q' \rangle, \tag{2.4.11a}$$

where we have assumed that the moisture at the top of the ABL is proportional (with proportionality constant $\kappa > 1$) to the free troposphere bulk moisture value. The last term on the right hand side gives

$$\left\langle w \frac{dQ}{dz} \right\rangle = -\tilde{Q}_0(\eta_q) \frac{\partial v_0}{\partial y} + \tilde{Q}_1(\eta_q) \frac{\partial v_1}{\partial y} + \tilde{Q}_2(\eta_q) \frac{\partial v_2}{\partial y}, \tag{2.4.11b}$$

where $\eta_q = H_T/H_q$ and

$$\tilde{Q}_0(x) = q_0\left(1 + \frac{1}{x}\left(\exp(-x) - 1\right)\right), \tag{2.4.11c}$$

$$\tilde{Q}_1(x) = \frac{\sqrt{2}q_0}{x + \pi^2/x}\left(1 + \exp(-x)\right), \tag{2.4.11d}$$

$$\tilde{Q}_2(x) = \frac{\sqrt{2}q_0}{x + 4\pi^2/x}\left(1 - \exp(-x)\right). \tag{2.4.11e}$$

Here $q_0 = q_0^*/\alpha = 2.39$, and $\tilde{Q}_0 = \tilde{Q}_0^*/\alpha$, $\tilde{Q}_1 = \tilde{Q}_1^*/\alpha$, $\tilde{Q}_2 = \tilde{Q}_2^*/\alpha$. With an estimated e-folding distance of 5 km, the following approximate values are calculated:

$$\begin{aligned} \eta_q &= \frac{16}{5}, \\ \tilde{Q}_0(\eta_q) &= 1.674, \\ \tilde{Q}_1(\eta_q) &= 0.559, \\ \tilde{Q}_2(\eta_q) &= 0.209. \end{aligned}$$

Parameter	Approximate Value	Description
L_v	2.501×10^3 J kg^{-1}	Latent heat of vaporization at 0°C
c_p	1005.7 J kg^{-1} K^{-1}	Heat capacity at constant pressure
q_0^*	37.3K	Constant reference background value of moisture at the top of the ABL
H_q	5 km	e-folding distance of moisture background
κ	2.0	Top of ABL moisture to vertically averaged free tropospheric moisture ratio
η_q	16/5	Ratio of H_T over H_q
$\tilde{Q}_0^*(\eta_q)$	26.1 K	Background contribution to barotropic vertical moisture advection
$\tilde{Q}_1^*(\eta_q)$	8.7 K	Background contribution to first baroclinic vertical moisture advection
$\tilde{Q}_2^*(\eta_q)$	3.3 K	Background contribution to second baroclinic vertical moisture advection
$\tilde{\alpha}_1$	0.1	First baroclinic relative contribution to the moisture convergence associated with the moisture anomalies
$\tilde{\alpha}_2$	1	Second baroclinic relative contribution to the moisture convergence associated with the moisture anomalies

Table 2.3: Large-scale moisture equation parameters

The details of the calculations for the second term on the left hand side of (2.4.10) can be found in Khouider and Majda (2006b) and we give here only the end result:

$$\frac{\partial \langle vq' \rangle}{\partial y} = v_0 \frac{\partial \langle q' \rangle}{\partial y} + \frac{\partial (\tilde{\alpha}_1 v_1 \langle q' \rangle)}{\partial y} + \frac{\partial (\tilde{\alpha}_2 v_2 \langle q' \rangle)}{\partial y}, \tag{2.4.11f}$$

where $\tilde{\alpha}_1 = 1$ and $\tilde{\alpha}_2 = 0.1$. Combining (2.4.11) with (2.4.10) gives

$$\begin{aligned} \frac{\partial \langle q' \rangle}{\partial t} + v_0 \frac{\partial \langle q' \rangle}{\partial y} + \frac{\partial (\tilde{\alpha}_1 v_1 \langle q' \rangle)}{\partial y} + \frac{\partial (\tilde{\alpha}_2 v_2 \langle q' \rangle)}{\partial y} - \tilde{Q}_0(\eta_q) \frac{\partial v_0}{\partial y} + \tilde{Q}_1(\eta_q) \frac{\partial v_1}{\partial y} \\ + \tilde{Q}_2(\eta_q) \frac{\partial v_2}{\partial y} - \kappa \langle q' \rangle \frac{\partial v_0}{\partial y} = -\mathcal{P}. \end{aligned} \tag{2.4.12}$$

Rearranging terms gives the equation for the free troposphere bulk moisture perturbation:

$$\boxed{\begin{aligned} \frac{D_0 q}{Dt} + \frac{\partial}{\partial y} \big((\tilde{\alpha}_1 v_1 + \tilde{\alpha}_2 v_2) q + \tilde{Q}_1(\eta_q) v_1 + \tilde{Q}_2(\eta_q) v_2 - \tilde{Q}_0(\eta_q) v_0 \big) \\ - \kappa q \frac{\partial v_0}{\partial y} = -\mathcal{P} + \mathcal{S}^q, \end{aligned}} \tag{2.4.13}$$

where we let $q = \langle q' \rangle$, and added a forcing term $\mathcal{S}^q$ to represent the sources of moisture. As before, (D_0/Dt) is the barotropic transport operator.

2.4.2 The Stochastic Multicloud Model for Organized Convection

The importance of clouds in the climate system is widely recognized, and their poor representation in GCM has been identified for decades as the source of much of the uncertainty surrounding predictions of climate variability (Arakawa, 1975; Lin et al., 2006; Moncrieff, 1992; Scinocca and McFarlane, 2004). Clouds strongly influence the climate system through their associated water phase change processes such as condensation and evaporation, and impact on the radiative budget through the reflection, absorption, and emission of solar radiation (Stensrud, 2007). They are associated with convection and turbulence on a range of scales, and play an essential role in the vertical transport of energy.

Organized Convection Clouds are organized in a hierarchy of scales ranging from individual convective cells of one to 10 kilometers, to mesoscale cloud clusters, to synoptic scale and planetary scale convectively coupled waves. Nonetheless, it is recognized that tropical convective systems are qualitatively self-similar in terms of their cloud morphology and flow structure (Kiladis et al., 2009; Majda, 2007; Mapes et al., 2006). Analysis of convectively coupled waves on large scales reveal that multicloud convective systems are formed principally of tri-modal "building blocks" (Johnson et al., 1999; Lin and Johnson, 1996): leading shallow congestus cloud decks that moisten and precondition the lower troposphere, followed by deep convective hot towers that extend to the top of the troposphere, which in turn are lagged by stratiform anvils, which cool the lower troposphere by evaporation of theirstratiform rain. The multicloud model, presented next, is based on the assumption that organized convection involves three cloud types, congestus, deep, and stratiform, which are associated with distinct cloud heating fields.

The Stochastic Multicloud Model Individual convective clouds have a few hundred meters of vertical and horizontal extent, and cannot be resolved by large scale models, whose grid size is of about 100 km. To account for the small scale effects of clouds in the model, *cloud parameterization* schemes are used to represent the subgrid scale cloud processes in terms of the grid scale, model variables.

The *multicloud model* (Khouider et al., 2010) is a stochastic cloud parameterization based on a Markov chain lattice model that mimics small scale convective elements which interact with each other and with the large scale environment according to some set of probability rules. The multicloud model is designed to represent the unresolved variability of organized tropical convection in a large-scale simulation with a mesh size of $\mathcal{O}(100 \text{ km})$. Our meridional (South-North) domain is thus meshed into uniform grid boxes of about 100 km. Each grid box is associated to a rectangular lattice of $n \times n$ sites, shown in Figure 2.3, which represents the free troposphere, above the boundary layer.

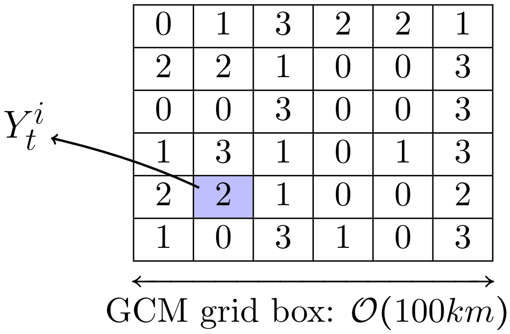

0	1	3	2	2	1
2	2	1	0	0	3
0	0	3	0	0	3
1	3	1	0	1	3
2	2	1	0	0	2
1	0	3	1	0	3

Figure 2.3: Cloud lattice of $n \times n$ sites covering a GCM gridbox. Each lattice site i is associated with a Markov process $(Y_t^i)_{t>0}$ which represents a column convective cell of the free troposphere. At any give time t, a lattice site is either cloud free (0) or occupied by a congestus cloud (1), a deep convective cloud (2), or a stratiform anvil cloud (3).

The parameter n is a positive integer of $\mathcal{O}(100)$, so that the lattice sites have horizontal extent of about 1 kilometre. The multicloud model associates to each lattice site i a four-state stochastic Markov process $(Y_t^i)_{t>0}$ taking value 0, 1, 2, or 3, depending on whether it is clear sky, or occupied by a congestus, deep, or stratiform cloud, respectively. A given site will switch from its current cloud configuration to another according to transition probabilities, which depend on the large scale resolved variables. In the simple case where local interactions are ignored, all n^2 stochastic processes $(Y_t^i)_{t>0}$ are independent and identically distributed (Khouider et al., 2010), and the probability rules depend only on the large-scale resolved variables. These large-scale variables are the convective available potential energy (CAPE) integrated over the whole troposphere (C), the convective available potential energy integrated over the lower troposphere (C_l), and the dryness of the midtroposphere (D). The interaction rules between the different cloud types and the environment, which are designed in accordance with observations of cloud dynamics in the tropics, are summarized as follows (Khouider et al., 2010):

1. A clear site turns into a congestus site with high probability if low level CAPE is positive and the middle troposphere is dry;
2. A congestus or clear sky turns into a deep convective site with high probability if CAPE is positive and the middle troposphere is moist;
3. A deep convective site turns into a stratiform site with high probability;
4. All three cloud types decay naturally to clear sky at some fixed rate;
5. All other transitions are assumed to have negligible probability.

These rules are formalized by the probability transition rates r_{kl} listed in Table 2.4, in terms of the activation function

$$\Gamma(x) = \{1 - e^{-x} \text{ if } x > 0,\ 0 \text{ otherwise}\}\,, \tag{2.4.14}$$

and some cloud transition timescale parameters τ_{kl}. A cartoon of the three cloud types and their associated transitions is sketched in Figure 2.4. Note that from Assumption 5, we have $r_{03} = r_{13} = r_{21} = r_{31} = r_{32} = 0$. It is easy to show that the equilibrium distribution $\mathcal{P}_e$ of the multistate Markov chain $(Y_t^i)_{t>0}$ introduced above is given by (Khouider et al., 2010):

$$\mathcal{P}_e = \frac{1}{Z}\begin{pmatrix} 1 \\ \frac{r_{01}}{r_{10}+r_{12}} \\ \frac{1}{r_{20}+r_{23}}\left(r_{02}+\frac{r_{12}r_{01}}{r_{10}+r_{12}}\right) \\ \frac{r_{23}}{r_{30}}\frac{1}{r_{20}+r_{23}}\left(r_{02}+\frac{r_{12}r_{01}}{r_{10}+r_{12}}\right) \end{pmatrix}, \tag{2.4.15}$$

where Z is a normalization constant.

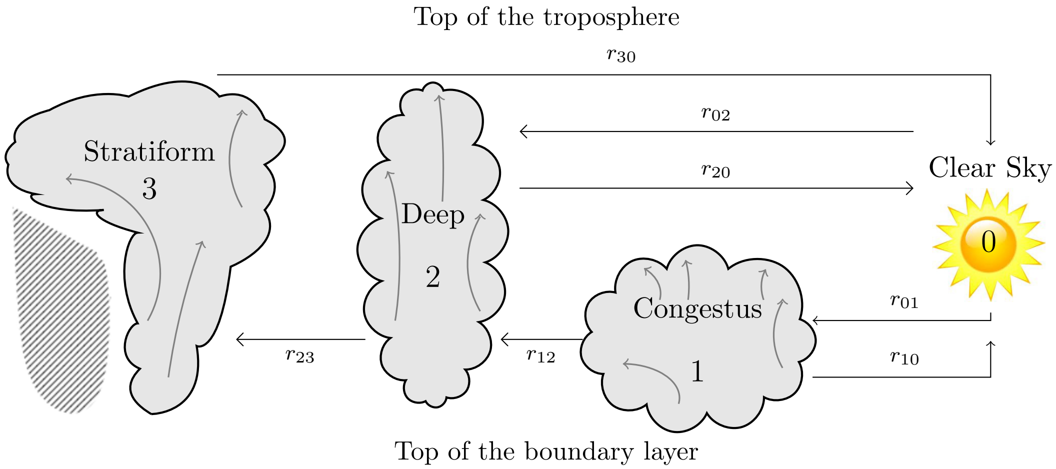

Figure 2.4: A cartoon of the three cloud types showing congestus, deep convective, and a decaying deep convective tower with a lagging large stratiform anvil, with stratiform rain falling into a dry region below it where it eventually evaporates and cools the environment (hatched area). The probability transition rates between the different clouds and clear sky state are given as functions r_{kl} of the large-scale variables C, C_l, and D.

In practical implementation, evolving in time each one of the $N = n^2$ microscopic Markov chains has a high computational overhead. Since the chains are independent, a coarse-graining technique is easily applied leading to the stochastic dynamics of the GCM gridbox cloud coverages alone, without the detailed knowledge of the microstate configuration (Katsoulakis et al., 2003; Khouider et al., 2003). The *cloud coverages* or *area fractions* σ_c, σ_d, and σ_s occupied by clouds of type congestus, deep, or stratiform are defined as:

$$\sigma_c^t = \frac{1}{N}\sum_{i=1}^{N} \mathbb{1}_{\{Y_t^i=1\}}, \quad \sigma_d^t = \frac{1}{N}\sum_{i=1}^{N} \mathbb{1}_{\{Y_t^i=2\}}, \quad \sigma_s^t = \frac{1}{N}\sum_{i=1}^{N} \mathbb{1}_{\{Y_t^i=3\}}, \tag{2.4.16}$$

where

$$\mathbb{1}_{\{Y_t^i=k\}} = \begin{cases} 1 & \text{if } Y_t^i = k, \\ 0 & \text{otherwise,} \end{cases}$$

and $N = n^2$ is the total number of lattice sites. As a function of time, $(\sigma_c^t, \sigma_d^t, \sigma_s^t)$ is effectively a three dimensional birth-death like process with probability transition rules that are given in terms of the microscopic rates r_{kl}. Given the large-scale thermodynamic state, the birth-death process is easily evolved in time using Gillespie's exact algorithm (Gillespie, 1975), and yields the dynamical evolution of the cloud fractions σ_c, σ_d, and σ_s.

Coupling the Stochastic Multicloud Model to the Large-Scale Equations

The multicloud model is coupled to the free troposphere model using a three heating mode paradigm. Congestus clouds heat the lower troposphere through condensation and induce cooling of the upper troposphere due to their high cloud albedo; Deep convective clouds heat the entire depth of the troposphere through condensation, while stratiform clouds heat the upper troposphere through condensation and cool the lower troposphere by precipitating stratiform rain which evaporates in the dry atmosphere below (Khouider et al., 2013b). Correspondingly, the first baroclinic mode is forced by deep convection, and the second baroclinic mode is forced by both congestus and stratiform clouds, as depicted in Figure 2.5. The multicloud model is coupled to the large scale free troposphere equations through heat forcing rates H_c,

Cloud transition	Probability rate	Time scale (hrs)
Formation of congestus	$r_{01} = \frac{1}{\tau_{01}}\Gamma(C_l)\Gamma(D)$	$\tau_{01} = 1$
Decay of congestus	$r_{10} = \frac{1}{\tau_{10}}\Gamma(D)$	$\tau_{10} = 1$
Conversion of congestus to deep	$r_{12} = \frac{1}{\tau_{12}}\Gamma(C)\big(1 - \Gamma(D)\big)$	$\tau_{12} = 0.25$
Formation of deep	$r_{02} = \frac{1}{\tau_{02}}\Gamma(C)\big(1 - \Gamma(D)\big)$	$\tau_{02} = 3$
Conversion of deep to stratiform	$r_{23} = \frac{1}{\tau_{23}}$	$\tau_{23} = 3$
Decay of deep	$r_{20} = \frac{1}{\tau_{20}}\big(1 - \Gamma(C)\big)$	$\tau_{20} = 2$
Decay of stratiform	$r_{30} = \frac{1}{\tau_{30}}$	$\tau_{30} = 5$

Table 2.4: Rates r_{jk} and timescales τ_{jk} of the cloud transitions in the multicloud model. The transition rates r_{jk} are functions of the large scale variables CAPE (C), low level CAPE (C_l), and mid troposphere dryness D, via the activation function Γ defined in (2.4.14). The transitions r_{03}, r_{13}, r_{21}, r_{31}, and r_{32} are assumed to have negligible probability.

H_d, and H_s associated with the three cloud types. The heating rates induced by the

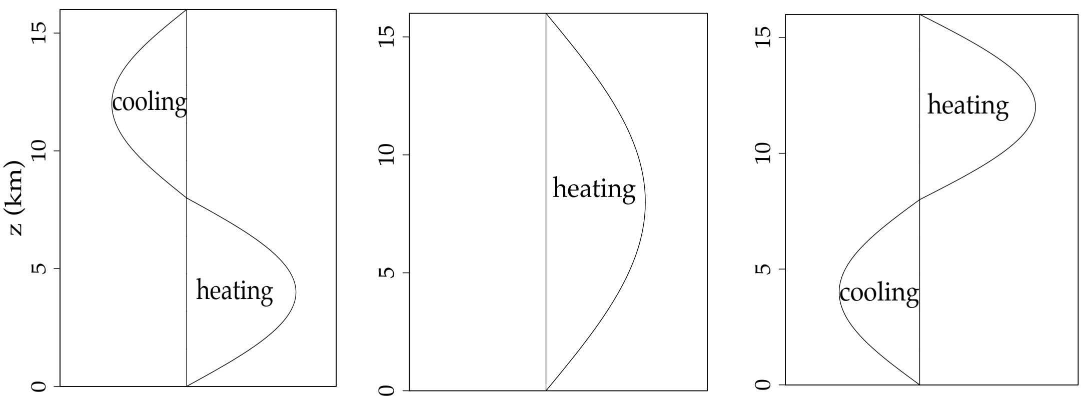

(a) Congestus (b) Deep (c) Stratiform

Figure 2.5: Vertical profiles of heating and cooling fields associated with the three cloud types of the multicloud model. The deep heating vertical profile has the half-sine structure of S_1, whereas the congestus and stratiform have the full sine structure of S_2. The heating curves intersect the vertical straight lines at zero heating points.

three cloud types are assumed to be proportional to the area coverages σ_c, σ_d, and σ_s, and are closed in terms of the large scale variables using the following formulas, which will be referred to in the rest of the thesis as the *Stochastic Multicloud Model*

(SMCM) (Khouider et al., 2010):

$$H_d = \left\{ \sigma_d \overline{Q} + \frac{1}{\tau_c(\sigma_d)} \left(a_1 \theta'_{eb} + a_2 q' - a_0 \left[\theta'_1 + \gamma_2 \theta'_2 \right] \right) \right\}^+ , \tag{2.4.17a}$$

$$\tau_c(\sigma_d) = \frac{\overline{\sigma_d}}{\sigma_d} \tau_c^0 \tag{2.4.17b}$$

$$H_s = \frac{\sigma_s \alpha_s}{H_m} \sqrt{\mathrm{CAPE}^+}, \tag{2.4.17c}$$

$$\text{(SMCM)} \qquad H_c = \frac{\sigma_c \alpha_c}{H_m} \sqrt{\mathrm{CAPE}_l^+}, \tag{2.4.17d}$$

$$\text{where} \tag{2.4.17e}$$

$$\mathrm{CAPE} = \overline{\mathrm{CAPE}} + R \left(\theta'_{eb} - a'_0 (\theta'_1 + \gamma_2 \theta'_2) \right), \tag{2.4.17f}$$

$$\mathrm{CAPE}_l = \overline{\mathrm{CAPE}} + R \left(\theta'_{eb} - a'_0 (\theta'_1 + \gamma'_2 \theta'_2) \right), \qquad \text{and} \tag{2.4.17g}$$

$$\overline{\mathrm{CAPE}} = H_m^2 \overline{Q}^2 . \tag{2.4.17h}$$

Here the primes indicate deviations from the radiative convective equilibrium (RCE), denoted by overbars. Equations (2.4.17f), (2.4.17g) and (2.4.17h) are, respectively, the convectively available potential energies integrated over the whole troposphere (CAPE), integrated over the lower troposphere (CAPE_l), and in radiative-convective equilibrium ($\overline{\mathrm{CAPE}}$). The statistical RCE of the cloud coverages, denoted by $\overline{\sigma_c}$, $\overline{\sigma_d}$, and $\overline{\sigma_s}$, are given by the equilibrium distribution $\mathcal{P}_e$ of the multistate Markov chain Y_t (Khouider et al., 2010). The equations in (2.4.17) are given in nondimensional form, and the function $\{x\}^+ = \max(x, 0)$ is a nonlinear switch that returns the positive part of x. Some convective related quantities are $H_m^* = H_m L$, the average height of the middle troposphere, $R^* = Rc^2/\alpha$, a CAPE constant, and $\tau_c^{0^*} = \tau_c^0 T$, a convective timescale. See Table 2.5 for the description of all other parameters in (2.4.17). The RCE value of CAPE is given by the solution of the nonlinear algebraic equation

(Khouider et al., 2010):

$$Q_{R1} = \frac{1}{H_m}\overline{\sigma_d}\left(\overline{\mathrm{CAPE}}\right)\sqrt{\overline{\mathrm{CAPE}}}, \tag{2.4.18}$$

where $Q_{R1} = Q^*_{R1}T/\alpha$ is the (nondimensional) first baroclinic radiative cooling rate. Equation (2.4.18) is solved by a numerical root-finding method (`gsl_root_fsolver` from the `gsl_root` package). The feedback from the resolved variables to the convective parameterization is done through C, C_l, and D mentioned earlier, using:

$$C = \frac{\mathrm{CAPE}}{\mathrm{CAPE}_0}, \quad C_l = \frac{\mathrm{CAPE}_l}{\mathrm{CAPE}_0}, \quad \text{and} \quad D = \frac{\theta_{eb} - \theta_{em}}{T_0}. \tag{2.4.19}$$

Here $\mathrm{CAPE}_0 = \mathrm{CAPE}^*_0/c^2$ and $T_0 = T^*_0/\alpha$ are (nondimensional) reference values for CAPE and dryness, respectively, θ_{eb} is given by (2.2.15d), and θ_{em} is the vertically averaged midtroposphere equivalent potential temperature:

$$\theta_{em} \approx \frac{2\sqrt{2}}{\pi}\left(\theta_1 + \alpha_2\theta_2\right) + q.$$

The inclusion of dryness of the middle troposphere accounts for mixing of the convective parcels with dry environmental air (Khouider and Majda, 2006b,c, 2007). Notice that the first coefficient $2\sqrt{2}/\pi$ results from the vertical average of the first baroclinic potential temperature $\theta_1 S_1$. Although the vertical average of $2\theta_2 S_2$ is zero, a small fraction ($2\sqrt{2}\alpha_2/\pi$, $\alpha_2 = 0.1$) of θ_2 is added to include its contribution from the lower middle troposphere (Khouider and Majda, 2006b).

The multicloud model is also coupled to the large scale equations via the total ABL downdraft velocity M_d (see Eqn. (2.2.12)), which is given in terms of

$$D_c = m_0\left\{1 + \frac{\mu}{Q_{R1}}\left(H_s - H_c\right)\right\}^+, \tag{2.4.20}$$

the mass flux velocity from large-scale and convective downdrafts. The constant m_0 is diagnosed at RCE, and represents the large-scale background downdraft velocity, and the parameter $\mu > 0$ is tunable.

Deterministic Multicloud Model. A deterministic version of the multicloud model, analyzed in Khouider and Majda (2006b) and Khouider and Majda (2008), takes into account the energy available for congestus and deep convection, denoted by Q_c and Q_d, and uses a nonlinear moisture switch Λ that allows natural transitions between congestus and deep convection. The *deterministic multicloud model* (DMCM) closure equations are:

$$H_d = (1 - \Lambda)\, Q_d, \tag{2.4.21a}$$

$$\frac{\partial H_s}{\partial t} = \frac{1}{\tau_s}\left(\alpha_s H_d - H_s\right), \tag{2.4.21b}$$

$$\frac{\partial H_c}{\partial t} = \frac{1}{\tau_c}\left(\alpha_c \Lambda Q_c - H_c\right), \tag{2.4.21c}$$

$$\text{where} \tag{2.4.21d}$$

$$\text{(DMCM)} \qquad Q_d = \left\{\overline{Q} + \frac{1}{\tau_{conv}}\left[a_1\theta'_{eb} + a_2 q' - a_0\left(\theta'_1 + \gamma_2\theta'_2\right)\right]\right\}^+, \tag{2.4.21e}$$

$$Q_c = \left\{\overline{Q} + \frac{1}{\tau_{conv}}\left[\theta'_{eb} - a'_0\left(\theta'_1 + \gamma'_2\theta'_2\right)\right]\right\}^+, \tag{2.4.21f}$$

$$\Lambda = \begin{cases} 1, & \text{for} \quad \Delta_m\theta_e \geq \theta^+, \\ 0, & \text{for} \quad \Delta_m\theta_e \leq \theta^-, \\ \text{linear and continuous}, & \text{for} \quad \theta^- < \Delta_m\theta_e < \theta^+. \end{cases} \tag{2.4.21g}$$

The nondimensional parameters τ_s, τ_c, τ_{conv} are stratiform and congestus adjustment timescales, and convective timescale, respectively. The moisture switch function has lower and upper nondimensional threshold values θ^- and θ^+. The dimensional counterpart values of these parameters, denoted by an asterisk, are given in Table 2.5.

Convective Forcings in the Large-Scale Energy and Moisture Equations The multicloud convective parameterization is coupled to the free troposphere energy and water budget equations via forcing terms involving the congestus, deep, and stratiform heating rates H_c, H_d, and H_s. The large-scale potential temperature equation (2.1.18d) is forced by a total heating rate

$$\mathcal{H}^\theta = H_d S_1 + 2(H_c - H_s)S_2, \tag{2.4.22}$$

which includes contributions for θ_1 and θ_2. The large-scale moisture equation (2.4.13) has a moisture sink due to the process of precipitation from deep cloud water vapor of the form

$$\mathcal{P} = \frac{2\sqrt{2}}{\pi} H_d.$$

Parameter	Approximate Value	Description
H_m^*	5 km	Average height of the middle troposphere
R^*	320 J kg^{-1} K^{-1}	CAPE constant
Q_{R1}^*	1 K/day	Longwave first baroclinic radiative cooling rate
Q_{R2}^*	Determined at RCE	Longwave second baroclinic radiative cooling rate
$\overline{Q}$	Determined at RCE	Heating potential at RCE
m_0	Determined at RCE	Large-scale background downdraft velocity
$\tau_c^{0^*}$	2 hrs	Reference convective timescale
α_c, α_s	0.25, 0.25	Contribution of CAPE to congestus, stratiform heating
a_0	1	Contribution of θ_1 to deep convective heating anomalies
a_1	0.45	Contribution of θ_{eb} to deep convective heating anomalies
a_2	$1 - a_1$	Contribution of q to deep convective heating anomalies
a_0'	1.7	Contribution of θ_1 to CAPE anomalies
γ_2	0.1	Relative contribution of θ_2 to deep convective anomalies
γ_2'	2.0	Relative contribution of θ_2 to low level CAPE anomalies
CAPE$_0^*$	200 J kg^{-1}	Reference value of CAPE
$T_0{}^*$	10 K	Reference value of CAPE
α_2	0.1	Relative contribution of θ_2 to θ_{em}
μ	0.25	Contribution of convective downdrafts to M_d
τ_c^*, τ_s^*	1 hr, 3hr	Congestus, stratiform adjustment timescales
τ_{conv}^*	2 hrs	Convective timescale
θ^{*^-}, θ^{*^+}	10 K, 20 K	Moisture switch threshold values
τ_D^*	50 days	Newtonian cooling timescale
τ_R^*	75 days	Rayleigh drag timescale
τ_T^*	8 h	Momentum entrainment timescale

Table 2.5: Multicloud model parameters

2.5 Full Model with Convective Radiative Forcing

We summarize here the dynamical core of the atmospheric model that will be used for the simulations of Chapter 4. The equations are those derived for the free troposphere (equations (2.3.4) and (2.4.13)), and for the boundary layer (equations (2.2.15)), with an equation for the boundary layer pressure (equation (2.3.6)). These equations, now combined with the multicloud radiative convective forcing terms described in Section 2.4.2, are summarized below. Additional source and sink terms, which can be found in Waite and Khouider (2009), are explained next. The full system of equations will be referred hereafter as the Hadley-Monsoon equations, or MOSNE.

$$\frac{D_b\theta_{eb}}{Dt} = -E\Delta_t\theta_e - M_d\Delta_m\theta_e + \frac{1}{\tau_e}\Delta_s\theta_e - Q_{Rb}, \tag{2.5.1a}$$

$$\frac{D_b\theta_b}{Dt} = -E\Delta_t\theta - M_d\Delta_m\theta + \frac{1}{\tau_e}\Delta_s\theta - Q_{Rb}, \tag{2.5.1b}$$

$$\frac{D_b u_b}{Dt} - yv_b = -E_u\Delta_t u - C_d U u_b, \tag{2.5.1c}$$

$$\frac{D_b v_b}{Dt} + yu_b = -\frac{\partial p_b}{\partial y} - E_u\Delta_t v - C_d U v_b, \tag{2.5.1d}$$

$$\frac{D_0 u_0}{Dt} + \frac{\partial\left(u_1 v_1\right)}{\partial y} + \frac{\partial\left(u_2 v_2\right)}{\partial y} - \sqrt{2}(u_1 + u_2)\frac{\partial v_0}{\partial y} - yv_0 = d_0^u, \tag{2.5.1e}$$

$$\frac{D_0 v_0}{Dt} + \frac{\partial(v_1^2)}{\partial y} + \frac{\partial(v_2^2)}{\partial y} - \sqrt{2}(v_1 + v_2)\frac{\partial v_0}{\partial y} + yu_0 = -\frac{\partial p_0}{\partial y} + d_0^v, \tag{2.5.1f}$$

$$\begin{aligned}\frac{D_0 u_1}{Dt} &+ v_1\frac{\partial u_0}{\partial y} + \frac{\sqrt{2}}{2}\left(v_1\frac{\partial u_2}{\partial y} + v_2\frac{\partial u_1}{\partial y} + 2u_2\frac{\partial v_1}{\partial y} + \frac{1}{2}u_1\frac{\partial v_2}{\partial y}\right)\\ &- \left(\frac{1}{2}u_1 + \frac{8}{3}u_2\right)\frac{\partial v_0}{\partial y} - yv_1 = -\frac{1}{\tau_R}u_1 + d_1^u,\end{aligned} \tag{2.5.1g}$$

$$\begin{aligned}\frac{D_0 v_1}{Dt} &+ \frac{3\sqrt{2}}{2}\left(\frac{1}{2}v_1\frac{\partial v_2}{\partial y} + v_2\frac{\partial v_1}{\partial y}\right) + \left(\frac{1}{2}v_1 - \frac{8}{3}v_2\right)\frac{\partial v_0}{\partial y}\\ &\qquad\qquad + yu_1 = \frac{\partial\theta_1}{\partial y} - \frac{1}{\tau_R}v_1 + d_1^v,\end{aligned} \tag{2.5.1h}$$

$$\begin{aligned}\frac{D_0\theta_1}{Dt} &- \frac{\partial v_1}{\partial y} + \frac{\sqrt{2}}{2}\left(2v_1\frac{\partial\theta_2}{\partial y} - v_2\frac{\partial\theta_1}{\partial y} + 4\theta_2\frac{\partial v_1}{\partial y} - \frac{1}{2}\theta_1\frac{\partial v_2}{\partial y}\right)\\ &+ \left(\frac{1}{2}\theta_1 - \frac{8}{3}\theta_2\right)\frac{\partial v_0}{\partial y} + \sqrt{2}\frac{\partial v_0}{\partial y} = H_d - Q_{R1} - \frac{1}{\tau_D}\theta_1,\end{aligned} \tag{2.5.1i}$$

$$\begin{aligned}\frac{D_0 u_2}{Dt} &+ v_2\frac{\partial u_0}{\partial y} + \frac{\sqrt{2}}{2}\left(v_1\frac{\partial u_1}{\partial y} - u_1\frac{\partial v_1}{\partial y}\right)\\ &+ \left(\frac{2}{3}u_1 - \frac{1}{2}u_2\right)\frac{\partial v_0}{\partial y} - yv_2 = -\frac{1}{\tau_R}u_2 + d_2^u,\end{aligned} \tag{2.5.1j}$$

$$\frac{D_0 v_2}{Dt} + \left(\frac{2}{3}v_1 + \frac{1}{2}v_2\right)\frac{\partial v_0}{\partial y} + yu_2 = \frac{\partial\theta_2}{\partial y} - \frac{1}{\tau_R}v_2 + d_2^v, \tag{2.5.1k}$$

$$\begin{aligned}\frac{D_0\theta_2}{Dt} &+ \frac{\sqrt{2}}{4}\left(v_1\frac{\partial\theta_1}{\partial y} - \theta_1\frac{\partial v_1}{\partial y}\right) - \frac{1}{4}\frac{\partial v_2}{\partial y}\\ &+ \left(\frac{2}{3}\theta_1 + \frac{1}{2}\theta_2\right)\frac{\partial v_0}{\partial y} + \frac{\sqrt{2}}{4}\frac{\partial v_0}{\partial y} = H_c - H_s - Q_{R2} - \frac{1}{\tau_D}\theta_2,\end{aligned} \tag{2.5.1l}$$

$$\begin{aligned}\frac{D_0 q}{Dt} &+ \frac{\partial}{\partial y}\left((\tilde{\alpha}_1 v_1 + \tilde{\alpha}_2 v_2)q + \tilde{Q}_1(\eta_q)v_1 + \tilde{Q}_2(\eta_q)v_2 - \tilde{Q}_0(\eta_q)v_0\right)\\ &- \kappa q\frac{\partial v_0}{\partial y} = -\frac{2\sqrt{2}}{\pi}H_d + \delta E\Delta_t\theta_e + \left(\delta M_d + \frac{\partial v_0}{\partial y}\right)\Delta_m\theta_e,\end{aligned} \tag{2.5.1m}$$

Here $(D_b/Dt) = (\partial/\partial t)+v_b(\partial/\partial y)$ and $(D_0/Dt) = (\partial/\partial t)+v_0(\partial/\partial y)$ are the meridional boundary layer and barotropic transport operators. The effects of radiative cooling on the first and second baroclinic potential temperature modes are represented by the nondimensional terms

$$-Q_{Ri} - \frac{1}{\tau_D}\theta_i, \qquad i = 1, 2,$$

where τ_D is the Newtonian cooling, and Q_{Ri} are the longwave baroclinic cooling rates associated with the first and second baroclinic modes. Convective momentum drag terms due to boundary layer convective updrafts and downdrafts have barotropic and first/second baroclinic contributions

$$d_0^{\boldsymbol{u}} = \delta E_u \Delta_t \boldsymbol{u} \quad \text{and} \quad d_i^{\boldsymbol{u}} = \frac{\sqrt{2}\delta}{\tau_T}\Delta_t \boldsymbol{u} \qquad (i = 1, 2),$$

respectively, where E_u, the ABL momentum entrainment velocity, is given by (2.2.15f), τ_T is the nondimensional momentum entrainment timescale, and

$$\Delta_t \boldsymbol{u} = \boldsymbol{u}_b - \boldsymbol{u}_t \qquad (\boldsymbol{u}_t \equiv \boldsymbol{u}_0 + \sqrt{2}\,(\boldsymbol{u}_1 + \boldsymbol{u}_2))$$

is the downward velocity gradient across the top of the ABL as defined in 2.2.16. Together, the terms

$$-\frac{1}{\tau_R}\boldsymbol{u}_i + d_i^{\boldsymbol{u}} = -\frac{1}{\tau_R}\boldsymbol{u}_i - \frac{\sqrt{2}\delta}{\tau_T}(\boldsymbol{u}_t - \boldsymbol{u}_b) \qquad (i = 1, 2)$$

are drag forces acting on the baroclinic modes due to the Rayleigh friction coefficient (with Rayleigh drag timescale τ_R) and boundary layer turbulent momentum flux. For the dimensional values $\tau_D^* = T\tau_D$, $\tau_T^* = T\tau_T$, $\tau_R^* = T\tau_R$, and $Q_{Ri}^* = \alpha Q_{Ri}/T$ of the quantities mentioned above, see Table 2.5. The moisture equation has source term

$$\delta E \Delta_t \theta_e + \left(\delta M_d + \frac{\partial v_0}{\partial y} \right) \Delta_m \theta_e,$$

which includes boundary layer entrainment and barotropic convergence (see Waite and Khouider, 2009), in addition to a downdraft velocity contribution (see Eqn. 2.2.12). With these new forcing terms, the Poisson equation for the ABL pressure (equation (2.3.6)) becomes:

$$\frac{\partial^2 p_b}{\partial y^2} = \frac{1}{\delta + 1} \left(\frac{\partial \Phi}{\partial y} - \frac{\partial^2 \phi}{\partial y^2} \right), \tag{2.5.1n}$$

where

$$\Phi := \sqrt{2}(v_1 + v_2) \frac{\partial v_0}{\partial y} - y(u_0 + \delta u_b) - \delta C_d U v_b, \tag{2.5.1o}$$

$$\phi := \frac{\delta}{2} {v_b}^2 + \frac{1}{2} {v_0}^2 + {v_1}^2 + {v_2}^2 + \frac{\delta \pi}{2} \theta_b + \sqrt{2}(\theta_1 + \theta_2). \tag{2.5.1p}$$

2.6 Conclusion

This chapter presented a zonally symmetric model for Hadley circulation and monsoon dynamics. It is based on the theoretical model of Waite and Khouider (2009) for convectively coupled waves, which explicitly incorporates boundary layer dynamics and shallow convection using the multicloud framework. Here the dynamics is zonally averaged, which allows to study the basic structure of the meridional circulation and propagation of organized convection in the absence of zonally propagating equatorial waves. The original model of Waite and Khouider (2009) is extended here to include the nonlinear interactions between the barotropic and baroclinic modes of vertical structure, in an attempt to account for the nonlinearity effects of gravity waves.

Chapter 3

Numerics

In Chapter 2 we proposed a model for the meridional circulation of the tropical atmosphere on the equatorial beta-plane, which incorporates both the bulk effects of a turbulent planetary boundary layer and the multiscale effects of a moist convective free troposphere. The bulk boundary layer model is composed of the 4 equations (2.2.15), which are coupled to the system (2.3.4) of 8 equations for the free troposphere, primarily via the barotropic meridional wind divergence relationship (2.3.3), and the elliptic equation for pressure (2.5.1n). The model also includes an equation for the vertically averaged water vapor content in the free troposphere, equation (2.5.1m). The full (MOSNE) system is a nonconservative system of PDE to be solved concurrently with an elliptic equation for pressure. This chapter presents the numerical method for the MOSNE system and a grid convergence test to verify its near second-order degree of accuracy. Essentially, the method combines the non-oscillatory central scheme of Nessyahu and Tadmor (1990) (NT in the following; see also Jiang and Tadmor, 1998) with the Wave-Propagation method of LeVeque (2002) and method of lines, using the Strang splitting scheme strategy (Strang, 1968). The general method is presented in Section 3.1 with careful considerations given to the pressure boundary condition problem in Section 3.2, while Sections 3.3, 3.4, and 3.5 give a short background on the NT, Wave-Propagation, and Strang methods, respectively. Convergence results are given in Section 3.6.

3.1 A nonconservative system of PDE

The MOSNE system has a total of 13 equations for prognostic variables (winds, temperature, moisture) and 1 equation for the boundary layer pressure. The strategy employed to solve the MOSNE system numerically is based on the approach of Stechmann et al. (2008) (see also Khouider and Majda, 2005; Stechmann, 2008), which relies on a judicious splitting of the advective portion of the system into its conservative and non-conservative parts. The splitting used here is of the form:

$$\frac{\partial \boldsymbol{\xi}}{\partial t} + \frac{\partial \boldsymbol{F}(\boldsymbol{\xi}, p_b)}{\partial y} + D_{nc}(\boldsymbol{\xi})\frac{\partial \boldsymbol{\xi}}{\partial y} + N_{nc}(\boldsymbol{\xi})\frac{\partial \boldsymbol{\xi}}{\partial y} = \boldsymbol{S}(\boldsymbol{\xi}), \tag{3.1.1}$$

where

$$\boldsymbol{\xi} = \begin{pmatrix} \theta_{eb} \\ \theta_b \\ u_b \\ v_b \\ u_0 \\ v_0 \\ u_1 \\ v_1 \\ u_2 \\ v_2 \\ \theta_1 \\ \theta_2 \\ q \end{pmatrix}, \qquad \boldsymbol{F}(\boldsymbol{\xi}, p_b) = \begin{pmatrix} 0 \\ 0 \\ 0 \\ \frac{1}{2}v_b^2 + p_b \\ u_1 v_1 + u_2 v_2 \\ \frac{1}{2}v_0^2 + v_1^2 + v_2^2 + p_b + \frac{\delta\pi}{2}\theta_b + \sqrt{2}(\theta_1 + \theta_2) \\ \frac{\sqrt{2}}{2}u_2 v_1 \\ -\theta_1 \\ \frac{\sqrt{2}}{2}u_1 v_1 \\ -\theta_2 \\ \sqrt{2}v_1\theta_2 - v_1 + \sqrt{2}v_0 \\ \frac{\sqrt{2}}{4}v_1\theta_1 - \frac{1}{4}v_2 + \frac{\sqrt{2}}{4}v_0 \\ (\tilde{\alpha}_1 v_1 + \tilde{\alpha}_2 v_2)q + \tilde{Q}_1 v_1 + \tilde{Q}_2 v_2 - \tilde{Q}_0 v_0 \end{pmatrix}, \quad (3.1.2)$$

$$D_{nc}(\boldsymbol{\xi}) = diag\left(v_b, v_b, v_b, 0, v_0, -\sqrt{2}(v_1 + v_2), v_0 + \frac{\sqrt{2}}{2}v_2, v_0 + \frac{3\sqrt{2}}{2}v_2, v_0, v_0, v_0 - \frac{\sqrt{2}}{2}v_2, v_0, v_0\right) \quad (3.1.3)$$

and

$$N_{nc}(\boldsymbol{\xi}) = \begin{pmatrix} 0_{3\times4} & 0_{3\times6} & 0_{3\times3} \\ 0_{10\times4} & \tilde{N}_{nc}(\boldsymbol{\xi}) & 0_{10\times3} \end{pmatrix}, \quad (3.1.4)$$

with the 6 × 6 block:

$$\tilde{N}_{nc}(\boldsymbol{\xi}) = \begin{pmatrix} 0 & 0 & 0 & 0 & 0 & 0 \\ 0 & -\sqrt{2}(u_1 + u_2) & 0 & 0 & 0 & 0 \\ 0 & 0 & 0 & 0 & 0 & 0 \\ v_1 & -\frac{1}{2}u_1 - \frac{8}{3}u_2 & 0 & \frac{\sqrt{2}}{2}u_2 & 0 & \frac{\sqrt{2}}{4}u_1 \\ 0 & \frac{1}{2}v_1 - \frac{8}{3}v_2 & 0 & 0 & 0 & \frac{3\sqrt{2}}{4}v_1 \\ v_2 & \frac{2}{3}u_1 - \frac{1}{2}u_2 & 0 & -\sqrt{2}u_1 & 0 & 0 \\ 0 & \frac{2}{3}v_1 + \frac{1}{2}v_2 & 0 & 0 & 0 & 0 \\ 0 & \frac{1}{2}\theta_1 - \frac{8}{3}\theta_2 & 0 & \sqrt{2}\theta_2 & 0 & -\frac{\sqrt{2}}{4}\theta_1 \\ 0 & \frac{2}{3}\theta_1 + \frac{1}{2}\theta_2 & 0 & -\frac{\sqrt{2}}{2}\theta_1 & 0 & 0 \\ 0 & -\kappa q & 0 & 0 & 0 & 0 \end{pmatrix}.$$

Here, $\boldsymbol{\xi}(y,t) : \mathbb{R} \times \mathbb{R} \to \mathbb{R}^{13}$ is a vector of the 13 unknown prognostic functions (winds, temperature, and moisture), $\boldsymbol{F}(\boldsymbol{\xi}, p_b) : \mathbb{R}^{13} \times \mathbb{R} \to \mathbb{R}^{13}$ is a flux vector, $D_{nc} \in \mathbb{R}^{13}$ is a diagonal matrix, and $N_{nc} \in \mathbb{R}^{13}$ is a matrix of nilpotency 4. As pointed out earlier, the barotropic divergence relationship

$$\frac{\partial v_0}{\partial y} = -\delta \frac{\partial v_b}{\partial y} \tag{3.1.5}$$

is enforced through the one-dimensional elliptic equation for pressure

$$\frac{\partial^2 p_b}{\partial y^2}(\boldsymbol{\xi}) = \frac{1}{1+\delta}\left[\frac{\partial \Phi}{\partial y}(\boldsymbol{\xi}) - \frac{\partial^2 \phi}{\partial y^2}(\boldsymbol{\xi})\right]. \tag{3.1.6}$$

where Φ and ϕ are given by (2.5.1o) and (2.5.1p), respectively. Since the equation for the barotropic meridional wind is also enforced through (3.1.6), it may be eliminated from (3.1.1) and v_0 is calculated from v_b using the low-cost divergence relation (3.1.5). The forcing term in (3.1.1) is given by

$$\mathbf{S}(\xi) = \begin{pmatrix} -E\Delta_t\theta_e - M_d\Delta_m\theta_e + \dfrac{1}{\tau_e}\Delta_s\theta_e - Q_{Rb} \\ -E\Delta_t\theta - M_d\Delta_m\theta + \dfrac{1}{\tau_e}\Delta_s\theta - Q_{Rb} \\ yv_b - E_u\Delta_t u - C_d U u_b \\ -yu_b - E_u\Delta_t v - C_d U v_b \\ yv_0 + \delta E_u\Delta_t u \\ -yu_0 + \delta E_u \Delta_t v \\ yv_1 - \dfrac{1}{\tau_R}u_1 + \dfrac{\sqrt{2}\delta}{\tau_T}\Delta_t u \\ -yu_1 - \dfrac{1}{\tau_R}v_1 + \dfrac{\sqrt{2}\delta}{\tau_T}\Delta_t v \\ yv_2 - \dfrac{1}{\tau_R}u_2 + \dfrac{\sqrt{2}\delta}{\tau_T}\Delta_t u \\ -yu_2 - \dfrac{1}{\tau_R}v_2 + \dfrac{\sqrt{2}\delta}{\tau_T}\Delta_t v \\ H_d - Q_{R1} - \dfrac{1}{\tau_D}\theta_1 \\ H_c - H_s - Q_{R2} - \dfrac{1}{\tau_D}\theta_2 \\ -\dfrac{2\sqrt{2}}{\pi}H_d + \delta E\Delta_t\theta_e + \left(\delta M_d + \dfrac{\partial v_0}{\partial y}\right)\Delta_m\theta_e \end{pmatrix}. \tag{3.1.7}$$

The choice of the split form (3.1.1) is preferred over various other mathematical forms because of the system's important following properties:

1. It has a nonlinear conservative part, that is, terms that can be arranged as

$$\frac{\partial \boldsymbol{\xi}}{\partial t} + \frac{\partial \boldsymbol{F}(\boldsymbol{\xi}, p_b)}{\partial y} = 0, \qquad \frac{\partial \boldsymbol{F}}{\partial \boldsymbol{\xi}} := A_c(\boldsymbol{\xi}), \tag{3.1.8a}$$

where the flux function $\boldsymbol{F}$ is a nonlinear function of $\boldsymbol{\xi}$, and A_c is the flux Jacobian matrix. Since the matrix of wave propagation speeds A_c depends on the solution $\boldsymbol{\xi}$, spontaneous discontinuities in the solution may develop from smooth initial data. The eigenstructure of A_c is not accessible analytically and thus regions of hyperbolicity of the system for physically relevant values of p_b are not known. In the nonhyperbolic regime, the solution can develop instabilities;

2. It has a nonconservative nonlinear hyperbolic part that can be written as

$$\frac{\partial \boldsymbol{\xi}}{\partial t} + D_{nc}(\boldsymbol{\xi}) \frac{\partial \boldsymbol{\xi}}{\partial y} = 0, \tag{3.1.8b}$$

where D_{nc} is a diagonal matrix which depends on the solution $\boldsymbol{\xi}$. The system (3.1.8b) is hyperbolic: The eigenvalues of D_{nc} are the diagonal elements, and the eigenvectors are the 13-component standard basis vectors. Nonlinear hyperbolic equations may also have non-smooth solutions even if initial data are smooth;

3. It has a nonconservative nonlinear advection system of the form

$$\frac{\partial \boldsymbol{\xi}}{\partial t} + N_{nc}(\boldsymbol{\xi}) \frac{\partial \boldsymbol{\xi}}{\partial y} = 0, \tag{3.1.8c}$$

where N_{nc} was chosen so that all its eigenvalues (linear wave speeds) are zero. In particular, N_{nc} has a nilpotency degree 4 ($N_{nc}^4 = 0$).

The list above highlights several physical properties that need to be considered when designing a numerical method for the nonconservative PDE system (3.1.1). It presents the system as a combination of three subproblems (four with the forcing term $\boldsymbol{S}$). Each subproblem can be solved independently, and their solutions combined in an alternating manner using a *fractional-step method* (LeVeque, 2007). Here we use a Strang splitting strategy (LeVeque, 2007; Strang, 1968) which offers a second-order degree accuracy provided each of the subproblems are at least of this accuracy.

The subproblem (3.1.8a) is the conservative part of the system and is tied to the evaluation of the pressure. Despite the fact that (for constant pressure) it is at most only conditionally hyperbolic, here we use the non-oscillatory *high-resolution central scheme* of Nessyahu and Tadmor (1990) that gives second-order accuracy in the case of hyperbolic conservation laws. The pressure is diagnosed simultaneously with the NT scheme by solving the one-dimensional elliptic equation (3.1.6) at every time step. We can expect a degradation of the method's accuracy and even possible instabilities occurring when the system falls into a nonhyperbolic regime. A careful analysis of the system's hyperbolic/nonhyperbolic regions of the state space is beyond the scope of this thesis.

High-resolution methods are based on the use of non-linear slope or limiters which provide high accuracy in smooth parts of the solution *as well as* around shock and discontinuities, and limit spurious oscillations in the solution (LeVeque, 2002). They have the ability to resolve (with respect to grid resolution) turbulent and complex flows stably without appealing to ad hoc dissipative mechanisms for the sake of numerical stability (Drikakis and Rider, 2006). *Central schemes*, on the other hand, are high-order extensions of the staggered Lax-Friedrichs (LxF) method and are designed to bypass the expensive cost of solving Riemann problems.

For the nonlinear hyperbolic part of the system, we use the *Wave-Propagation method* of LeVeque (2007) with a linearized Riemann solver. Although the method gives second-order accuracy when applied to quasilinear hyperbolic problems with a constant coefficient matrix, it does not preserve second-order accuracy formally when used on variable-coefficient problems of the form (3.1.8b) (LeVeque, 1997).

Finally, the *method of lines* (LeVeque, 2007) is used to solve the nonconservative subproblem (3.1.8c). The method of lines reduces the initial PDE system (3.1.8c) into a system of ODEs after using finite-difference on the spatial derivatives. We solve the resulting system in time using conventional ODE solvers. Here we use the second-order centered difference

$$\left.\frac{\partial \boldsymbol{\xi}}{\partial y}\right|_{y=y_i} = \frac{\boldsymbol{\xi}_{i+1} - \boldsymbol{\xi}_{i-1}}{2\Delta y}$$

for the spatial derivative, and second-order Runge-Kutta to advance in time. Since the matrix N_{nc} is well conditioned (it is nilpotent), the resulting method is stable.

3.2 Pressure Boundary Conditions

Before moving ahead with the numerical schemes, an analytical solution to the 1D elliptic Poisson equation is given and the associated problem of pressure boundary conditions (BC) is discussed. Inverting (3.1.6) for $\frac{\partial p_b}{\partial y}$ and p_b readily gives:

$$\frac{\partial p_b}{\partial y} = C_1 + \frac{1}{1+\delta}\left[\Phi - \Phi\big|_{y=a} - \frac{\partial \phi}{\partial y} + \left.\frac{\partial \phi}{\partial y}\right|_{y=a}\right], \quad y \in [a,b], \tag{3.2.1}$$

and

$$p_b = C_2 + C_1(y-a) + \frac{1}{1+\delta}\Bigg[\phi\big|_{y=a} - \phi + \int_a^y \Phi(\boldsymbol{\xi}(x))dx + \left.\left(\frac{\partial \phi}{\partial y} - \Phi\right)\right|_{y=a}(y-a)\Bigg], \quad y \in [a,b], \tag{3.2.2}$$

where C_1 and C_2 are integration constants. The pressure gradient, which arises naturally as a forcing term in the momentum equations, is thus determined up to an arbitrary additive constant by this method. The choice here for that constant is

$$C_1 = \left.\frac{\partial p_b}{\partial y}\right|_{y=a} = 0, \tag{3.2.3}$$

which is obtained by setting $y = a$ in (3.2.1). This in turn constrains the barotropic pressure gradient and ABL/baroclinic temperature gradients via the relationship (2.3.5):

$$\frac{\partial p_b}{\partial y} = \frac{\partial p_0}{\partial y} + \frac{\delta\pi}{2}\frac{\partial \theta_b}{\partial y} + \sqrt{2}\frac{\partial}{\partial y}(\theta_1 + \theta_2) = 0 \quad \text{at} \quad y = a, b. \tag{3.2.4}$$

The simplest way to satisfy (3.2.4) is to prescribe all temperature and pressure gradients to vanish at $y = a$:

$$\frac{\partial p_b}{\partial y} = \frac{\partial p_0}{\partial y} = \frac{\partial \theta_b}{\partial y} = \frac{\partial \theta_1}{\partial y} = \frac{\partial \theta_2}{\partial y} = 0 \quad \text{at} \quad y = a, b. \tag{3.2.5}$$

This corresponds to a flow situation where the fluid is not driven out of the computational domain by a pressure gradient; we are interested in the case of pure Boussinesq buoyancy driven flows. The condition (3.2.5) is realized by extending the temperature fields to the ghost cells (fictitious grid points beyond $y = a$ and $y = b$) using a zeroth-order polynomial extrapolation.

As pointed out in the next section, the numerical scheme requires the evaluation of the pressure p_b but is oblivious to the choice of the constant C_1 as it is either differentiated out or canceled by successive addition-subtraction steps.

3.3 Non-Oscillatory Central Scheme

This section gives a short introduction to the NT central scheme (Tadmor, 1998), and looks at the particular details related to the numerical treatment of the pressure that are specific to this problem. We want to solve the combined system of conservation laws and elliptic equation for pressure

$$\begin{cases} \dfrac{\partial \boldsymbol{\xi}}{\partial t} + \dfrac{\partial \boldsymbol{F}(\boldsymbol{\xi}, p_b)}{\partial y} = 0, \\ \dfrac{\partial^2 p_b}{\partial y^2}(\boldsymbol{\xi}) = \dfrac{1}{1+\delta}\left[\dfrac{\partial \Phi}{\partial y}(\boldsymbol{\xi}) - \dfrac{\partial^2 \phi}{\partial y^2}(\boldsymbol{\xi})\right], \\ \text{BC on } \boldsymbol{\xi}, \ \dfrac{\partial \boldsymbol{\xi}}{\partial y}, \end{cases} \tag{3.3.1}$$

where Φ and ϕ are given by (2.5.1o) and (2.5.1p), respectively.

The NT scheme is part of the larger family of *finite volume methods* which are derived on the basis of the integral form of the conservation law. This formulation leads naturally to the construction of finite volume integrals which correspond to the grid *cell averages* of $\boldsymbol{\xi}$. This is in contrast with finite difference methods which are based on the differential form of the conservation law and give an approximation of the solution at the cell grid points. Before introducing the NT scheme, we first look at the more general Godunov-Type schemes, which will also lay the groundwork for the Wave-Propagation method described in Section 3.4.

Godunov-Type Schemes (LeVeque, 2002) To start, we subdivide the spatial domain into intervals of length Δy, also called *grid cells*, and define the *sliding average* of $\boldsymbol{\xi}$ over the cell I_y centered at y:

$$\bar{\boldsymbol{\xi}}(y,t) := \frac{1}{\Delta y}\int_{I_y} \boldsymbol{\xi}(x,t)dx, \qquad I_y = \left\{x \;\middle|\; |x-y| \le \frac{\Delta y}{2}\right\}. \tag{3.3.2}$$

Integrating the conservation law in (3.3.1) over the cell I_y gives

$$\frac{d}{dt}\bar{\boldsymbol{\xi}}(y,t) = \frac{1}{\Delta y}\left[\boldsymbol{F}(\boldsymbol{\xi}(y-\frac{\Delta y}{2},t),p_b(\boldsymbol{\xi}(y-\frac{\Delta y}{2},t))) - \boldsymbol{F}(\boldsymbol{\xi}(y+\frac{\Delta y}{2},t),p_b(\boldsymbol{\xi}(y+\frac{\Delta y}{2},t)))\right] \tag{3.3.3}$$

We can obtain an explicit time-marching algorithm by integrating (3.3.3) in time from t^n to t^{n+1}, where $t^n = n\Delta t$ are discrete time levels:

$$\begin{aligned}\bar{\boldsymbol{\xi}}(y,t^{n+1}) = \bar{\boldsymbol{\xi}}(y,t^n) + \frac{1}{\Delta y}\Bigg[\int_{t^n}^{t^{n+1}} &\boldsymbol{F}(\boldsymbol{\xi}(y-\frac{\Delta y}{2},\tau),p_b(\boldsymbol{\xi}(y-\frac{\Delta y}{2},\tau)))d\tau \\ &- \int_{t^n}^{t^{n+1}} \boldsymbol{F}(\boldsymbol{\xi}(y+\frac{\Delta y}{2},\tau),p_b(\boldsymbol{\xi}(y+\frac{\Delta y}{2},\tau)))d\tau\Bigg].\end{aligned} \tag{3.3.4}$$

We end up with a reformulation of the conservation law (3.3.1) in terms of the sliding averages $\bar{\boldsymbol{\xi}}(y,t^n)$ and their underlying *pointvalues* $\boldsymbol{\xi}(\cdot,\tau)$, $t^n \le \tau \le t^{n+1}$. Here we need to recover these pointvalues in terms of their known cell averages, a process involving the following two steps:

1. *Reconstruction*: The discrete pointvalues $\boldsymbol{\xi}(\cdot,\tau)$ at $\tau = t^n$ are recovered by reconstruction of a piecewise polynomial *approximation* of the form

$$\tilde{\boldsymbol{\xi}}(y,t^n) = \sum_j \boldsymbol{p}_j(y)\chi_j(y), \quad \chi_j(y) := \mathbb{1}_{\{y\in I_j\}}, \tag{3.3.5}$$

   where $\boldsymbol{p}_j$ are algebraic polynomials supported at the discrete cells $I_j = I_{y_j}$, centered around the midpoints, $y_j = j\Delta y$. That step typically involves the use of nonlinear limiters to guarantee an overall non-oscillatory piecewise reconstruction;

2. *Evolution*: We evaluate (3.3.4) at discrete gridpoints, i.e we perform an *exact* evolution of the sliding averages $\bar{\boldsymbol{\xi}}(y,t^n)$. Depending on the way to sample (3.3.4), e.g. at midcells $y = y_j$ or at cell interfaces $y = y_{j+\frac{1}{2}}$, this step may require

the use of a Riemann solver.

The reconstruction-evolution scheme described above is known as *Godunov-Type* scheme. We first introduce the background theory of the NT scheme, which is obtained from a piecewise linear reconstruction of the solution at t^n and evaluation of the integral form of the evolution equation (3.3.4) at the cell interfaces, avoiding Riemann problems altogether. The Wave-Propagation method, which requires the solutions of Riemann problems, is described in Section 3.4.

The NT Scheme (Nessyahu and Tadmor, 1990) The original second-order NT scheme is based on using a piecewise linear approximate solution at the discrete time level t^n, based on linear functions $\boldsymbol{p}_j$ supported at the cell I_j:

$$\begin{aligned}\tilde{\boldsymbol{\xi}}(y,t^n) &= \sum_j \boldsymbol{p}_j(y)\chi_j(y) \\ &= \sum_j \left[\bar{\boldsymbol{\xi}}_j^n + \boldsymbol{\xi}_j'^n\left(\frac{y-y_j}{\Delta y}\right)\right]\chi_j(y). \qquad (3.3.6)\end{aligned}$$

Here $\bar{\boldsymbol{\xi}}_j^n := \bar{\boldsymbol{\xi}}(y_j,t^n)$ denotes the average of $\boldsymbol{\xi}$ over the cell I_j at discrete time t^n. The solution over the cell I_j is now interpolated within the cell interfaces by a linear function with "discrete" slope $\boldsymbol{\xi}_j'^n$, as illustrated in Figure 3.1.

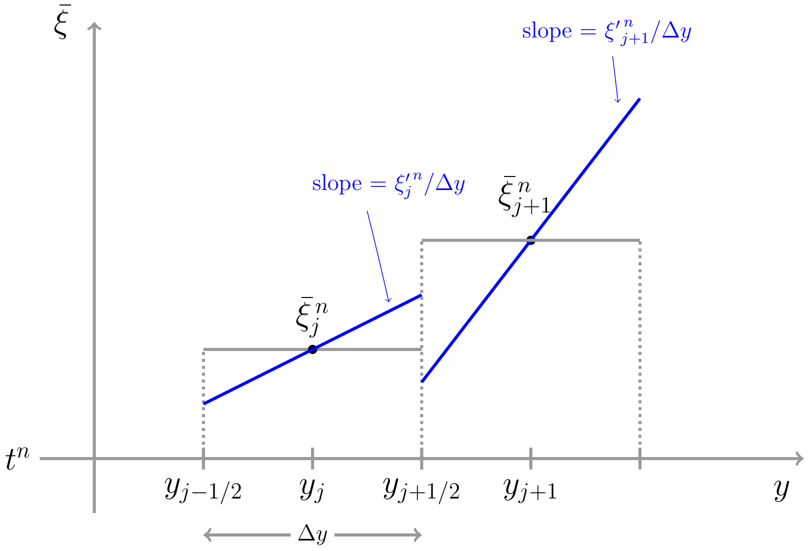

Figure 3.1: Schematic representation of the piecewise linear reconstruction in the NT central scheme. The dots represent the cell averages of the scalar ξ at time level t^n. The blue lines show possible interpolations of $\bar{\xi}$ within the cell interfaces. The discrete "slopes" ξ'^{n}_{j} are chosen to give a second-order accuracy and maintain a monotonic profile.

The discrete slope is calculated based on the known neighbouring cell averages using nonlinear *limiters* that are aimed to avoid spurious oscillations around sharp regions or discontinuities of the solution while not being too dissipative.

Nonlinear Slope Limiters One choice of slope that gives second-order accuracy in the smooth portions of the solution while remaining nonoscillatory in the discontinuous portions is the *minmod slope* (Tadmor, 1998) of the form

$$\boldsymbol{\xi}'^{n}_{j} = \mathrm{MM}_{\sigma}\{\sigma(\bar{\boldsymbol{\xi}}^{n}_{j+1} - \bar{\boldsymbol{\xi}}^{n}_{j}), \frac{1}{2}(\bar{\boldsymbol{\xi}}^{n}_{j+1} - \bar{\boldsymbol{\xi}}^{n}_{j-1}), \sigma(\bar{\boldsymbol{\xi}}^{n}_{j} - \bar{\boldsymbol{\xi}}^{n}_{j-1})\}, \tag{3.3.7}$$

where $\sigma \in [0,2)$ is a non-oscillatory limiter and MM denotes the minmod function, defined by

$$\mathrm{MM}\{x_1, x_2, \dots\} = \begin{cases} \min_i\{x_i\} & \text{if } x_i > 0, \forall i, \\ \max_i\{x_i\} & \text{if } x_i < 0, \forall i, \\ 0 & \text{otherwise.} \end{cases}$$

Evolution Step of the NT Scheme A central scheme is obtained by evaluating (3.3.4) at the interfacing breakpoints, $y = y_{j+\frac{1}{2}}$, which yields:

$$\begin{aligned} \bar{\boldsymbol{\xi}}^{n+1}_{j+\frac{1}{2}} &= \bar{\boldsymbol{\xi}}^{n}_{j+\frac{1}{2}} + \frac{1}{\Delta y}\left[\int_{t^n}^{t^{n+1}} \boldsymbol{F}(\boldsymbol{\xi}(y_j,\tau), p_b(\boldsymbol{\xi}(y_j,\tau)))d\tau \right. \\ &\qquad \left. - \int_{t^n}^{t^{n+1}} \boldsymbol{F}(\boldsymbol{\xi}(y_{j+1},\tau), p_b(\boldsymbol{\xi}(y_{j+1},\tau)))d\tau \right] \end{aligned} \tag{3.3.8}$$

The first term on the right hand side of (3.3.8) is the staggered cell average at discrete time t^n, $\bar{\xi}^n_{j+\frac{1}{2}}$, which can be computed directly from the reconstruction (3.3.6):

$$\begin{aligned} \bar{\boldsymbol{\xi}}^{n}_{j+\frac{1}{2}} &= \frac{1}{\Delta y}\int\limits_{y_j}^{y_{j+1}} \tilde{\boldsymbol{\xi}}(y,t^n)dy \\ &= \underbrace{\frac{1}{\Delta y}\int\limits_{y_j}^{y_{j+\frac{1}{2}}} \left[\bar{\boldsymbol{\xi}}^n_j + \boldsymbol{\xi}'^n_j\left(\frac{y-y_j}{\Delta y}\right)\right]dy}_{\frac{\Delta y}{2}\bar{\boldsymbol{\xi}}^n_j + \frac{\Delta y}{8}\boldsymbol{\xi}'^n_j} + \underbrace{\frac{1}{\Delta y}\int\limits_{y_{j+\frac{1}{2}}}^{y_{j+1}} \left[\bar{\boldsymbol{\xi}}^n_{j+1} + \boldsymbol{\xi}'^n_{j+1}\left(\frac{y-y_{j+1}}{\Delta y}\right)\right]dy}_{\frac{\Delta y}{2}\bar{\boldsymbol{\xi}}^n_{j+1} - \frac{\Delta y}{8}\boldsymbol{\xi}'^n_{j+1}} \\ &= \frac{1}{2}(\bar{\boldsymbol{\xi}}^n_j + \bar{\boldsymbol{\xi}}^n_{j+1}) + \frac{1}{8}(\boldsymbol{\xi}'^n_j - \boldsymbol{\xi}'^n_{j+1}). \end{aligned} \tag{3.3.9}$$

Approximation of the Flux Integrals We now turn to the flux integrals in (3.3.8). We follow the evolution of the solution pointvalues within the cell I_j centered at midpoint y_j, which are governed by

$$\boldsymbol{\xi}_t + \boldsymbol{F}(\boldsymbol{\xi}, p_b)_y = 0; \quad \tau \geq t^n \qquad \boldsymbol{\xi}(y,t^n) = \boldsymbol{p}_j(y) \quad y \in I_j. \tag{3.3.10}$$

Assume that the matrix of wavespeeds $A_c = \frac{\partial \boldsymbol{F}}{\partial \boldsymbol{\xi}}$ has real eigenvalues $\{\lambda_m(\boldsymbol{\xi})\}_m$, $1 \leq m \leq 13$. By hyperbolicity, the discontinuities of piecewise linear function (3.3.6) at the interfaces $(y_{j\pm1+1/2}, t^n)$ will propagate along the characteristics no faster than $c = \max_m |\lambda_m(\boldsymbol{\xi})|$. Hence the midcell values $\boldsymbol{\xi}(y_j, \tau \geq t^n)$, which evolve according to (3.3.10), will remain free of discontinuities as long as the CFL condition (LeVeque, 2002)

$$\frac{c}{2\Delta y/\Delta t} < 1$$

is satisfied, that is, as long as the maximum propagation speed c of the discontinuities at the cell interfaces is smaller than the numerical speed (see Figure 3.2).

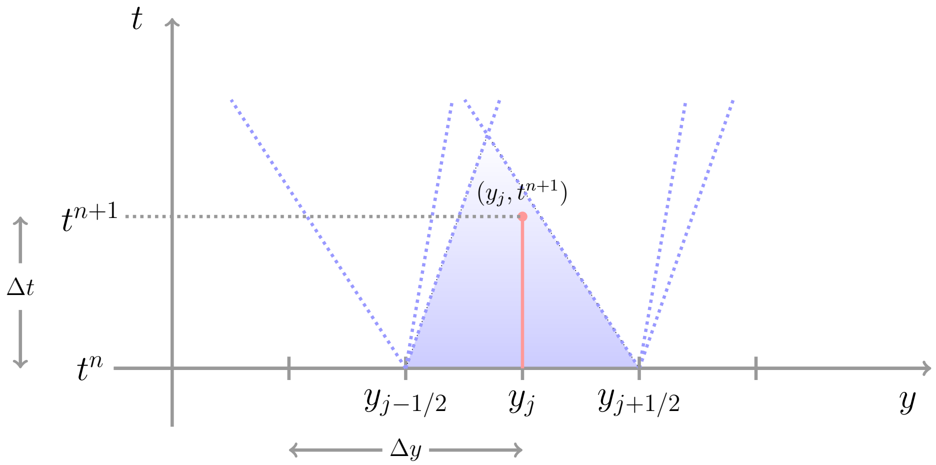

Figure 3.2: CFL condition for the NT scheme. The discontinuities at the cell interfaces $y_{j\pm1/2}$ propagate along the characteristics (dotted blue lines) no faster than $c = \max_m |\lambda_m(\boldsymbol{\xi})|$ ($m = 3$ in this example). The solution at the cell midpoint (y_j, t^n) evolves in time along the red path. It remains free of discontinuities for a sufficiently small time step $\Delta t < 2\Delta y/c$, which guarantees that the solution is secured within the smooth region bounded by the characteristics (shaded blue area).

Consequently, the flux integrals $\int_{t^n}^{t^{n+1}} \boldsymbol{F}(\boldsymbol{\xi}(y_{j\pm1}, \tau), p_b(\boldsymbol{\xi}(y_{j\pm1}, \tau)))d\tau$ along the midcells $y_{j\pm1}$ involve only smooth integrands, and can be approximated using a numerical quadrature formula. This is, in essence, what characterizes the *central* scheme: the staggered cell average $\bar{\xi}^{n+1}_{j+1/2}$ is based on the midcell values $(y_{j\pm1}, \tau > t^n)$ integrated "under" the Riemann fans centered at the cell interfaces $y_{j+1/2}$ (see Figure 3.3). Riemann solvers are thus avoided.

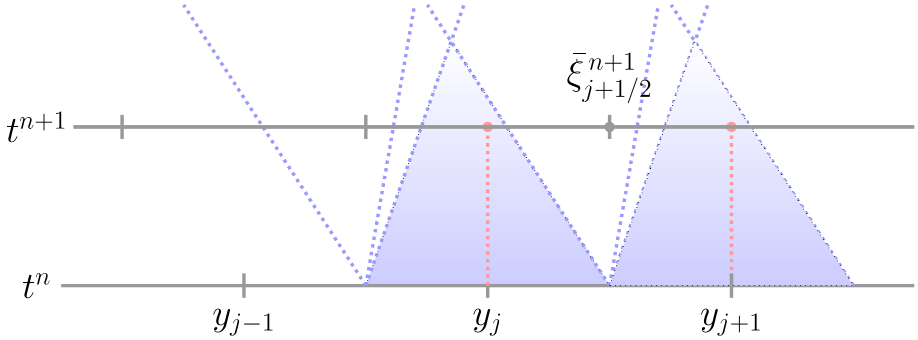

Figure 3.3: Central differencing in the NT scheme. The staggered cell average $\bar{\xi}^{n+1}_{j+1/2}$ is based on the evaluation of the numerical fluxes along the midcells $(y_{j\pm1}, \tau > t^n)$ (red dashed), which remain smooth as long as the CFL condition is satisfied.

The flux integrals are computed using a second-order[1] accurate midpoint quadrature rule

$$\int_{t_n}^{t_{n+1}} \boldsymbol{F}(\tilde{\boldsymbol{\xi}}(y_j,t), p_b(\tilde{\boldsymbol{\xi}}(y_j,t)))dt = \boldsymbol{F}(\tilde{\boldsymbol{\xi}}(y_j,t^{n+1/2}), p_b(\tilde{\boldsymbol{\xi}}(y_j,t^{n+1/2})))\Delta t + \mathcal{O}(\Delta t)^3, \tag{3.3.11}$$

where we used the reconstruction (3.3.6). The values at half time step in (3.3.11) are predicted using Taylor expansion and the conservation law (3.3.1):

$$\begin{aligned}
\tilde{\boldsymbol{\xi}}(y_j, t^{n+\frac{1}{2}}) &= \tilde{\boldsymbol{\xi}}(y_j, t^n) + \frac{\Delta t}{2}\frac{\partial \tilde{\boldsymbol{\xi}}}{\partial t}\Big|_{\{t=t^n, y=y_j\}} + \mathcal{O}(\Delta t)^2 \\
&= \bar{\boldsymbol{\xi}}^n_j - \frac{\Delta t}{2}\frac{\partial \boldsymbol{F}}{\partial y}\Big|_{\{t=t^n, y=y_j\}} + \mathcal{O}(\Delta t)^2, \\
&= \bar{\boldsymbol{\xi}}^n_j - \frac{\lambda}{2}\boldsymbol{F}'^n_j + \mathcal{O}(\Delta t)^2.
\end{aligned} \tag{3.3.12}$$

---

[1] The midpoint rule has a local truncation error of $\mathcal{O}(\Delta)^3$. Hence it is second-order accurate globally.

Here, the numerical derivative of the components of $\boldsymbol{F}$ are calculated using the limiter (3.3.7), and $\lambda := \Delta t/\Delta y$ is a mesh ratio.

In summary, we end up with the central scheme which consists of a first-order *predictor* step,

$$\tilde{\boldsymbol{\xi}}_j^{n+\frac{1}{2}} = \bar{\boldsymbol{\xi}}_j^{\,n} - \frac{\lambda}{2}\boldsymbol{F}'^{n}_{\ j}, \qquad \tilde{\boldsymbol{\xi}}_j^{n+\frac{1}{2}} := \tilde{\boldsymbol{\xi}}(y_j, t^{n+\frac{1}{2}}), \tag{3.3.13}$$

followed by a second-order *corrector* step,

$$\bar{\boldsymbol{\xi}}_{j+\frac{1}{2}}^{n+1} = \frac{1}{2}\left(\bar{\boldsymbol{\xi}}_j^{\,n} + \bar{\boldsymbol{\xi}}_{j+1}^{\,n}\right) + \frac{1}{8}\left(\boldsymbol{\xi}'^{\,n}_j - \boldsymbol{\xi}'^{n}_{j+1}\right) - \lambda\left[\boldsymbol{F}(\tilde{\boldsymbol{\xi}}_{j+1}^{n+\frac{1}{2}}, p_{b_{j+1}}^{n+\frac{1}{2}}) - \boldsymbol{F}(\tilde{\boldsymbol{\xi}}_j^{n+\frac{1}{2}}, p_{b_j}^{n+\frac{1}{2}})\right] \tag{3.3.14}$$

where

$$p_{b_j}^{n+\frac{1}{2}} := p_b(\tilde{\boldsymbol{\xi}}_j^{n+1/2}) \tag{3.3.15}$$

The method is overall second-order with $\mathcal{O}(\Delta x) = \mathcal{O}(\Delta t)$. The numerical pressure (3.3.15) is treated next.

3.3.1 Numerical Treatment of the Pressure

The numerical pressure is required both at the predictor (for the slope of the numerical flux) and corrector steps, i.e. at integral and half time steps t^m, $m = \{n, n+1/2\}$. The solution (3.2.2) of the Poisson pressure equation (2.5.1n)-(2.5.1p) is discretized according to

$$p_{b_j}^m = \frac{1}{1+\delta}\left[\phi_1^m - \phi_j^m + I_j^m + (\phi'^{\,m}_{\ 1} - \Phi_1^m \Delta y)\,(j-1)\right] \tag{3.3.16}$$

where

$$I_j^m = \frac{\Delta y}{2}\left(\Phi_1^m + \Phi_j^m\right) + \Delta y \sum_{k=2}^{j-1} \Phi_k^m \tag{3.3.17}$$

is the result of the midpoint rule for the integral $\int_a^y \Phi(\tilde{\boldsymbol{\xi}}(x))dx$ using $a = y_1$ as the left boundary, $\Phi_j^m := \Phi(\tilde{\boldsymbol{\xi}}(y_j, t^m), y_j)$ and $\phi_j^m := \phi(\tilde{\boldsymbol{\xi}}(y_j, t^m))$. Note that the pressure gradient BC (3.2.3) was set to zero and the additional pressure BC in (3.2.2) is immaterial since it gets either differentiated out at the predictor step (3.3.13) or canceled by successive addition-subtraction steps in the corrector step (3.3.14).

3.4 Wave-Propagation Method

In this section we give the salient features of Wave-Propation method of LeVeque (1997) to solve the nonlinear hyperbolic problem (3.1.8b)

$$\frac{\partial \boldsymbol{\xi}}{\partial t} + D_{nc}(\boldsymbol{\xi})\frac{\partial \boldsymbol{\xi}}{\partial y} = 0, \tag{3.4.1}$$

where $D_{nc} \in \mathbb{R}^{13}$ is the diagonal matrix (3.1.3). For a comprehensive description of the method, see LeVeque (2002). The method is best introduced by first looking at the linear corresponding case in which the matrix D_{nc} is independent of the solution $\boldsymbol{\xi}$, namely the system

$$\boldsymbol{\xi}_t + D\,\boldsymbol{\xi}_y = 0, \tag{3.4.2}$$

where D is a matrix of constant coefficients. The matrix D is real and diagonal, hence it has real constant eigenvalues given by its diagonal elements, which we denote by

$$\lambda^1 \le \lambda^2 \le \cdots \le \lambda^{13},$$

and its eigenvectors are the standard basis in $\mathbb{R}^{13}$, $\boldsymbol{e}^1, \ldots, \boldsymbol{e}^{13}$. Since D is diagonal, this system decouples into m independent advection equations for the components ξ^m of $\boldsymbol{\xi}$:

$$\xi_t^m + \lambda^m \xi_y^m = 0 \quad \text{for} \quad m = 1, 2, \ldots, 13. \tag{3.4.3}$$

Consider the Cauchy problem for the m^{th} linear advection equation of (3.4.3) in which we are given data

$$\xi^m(y,0) = \mathring{\xi}^m(y) \qquad \text{for } -\infty < y < \infty. \tag{3.4.4}$$

The m^{th} advection equation has thus the *characteristic* solution

$$\xi^m(y,t) = \xi^m(y_0,0) = \mathring{\xi}^m(y - \lambda^m t),$$

which is a simple wave advected at constant speed λ^m as time evolves, i.e. $\xi^m(y,t) \equiv \xi^m(y_0)$ all along the *characteristic curve* $y(t) = y_0 + \lambda^m t$. The solution of the linear system (3.4.2) is a linear combination of 13 waves traveling at characteristic speeds $\lambda^1, \lambda^2, \ldots, \lambda^{13}$:

$$\boldsymbol{\xi}(y,t) = \sum_{m=1}^{13} \xi^m(y,t)\boldsymbol{e}^m. \tag{3.4.5}$$

Godunov's Method The Wave-Propagation method is a Godunov-Type scheme based on a sampling of the formula (3.3.4) at the cell midpoints $y = y_j$:

$$\bar{\boldsymbol{\xi}}_j^{n+1} = \bar{\boldsymbol{\xi}}_j^{n} + \frac{1}{\Delta y}\left[\int_{t^n}^{t^{n+1}} \boldsymbol{G}(\boldsymbol{\xi}(y_{j-1/2},\tau))d\tau - \int_{t^n}^{t^{n+1}} \boldsymbol{G}(\boldsymbol{\xi}(y_{j+1/2},\tau))d\tau\right] \tag{3.4.6}$$

where

$$\boldsymbol{G} = D\,\boldsymbol{\xi}_y.$$

The time integrals on the right-hand side cannot be found exactly because the integrands depend on the solution which varies with t. However we can compute this integral exactly if we replace the function $\boldsymbol{\xi}(\cdot,\tau)$ by a first-order piecewise constant reconstruction of the form (3.3.5) at time level $\tau = t^n$:

$$\tilde{\boldsymbol{\xi}}(y,t^n) = \sum_j \boldsymbol{p}_j(y)\chi_j(y) = \sum_j \bar{\boldsymbol{\xi}}_j^n \chi_j(y).$$

This piecewise constant function simply takes the cell average value $\bar{\boldsymbol{\xi}}_j^n$ in the j^{th} grid cell centered at y_j, and contains single jump discontinuities at the cell interfacing points. As we shall see next, the cell interfacing value $\tilde{\boldsymbol{\xi}}(y_{j-1/2}, \tau)$ is in fact (componentwise) constant over the time interval $t^n < \tau \leq t^{n+1}$ in the case of linear hyperbolic systems such as (3.4.2), and the *numerical flux function*

$$\boldsymbol{\mathcal{G}}_{j-1/2} = \frac{1}{\Delta t} \int_{t^n}^{t^{n+1}} \boldsymbol{G}(\tilde{\boldsymbol{\xi}}(y_{j-1/2}, \tau)) d\tau$$

can be evaluated exactly. We then obtain an approximate scheme for (3.4.6) of the form

$$\bar{\boldsymbol{\xi}}_j^{n+1} \quad = \quad \bar{\boldsymbol{\xi}}_j^n + \frac{\Delta t}{\Delta y} \left(\boldsymbol{\mathcal{G}}_{j-1/2}^n - \boldsymbol{\mathcal{G}}_{j+1/2}^n \right). \tag{3.4.7}$$

The rest of this section is concerned with calculating the numerical flux functions $\boldsymbol{\mathcal{G}}_{j-1/2}^n$ and $\boldsymbol{\mathcal{G}}_{j+1/2}^n$ (or rather the numerical flux *difference* $\boldsymbol{\mathcal{G}}_{j-1/2}^n - \boldsymbol{\mathcal{G}}_{j+1/2}^n$) which require the solution of the fundamental *Riemann problem.*

The Riemann Problem for Linear Hyperbolic Systems The Riemann problem for the linear hyperbolic equation (3.4.2) consist of the PDE (3.4.2) together with special initial data that is piecewise constant with a single jump discontinuity put for simplicity at $y = 0$:

$$\mathring{\boldsymbol{\xi}}(y) = \begin{cases} \boldsymbol{\xi}_l & \text{if} \quad y < 0, \\ \boldsymbol{\xi}_r & \text{if} \quad y > 0, \end{cases} \qquad (t = 0). \tag{3.4.8}$$

For linear systems, we expect this discontinuity to propagate *only* along the characteristic curves. We can decompose $\boldsymbol{\xi}_l$ and $\boldsymbol{\xi}_r$ as

$$\boldsymbol{\xi}_l = \sum_{m=1}^{13} \xi_l^m \boldsymbol{e}^m \quad \text{and} \quad \boldsymbol{\xi}_r = \sum_{m=1}^{13} \xi_r^m \boldsymbol{e}^m.$$

Then the m^{th} advection equation (3.4.3) has Riemann data

$$\mathring{\xi}^m(y) = \begin{cases} \xi_l^m & \text{if} \quad y < 0, \\ \xi_r^m & \text{if} \quad y > 0, \end{cases} \qquad (t = 0),$$

and this discontinuity simply propagates with speed λ^m along the characteristics $y(t) = \lambda^m t$, that is:

$$\xi^m(y,t) = \begin{cases} \xi_l^m & \text{if} \quad y < \lambda^m t, \\ \xi_r^m & \text{if} \quad y > \lambda^m t. \end{cases}$$

The solution to the original problem can be written as (see Figure 3.4)

$$\boldsymbol{\xi}(y,t) = \sum_{m:\, y/t<\lambda^m} \xi_l^m \boldsymbol{e}^m + \sum_{m:\, y/t>\lambda^m} \xi_r^m \boldsymbol{e}^m \quad (t > 0). \tag{3.4.9}$$

The discontinuities themselves can be viewed as waves travelling through the domain. If we project the jumps in $\boldsymbol{\xi}_l - \boldsymbol{\xi}_m$ across the characteristics onto the eigenvectors,

$$\boldsymbol{\xi}_r - \boldsymbol{\xi}_l = \sum_{m=1}^{13} \alpha^m \boldsymbol{e}^m, \tag{3.4.10}$$

and define

$$\boldsymbol{\mathcal{W}}^m = \alpha^m \boldsymbol{e}^m$$

as the wave travelling at speed λ^m through the characteristic $y = \lambda^m t$, the solution then becomes

$$\boldsymbol{\xi}(y,t) = \boldsymbol{\xi}_r(y,t) - \sum_{m:\, y/t<\lambda^m} \boldsymbol{\mathcal{W}}^m = \boldsymbol{\xi}_l(y,t) + \sum_{m:\, y/t>\lambda^m} \boldsymbol{\mathcal{W}}^m .$$

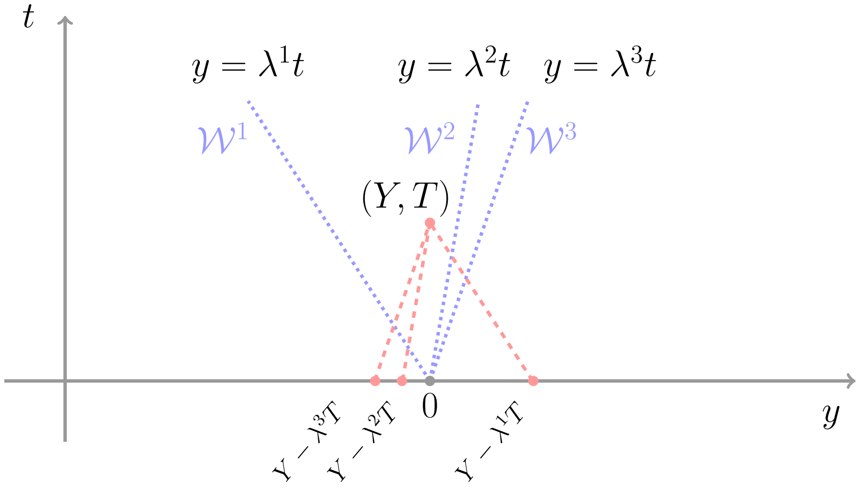

Figure 3.4: Construction of the solution to the Riemann problem at (Y,T) for a linear hyperbolic system of dimension 3 with $\lambda^1 < 0 < \lambda^2 < \lambda^3$. The solution value of $\boldsymbol{\xi}$ is constant in every four wedges of the $y-t$ plane delimited by the characteristics $\lambda^1 t$, $\lambda^2 t$, and $\lambda^3 t$ (dotted blue) that are emerging from the initial discontinuities at $(0,0)$. The solution at a point $(y, t>0)$ is obtained by tracing back along the characteristics (dashed red) to determine the value of ξ^m from the initial data. For instance, the solution at (Y,T) to given by $\boldsymbol{\xi}(Y,T) = \xi_r^1 \boldsymbol{e}^1 + \xi_l^2 \boldsymbol{e}^2 + \xi_l^3 \boldsymbol{e}^3$. The initial discontinuities propagate along the characteristics at speeds λ^1, λ^2, and λ^3, and can be viewed as waves $\mathcal{W}^1$, $\mathcal{W}^2$, $\mathcal{W}^3$.

The Wave-Propagation Form of Godunov's Method Instead of trying to determine the numerical flux functions $\boldsymbol{\mathcal{G}}^n_{j-1/2}$ and $\boldsymbol{\mathcal{G}}^n_{j+1/2}$ directly, we look at how the wave decomposition of the form (3.4.10) affects the cell average $\bar{\boldsymbol{\xi}}^n_j$. For the linear hyperbolic system (3.4.2), the solution to the Riemann problem centered at the cell interfacing discontinuity $y_{j-1/2}$ is the set of waves

$$\bar{\boldsymbol{\xi}}_j - \bar{\boldsymbol{\xi}}_{j-1} = \sum_{m=1}^{13} \alpha_{j-1/2}^m \boldsymbol{e}^m = \sum_{m=1}^{13} \boldsymbol{\mathcal{W}}_{j-1/2}^m. \tag{3.4.11}$$

Each wave $\mathcal{W}_{j-1/2}^m$ propagates along its characteristics at a speed λ^m, and thus after a time interval Δt it will have travelled a distance $\lambda^m \Delta t$. If $\lambda^m > 0$, then the wave $\mathcal{W}_{j-1/2}^m$ will have modified the cell average component $\bar{\xi}_j^m$ by a fraction $\lambda^m \Delta t/\Delta y$ of the jump $\bar{\xi}_{j-1}^m - \bar{\xi}_j^m$ across the m^{th} wave. It follows that the passage of the m^{th} wave over the grid cell I_j will change its initial cell average $\bar{\xi}_j^m$ by an amount

$$-(\bar{\xi}_j^m - \bar{\xi}_{j-1}^m)\frac{\lambda^m \Delta t}{\Delta y} = -\mathcal{W}_{j-1/2}^m \frac{\lambda^m \Delta t}{\Delta y} \qquad (\lambda^m > 0).$$

If we set

$$\lambda^+ = \max(\lambda, 0) \quad \text{and} \quad \lambda^- = \min(\lambda, 0),$$

we can conveniently write the cell average (3.4.7) update as

$$\bar{\boldsymbol{\xi}}_j^{n+1} = \bar{\boldsymbol{\xi}}_j^n - \frac{\Delta t}{\Delta y}\left[\sum_{m=1}^{13} (\lambda^m)^+ \boldsymbol{\mathcal{W}}_{j-1/2}^m + \sum_{m=1}^{13} (\lambda^m)^- \boldsymbol{\mathcal{W}}_{j+1/2}^m\right]. \tag{3.4.12}$$

As a shorthand, we introduce the following symbolic notations:

$$\begin{aligned} \mathcal{A}^- \Delta \bar{\boldsymbol{\xi}}_{j-1/2} &= \sum_{m=1}^{13} (\lambda^m)^- \boldsymbol{\mathcal{W}}_{j-1/2}^m, \\ \mathcal{A}^+ \Delta \bar{\boldsymbol{\xi}}_{j-1/2} &= \sum_{m=1}^{13} (\lambda^m)^+ \boldsymbol{\mathcal{W}}_{j-1/2}^m, \end{aligned}$$

where

$$\Delta \bar{\boldsymbol{\xi}}_{j-1/2} = \bar{\boldsymbol{\xi}}_j - \bar{\boldsymbol{\xi}}_{j-1}$$

is the jump in the solution at the cell interface $y_{j-1/2}$. In this wave-propagation form of Godunov's method, all that was required is the numerical flux *difference* $\mathcal{G}^n_{j+1/2} - \mathcal{G}^n_{j-1/2}$, which is decomposed into a *left-going flux difference* $\mathcal{A}^- \Delta\bar{\boldsymbol{\xi}}$ and a *right-going flux difference* $\mathcal{A}^+ \Delta\bar{\boldsymbol{\xi}}$, with the property that

$$\mathcal{G}^n_{j+1/2} - \mathcal{G}^n_{j-1/2} = \mathcal{A}^- \Delta\bar{\boldsymbol{\xi}}_{j+1/2} + \mathcal{A}^+ \Delta\bar{\boldsymbol{\xi}}_{j-1/2}.$$

This gives the first-order Wave-Propagation method for the linear hyperbolic system (3.4.2):

$$\bar{\boldsymbol{\xi}}^{n+1}_j = \bar{\boldsymbol{\xi}}^n_j - \frac{\Delta t}{\Delta y}\left(\mathcal{A}^+ \Delta\boldsymbol{\xi}_{j-1/2} + \mathcal{A}^- \Delta\boldsymbol{\xi}_{j+1/2}\right). \tag{3.4.13}$$

Second-Order Correction Godunov's method is extended to a high resolution method by adding an additional term. The form of the extended method is

$$\bar{\boldsymbol{\xi}}^{n+1}_j = \bar{\boldsymbol{\xi}}^n_j - \frac{\Delta t}{\Delta y}\left(\mathcal{A}^+ \Delta\boldsymbol{\xi}_{j-1/2} + \mathcal{A}^- \Delta\boldsymbol{\xi}_{j+1/2}\right) - \frac{\Delta t}{\Delta y}\left(\boldsymbol{F}_{j+1/2} - \boldsymbol{F}_{j-1/2}\right),$$

where $\boldsymbol{F}_{j-1/2}$ is a correction flux defined in terms of the waves $\boldsymbol{\mathcal{W}}^m_{j-1/2}$ and speeds $\lambda^m_{j-1/2}$ arising from the Riemann problem centered at $j - 1/2$ of the form

$$\boldsymbol{F}_{j-1/2} = \frac{1}{2}\sum_{m=1}^{13} |\lambda^m_{j-1/2}| \left(1 - \frac{\Delta t}{\Delta y}|\lambda^m_{j-1/2}|\right) \boldsymbol{\mathcal{W}}^m_{j-1/2}. \tag{3.4.14}$$

For linear systems, the wave method with fluctuations (3.4.13) and corrections (3.4.14) yields a second-order accurate method. For nonlinear problems such as (3.4.1), this form of corrections does not give second-order accuracy formally (LeVeque, 1997).

Linearized Riemann Solvers We now turn back to the original nonlinear problem (3.4.1). The eigenvalues of the matrix D_{nc} are its diagonal elements, with corresponding eigenvectors that are given by the standard basis in $\mathbb{R}^{13}$:

$$\begin{aligned}
\lambda^1 &= v_b, & \boldsymbol{r}^1 &= \boldsymbol{e}^1, \\
&& \vdots && \\
\lambda^6 &= -\sqrt{2}(v_1 + v_2), & \boldsymbol{r}^6 &= \boldsymbol{e}^6, \\
&& \vdots && \\
\lambda^{13} &= v_0, & \boldsymbol{r}^{13} &= \boldsymbol{e}^{13}.
\end{aligned}$$

The wave speeds λ^m depend now on the solution $\boldsymbol{\xi}$, and the Riemann problems in Wave-Propagation method (3.4.14) are nonlinear. A very natural approach to defining an approximate Riemann solution is to replace the nonlinear Riemann problem $\boldsymbol{\xi}_t + D_{nc}(\boldsymbol{\xi})\boldsymbol{\xi}_y$ by the linearized problem defined locally at each cell interface,

$$\hat{\boldsymbol{\xi}}_t + \hat{D}_{j-1/2}\hat{\boldsymbol{\xi}}_y = 0.$$

The matrix $\hat{D}_{j-1/2}$ is chosen to be some approximation to $D_{nc}(\boldsymbol{\xi})$ valid in a neighbourhood of the data $\boldsymbol{\xi}_{j-1}$ and $\boldsymbol{\xi}_{\boldsymbol{j}}$. The choice for that matrix $\hat{D}_{j-1/2}$ is here

$$\hat{D}_{j-1/2} = \frac{D_{nc}(\boldsymbol{\xi}_{j-1}) + D_{nc}(\boldsymbol{\xi}_j)}{2},$$

so that

$$\hat{D}_{j-1/2} \to D_{nc}(\bar{\boldsymbol{\xi}}) \quad \text{as} \quad \boldsymbol{\xi}_{j-1}, \boldsymbol{\xi}_j \to \bar{\boldsymbol{\xi}},$$

and the method remains consistent with the original nonlinear problem since $D_{nc}(\bar{\boldsymbol{\xi}})$ depends continuously on $\bar{\boldsymbol{\xi}}$. This choice is justified in regions where the solution is smooth since in these regions, the variation in $\bar{\boldsymbol{\xi}}$ is $\Delta\bar{\boldsymbol{\xi}}_{j-1/2} = \mathcal{O}(\Delta y)$ and the matrix D_{nc} is nearly constant, $D_{nc}(\bar{\boldsymbol{\xi}}_{j-1}) \approx D_{nc}(\bar{\boldsymbol{\xi}}_j)$.

3.5 Strang Splitting

So far we have described how to approximate numerically the solution of the homogenous conservative problem

$$\boldsymbol{\xi}_t + \boldsymbol{F}(\boldsymbol{\xi})_y = 0 \tag{3.5.1a}$$

and the homogeneous hyperbolic problem

$$\boldsymbol{\xi}_t + D_{nc}(\boldsymbol{\xi})\boldsymbol{\xi}_y = 0 \tag{3.5.1b}$$

by the non-oscillatory NT central scheme and the Wave Propagation method, respectively. As mentioned before, the homogeneous system with nilpotent advection matrix,

$$\boldsymbol{\xi}_t + N_{nc}(\boldsymbol{\xi})\boldsymbol{\xi}_y = 0, \tag{3.5.1c}$$

is solved by the method of lines. The full nonhomogenous problem

$$\boldsymbol{\xi}_t + \boldsymbol{F}(\boldsymbol{\xi})_y + D_{nc}(\boldsymbol{\xi})\boldsymbol{\xi}_y + N_{nc}(\boldsymbol{\xi})\boldsymbol{\xi}_y = \boldsymbol{S}(\boldsymbol{\xi}) \tag{3.5.2}$$

with source term $\boldsymbol{S}$ is solved using *Strang splitting*, a fractional-step method first introduced by Strang (1968) (see also LeVeque, 2002). The idea of Strang splitting is is to somehow alternate between the simpler subproblems (3.5.1) for which there are known numerical methods, in order to approximate the solution for the full problem (3.5.2). Consider for instance the general linear PDE

$$\boldsymbol{\xi}_t = (\mathcal{A} + \mathcal{B})\boldsymbol{\xi} \tag{3.5.3}$$

where $\mathcal{A}$ and $\mathcal{B}$ are linear differential operators. The Strang splitting strategy consists of solving the first subproblem $\boldsymbol{\xi}_t = \mathcal{A}\boldsymbol{\xi}$ over a time step of $\Delta t/2$, followed by a solve of $\boldsymbol{\xi}_t = \mathcal{B}\boldsymbol{\xi}$ over a time step of Δt, and finally take another half time step on $\boldsymbol{\xi}_t = \mathcal{A}\boldsymbol{\xi}$. After the first solve, the solution gets updated by

$$\boldsymbol{\xi}^* = e^{\mathcal{A}\Delta t/2}\boldsymbol{\xi}(y,0).$$

This solution is used as data for the second update:

$$\boldsymbol{\xi}^{**} = e^{\mathcal{B}\Delta t}\boldsymbol{\xi}^* = e^{\mathcal{B}\Delta t}e^{\mathcal{A}\Delta t/2}\boldsymbol{\xi}(y,0).$$

The third update is equivalent to advancing the original full problem (3.5.3) by one single time step of length Δt:

$$\boldsymbol{\xi}(y,\Delta t) = e^{\mathcal{A}\Delta t/2}e^{\mathcal{B}\Delta t}e^{\mathcal{A}\Delta t/2}\boldsymbol{\xi}(y,0) = e^{\Delta t(\mathcal{A}+\mathcal{B})}\boldsymbol{\xi}(y,0) + \mathcal{O}(\Delta t^3).$$

Comparing the Taylor series of the middle and right-hand side terms confirms that the two methods agree to $\mathcal{O}(\Delta t^3)$. The splitting error alone will then introduce an $\mathcal{O}(\Delta t^3)$ error at each time step, which accumulates to an $\mathcal{O}(\Delta t^2)$ error after $T/\Delta t$ time steps. The convergence and accuracy of the method in the nonlinear case is not clear, since the Taylor series argument above breaks down if the solution is nonsmooth. The applications of the Strang strategy to nonlinear problems are however numerous (LeVeque, 2002), and most notably second-order convergence was obtained in the case of a similar but simpler nonlinear PDE in Stechmann et al. (2008).

The full nonconservative system with source terms (3.5.2) is solved over a time step Δt using the following steps:

(1) Use the Runge-Kutta ODE solver to solve $\boldsymbol{\xi}_t = -\boldsymbol{S}(\boldsymbol{\xi})$ over $\Delta t/2$;

(2) Apply the method of lines to solve (3.5.1c) over $\Delta t/2$;

(3) Apply the Wave Propagation method to solve (3.5.1b) over $\Delta t/2$;

(4) Apply the central NT scheme to solve (3.5.1a) over Δt;

(5) Repeat Step 3;

(6) Repeat Step 2;

(7) Repeat Step 1;

Note that this particular order of operators is chosen to minimize computation time: The NT central scheme being the most expensive task, it is assigned to the middle step update over Δt and hence gets executed only once.

3.6 Grid Convergence Error Analysis

In this section we look at the accuracy and convergence properties of the numerical scheme described in Section 3.5 designed to solve the nonconservative system of PDE (3.5.2). We demonstrate by numerical tests that the scheme converges to the correct solution as the grid is refined with a second-order rate of convergence, and also that reasonable error estimates are obtained.

Although the true solution to the governing PDE is not known, we can monitor grid convergence towards a nontrivial exact solution adding the appropriate forcing to the PDE. The necessary condition is that the solution be nontrivial, that is, that it has significant solution structure to exercise higher-derivative calculations (Roache, 1997). To this end, we use a travelling sine wave solution on a 2π-periodic domain for each one the components of $\boldsymbol{\xi}$:

$$\xi^m_{wav}(y,t) = \sin(y-t), \qquad m = 1,\dots,13, \quad y \in [0,2\pi], \ t \geq 0. \tag{3.6.1}$$

Although this mathematically naive solution is unphysical, it allows to accomplish the code verification just as well as physically realistic solutions.

We verify the numerical scheme for the advection part of the PDE with no forcings, which we denote $\mathcal{L}(\boldsymbol{\xi}) \coloneqq \boldsymbol{\xi}_t + [\boldsymbol{F}(\boldsymbol{\xi}, p_b)]_y + N_{nc}(\boldsymbol{\xi})\boldsymbol{\xi}_y + D_{nc}(\boldsymbol{\xi})\boldsymbol{\xi}_y = 0$. The vector $\boldsymbol{\xi}_{wav}$ of travelling wave solutions (3.6.1) will then satisfy the following "balanced" system

$$\mathcal{L}(\boldsymbol{\xi}) = \boldsymbol{\Psi} \tag{3.6.2}$$

exactly, where $\boldsymbol{\Psi} = \mathcal{L}(\boldsymbol{\xi}_{wav})$ is given by

$$\boldsymbol{\Psi}(y,t) = \begin{pmatrix} -\cos(y-t) + \frac{1}{2}\sin[2(y-t)] \\ -\cos(y-t) + \frac{1}{2}\sin[2(y-t)] \\ -\cos(y-t) + \frac{1}{2}\sin[2(y-t)] \\ -\cos(y-t) + \frac{1}{2}\sin[2(y-t)] + \delta P_b(y,t) \\ -\cos(y-t) + \left(\frac{5}{2} - \sqrt{2}\right)\sin[2(y-t)] \\ \left(\frac{\delta\pi}{2} + 2\sqrt{2} - 1\right)\cos(y-t) + \left(\frac{5}{2} - \sqrt{2}\right)\sin[2(y-t)] + \delta P_b(y,t) \\ -\cos(y-t) + \frac{1}{4}\left(\frac{9}{2}\sqrt{2} - \frac{13}{3}\right)\sin[2(y-t)] \\ -2\cos(y-t) + \frac{1}{4}\left(\frac{9}{2}\sqrt{2} - \frac{7}{3}\right)\sin[2(y-t)] \\ -\cos(y-t) + \frac{13}{12}\sin[2(y-t)] \\ -2\cos(y-t) + \frac{13}{12}\sin[2(y-t)] \\ \left(\sqrt{2} - 2\right)\cos(y-t) + \frac{1}{4}\left(\frac{9}{2}\sqrt{2} - \frac{7}{3}\right)\sin[2(y-t)] \\ \frac{1}{4}\left(\sqrt{2} - 5\right)\cos(y-t) + \frac{13}{12}\sin[2(y-t)] \\ \left(\tilde{Q}_0 + \tilde{Q}_1 + \tilde{Q}_2 - 1\right)\cos(y-t) + \left(\frac{1}{2} + \tilde{\alpha}_1 + \tilde{\alpha}_2 - \frac{\kappa}{2}\right)\sin[2(y-t)] \end{pmatrix} . \quad (3.6.3)$$

Here, δP_b is meant to represent the exact ABL pressure gradient:

$$\delta P_b(y,t) := \frac{\partial p_b}{\partial y}(\boldsymbol{\xi}_{wav}(y,t)) = \frac{1}{1+\delta}\Big[\Phi(\boldsymbol{\xi}_{wav}(y,t)) - \Phi(\boldsymbol{\xi}_{wav}(a,t)) \\ -\frac{\partial \phi}{\partial y}(\boldsymbol{\xi}_{wav}(y,t)) + \frac{\partial \phi}{\partial y}(\boldsymbol{\xi}_{wav}(a,t))\Big],$$

where the exact functions $\Phi(\boldsymbol{\xi}_{wav})$ and $\phi_y(\boldsymbol{\xi}_{wav})$ are given by

$$\Phi(\boldsymbol{\xi}_{wav}(y,t)) = \sqrt{2}\sin[2(y-t)],$$

and

$$\frac{\partial\phi}{\partial y}(\boldsymbol{\xi}_{wav}(y,t)) = \left(\frac{5}{2}+\frac{\delta}{2}\right)\sin[2(y-t)] + \left(\frac{\delta\pi}{2}+2\sqrt{2}\right)\cos(y-t).$$

In summary, the grid-convergence test is carried on the following problem:

$$\begin{cases} \mathcal{L}(\boldsymbol{\xi}) = \boldsymbol{\Psi}, \qquad y \in [0,2\pi], \\ 2\pi - \text{periodic BC on } \boldsymbol{\xi} : \boldsymbol{\xi}(0) = \boldsymbol{\xi}(2\pi), \\ \dfrac{\partial^2 p_b}{\partial y^2} = \dfrac{1}{1+\delta}\left[\dfrac{\partial\Phi}{\partial y} - \dfrac{\partial^2\phi}{\partial y^2}\right], \\ \text{BC on } \partial p_b/\partial y \\ \boldsymbol{\xi}(y,0) = \boldsymbol{\xi}_{wav}(y,0). \end{cases} \tag{3.6.4}$$

Note that Φ and ϕ are given by (2.3.6c) and (2.3.6d) except for the Coriolis and radiative convective forcing terms which are neglected. The ABL pressure gradient BC is merely a constant and is immaterial for the convergence results; It is set here to zero for simplicity, albeit inconsistent with periodic BC on the field variables. The system is solved using the Strang splitting strategy described in Section (3.5), with a trapezoidal second-order ODE solver for the forcing term.

The error is quantified at a fixed time for the m^{th} component of $\boldsymbol{\xi}$ using the 1-norm

$$\|e^m\|_1 = \Delta y \sum_{j=1}^{J} |\xi_j^m - \xi_{wav_j}^m|,$$

and the max norm (or ∞-norm)

$$\|e^m\|_\infty = \max_{1\le j\le J} |\xi_j^m - \xi_{wav_j}^m|,$$

where J is the total number of grid points. The method is said to be convergent at time T if $\lim_{\Delta y \to 0} \|e^m\|_{(\cdot)} = 0$ and accurate of order p if $\|e^m\|_{(\cdot)} = \mathcal{O}(\Delta y^p)$ as $\Delta y \to 0$. Since the solution $\boldsymbol{\xi}_{wav}$ is smooth, we expect pointwise convergence as measured by the max norm, and $\|e^m\|_1 \le 2\pi \|e^m\|_\infty$. Error estimates in the 1-norm and max-norm are reported in Table 3.1 as the grid resolution increases with the number of grid points used. The error estimates using 1024 points are of order 10^{-5} for most variable fields, in either norm. A second-order rate of convergence for all variables is demonstrated in Figures 3.5 and 3.6 in both the 1-norm and max-norm, respectively. A graphical comparison of the exact and numerical solutions is shown in Figure 3.7 for the v_b variable using a grid with 32, 64, 128, and 256 points.

	θ_{eb}, θ_b, u_b		v_b		u_0		v_0	
Δy	1-norm error	∞-norm error	1-norm error	∞-norm error	1-norm error	∞-norm error	1-norm error	∞-norm error
$2\pi/32$	4.030E-01	1.106E-01	5.435E-01	1.634E-01	3.351E-01	1.424E-01	4.438E-01	1.372E-01
$2\pi/64$	4.781E-02	1.469E-02	7.855E-02	2.516E-02	4.506E-02	2.934E-02	5.814E-02	2.769E-02
$2\pi/128$	5.605E-03	2.130E-03	1.205E-02	5.583E-03	6.680E-03	5.893E-03	8.033E-03	6.195E-03
$2\pi/256$	7.143E-04	3.257E-04	1.931E-03	1.258E-03	1.141E-03	1.258E-03	1.289E-03	1.421E-03
$2\pi/512$	1.273E-04	5.596E-05	3.396E-04	3.092E-04	2.319E-04	2.750E-04	2.394E-04	3.153E-04
$2\pi/1024$	2.864E-05	1.081E-05	6.643E-05	6.895E-05	5.272E-05	6.095E-05	5.385E-05	6.966E-05
	u_1		v_1		u_2		v_2	
$2\pi/32$	3.168E-01	1.351E-01	3.279E-01	1.425E-01	3.797E-01	1.142E-01	4.296E-01	1.350E-01
$2\pi/64$	4.293E-02	2.923E-02	4.642E-02	2.666E-02	4.796E-02	1.630E-02	5.394E-02	2.132E-02
$2\pi/128$	5.606E-03	2.130E-03	1.205E-02	5.583E-03	6.680E-03	5.893E-03	8.033E-03	6.195E-03
$2\pi/256$	7.143E-04	3.257E-04	1.931E-03	1.359E-03	1.141E-03	1.258E-03	1.289E-03	1.421E-03
$2\pi/512$	1.273E-04	5.596E-05	3.396E-04	3.092E-04	2.319E-04	2.750E-04	2.394E-04	3.153E-04
$2\pi/1024$	2.864E-05	1.081E-05	6.643E-05	6.895E-05	5.272E-05	6.095E-05	5.385E-05	6.966E-05
	θ_1		θ_2		q			
$2\pi/32$	2.874E-01	1.155E-01	4.308E-01	1.123E-01	6.286E-01	2.233E-01		
$2\pi/64$	3.387E-02	2.039E-02	5.571E-02	1.641E-02	9.623E-02	5.447E-02		
$2\pi/128$	4.585E-03	3.616E-03	7.272E-03	2.407E-03	1.593E-02	1.317E-02		
$2\pi/256$	9.115E-04	6.741E-04	1.019E-03	4.004E-04	2.968E-03	3.115E-03		
$2\pi/512$	2.159E-04	1.340E-04	1.708E-04	9.421E-05	6.183E-04	7.065E-04		
$2\pi/1024$	5.412E-05	2.793E-05	3.453E-05	2.148E-05	1.394E-04	1.572E-04		

Table 3.1: Error at time $t = 0.6$ calculated in 1-norm and max-norm for the PDE (3.6.4) solved using the Strang splitting strategy described in Section 3.5. A time step of $\Delta t = \text{CFL}\Delta y/100$ is used, with CFL=0.1.

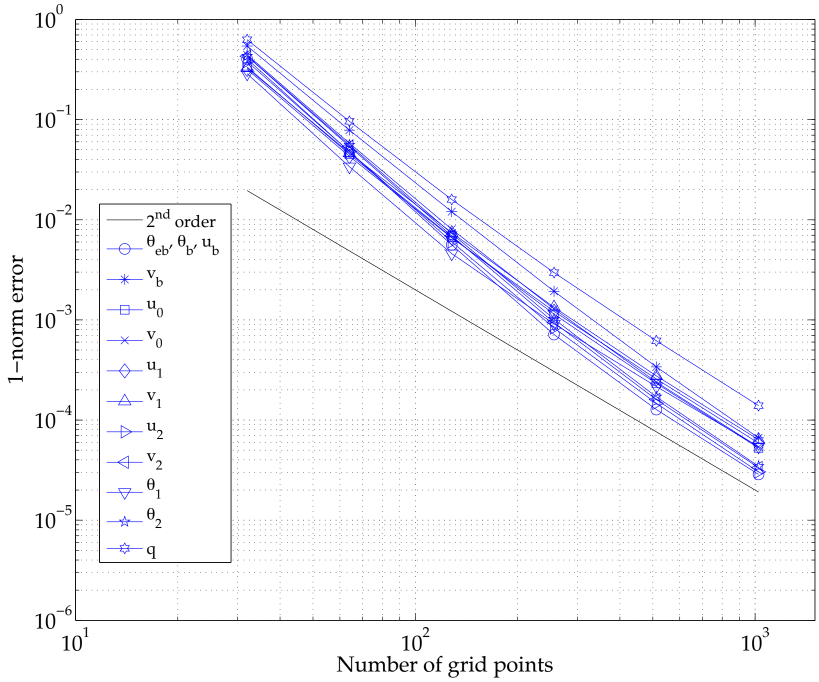

Figure 3.5: Second order convergence in the 1-norm.

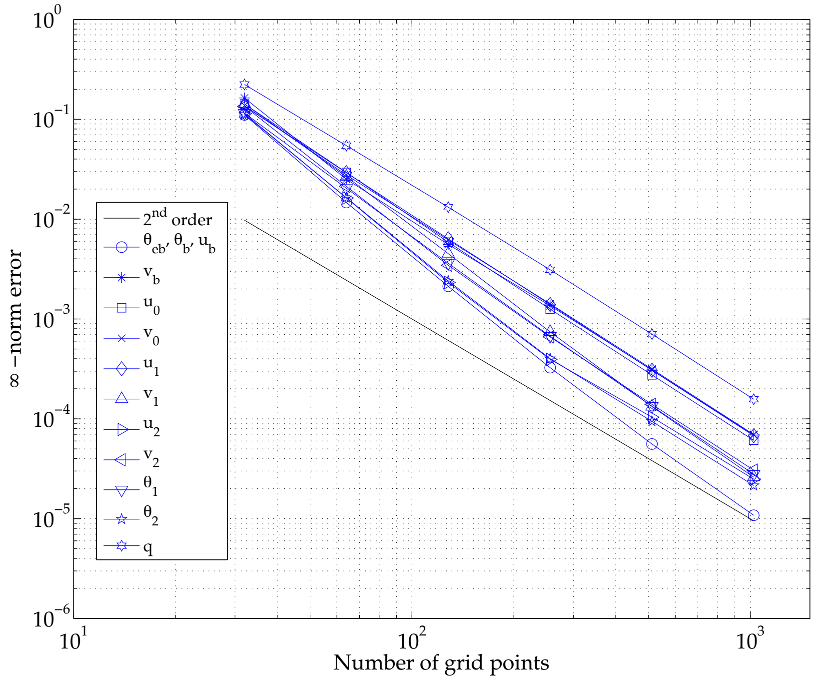

Figure 3.6: Second order convergence in the ∞-norm.

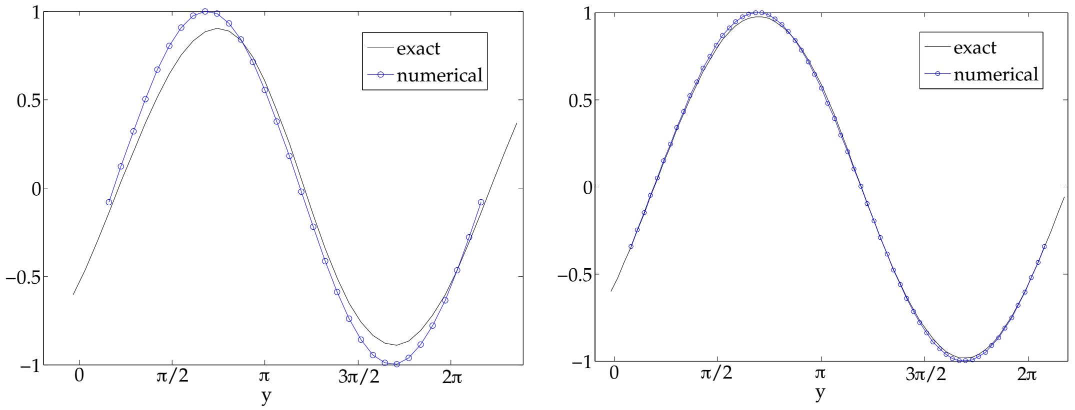

(a) 32 grid points (b) 64 grid points

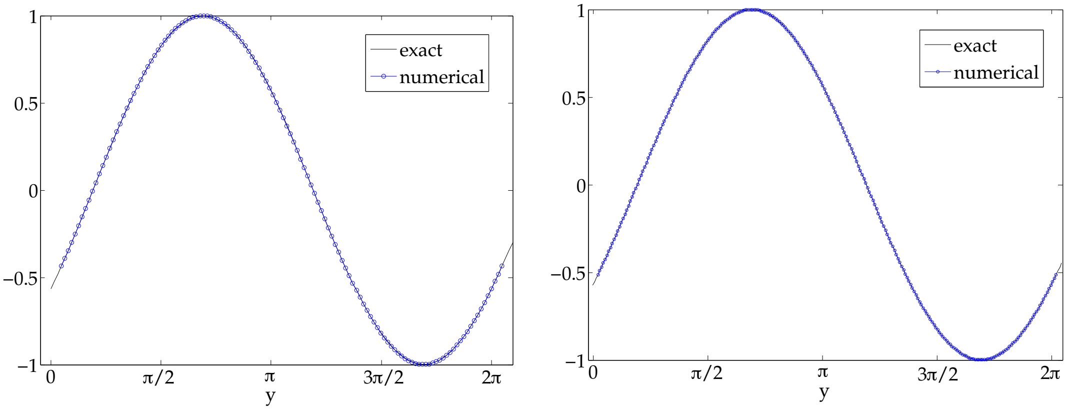

(c) 128 grid points (d) 256 grid points

Figure 3.7: Comparison of exact (black) and numerical (blue) solutions for the v_b sine wave (3.6.1) at $t = 0.6$ using a grid with 32, 64, 128, and 256 points. The time step is $\Delta t = \text{CFL}\Delta y/100$ with CFL=0.1.

3.7 Conclusion

In this chapter we designed and validated a numerical scheme for the MOSNE system, a nonconservative system of PDE, with an elliptic equation for pressure. This scheme is designed following the approach of Stechmann et al. (2008), which is based on a splitting of the advective portion of the system into its conservative and non-conservative parts. Here the conservative part is solved using the non-oscillatory central scheme of Nessyahu and Tadmor (1990), and the nonconservative part is solved using the Wave-Propagation method of LeVeque (2002) and the method of lines. The three methods are solved in an alternating manner using the Strang splitting scheme strategy (Strang, 1968). The pressure equation is solved within the central scheme, by modifying the predictor-corrector steps to include the numerical pressure at each step. The second-order convergence of the full numerical scheme is verified by a grid convergence error analysis using on a nontrivial exact solution and adding the appropriate forcing.

Chapter 4

Simulations of Mock Hadley Monsoon Flow

The dynamics of the large-scale circulation of the atmosphere in the tropics differs greatly from that in the middle latitude regions. The simplest observation one can make about the tropics is that they are much warmer than the poles. This is a direct consequence of the geometry and axial tilt of the Earth: the incoming solar radiation per unit area of the Earth's surface is much greater near the equator than at the poles.

To reduce the resulting equator-to-pole temperature gradient, the atmospheric and oceanic circulations transport energy polewards. In the atmosphere, the transport of energy is partly done by overturning of the atmosphere, which on annual average is characterized by rising air near the equator, poleward flow aloft, subsidence in the subtropics and equatorward return flow near the surface. This large-scale meridional circulation driven by the underlying meridional surface temperature difference is known as the idealized *Hadley circulation* (Vallis, 2006). Moist convection, which develops in association with this warm surface temperature anomaly, helps to drive this large-scale circulation. The Hadley cell structure is changed by monsoon patterns of clouds, rainfall and prevailing surface winds. This coupling of clouds and large-scale dynamics greatly affect our ability to predict weather and climate.

In Chapter 2 we introduced the MOSNE model for the large-scale meridional circulation, and the stochastic multicloud parameterization for organized tropical convection (SMCM) and its deterministic version (DMCM). As described in Section 2.4.2, both the SMCM and DMCM capture the dynamical interactions among the three cloud types, congestus, deep, and stratiform, that characterize organized tropical convection. The SMCM represents the GCM gridbox cloud populations by a Markov birth-death-like process whose stochastic dynamics over time is constrained by the large-scale environmental state, namely the mid-troposphere dryness and convective available potential energy (CAPE). In the DMCM, convective (deep) and non-convective (congestus) regimes are alternated using a nonlinear switch Λ which is function of the mid-troposphere dryness. In both models, closure equations are used to represent the free troposphere heating associated with each cloud type.

In this chapter we present simulation results of the dynamics of the Hadley-Monsoon circulation using the MOSNE model coupled with the SMCM/DMCM. We compare both the skills of DMCM and SMCM at capturing the observed dynamical and physical features of organized convection and large-scale meridional circulation patterns. We show by several simulations on an aquaplanet with nonuniform sea-surface temperature (SST) that realistic mean Hadley cells with monsoonal-type flow are reproduced with this simple model.

In Section 4.1, we define the *radiative convective equilibrium* (RCE) state for the system, a neutral atmospheric state which can support the propagation of large-scale waves. In Section 4.2 we look at the case of an aquaplanet with a warm pool forcing near the equator.

4.1 Radiative Convective Equilibrium

Radiative-convective equilibrium (RCE) is the equilibrium state where the convective heating is balanced by the radiative cooling, in the absence of lateral transport (Emanuel, 1994). It was first introduced by Manabe and Wetherald (1967) to describe an idealized atmosphere in which the vertical temperature distribution is determined by an equilibrium between radiative and convective fluxes. The RCE represents a state in which, on average, convective motions compensate for the destabilization of the atmosphere by radiation. The RCE sets up a background state solution from which large-scale waves are allowed to develop spontaneously and propagate. Next, we derive the RCE equations for the MOSNE model. For this we first consider a solution of the type $\xi = \bar{\xi} + \xi'$, where overbars denote the RCE basic state, and primes, the deviation from that state. The RCE is a space and time homogeneous (steady) state at rest where $\bar{\boldsymbol{u}}_b = \bar{\boldsymbol{u}}_0 = \bar{\boldsymbol{u}}_1 = \bar{\boldsymbol{u}}_2 = 0$. Without loss of generality we may assume that $\bar{\theta}_1 = \bar{\theta}_2 = 0$. Substituting this solution in the MOSNE system gives:

$$\frac{D_b'\theta_{eb}'}{Dt} = -E\left(\Delta_t\bar{\theta}_e + \theta_{eb}' - \theta_{et}'\right) - M_d\left(\Delta_m\bar{\theta}_e + \theta_{eb}' - \theta_{em}'\right) + \frac{1}{\tau_e}\left(\Delta_s\bar{\theta}_e - \theta_{eb}'\right) - Q_{Rb}, \tag{4.1.1a}$$

$$\frac{D_b'\theta_b'}{Dt} = -E\left(\Delta_t\bar{\theta} + \theta_b' - \theta_t'\right) - M_d\left(\Delta_m\bar{\theta} + \theta_b' - \theta_m'\right) + \frac{1}{\tau_e}\left(\Delta_s\bar{\theta} - \theta_b'\right) - Q_{Rb}, \tag{4.1.1b}$$

$$\frac{D_b'u_b'}{Dt} - yv_b' = -E_u\left(u_b' - u_t'\right) - C_dUu_b', \tag{4.1.1c}$$

$$\frac{D_b'v_b'}{Dt} + yu_b' = -\frac{\partial p_b'}{\partial y} - E_u\left(v_b' - v_t'\right) - C_dUv_b', \tag{4.1.1d}$$

$$\frac{D_0'u_0'}{Dt} + \frac{\partial\left(u_1'v_1'\right)}{\partial y} + \frac{\partial\left(u_2'v_2'\right)}{\partial y} - \sqrt{2}(u_1' + u_2')\frac{\partial v_0'}{\partial y} - yv_0' = \delta E_u(u_b' - u_t'), \tag{4.1.1e}$$

$$\frac{D_0'v_0'}{Dt} + \frac{\partial({v'}_1^2)}{\partial y} + \frac{\partial({v'}_2^2)}{\partial y} - \sqrt{2}(v_1' + v_2')\frac{\partial v_0'}{\partial y} + yu_0' = -\frac{\partial p_0'}{\partial y} + \delta E_u(u_b' - u_t'), \tag{4.1.1f}$$

$$\begin{aligned}\frac{D_0'u_1'}{Dt} + v_1'\frac{\partial u_0'}{\partial y} + \frac{\sqrt{2}}{2}\left(v_1'\frac{\partial u_2'}{\partial y} + v_2'\frac{\partial u_1'}{\partial y} + 2u_2'\frac{\partial v_1'}{\partial y} + \frac{1}{2}u_1'\frac{\partial v_2'}{\partial y}\right)& \\ -\left(\frac{1}{2}u_1' + \frac{8}{3}u_2'\right)\frac{\partial v_0'}{\partial y} - yv_1' = -\frac{1}{\tau_R}u_1' + \frac{\sqrt{2}\delta}{\tau_T}(u_b' - u_t'),&\end{aligned} \tag{4.1.1g}$$

$$\begin{aligned}\frac{D_0'v_1'}{Dt} + \frac{3\sqrt{2}}{2}\left(\frac{1}{2}v_1'\frac{\partial v_2'}{\partial y} + v_2'\frac{\partial v_1'}{\partial y}\right) + \left(\frac{1}{2}v_1' - \frac{8}{3}v_2'\right)\frac{\partial v_0'}{\partial y}& \\ + yu_1' = \frac{\partial\theta_1'}{\partial y} - \frac{1}{\tau_R}v_1' + \frac{\sqrt{2}\delta}{\tau_T}(u_b' - u_t'),&\end{aligned} \tag{4.1.1h}$$

$$\begin{aligned}\frac{D_0'\theta_1'}{Dt} - \frac{\partial v_1'}{\partial y} + \frac{\sqrt{2}}{2}\left(2v_1'\frac{\partial\theta_2'}{\partial y} - v_2'\frac{\partial\theta_1'}{\partial y} + 4\theta_2'\frac{\partial v_1'}{\partial y} - \frac{1}{2}\theta_1'\frac{\partial v_2'}{\partial y}\right)& \\ + \left(\frac{1}{2}\theta_1' - \frac{8}{3}\theta_2'\right)\frac{\partial v_0'}{\partial y} + \sqrt{2}\frac{\partial v_0'}{\partial y} = H_d - Q_{R1} - \frac{1}{\tau_D}\theta_1',&\end{aligned} \tag{4.1.1i}$$

$$\begin{aligned}\frac{D_0'u_2'}{Dt} + v_2'\frac{\partial u_0'}{\partial y} + \frac{\sqrt{2}}{2}\left(v_1'\frac{\partial u_1'}{\partial y} - u_1'\frac{\partial v_1'}{\partial y}\right)& \\ + \left(\frac{2}{3}u_1' - \frac{1}{2}u_2'\right)\frac{\partial v_0'}{\partial y} - yv_2' = -\frac{1}{\tau_R}u_2' + \frac{\sqrt{2}\delta}{\tau_T}(u_b' - u_t'),&\end{aligned} \tag{4.1.1j}$$

$$\frac{D_0'v_2'}{Dt} + \left(\frac{2}{3}v_1' + \frac{1}{2}v_2'\right)\frac{\partial v_0'}{\partial y} + yu_2' = \frac{\partial\theta_2'}{\partial y} - \frac{1}{\tau_R}v_2' + \frac{\sqrt{2}\delta}{\tau_T}(v_b' - v_t'), \tag{4.1.1k}$$

$$\frac{D_0'\theta_2'}{Dt} + \frac{\sqrt{2}}{4}\left(v_1'\frac{\partial\theta_1'}{\partial y} - \theta_1'\frac{\partial v_1'}{\partial y}\right) - \frac{1}{4}\frac{\partial v_2'}{\partial y} + \left(\frac{2}{3}\theta_1' + \frac{1}{2}\theta_2'\right)\frac{\partial v_0'}{\partial y} + \frac{\sqrt{2}}{4}\frac{\partial v_0'}{\partial y} = H_c - H_s - Q_{R2} - \frac{1}{\tau_D}\theta_2', \tag{4.1.1l}$$

$$\frac{D_0'q'}{Dt} + \frac{\partial}{\partial y}\left((\tilde{\alpha}_1 v_1' + \tilde{\alpha}_2 v_2')q' + \tilde{Q}_1(\eta_q)v_1' + \tilde{Q}_2(\eta_q)v_2' - \tilde{Q}_0(\eta_q)v_0'\right) - \kappa q'\frac{\partial v_0'}{\partial y} = -\frac{2\sqrt{2}}{\pi}H_d + \delta E(\Delta_t\bar{\theta}_e + \theta_{eb}' - \theta_{et}') + \left(\delta M_d + \frac{\partial v_0'}{\partial y}\right)(\Delta_m\bar{\theta}_e - \theta_{eb}' - \theta_{em}'). \tag{4.1.1m}$$

Here $(D_b'/Dt) = (\partial/\partial t)+v_b'(\partial/\partial y)$ and $(D_0'/Dt) = (\partial/\partial t)+v_0'(\partial/\partial y)$ are the meridional boundary layer and barotropic transport operators for the perturbed motion. The surface temperature perturbations are assumed to be negligible, i.e. $\theta_s' = \theta_{es}' = 0$. We note that the RCE values of moist thermodynamic variables such as $\bar{\theta}_{es}$, $\bar{\theta}_{et}$, $\bar{\theta}_{em}$, are absorbed within the differences $\Delta_{s,t,m}\bar{\theta}_e$ and their values are actually not needed.

4.1.1 RCE Equations

A static homogeneous RCE solution to the equations (4.1.1) is obtained by setting all perturbations to zero. In this case, (4.1.1i) yields $\overline{H_d} = Q_{R1}$ and from (4.1.1m) we get

$$\overline{M_u} = \frac{2\sqrt{2}Q_{R1}}{\delta\pi\left[(1-\alpha_m)\Delta_t\overline{\theta_e} + \alpha_m\Delta_m\overline{\theta_e}\right]},$$

where we used (2.2.13), (2.2.12), (2.2.15e) to write $\overline{M_d} = \alpha_m\overline{M_u}$ and $\overline{E} = \overline{M_u}(1-\alpha_m)$. It follows from (2.4.20) that the RCE background velocity due to large-scale subsidence is

$$m_0 = \frac{\alpha_m\overline{M_u}}{\left[1 + \frac{\mu}{Q}\left(\overline{H_s} - \overline{H_c}\right)\right]^+}.$$

From the θ_{eb} and θ_b perturbation equations (4.1.1a) and (4.1.1b) we diagnose the surface evaporation time scale and the ABL radiative cooling rate at RCE:

$$\begin{aligned} \tau_e &= \frac{\Delta_s\overline{\theta_e} - \Delta_s\overline{\theta}}{\overline{M_u}\left[(1-\alpha_m)(\Delta_t\overline{\theta_e} - \Delta_t\overline{\theta}) + \alpha_m(\Delta_m\overline{\theta_e} - \Delta_m\overline{\theta})\right]}, \\ Q_{Rb} &= \overline{M_u}\left[(\alpha_m - 1)\Delta_t\overline{\theta} - \alpha_m\Delta_m\overline{\theta}\right] + \frac{1}{\tau_e}\Delta_s\overline{\theta}. \end{aligned}$$

From the θ_2 perturbation equation (4.1.1l), the radiative cooling rate of mode 2 at RCE is $Q_{R2} = \overline{H_c} - \overline{H_s}$. The RCE values $\overline{H_d}$, $\overline{H_s}$, and $\overline{H_c}$, fixed by the steady state solution of the heating rate closure equations, are reported in Table 4.1 for both the deterministic (DMCM) and stochastic (SMCM) versions of the multicloud model.

Note that m_0, $\overline{M_u}$, Q_{R2}, and τ_e are completely determined by specifying $\Delta_s\overline{\theta}_e$, $\Delta_s\overline{\theta}$, $\Delta_m\overline{\theta}_e$, $\Delta_m\overline{\theta}$, $\Delta_t\overline{\theta}_e$, $\Delta_t\overline{\theta}$, and Q_{R1}. Remember from Sections 2.2.2 and 2.5 that the scalar gradients $\Delta_k\theta$ and $\Delta_k\theta_e$, where $k = s, m, t$, represent the effects of boundary layer mixing associated with the shallow convection and surface fluxes, and Q_{R1} is the first baroclinic radiative cooling rate.

Stability of the RCE Solution The stability of the RCE solution for the nonlinear MOSNE system was investigated numerically and was shown to be stable for the regimes of parameters considered in the simulations of this chapter. To test the stability of the RCE, a small initial perturbation to the RCE background state is applied, and the RCE solution is considered stable if the system returns to the background state in finite time (i.e. if the perturbation dampens out for each field). One such test is shown in Figure 4.1 for an initial Gaussian perturbation of amplitude of order 3 K.

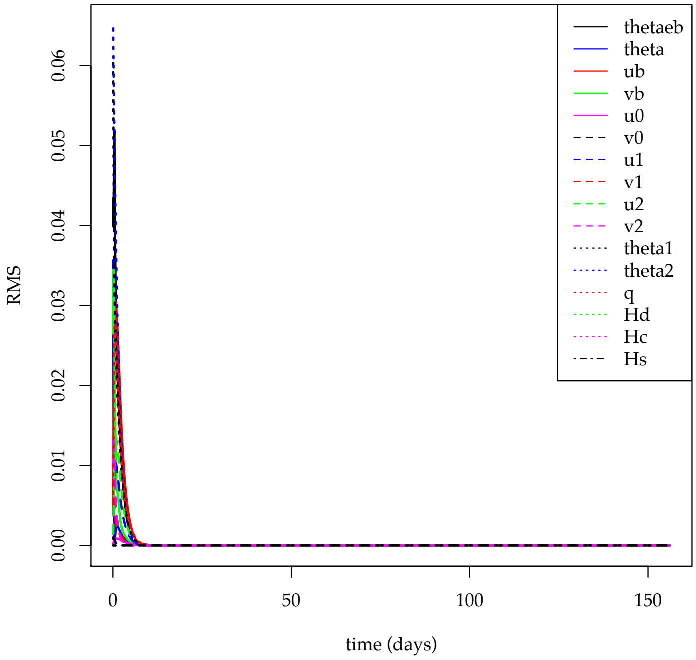

Figure 4.1: *Stability of the RCE solution.* Root-mean-square (RMS) of model variables for an initial gaussian perturbation (amplitude of order 3 K) to the RCE solution, with an imposed ocean regime $\Delta_s\bar{\theta}_e = 10$ K, $\Delta_s\bar{\theta} = 0$ K, $\Delta_t\bar{\theta}_e = 5$ K, $\Delta_t\bar{\theta} = 0$ K, $\Delta_m\bar{\theta}_e = 11$ K, $\Delta_m\bar{\theta} = -5.5$ K. A homogeneous steady state seems visually to have been reached in less than 20 days, after which the amplitude of the solutions do not exceed 10^{-13}. The simulation uses a spatial resolution of 303 km and a time step of 2.97 seconds.

<table>
<tr><th>SMCM</th><th>DMCM</th></tr>
<tr><td colspan="2">$Q_{R1} = \overline{H_d}$
$Q_{R2} = \overline{H_c} - \overline{H_s}$
$m_0 = \alpha_m \overline{M_u} / \left[1 + \mu\left(\overline{H_s} - \overline{H_c}\right)/\overline{Q}\right]^+$
$\overline{M_u} = \dfrac{2\sqrt{2}Q_{R1}}{\delta\pi\left[(1-\alpha_m)\Delta_t\overline{\theta_e} + \alpha_m\Delta_m\overline{\theta_e}\right]}$
$\tau_e = \dfrac{\Delta_s\overline{\theta_e} - \Delta_s\overline{\theta}}{\overline{M_u}\left[(1-\alpha_m)(\Delta_t\overline{\theta_e} - \Delta_t\overline{\theta}) + \alpha_m(\Delta_m\overline{\theta_e} - \Delta_m\overline{\theta})\right]}$
$Q_{Rb} = \overline{M_u}\left[(\alpha_m - 1)\Delta_t\overline{\theta} - \alpha_m\Delta_m\overline{\theta}\right] + \dfrac{1}{\tau_e}\Delta_s\overline{\theta}$</td></tr>
<tr><td>$\overline{H_d} = \overline{\sigma_d}\,\overline{Q}$
$\overline{H_s} = \overline{\sigma_s}\alpha_s\overline{Q}$
$\overline{H_c} = \overline{\sigma_c}\alpha_c\overline{Q}$
$\overline{\text{CAPE}} = H_m^2\overline{Q}^2$
$Q_{R1} = \dfrac{1}{H_m}\overline{\sigma_d}\left(\overline{\text{CAPE}}\right)\sqrt{\overline{\text{CAPE}}} = \overline{\sigma_d}\,\overline{Q}$
$\overline{\sigma_c}$, $\overline{\sigma_d}$, and $\overline{\sigma_s}$ given by (2.4.15)</td><td>$\overline{H_d} = \left(1 - \overline{\Lambda}\right)\overline{Q}$
$\overline{H_s} = \alpha_s\left(1 - \overline{\Lambda}\right)\overline{Q}$
$\overline{H_c} = \alpha_c\overline{\Lambda}\,\overline{Q}$
$Q_{R1} = (1 - \overline{\Lambda})\overline{Q}$</td></tr>
</table>

Table 4.1: RCE solutions for both the stochastic and deterministic versions of the multicloud model.

4.2 Ocean Case with Nonuniform SST

In this section we present long run nonlinear simulations using both the deterministic and stochastic multicloud models with the MOSNE dynamical core that aim to investigate the meridional movement of convection in the absence of zonally propagating atmospheric waves. The 1D model (excluding the vertical dimension) is zonally averaged, and here we consider the case where the zonal boundary pressure and temperature jumps $\Delta_x p_b$, $\Delta_x p_0$, $\Delta_x \theta_1$, $\Delta_x \theta_2$ are negligible. The domain of the model is confined to an equatorial β-plane between 40°S and 40°N with a meridional resolution of 0.33° (1° $\approx$ 111.2 km). This corresponds to a GCM grid box size of 36.8 km. At the meridional boundaries, Neumann pressure and temperature conditions (derivative vanishes), and zero Dirichlet wind conditions are imposed. The governing equations are solved numerically from a random initial condition using a time step of 3 min integrated for 2000 days. The solution enters a statistical steady state after a short transient period of 100 to 200 days. For each case presented, the last 1000 days only are analyzed to estimate the background and wave disturbances.

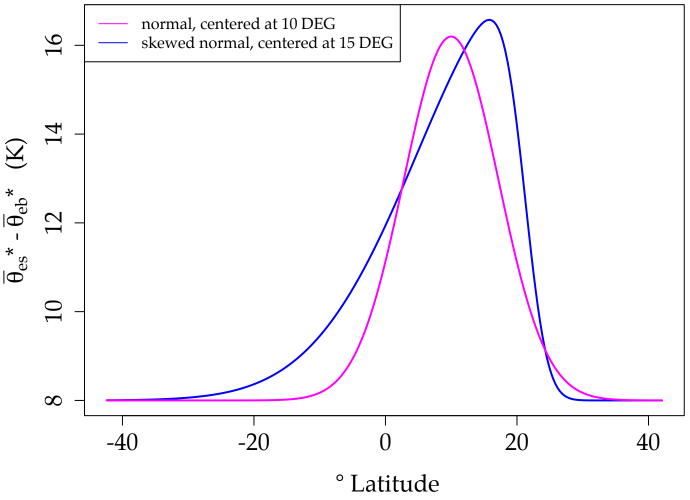

Figure 4.2: Two examples of the warm pool meridional profile $\overline{\theta^*}_{es} - \overline{\theta^*}_{eb}$. The surface equivalent potential temperature $\overline{\theta^*}_{es}$ exceeds the boundary layer equivalent potential temperature $\overline{\theta^*}_{eb}$ by about 8 K in the high latitudes (at the tails), and by as much as 16 K slightly North of the Equator (at the peaks of the distributions).

The climatological value for the surface gradient $\Delta_s \bar{\theta}_e$ is prescribed to a fixed but spatially varying profile to mimic the non-homogeneous SST of a maritime warm pool. We consider two different profiles for the warm pool, as shown in Figure 4.2: a normal and a skewed normal profile, centered either at the 10°N and 15°N northern latitudes. Consistent with an ocean regime in which the ocean surface absorbs most of the incoming solar radiation and radiates little heat (low Bowen ratio), we set $\Delta_s\overline{\theta^*} = 0$ K. As before, the star symbol $(^*)$ denotes the dimensional value.

Above the surface layer, the mixed boundary layer is capped with an inversion layer, in which the potential temperature increases with height. Over the ocean we assume no temperature inversion, in the sense that $\Delta_t\overline{\theta^*} = 0$ K. A strong inversion is characterized by warm air over cold air, which suppresses convection by "capping" the boundary layer. The absence of inversion promotes the entrainment of air from the free troposphere to the boundary layer, and the rising of convective thermals into the free troposphere (Stensrud, 2007). The effective inversion is $\Delta_t\overline{\theta^*}_e = 5$ K, which is due solely to a moisture discrepancy at the top of the ABL of $\Delta_t\overline{q^*} = \Delta_t\overline{\theta^*}_e - \Delta_t\overline{\theta^*} = 5$ K.

The ratio of the potential and equivalent potential temperature "fluxes" is given by the parameter $\gamma = -\Delta_m\overline{\theta}/\Delta_m\overline{\theta}_e$, which is set to 0.5 in the cases presented here. To preserve the environmental lapse rate of the free troposphere, we set $\Delta_m\overline{\theta^*} = -5.5$ K ($\Gamma \approx 0.6875$ K/km), which gives $\Delta_m\overline{\theta^*}_e = 11$ K.

As mentioned in Section 4.1.1, the equilibrium profiles for θ and θ_e determine $\overline{M_u}$, the RCE upward mass flux velocity at the top of the ABL, m_0, the RCE background velocity due to large-scale subsidence, and τ_e and Q_{Rb}, the surface evaporation time scale and ABL radiative cooling rate at RCE, respectively. With the parameter values given as in Table 2.5, these values are (see Table 4.1):

$$\overline{M_u^*} = 2.68 \text{ cm/s}, \quad m_0^* = 5.77 \text{ cm/s}, \quad \tau_e^* = 7.075 \text{ hrs}, \quad \text{and} \quad Q_{Rb}^* = 5.111 \text{ K/day}.$$

We investigate 7 different simulation parameter regimes and warm pool (WP) configurations, shown in Table 4.2. Both the deterministic and stochastic versions of the multicloud model are tested with the results discussed in Sections 4.2.1 and 4.2.2, respectively. For each simulation, two series of plots are presented: the mean meridional circulation and mean meridional structure, in Appendix A.1, and Hovmöller diagrams of the wave fluctuations from the mean solutions in Appendix A.2.

Simulation	1	2	3	4	5	6	7
SMCM/DMCM	DMCM	DMCM	SMCM	SMCM	SMCM	SMCM	SMCM
Convective timescales	–	–	G-LES	G-LES	G-LES	G-LES	FMK12
WP centered at	10°N	15°N	10°N	15°N	15°N	15°N	15°N
WP profile	normal	normal	normal	normal	normal	skewed	normal
a_0	1	1	1	1	3	3	3

Table 4.2: Multicloud model version, parameter regime, and warm pool (WP) configuration used in simulations. The values for the convective timescales are reported in Table 6.3.

4.2.1 Deterministic Simulations

In this section we couple the deterministic multicloud parameterization (DMCM) to the MOSNE dynamical core. The DMCM is designed to take into account the energy available for congestus and deep convection (respectively Q_c and Q_d; see equations (2.4.21f) and (2.4.21e)), and uses the nonlinear moisture switch Λ (see equation (2.4.21g)) to mimic the natural transitions between congestus and deep convection. At RCE, $\overline{Q_c^*} = \overline{Q_d^*} = \overline{Q^*} = 1.11$ K/day, and the heating rates are $\overline{H_d^*} = 1$ K/day, $\overline{H_s^*} = 0.25$ K/day, and $\overline{H_c^*} = 2.77\text{E-}02$ K/day (see Table 4.1).

Meridional Structure The results for a WP normal profile centered at two northern latitudes 10°N and 15°N using the DMCM are presented as **Simulation 1** (Sections A.1.1, A.2.1) and 2 (Sections A.1.2, A.2.2), respectively. The root-mean-square (RMS) of the model variables are shown in Figure 4.3 for Simulation 1.

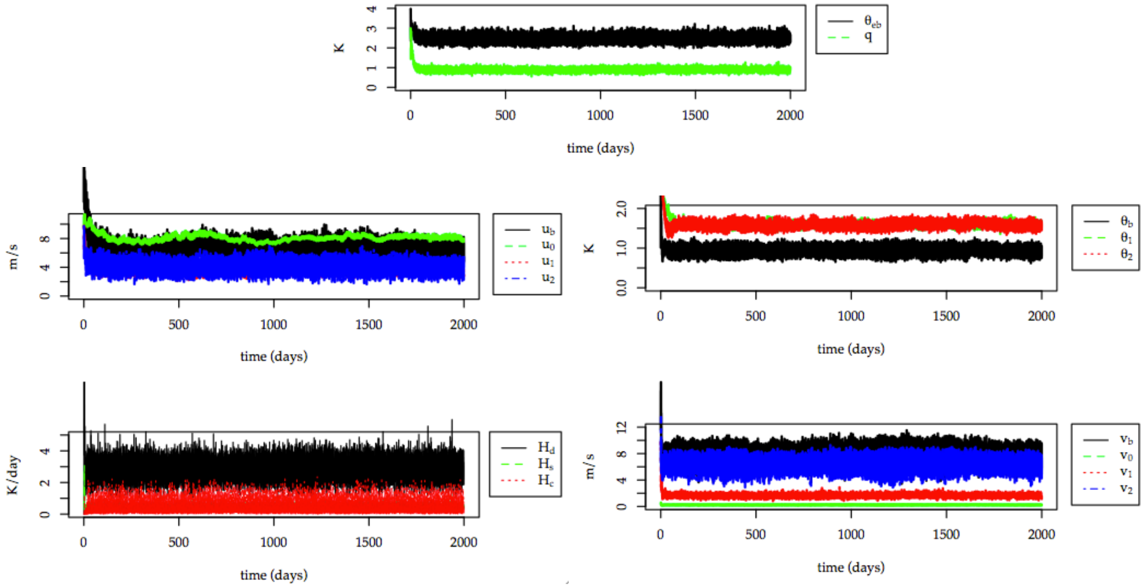

Figure 4.3: *Simulation 1.* Root-mean square (RMS) of model variables. The transient period is less than 200 days. The first 1000 days are discarded for the result analysis.

Figures A.1 and A.3 show the mean (background) meridional circulation of winds, potential temperature, and total heating rate $\mathcal{H}^{\theta}$ (see equation (2.4.22)) for both WP locations. Rising air over the WP moves polewards near the tropopause, descending in the subtropics and returning near the surface. This meridional circulation is consistent with the observed local Hadley cell during the summer monsoon over India and North Africa. The background structure reveals a first baroclinic deep heating mode over the WP, with a second baroclinic stratiform heating mode in the high latitudes. Surprisingly, although the heating has a first baroclinic structure, the potential temperature is dominated by a more shallow congestus second baroclinic mode. The high pressure anomaly aloft (maximum at a 10 km altitude) over the 20°S-20°N band indicates a region of divergence in the upper troposphere. In the boundary layer, a high pressure anomaly North of the 20°S latitude and South of the Equator is associated with the sinking of air in the descending branch of the Hadley cell. The surface zonal winds have a westerly-easterly-westerly pattern located approximately at the 20°S–EQ–20°N latitudes somewhat mimicking the trade winds. The returning of zonal winds occur at about $10 - 15°$S and over the warm pool region. The zonal winds reveal a baroclinic asymmetric structure with respect to the Equator. **Simulation 2**, with WP at 15°N, displays a strong asymmetry in the zonal winds and pressure field suggesting a horizontal flow reminiscent of the monsoon trough that takes place over India and North-West Africa during summer for example, consistent with the simulations of Ravindran et al. (2014) based on a full 3D GCM.

The mean meridional profiles of velocity and temperature components, moisture, and heating rates for the two WP locations are shown in Figures A.2 and A.4. The model produces a relatively sharp peak in the deep heating and moist region near the center of the WP. The meridional velocity is dominated by its first baroclinic component, whereas the barotropic mode of the zonal velocity seems to dominate. The profiles of θ_1 and θ_2 are qualitatively very similar, at least for Simulation 1, which is consistent with the observed dominating congestus baroclinic component in the vertical structure of θ.

Hovmöller Diagrams The Hovmöller diagrams for both WP locations are presented in Sections A.2.1 and A.2.2. The first figure shows the velocity components, and the second figure shows the temperature components together with the ABL equivalent potential temperature and moisture. The last figure shows deep, congestus, and stratiform heatings. Some prominent features of the heating contours are: small–scale intermittent strong congestus events mostly located over the WP on top of weak large-scale waves, and mesoscale and synoptic scale deep convective and stratiform anvil systems propagating as southward and northward wave disturbances. The model produces a significant amount of variability in the ABL equivalent potential temperature, with a pattern of waves that seem to correlate well with the heating contours, and strong small–scale moist events over the WP region. The free troposphere moisture also follows similar wave formations, but the small–scale moist events are localized near or south of the Equator. Southward and northward propagating waves are also present in the contours of the velocity and potential temperature modes. Interestingly, the barotropic and baroclinic modes of zonal velocity reveal slower southward propagating oscillations of a period of about 15 days.

4.2.2 Stochastic Simulations

In this section we couple the stochastic multicloud parameterization (SMCM) to the MOSNE dynamical core. The SMCM stochastically evolves the cloud area fractions covering the GCM grid box, constrained on the large-scale convection indicators D, C_l, and C (see equation (2.4.19)). As described in Section 2.4.2, the SMCM overlays a rectangular lattice of $N = n \times n$ sites over each GCM horizontal grid (see Figure 2.3). Here we assume $n = 30$, which for our model resolution of 36.8 km corresponds to lattice sites which have a meridional extent of 1.23 km. The equilibrium statistics of the cloud area fractions is determined by the seven convective timescales (see Table 2.4), and the climatological reference values T_0 and CAPE_0, which are set here to the values in Table 2.5. Here we contrast two sets of convective timescales, one obtained from the SMCM parameter estimation model presented in Part II of the thesis, and the other used in Frenkel et al. (2012) (see Tables 4.2 and 6.3). The RCE values for the stochastic simulations are reported in Table 4.3.

RCE parameters	G-LES	FMK12
$\overline{\sigma}_d/\overline{\sigma}_c/\overline{\sigma}_s$	8.23E-04/4.49E-03/3.59E-03	2.27E-03/1.29E-02/3.78E-03
$\overline{H}_d/\overline{H}_c/\overline{H}_s$	1/1.36/1.09 K day^{-1}	1/1.43/0.42 K day^{-1}
$\overline{\text{CAPE}}$	20.34 J kg^{-1}	2.67 J kg^{-1}
m_0	5.77 cm s^{-1}	0.719 cm s^{-1}

Table 4.3: RCE values for the stochastic simulations. The values for the convective timescales are reported in Table 6.3.

The meridional structure and Hovmöller diagrams for the stochastic simulations 3 through 7 are presented in Sections A.1.3 to A.1.7, and A.2.3 to A.2.7, respectively. The root-mean-square (RMS) of the model variables are shown in Figure 4.4 for Simulation 3. Table 4.2 describes the parameter regime and WP profile settings for each simulation.

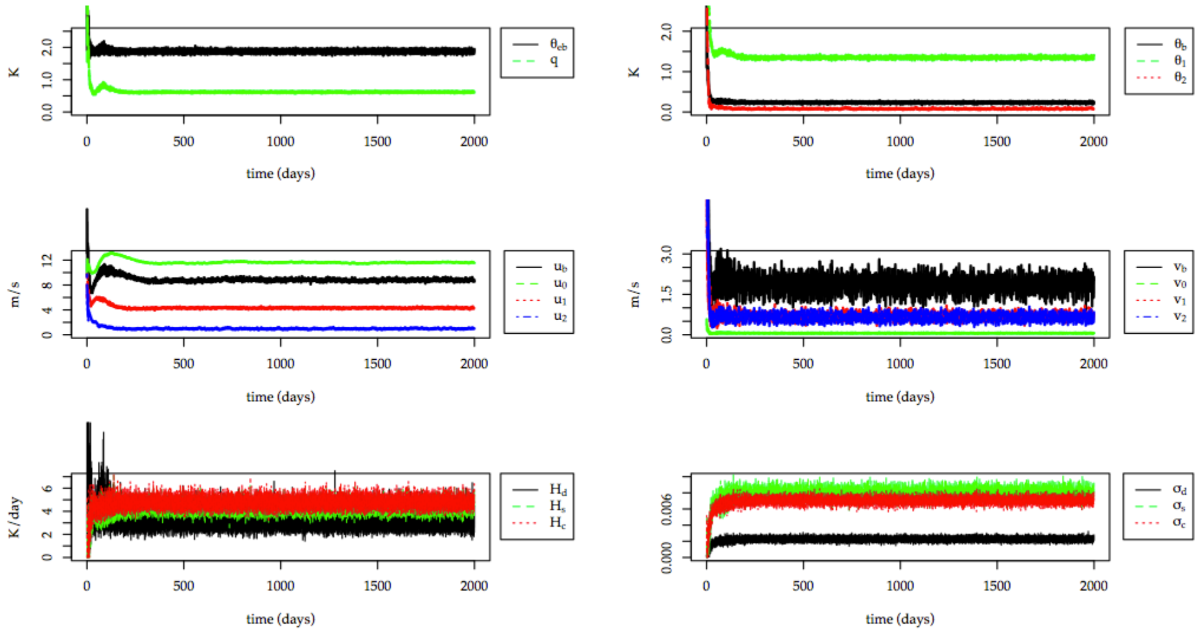

Figure 4.4: *Simulation 3.* Root-mean square (RMS) of model variables.

Meridional Structure We first contrast **Simulations 3 and 4**, which differ only by the emplacement of the WP. The mean meridional circulation for both (see Figures A.5 and A.7) are qualitatively similar, with a weak heating dominated by a shallow congestus second baroclinic mode, and a first baroclinic potential temperature structure, both located north of the WP, at about 20°N. There is also a mean rising motion of air near the 20°N latitude with an equatorial tilted structure, perhaps due to congestus activity on the northern edge of the warm pool and stratiform activity to the south. The model produces a fair amount of moisture in the region of the WP, which might indicate that the deep convective heating is not sensitive enough to the moisture fields. The meridional profiles, shown in Figures A.6 and A.8, reveal peaked congestus and stratiform area fractions over the WP, with lower deep fraction. Both the heatings and cloud area fractions show an active phase south of 20°S and north of 25°N.

One way to increase the heating dependence on moisture is to turn on the parameter a_0. Here we try augmenting a_0 from 1 to 3, giving the results of **Simulation 5**. The mean meridional circulation, shown in Figure A.9, now displays a strong heating and upward vertical velocity just over the WP. The potential temperature is now dominated by a stratiform second baroclinic component. The surface zonal winds are easterlies over the Equator, and shift to westerlies over the WP region. This is accompanied by zonal pressure variation reminiscent of the monsoon trough over India and North Africa: a region of high pressure between the Equator and south of 20°N, and a region of low pressure north of 20°N. The zonal winds of the troposphere show a baroclinic structure also consistent with the summer monsoon circulation. The mean meridional profiles of Figure A.10 reveal a peaked congestus and stratiform heating over the WP, accompanied by strong stratiform and congestus cloud area fractions, with weak deep heating and low deep cloud area fraction.

Simulation 6 differs from Simulation 5 only by the profile (normal or skewed) of the WP. The meridional structure of Simulation 6 is presented in Figures A.11 and A.12. It shows an irregular meridional circulation with two cells stacked one on top of the other, with a shallow congestus heating curiously located south of the Equator. Given the suboptimal results of Simulation 6, a skewed normal WP centered at 15°N (see Figure 4.2) may be an unrealistic SST profile over the tropics.

Simulations 4 through 6 use the G-LES convective timescale parameter regime (see Table 4.2), with the best characteristics of a mean Hadley circulation reproduced in Simulation 5. The benchmark Simulation 5 is then contrasted with the FMK12 parameter regime in **Simulation 7**. The meridional circulation of Simulation 7, shown in Figure A.11, displays a two cell structure similar to that of Simulation 6, with a shallow congestus baroclinic heating mode at the Equator, and a stratiform baroclinic heating mode near 20°N.

We note that the simulations that reproduce a realistic local Hadley circulation, namely with air rising over the warm pool, and co-located with the heating maximum (Simulations 3, 4, and 5) are the ones that also present strong asymmetries in the zonal wind and pressure fields, suggesting a monsoon trough horizontal flow. Notice, however unlike the deterministic case, here such monsoon trough is also observed with a WP located at 10°N (Simulation 3). This is consistent with GCM simulations of Ravindran et al. (2013) using the DMCM and those obtained in Ravindran et al. (2015) using the SMCM. Note also the realistic feature of warm and cold anomalies over the WP region for these simulations.

Hovmöller Diagrams The $y - t$ contours of heating rates and cloud area fractions for **Simulation 3** are presented in Figure A.23. In the northern hemisphere, mesoscale cloud clusters are seen over the Equator–20°N band and north of 20°N, and are organized in bands that peak in intensity every 2 or 3 days. In the southern hemisphere, south of 20°S, similar cloud formations oscillate over time about every 5 days. Suppressed regions of convection are seen over the 20°S–Equator band, and over a narrow strip located approximately at 20°N. The chevron-like patterns observed in the heating and cloud area fraction contours are also seen in the ABL equivalent potential temperature and free troposphere moisture contours, in Figure A.22. Moreover the θ_{eb} contours correlate well with the large peaks of heating and cloud area fractions. The contours of velocity and temperature modes, shown in Figures A.21 and A.22, have an oscillating pattern of strong events followed by weak events. This oscillation in the cross equatorial flow is associated with intermittent weakening and strengthening of the Hadley cell. Stronger such oscillations could lead to a shutdown of the Hadley circulation yielding a double Atlantic Inter-Tropical Convergence Zone (ITCZ) regime as in the work of Pauluis (2004) by changing the boundary layer depth. This is however beyond the scope of this thesis and will be pursued in the near future.

The $y - t$ heating contours of **Simulation 4** (see Figure A.26) are qualitatively very similar to those of Simulation 3. The ABL equivalent potential temperature (Figure A.25) is well correlated with the heating and cloud area fractions. In both the θ_{eb} and q contours, a strong dry anomaly can be seen south of the 30°N latitude. Large synoptic scale waves can be seen in the contours of the velocity and potential temperature modes (Figures A.25 and A.26).

The suppressed phases of convection observed in Simulations 3 and 4 are no longer present in **Simulations 5 and 6**, due to an enhanced deep convective regime (higher a_0). Stronger and larger cloud decks as well as more pronounced heatings can be seen in both the contours of Figures A.29 and A.32, although the skewed normal WP case (Simulation 6) shows even more convective activity. The strong events in the contours of θ_{eb} and q (see Figures A.28 and A.31) correlate well with the peaks of heating and cloud area fractions. The contours of velocity and potential temperature modes, shown in Figures A.27 and A.30, reveal synoptic scale waves propagating poleward from an approximate 20°N latitude.

Simulation 7 tests the FMK12 convective timescale parameter regime and is otherwise the same as Simulation 5. The $y - t$ contours, shown in Figures A.33, A.34, and A.35 are qualitatively different than those of Simulation 5. The convective heating field is dominated by congestus and stratiform anomalies. This is probably the main reason why this simulation doesn't exhibit nice correlations between the heating and fluid dynamic patterns and an overall unrealistic variability. This together with the mean circulation provide a useful demonstration of the superiority of the parameters inferred from the Giga-LES dataset.

4.3 Conclusion

Simulations of a mock Hadley monsoon flow using the MOSNE dynamical core coupled with the multicloud framework for congestus, deep, and stratiform convection were presented here. The free tropospheric dynamical core is based on the hydrostratic primitive equations, with a coarse vertical resolution reduced to the barotropic and first two baroclinic modes. The background climatology consists of a homogenous stratification with a constant Brunt–Väisälä buoyancy frequency. The free troposphere has a vertically averaged moisture equation with a background moisture profile exponentially decaying in the vertical. The model explicitly incorporates a bulk boundary layer dynamics with velocity, potential and equivalent potential temperatures, as well as environmental downdrafts from above. The background state is that of an atmosphere in radiative convective equilibrium, a homogeneous steady state where the convective heating is balanced by the radiative cooling. The model is zonally symmetric and it thus allows to study the initiation and propagation of convection in the absence of zonally propagating atmospheric waves. The model is confined to an equatorial β-plane over the 40°S and 40°N belt, in an ocean regime with nonhomogeneous SST forcing. Both the DMCM and SMCM were compared with different parameter regimes and warm pool profiles.

The DMCM uses a nonlinear switch function that is function of midtroposphere dryness to mimics the natural transitions between congestus and deep convection. The closure equations for the heating associated with congestus and stratiform clouds are relaxation-type equations, and a simple diagnostic equation gives the deep heating. The deterministic simulations produce a realistic mean Hadley meridional circulation, with the ascending branch of the Hadley cell located over the warm pool region. The total heating also peaks over the warm pool with a deep first baroclinic vertical structure. Simulation 2 captures better the observed features of monsoon trough than Simulation 1, with easterly surface winds over the Equator, westerlies north of the WP, and a high to low pressure anomaly variation across that region. Both Simulations 1 and 2 produce convection that is organized in mesoscale and synoptic scale systems, with small-scale intermittent events. An oscillation pattern can be detected in the intensity of the heating fields with a period of a few days.

In the SMCM, cloud populations over a GCM gridbox are evolved stochastically using a Markov birth-death-like process, with the transitions between the different cloud types determined by the midtroposphere dryness, environment convective available potential energy (CAPE), and the cloud convective timescales. The heating closure equations are diagnostic equations expressed in terms of the stochastic cloud area fractions. The stochastic simulations using $a_0 = 1$ have a meridional circulation with Hadley cell characteristics, but produce weak heating. In the case of a normal SST profile, increasing the sensitivity of deep heating to θ_1 and θ_2 by setting $a_0 = 3$ amplifies the heating and rising of moist warm air over the WP (≈ 15°N). The stochastic simulations produce large mesoscale cloud systems with correlated heating fields, and show greater variability than the deterministic simulations. A significant increase of variability compared to the deterministic case can be found in the contours of velocity and potential temperature, θ_{eb} and q, and the velocity and temperature modes. Simulation 5 captures well the mean local Hadley cell structure, with the ascending branch of the Hadley circulation associated with a region of intense convection. It also displays characteristics of the monsoon trough observed over India and North Africa with easterly surface winds over the Equator, westerlies around 20°N, and a pressure anomaly depression north of that latitude.

Comparing the G-LES parameter regime of the benchmark Simulation 5 with the FKM12 parameter regime in Simulation 7 reveals a suboptimal FKM12 regime, with weak heating over the WP region resulting in a 2-cell Hadley structure. The deep heating contour anomalies are almost nonexistent despite the presence of deep cloud systems.

Part II

Rigorous Parameter Estimation for the Stochastic Multicloud Model

In Section 2.4.2 we introduced the stochastic multicloud model of Khouider et al. (2010), a convective parameterization that aims at representing the missing variability in GCMs due to unresolved processes of organized tropical convection. The underlying assumption of the multicloud model is that tropical convective systems are self-similar across different scales and are formed principally of a tri-mode cloud types: congestus clouds, deep convective clouds, and stratiform clouds.

Each GCM gridbox is overlaid with a lattice of $n \times n$ convective sites, each of which is associated with a four state Markov process that takes the values 0, 1, 2, or 3 according to whether the site is either cloud free, or occupied by one of the three cloud types. The transitions between the different cloud types are governed by a set of probability rules that are conditioned on the large scale atmospheric state, and occur at rates determined by a set of arbitrary cloud transition timescales chosen based on physical intuition. The multicloud model accounts for the temporal evolution of the gridbox cloud area fractions, which in turn impact the large-scale dynamics by modifying the precipitation rate and vertical cloud heating distributions.

In Chapter 4 of this work, detailed simulations of the meridional mean circulation and waves show complex nonlinear interactions between the stochastic area fractions and the large-scale flow that are extremely sensitive to the choice of the convective timescales. In their introductory paper (Khouider et al., 2010) (KBM10 below), the authors conclude from case studies (see Table 6.3 for the parameter regimes used) that the dynamics of the stochastic lattice and associated gridbox fractional cloudiness is very sensitive to the prescribed values of the cloud transition timescales. In Frenkel et al. (2012) (FMK12 below), the authors use yet a different set of parameter values, reported in Table 6.3, to study flows above the equator without rotation effects, and look at the impact of convective time scale dilation on the variability of convective coherent structures.

Efforts towards a more systematic way of determining these parameters have recently been undertaken, most notably by Peters et al. (2013) (P2013 below) who visually constrained the equilibrium distribution of the multicloud area fractions to radar spectrometry data (covering a 36 000 km^2 area over Darwin, Australia) to find best-fit transition time scales (see Table 6.3) that better represent the statistics of observed rainfall time series.

This part of the thesis is concerned with developing a rigorous statistical method to estimate the multicloud transition timescale parameters from data. In Chapter 5 we present a numerical procedure on Bayesian inference to solve the multicloud parameter estimation problem, and validate it using a synthetic experiment. Chapter 6 is an inference study carried on a Large-Eddy Simulation (LES) dataset from which we obtain the parameter estimated values used earlier in the numerical simulations of Chapter 4.

Chapter 5

The Bayesian Inference Procedure

5.1 Introduction

The multicloud parameter estimation problem can be viewed as an inversion problem where the (forward) multicloud model is calibrated against atmospheric data to find the best-fit parameter set. The adjustment of the model parameters so that the model best reproduce the true system is known as *parameter estimation*.

There exists various techniques for parameter estimation which can mostly be classified in two categories: the static inversion problems where the unknown parameters are assumed constant, and the dynamic inversion problems in which parameters are assumed to vary with time along with the state of the system. In the latter category, one method that has numerous applications in engineering and science is the *state-augmented Kalman filter*, which extends the idea of Kalman filtering to model parameters treating them virtually as state variables. The classical machinery of the Kalman filter can also be applied to nonlinear system by linearizing the model around the current predictor update, but the filter optimality is not guaranteed in this case. Related to (ensemble; Chen, 2003) Kalman filters are *Particle filters*, also called sequential Monte Carlo, which track "particles" with some weighted probability measures instead of the density estimated mean state and covariance matrix (see Chen, 2003).

Here our approach is that of a static problem, in which the model parameters are fixed in time and the nonlinear forward model is kept "exact" (i.e. no imposed linearization). We use a Bayesian framework to formulate a posterior distribution over the model parameters. The challenge of the Bayesian method is that posterior exploration may be hard for computationally intensive forward models. In the multicloud problem, the calculation of the likelihood function requires solving a large system of differential equations (the Kolmogorov equations) as many times as there are data points, which is prohibitive both in terms of computation time and storage requirements. The most attractive numerical techniques to compute the transient solutions to large Markov chains are based on matrix exponentials, but none is unconditionally acceptable for all classes of problems. Here, a parallel version of a preconditioning technique known as the Uniformization Method is developed using the `PETSc` (Portable, Extensible Toolkit for Scientific Computation, Balay et al. 2015) suite of sparse matrix-vector operations. The parallel Uniformization Method allows for fast and scalable approximations of large sparse matrix exponentials, without sacrificing accuracy.

This chapter is divided as follows. Section 5.2 resumes the discussion on the multicloud model started in Section 2.4.2, and gives a description of the birth/death process associated with the forward model. The Bayesian inverse problem is formulated in Section 5.3, and the three concepts of the Bayesian paradigm, posterior, prior, and likelihood, are outlined. The numerical calculation of the likelihood function is explained in Section 5.4, and the MCMC technique used to sample the high dimensional posterior is briefly covered in Section 5.5. Validation results using synthetic data produced by the SMCM coupled to a toy GCM/single column model is reported in Section 5.6. The results of this chapter are reported in De La Chevrotière et al. (2014).

5.2 Forward Model: Birth–Death Process

Given the time evolution of the large-scale atmospheric state at the grid points, the multicloud model simulates the evolution of the gridbox area cloud fractions σ_c, σ_d, and σ_s of congestus, deep, and stratiform clouds. For the purpose of this model, it is more convenient to track the cloud *populations* N_c, N_d, and N_s, naturally expressed as

$$N_c^t = N\sigma_c^t, \qquad N_d^t = N\sigma_d^t, \qquad \text{and} \qquad N_s^t = N\sigma_s^t, \tag{5.2.1}$$

where σ_c^t, σ_d^t, and σ_s^t are given by (2.4.16), and $N = n^2$ is the total number of sites of the cloud lattice. Hence at any given time, the total number of cloud free sites at time t, N_{cs}^t, is given by $N_{cs}^t = N - N_c^t - N_d^t - N_s^t$.

Since local interactions are ignored (Khouider et al., 2010), all n^2 stochastic processes $(Y_t)_{t>0}$ are independent (and identically) distributed, and thus the cloud population species N_c, N_d, and N_s effectively form a three dimensional birth/death process with immigration, denoted as

$$(\boldsymbol{X}_t)_{t>0}, \qquad \boldsymbol{X}_t = (N_c^t, N_d^t, N_s^t).$$

We next derive the *Kolmogorov equations*, a set of differential equations that describe the probability laws for the system.

Transition Probability Functions $P_{\boldsymbol{i},\boldsymbol{j}}(t)$ Let $\boldsymbol{i} = (i_1, i_2, i_3)$ and $\boldsymbol{j} = (j_1, j_2, j_3)$ be triplets of non-negative integers in the range space $\mathcal{S}$ of $(\boldsymbol{X}_t)_{t>0}$. The conditional probability that at time t the populations of congestus, deep and stratiform are respectively j_1, j_2, and j_3, given that there were i_1 congestus, i_2 stratiform, and i_3 deep clouds at time $t = 0$ is denoted by

$$P_{\boldsymbol{ij}}(t) = P\{\boldsymbol{X}_t = \boldsymbol{j} | \boldsymbol{X}_0 = \boldsymbol{i}\}.$$

The transition probabilities $P_{\boldsymbol{ij}}(t)$ satisfy the initial condition $P_{\boldsymbol{ij}}(0) = \delta_{i_1 j_1}\delta_{i_2 j_2}\delta_{i_3 j_3}$, where $\delta_{\alpha\beta}$ is the Kronecker delta, and we assume that $P_{\boldsymbol{ij}}(t)$ are differentiable functions of t for $t > 0$. Transitions $\boldsymbol{i} \to \boldsymbol{j}$ can occur as a single birth (with the clear sky population N_{cs} loosing one site), a death (with the clear sky population N_{cs} gaining one site), or an immigration event (when a congestus becomes a deep cloud, or a deep cloud becomes a stratiform). Let $\boldsymbol{\varepsilon_1} = (1,0,0)$, $\boldsymbol{\varepsilon_2} = (0,1,0)$, and $\boldsymbol{\varepsilon_3} = (0,0,1)$ be the canonical unit vectors of $\mathbb{R}^3$, then the admissible transitions from state $\boldsymbol{i}$ are given as (transition in parentheses; see Khouider et al. (2010)):

$$\begin{aligned}
P\{\boldsymbol{X}_{t+h} = \boldsymbol{i} - \boldsymbol{\varepsilon_1} + \boldsymbol{\varepsilon_2} | \boldsymbol{X}_t = \boldsymbol{i}\} &= R^{\boldsymbol{i}}_{12}h + o(h) && \text{(congestus to deep)},\\
P\{\boldsymbol{X}_{t+h} = \boldsymbol{i} - \boldsymbol{\varepsilon_2} + \boldsymbol{\varepsilon_3} | \boldsymbol{X}_t = \boldsymbol{i}\} &= R^{\boldsymbol{i}}_{23}h + o(h) && \text{(deep to stratiform)},\\
P\{\boldsymbol{X}_{t+h} = \boldsymbol{i} - \boldsymbol{\varepsilon_1} | \boldsymbol{X}_t = \boldsymbol{i}\} &= R^{\boldsymbol{i}}_{10}h + o(h) && \text{(congestus to clear sky)},\\
P\{\boldsymbol{X}_{t+h} = \boldsymbol{i} - \boldsymbol{\varepsilon_2} | \boldsymbol{X}_t = \boldsymbol{i}\} &= R^{\boldsymbol{i}}_{20}h + o(h) && \text{(deep to clear sky)}, \qquad (5.2.2a)\\
P\{\boldsymbol{X}_{t+h} = \boldsymbol{i} - \boldsymbol{\varepsilon_3} | \boldsymbol{X}_t = \boldsymbol{i}\} &= R^{\boldsymbol{i}}_{30}h + o(h) && \text{(stratiform to clear sky)},\\
P\{\boldsymbol{X}_{t+h} = \boldsymbol{i} + \boldsymbol{\varepsilon_1} | \boldsymbol{X}_t = \boldsymbol{i}\} &= R^{\boldsymbol{i}}_{01}h + o(h) && \text{(clear sky to congestus)},\\
P\{\boldsymbol{X}_{t+h} = \boldsymbol{i} + \boldsymbol{\varepsilon_2} | \boldsymbol{X}_t = \boldsymbol{i}\} &= R^{\boldsymbol{i}}_{02}h + o(h) && \text{(clear sky to deep)},
\end{aligned}$$

where h is a small increment, and $R^{\boldsymbol{i}}_{kl} = i_k r_{kl}$ with the rates r_{kl} depending upon the exogenous factors C, C_l, D as defined in Table 2.4. The probabilities of transitions other than those listed in (5.2.2) in a time interval $(t, t+h)$ are small, on the order

$o(h)$, and the probability of no transition in $(t, t+h)$ is given by

$$P\{\boldsymbol{X}_{t+h} = \boldsymbol{i} | \boldsymbol{X}_t = \boldsymbol{i}\} = 1 - h\Big(R^{\boldsymbol{i}}_{10} + R^{\boldsymbol{i}}_{01} + R^{\boldsymbol{i}}_{02} + R^{\boldsymbol{i}}_{12} + R^{\boldsymbol{i}}_{20} + R^{\boldsymbol{i}}_{23} + R^{\boldsymbol{i}}_{30}\Big) + o(h). \tag{5.2.3}$$

The transition probability matrix of the continuous time birth/death process $(\boldsymbol{X}_t)_{t>0}$ defined by the probabilities (5.2.2) solves the so-called system of Kolmogorov *backward* differential equations (Feller, 1949):

$$\begin{aligned}
\frac{dP_{\boldsymbol{ij}}(t)}{dt} &= R^{\boldsymbol{i}}_{12} P_{\boldsymbol{i}-\boldsymbol{\varepsilon_1}+\boldsymbol{\varepsilon_2},\boldsymbol{j}}(t) + R^{\boldsymbol{i}}_{23} P_{\boldsymbol{i}-\boldsymbol{\varepsilon_2}+\boldsymbol{\varepsilon_3},\boldsymbol{j}}(t) + R^{\boldsymbol{i}}_{10} P_{\boldsymbol{i}-\boldsymbol{\varepsilon_1},\boldsymbol{j}}(t) \\
&\quad + R^{\boldsymbol{i}}_{20} P_{\boldsymbol{i}-\boldsymbol{\varepsilon_2},\boldsymbol{j}}(t) + R^{\boldsymbol{i}}_{30} P_{\boldsymbol{i}-\boldsymbol{\varepsilon_3},\boldsymbol{j}}(t) + R^{\boldsymbol{i}}_{01} P_{\boldsymbol{i}+\boldsymbol{\varepsilon_1},\boldsymbol{j}}(t) + R^{\boldsymbol{i}}_{02} P_{\boldsymbol{i}+\boldsymbol{\varepsilon_2},\boldsymbol{j}}(t) \\
&\quad - \Big(R^{\boldsymbol{i}}_{12} + R^{\boldsymbol{i}}_{23} + R^{\boldsymbol{i}}_{10} + R^{\boldsymbol{i}}_{20} + R^{\boldsymbol{i}}_{30} + R^{\boldsymbol{i}}_{01} + R^{\boldsymbol{i}}_{02}\Big) P_{\boldsymbol{ij}}(t),
\end{aligned}$$

with the initial conditions $P_{\boldsymbol{ij}}(0) = \delta_{\boldsymbol{ij}}$. Let $P = \{P_{\boldsymbol{ij}}(t)\} \in \mathbb{R}^{|\mathcal{S}| \times |\mathcal{S}|}$ be the matrix of transition probability functions. We may cast the Kolmogorov system in its matrix form:

$$P'(t) = RP(t), \qquad P(0) = Id, \tag{5.2.4}$$

where Id is the identity matrix of order $|\mathcal{S}|$, and $R \in \mathbb{R}^{|\mathcal{S}| \times |\mathcal{S}|}$ is the matrix of transition rates $R^{\boldsymbol{i}}_{kl}$ (the infinitesimal generator of the birth/death process).

5.3 The Bayesian Paradigm: Prior, Likelihood and Posterior

The multicloud model simulates the evolution of the cloud populations $\boldsymbol{x} = (N_c, N_d, N_s)$[1] constrained by the large-scale atmospheric state $\boldsymbol{u} = (C, C_l, D)$. We label the corresponding sequence of observations $x_1, x_2, x_3, \ldots$ and $u_1, u_2, u_3, \ldots$ by $\boldsymbol{x}_t$ and $\boldsymbol{u}_t$,

---

[1] Observations of the random variable $\boldsymbol{X}$ are here written in lower case.

respectively. The parameterization includes seven numerical inputs (or parameters), namely the cloud convective timescales (see Table 2.4), which we stack in the vector

$$\boldsymbol{\theta} = (\tau_{01}, \tau_{10}, \tau_{12}, \tau_{02}, \tau_{23}, \tau_{20}, \tau_{30}).$$

The relationship between the parameters, large-scale variables, and model output can be represented by the mapping $\boldsymbol{x}_t = g(\boldsymbol{\theta}, \boldsymbol{u}_t)$, where g is a function that represents the multicloud model (coupled to a GCM). The parameters, or inputs $\boldsymbol{\theta}$, can be 'tuned' to find $\boldsymbol{\theta}^*$, the 'best' input configuration, so that the model reproduces some observed data well. The role of the data is to help us *learn* which parameter values best simulate the climate we have. Learning which choice of parameter values yield the given model to best reproduce the climate variability is the process of *calibration.* The calibration problem can be viewed as an *inverse problem*: given the multicloud-GCM coupled model (represented by the function g), the cloud data $\boldsymbol{x}_t$, and the large-scale atmospheric state $\boldsymbol{u}_t$, we need to find the best parameter values $\boldsymbol{\theta}^*$ so that $\boldsymbol{x}_t^* = g(\boldsymbol{\theta}^*, \boldsymbol{u}_t)$ is statistically close to $\boldsymbol{x}_t$.

In the inversion process, uncertainties arise from imperfect data (measurement or preprocessing error) and from the assumption that the model is a true representation of the climate dynamics (model error). The Bayesian statistical approach provides a solution by formulating a complete probabilistic description of the unknowns and uncertainties given the data. It incorporates the initial information and residual uncertainty about the model parameters $\boldsymbol{\theta}$ into a *prior* distribution $\pi(\boldsymbol{\theta})$, which is then updated by the model *likelihood* function $f(\boldsymbol{x}_t|\boldsymbol{\theta})$ to formulate a *posterior* distribution $\pi(\boldsymbol{\theta}|\boldsymbol{x}_t)$ of the parameters given the data (Robert, 2007). Hence it does not find a single best-fit parameter configuration $\boldsymbol{\theta}^*$ but a distribution $\pi(\boldsymbol{\theta}|\boldsymbol{x}_t)$, informed by the data $\boldsymbol{x}_t$.

The inversion of probabilities is given by *Bayes' Theorem.* It finds the posterior distribution $\pi(\boldsymbol{\theta}|\boldsymbol{x}_t)$ in terms of the two antecedents $\pi(\boldsymbol{\theta})$ and $f(\boldsymbol{x}_t|\boldsymbol{\theta})$ (Robert, 2007):

$$\pi(\boldsymbol{\theta}|\boldsymbol{x}_t) = \frac{f(\boldsymbol{x}_t|\boldsymbol{\theta})\pi(\boldsymbol{\theta})}{\int f(\boldsymbol{x}_t|\boldsymbol{\theta})\pi(\boldsymbol{\theta})d\boldsymbol{\theta}}.$$

In other words, $\pi(\boldsymbol{\theta}|\boldsymbol{x}_t)$ is proportional to the distribution of $\boldsymbol{x}_t$ conditional upon $\boldsymbol{\theta}$, i.e. the likelihood, multiplied by the prior distribution on $\boldsymbol{\theta}$:

$$\pi(\boldsymbol{\theta}|\boldsymbol{x}_t) \propto f(\boldsymbol{x}_t|\boldsymbol{\theta})\pi(\boldsymbol{\theta}).$$

Conditioning further on $\boldsymbol{u}_t$ we obtain:

$$\pi(\boldsymbol{\theta}|\boldsymbol{x}_t, \boldsymbol{u}_t) \propto f(\boldsymbol{x}_t|\boldsymbol{u}_t, \boldsymbol{\theta})\pi(\boldsymbol{\theta}). \tag{5.3.1}$$

In this Bayesian context, the large-scale variables $\boldsymbol{u}_t$ are seen as covariates to the model and we may think of them as having Dirac delta distributions.

We now consider series of observations $\boldsymbol{x}_{1:T} = (\boldsymbol{x}_1, \ldots, \boldsymbol{x}_T)$ and $\boldsymbol{u}_{1:T} = (\boldsymbol{u}_1, \ldots, \boldsymbol{u}_T)$ of length T. By conditioning on past events, the likelihood is effectively factorized into a product of T *one-step transition likelihoods*:

$$f(\boldsymbol{x}_{1:T}|\boldsymbol{u}_{1:T}, \boldsymbol{\theta}) = \prod_{t=1}^{T} f_{t-1}(\boldsymbol{x}_t|\boldsymbol{x}_{t-1}, \boldsymbol{u}_{t-1}, \boldsymbol{\theta}). \tag{5.3.2}$$

Here we resorted to the Markov property of the probabilistic multicloud model to exclude old events from the representation.

5.4 Approximation of the Likelihood Function

On the time interval $[t, t + \Delta t]$, during which the large-scale variables $\boldsymbol{u}_t$ may be assumed constant, the solution to the system (5.2.4) is approximately given by

$$P(s) = \exp\left[R(\bar{\boldsymbol{u}}_t, \boldsymbol{\theta})s\right], \quad s \in [t, t + \Delta t] \tag{5.4.1}$$

for some fixed model parameter values $\boldsymbol{\theta}$ and constant values $\bar{\boldsymbol{u}}_t$ of the large-scale variables. The one-step transition likelihoods in (5.3.2) are merely the density functions associated with the probability matrix entries (5.4.1), as functions of $\boldsymbol{\theta}$. The computation of the likelihood function (5.3.2) in full requires repeated solves of the forward problem, more precisely $T - 1$ evaluations of a large matrix exponential for an observed sample of length T.

Large Matrix Exponential How large the matrix R is depends on the size of the cloud lattice. Given a lattice of size N, the stochastic process $(\boldsymbol{X}_t)_{t>0}$ evolves in a finite space $\mathcal{S} \subset \mathbb{N}^3$, where $\mathcal{S}$ is the set of all ordered triplets of nonnegative integers (a, b, c) satisfying the relation $a + b + c \le N$. The geometrical domain associated with $\mathcal{S}$ is illustrated in Figure 5.1a.

The state space $\mathcal{S}$ is countable, so we can find an ordering formula $\phi : \mathcal{S} \to \mathbb{N}$ for the triples in $\mathcal{S}$ (in practice, ϕ is needed to construct the large matrix R incrementally). One such injection is given by the mapping

$$\begin{aligned} \phi(d, b, c) &= \underbrace{\sum_{s=0}^{d-1}\sum_{b=0}^{s}(s - b + 1)}_{\text{rank given plane } d} + \underbrace{\sum_{s=0}^{b-1}(d - s + 1)}_{\text{rank given stride } b} + c, \\ &= \frac{d^3}{6} + \frac{d^2}{2} + \frac{d}{3} + db - \frac{b^2}{2} + \frac{3b}{2} + c, \end{aligned} \tag{5.4.2}$$

for which we set $a + b + c = d$ for $0 \le d \le N$, $0 \le b \le d$, and $0 \le c \le d - b$. The counting

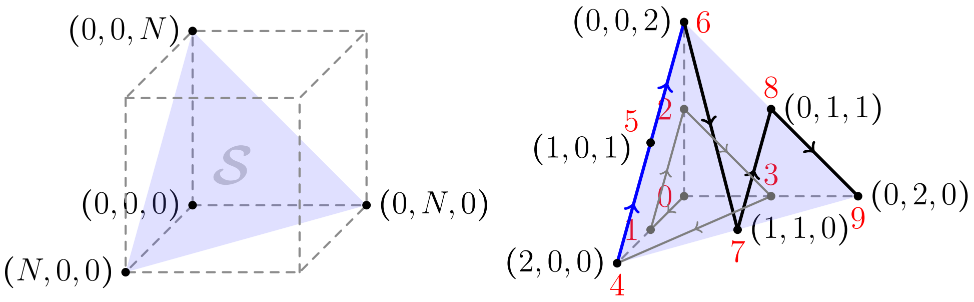

(a)

(b)

Figure 5.1: (*left*) The state space $\mathcal{S}$ of the birth/death/immigration process $(\boldsymbol{X}_t)_{t>0}$ is the subset of $\mathbb{N}^3$ of all ordered triples of nonnegative integers (a, b, c) that lie below and on the plane $a + b + c = N$. (*right*) Sequence of triples given by the counting function ϕ (in red) for $N = 2$. The *stride* $b = 0$ for the plane $d = 2$ is colored in blue.

increment is determined first by planes, then by strides within those planes. The function ϕ maps each triple in $\mathcal{S}$ to a counting order (address). An illustration of the mapping is given in Figure 5.1b. We may now write the likelihood (5.3.2) as

$$\begin{aligned} f(\boldsymbol{x}_{1:T}|\boldsymbol{u}_{1:T}, \boldsymbol{\theta}) &= \prod_{t=1}^{T} f_{t-1}(\boldsymbol{x}_t|\boldsymbol{x}_{t-1}, \boldsymbol{u}_{t-1}, \boldsymbol{\theta}) \\ &= \prod_{t=1}^{T} \mathbb{1}^{*}_{\boldsymbol{\phi}(\boldsymbol{d}^{t-1}, \boldsymbol{N}_d^{t-1}, \boldsymbol{N}_s^{t-1})} \exp[R(\boldsymbol{u}_{t-1}, \boldsymbol{\theta})h] \mathbb{1}_{\boldsymbol{\phi}(\boldsymbol{d}^{t}, \boldsymbol{N}_d^{t}, \boldsymbol{N}_s^{t})}, \end{aligned} \tag{5.4.3}$$

where $\boldsymbol{x}_t = (N_c^t, N_d^t, N_s^t)$, $d^t = N_c^t + N_d^t + N_s^t$, h is the sampling time interval, and $\mathbb{1}_{\boldsymbol{\phi}(\cdot)}$ is a vector in $\mathbb{R}^{|\mathcal{S}|}$ that has 1 at the index corresponding to $\phi(\cdot)$, and 0's everywhere else. Here $\mathbb{1}^{*}_{\boldsymbol{\phi}(\cdot)}$ is the transpose of $\mathbb{1}_{\boldsymbol{\phi}(\cdot)}$, and ϕ is given by (5.4.2).

From the counting formula (5.4.2), we can get the dimension of the infinitesimal generator R, i.e. the cardinality of $\mathcal{S}$, as the last element in the counting sequence:

$$|\mathcal{S}| = \phi(N, N, 0) + 1 = \frac{N^3}{6} + N^2 + \frac{11}{6}N + 1 = \dim(R).$$

We find that $\dim(R) = \mathcal{O}(N^3)$, so the size and memory requirements of R become prohibitively large with the dimensions of the cloud lattice. For instance, for a 10×10

lattice ($N = 100$) the size of R is 176,851, which requires about 70 Mb of storage in the compressed standard `PETSc` AIJ format. The memory requirement escalates to about 50 Gb for a 30×30 lattice ($N = 900$) and correspondingly, $\dim(R) = 122,311,651$. But although R is large, its density (fraction of non-zero elements) is quite low: $4.52 \times 10^{-3}\%$ for $N = 100$ and $6.54 \times 10^{-6}\%$ for $N = 900$. Sparse matrix compression alone is however not sufficient as indicated by the memory storage numbers above, so further scalability is gained using distributed memory. We achieved considerable performances (in matrix assembly and operations) using distributed sparse `PETSc` (Balay et al., 2015) matrices and related routines.

Uniformization Method We are led to consider the problem of computing the exponential of a large sparse matrix. Since the matrix exponential is dense even when the matrix R is sparse, the computation of $\exp(Rt)$ in full (based on matrix-matrix operations) remains possible only when R is relatively small. These include Padé-type or matrix decompositions (Moler and Van Loan, 1978). For large-scale problems, the family of series methods, based on matrix-vector products, are preferable (Sidje and Stewart, 1999). In Markov chain modelling the use of Jensen's *Uniformization Method* (Jensen, 1953; Sidje and Stewart, 1999) is widespread, but an alternative technique based on *Krylov subspaces* (Sidje, 1998; Sidje and Stewart, 1999) rivals in performance in some select cases. We implemented both methods in parallel and compared their applicability and performance in extensive numerical tests that are not reported here. The Krylov-based Method is an iterative technique which comes with a serious caveat: there exists no practical and satisfactory stopping criterion for the method. While the performance results in Sidje and Stewart (1999) are obtained by fixing the size of the Krylov basis beforehand, Saad's (Saad, 1992) residual-based stopping criterion used in Botchev (2012) and Dulat et al. (2010) fails the convergence test in our case. Ultimately we resorted to the Uniformization Method for which there exists an established stopping criterion, and which revealed to be both reliable and accurate in our series of numerical tests.

The Uniformization Method is based on the partial Taylor series expansion of the matrix exponential:

$$\boldsymbol{w}(t) := \exp(Rt)\boldsymbol{e_j} \approx \sum_{k=0}^{p} \frac{t^k}{k!} R^k \boldsymbol{e_j}, \tag{5.4.4}$$

where $\boldsymbol{e_j}$ is the standard canonical vector in $\mathbb{R}^{|\mathcal{S}|}$. However, because R is essentially nonnegative (the diagonal elements of R are negative and the off-diagonal elements are nonnegative), a direct use of (5.4.4) leads to severe roundoff errors in finite floating point arithmetic due to catastrophic cancellation. For numerical stability, the series expansion (5.4.4) is combined with the preconditioner $Q = \frac{1}{\alpha}R + Id$, where $\alpha = \max_i |R_{ii}|$. It follows that Q is a stochastic matrix, that is, its entries satisfy $\sum_j Q_{ij} = 1$, and $Q_{ij} \geq 0$. Once preconditioned, the truncated approximation

$$\boldsymbol{w_p}(t) := e^{-\alpha t} \sum_{k=0}^{p} \frac{(\alpha t)^k}{k!} Q^k \boldsymbol{e_j}, \tag{5.4.5}$$

involves nonnegative terms only and is numerically stable. Using the fact that $\|Q\|_\infty = 1$, it is easy to show that the error of the approximation (5.4.5) satisfies

$$\|\boldsymbol{w}(t) - \boldsymbol{w_p}(t)\|_\infty \leq 1 - e^{-\alpha t} \sum_{k=0}^{p} \frac{(\alpha t)^k}{k!}. \tag{5.4.6}$$

The a priori bound (5.4.6) on the series truncation error is used as a stopping criterion in the Uniformization Method: If ϵ_{tol} is a prescribed error tolerance, then we truncate the series at order p_ϵ, where p_ϵ is the smallest integer that satisfies

$$1 - e^{-\alpha t} \sum_{k=0}^{p_\epsilon} \frac{(\alpha t)^k}{k!} \leq \epsilon_{tol} \Leftrightarrow \sum_{k=0}^{p_\epsilon} \frac{(\alpha t)^k}{k!} \geq e^{\alpha t}(1 - \epsilon_{tol}).$$

As such, the Uniformization Method is accurate and numerically very reliable. We used the `PETSc` (Balay et al., 2015) parallel suite for distributed sparse matrix–vector products. A tolerance error $\epsilon_{tol} = 10^{-10}$ was set for all numerical results reported herein.

5.5 Markov Chain Monte Carlo Posterior Sampling

In the Bayesian paradigm, all inferences about the model parameters $\boldsymbol{\theta}$ are carried out based on the posterior distribution

$$\pi(\boldsymbol{\theta}|\boldsymbol{x}_{1:T}, \boldsymbol{u}_{1:T}) \propto \pi(\boldsymbol{\theta}) \prod_{t=1}^{T} \mathbb{1}^{*}_{\boldsymbol{\phi(d^{t-1}, N_d^{t-1}, N_s^{t-1})}} \exp[R(\boldsymbol{u}_{t-1}, \boldsymbol{\theta})h] \mathbb{1}_{\boldsymbol{\phi(d^{t}, N_d^{t}, N_s^{t})}}, \tag{5.5.1}$$

for a suitable choice of the prior $\pi(\boldsymbol{\theta})$. Equation (5.5.1) is found by combining (5.3.1) with (5.4.3). Bayesian point-estimators of interest, like the posterior mean $\mathbb{E}_{\pi}[\boldsymbol{\theta}] = \int_{\Theta} \boldsymbol{\theta}\, \pi(\boldsymbol{\theta}|\boldsymbol{x}_{1:T}, \boldsymbol{u}_{1:T}) d\boldsymbol{\theta}$, require to evaluate an integral on a parameter space Θ of dimension 7. A classical approximation method for complex multidimensional integrals is the MCMC technique (Robert and Casella, 2004). The underlying idea of MCMC is to construct a Markov chain in $\boldsymbol{\theta}$ with ergodic (stationary) distribution $\pi(\boldsymbol{\theta}|\boldsymbol{x}_{1:T}, \boldsymbol{u}_{1:T})$, which is guaranteed under the conditions of irreducibility and aperiodicity of the chain: Starting with some initial state $\boldsymbol{\theta}^{(0)}$, simulate M Markov chain transitions and record the observed values $\boldsymbol{\theta}^{(j)}$, $j = 0, \ldots, M$. If $\mathbb{E}_{\pi}|\boldsymbol{\theta}| < \infty$, then the ergodic sample average $\hat{\boldsymbol{\theta}} = \frac{1}{M+1} \sum_{j=0}^{M} \boldsymbol{\theta}^{(j)}$ converges almost surely to $\mathbb{E}_{\pi}[\boldsymbol{\theta}]$ by the Markov chain strong law of large numbers (SLLN; see Brooks et al., 2011). Here we use a standard Metropolis within Gibbs sampler, also known as component-wise Metropolis Hastings, which breaks down the 7-dimensional target $\pi(\boldsymbol{\theta}|\boldsymbol{x}_{1:T}, \boldsymbol{u}_{1:T})$ into simpler, one dimensional, targets. As recommended by Robert and Casella (2004) in the case of high dimensional models, a truncated normal distribution $\mathcal{TN}(0, \sigma^2, 0, +\infty)$ proposal was σ-calibrated so as to obtain an optimal acceptance rate of 1/4. For technical details on the algorithm, see Robert and Casella (2010) and Brooks et al. (2011). Here, the MCMC posterior simulator is written in the MPI C programming language; All simulations were performed using the WestGrid Nestor platform (`www.westgrid.ca`).

5.6 Validation Using Synthetic Data

In this section we present validation tests for the Bayesian procedure (and MCMC posterior simulator) using synthetic data. The synthetic experiment consists of 5 steps.

1. Fix the input cloud timescale parameters values as in Table 2.4.
2. Run the coupled toy multicloud-GCM model with those input parameters for a given size of the cloud lattice. The model outputs the cloud population (i.e. cloud cover) time series, and large-scale variable time series.
3. Isolate the stationary cloud population and large-scale variable time series to be used as "synthetic" observed time series for the Bayesian procedure.
4. Run the Bayesian procedure using the synthetic time series obtained in Step 3 and selected priors on the cloud timescale parameters. The Bayesian procedure outputs distributions on the parameters, from which point estimates are calculated.
5. Compare the inferred parameter values with the "true" input values selected in Step 1.

Arguably the choice of priors has a significant impact on the Bayesian inference. We work under the assumption that we have little to no prior information on the timescale parameters, which motivates our choice of a diffuse normal and uniform priors, respectively.

The consistency check described above is performed for synthetic time series of increasing lengths, with the goal of testing the sensitivity of the inference method to observing more data. The results of these tests are reported in Section 5.6.2 for the normal and uniform priors, while the synthetic data are first presented in Section 5.6.1.

A second consistency check consists of carrying the inference in a sequential manner, using small successive batches of data, as opposed to a large contiguous one. This technique, which is called here *sequential learning*, is required in the cases when only multiple short samples of real data are available (ref. Chapter 6). We discuss our results on sequential learning in Section 5.6.3 in the case of a normal prior.

5.6.1 Synthetic Data

The synthetic data used for the verification are generated using the SMCM closure equations (2.4.17) on a lattice of size $n = 10$, coupled with the simple one-column atmospheric climate model of Khouider et al. (2010). The cloud timescales are fixed at the values listed in Table 2.4.

One-Column Climate Model. The one–column toy GCM consists of a one-dimensional model with a crude vertical resolution of the free troposphere reduced to the first two baroclinic modes, coupled with a single equation for the ABL moist entropy. The model dimensional equations reduce to the following ODE system (Khouider et al., 2010):

$$\begin{aligned}
\frac{\partial \theta_1}{\partial t} &= H_d - Q_{R1} - \frac{\theta_1}{\tau_R}, \\
\frac{\partial \theta_2}{\partial t} &= H_c - H_s - Q_{R2} - \frac{\theta_2}{\tau_R}, \\
\frac{\partial \theta_{eb}}{\partial t} &= \frac{1}{\tau_e}\left(\theta^*_{eb} - \theta_{eb}\right) - \frac{1}{h_b} D_c \, \Delta_m \theta_e, \\
\frac{\partial q}{\partial t} &= -\frac{2\sqrt{2}}{\pi} H_d,
\end{aligned}$$

where D_c is given by (2.4.20), θ^*_{eb} is the saturation equivalent potential temperature in the boundary layer, and all other variables and parameters are defined as in Chapter 2. The ODE system describes the evolution of the large-scale atmospheric variables θ_1, θ_2, q, and θ_{eb} for the one atmospheric GCM column. These large-scale variables are used to calculate the large-scale convection indicators C, C_l, and D needed by the SMCM parameterization to evolve the cloud area fractions σ_c, σ_d, and σ_s within the vertical column. The cloud area fractions, in turn, affect the large-scale atmospheric state by driving the heat forcings H_c, H_d, and H_s.

Synthetic Time Series. The synthetic data obtained from running the SMCM-toy GCM described above is shown in Figure 5.2: It comprises the time series of the cloud populations N_c, N_d, and N_s, and of the large-scale variables C, C_l, and D, calculated as per (2.4.19) using $\text{CAPE}_0 = 1500$ J kg^{-1} and $T_0 = 10$ K. Each time series totals 28,800 sample points with a 5 minute sampling time interval, which corresponds to 100 days in real time. For verification purposes, we use a shorter 9-day interval (between days 52 and 61, approximately 2500 sample points) taken from the radiative–convective equilibrium regime, as shown in the insets of Figure 5.2.

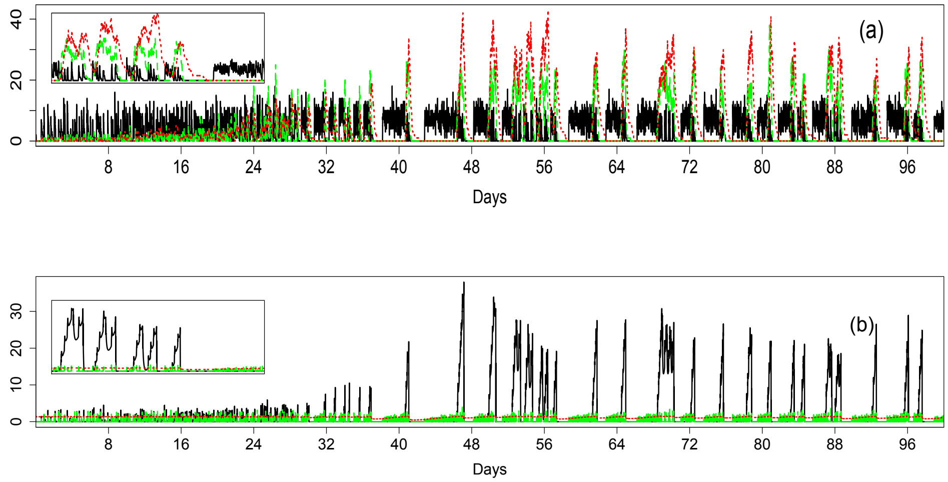

Figure 5.2: (a) *(Main)* Synthetic time series of the cloud populations of congestus N_c (*black solid*), deep N_d (*green dashed*) and stratiform N_s (*red dotted*) obtained with the GCM-multicloud model, using the “true” parameter values of Table 2.4. *(Inset)* Interval from day 52 to day 61 in the equilibrium regime used for the verification test. (b) Same as in (a) but for the large-scale variables C (*black solid*), C_l (*green dashed*), and D (*red dotted*).

5.6.2 Sensitivity Tests

We first run the validation tests using a 7-dimensional truncated normal prior

$$\mathcal{TN}_7(10, 10\, Id_7, 0, +\infty)$$

with mean 10 and covariance matrix $10 \cdot Id_7$, where Id_7 is the 7-dimensional identity matrix. The normal prior is restricted to the positive real half space to reflect the fact that the timescales are nonnegative values. The choice of this distribution is motivated by the need for a weakly informative prior in the sense that (1) the prior mean of 10 is chosen sufficiently far from the true values in an attempt to demonstrate Bayesian learning towards the true values, but not too far to mitigate the limited amount of data information (increasing the amount of data T is cost prohibitive), and (2) the variance is large enough to have a significant amount of prior uncertainty, but not too large to reflect some degree of prior belief.

Sensitivity to the Length of the Time Series We used $T = 100$, 500, 1000, 1500, 2000, and 2500 contiguous observations of the synthetic time series, and ran our MCMC posterior simulator. In physical time, these numbers correspond approximately to 8.3 hrs, 41.7 hrs, 3 days 11 hrs, 5 days 5 hrs, 6 days 23 hrs, and 8 days 16 hrs, respectively.

The Bayes estimates (mean, standard deviation, percentiles) and Monte Carlo standard error (MCSE; Martin et al., 2011) for $T = 100$, 500, and 2500 are shown in Table 5.1 for all 7 parameter marginal posterior distributions. The MCSE and Bayes estimates are calculated using the `MCMCpack R` package (Martin et al., 2011), after the burn-in portions of the chains have been removed. Convergence to stationarity was monitored running several well-dispersed chains, using graphical diagnoses, comparing within and between chains' means and variances, and ensuring that the acceptance rates were roughly around 25%.

Also reported in Table 5.1 are the MCMC sample sizes, approximate runtimes, and number of processors used. As discussed in Section 5.4, the forward problem is computationally expensive, and increasing the number T of observations results in much longer computing time, which is mitigated by using a greater number of processors and smaller MCMC sample size.

We highlight a few results. First we note that we expect the prior to dominate the posterior when the number T of observations used is too small, and the likelihood to dominate the posterior when a sufficiently large number of observations is used. When only 100 observations are used, the parameters τ_{01} and τ_{10} are recovered with good enough accuracy (0.934 and 0.894, respectively; their true value is 1.0 for both), while the estimated mean and standard deviation of the remaining parameters are essentially those of the prior. This seems to correlate well with data, as much of the activity happens mainly between congestus and clear skies during that lapse of time; the 100 observations used for that verification correspond to the first 1/25 of the time series shown in the inset of Figure 5.2, and covers only a small section of the first onsets of deeps and stratiforms. When 500 observations are used, all parameters except τ_{20} roughly recover their true value within one standard deviation not exceeding 21%. When 2500 observations are used, τ_{20}'s true value is recovered within a standard deviation of 19%, while the remaining parameters' relative error do not exceed 7%.

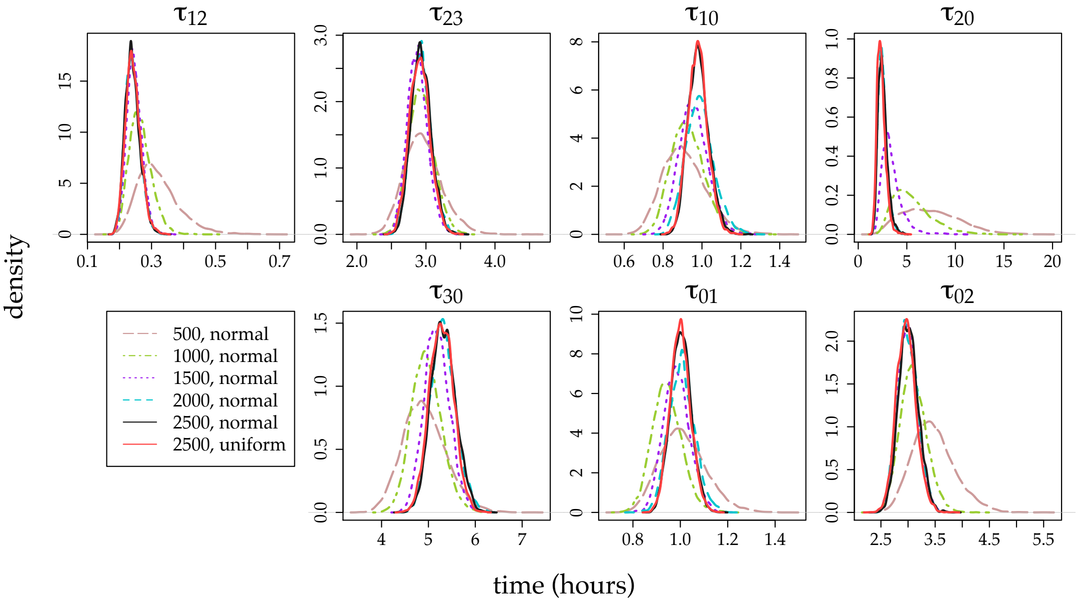

Figure 5.3: Comparison of marginal posterior densities using from $T = 500$ to 2500 observations, by increments of 500, for a normal prior. Also shown (in red) is the marginal posterior density for the uniform prior using $T = 2500$.

In Figure 5.3, we compare the marginal posterior densities for all seven parameters using from $T = 500$ to 2500 observations, by increments of 500. It is interesting to see the convergence to a limiting posterior distribution, as we increase the number

	True Value	Mean	SD (MCSE)	2.5%	97.5%
$T = 100$ (100,000, 24 days, 16 cores)					
τ_{01}	1	0.934	0.1727 (0.003028)	0.6547	1.328
τ_{10}	1	0.894	0.1534 (0.001701)	0.6450	1.243
τ_{12}	.25	9.779	2.9458 (0.395798)	3.9921	15.590
τ_{02}	3	6.370	2.8332 (0.137016)	1.9763	12.572
τ_{23}	3	7.584	3.2871 (0.222591)	1.7847	14.201
τ_{20}	2	10.088	3.0369 (0.067716)	4.1766	16.048
τ_{30}	5	10.004	3.0264 (0.108871)	4.1161	15.884
$T = 500$ (25,293, 42 days, 16 cores)					
τ_{01}	1	1.0116	0.09669 (0.001547)	0.8422	1.2204
τ_{10}	1	0.9111	0.11283 (0.002064)	0.7178	1.1558
τ_{12}	.25	0.3206	0.06582 (0.001334)	0.2198	0.4776
τ_{02}	3	3.4709	0.39302 (0.007823)	2.8028	4.3413
τ_{23}	3	2.9576	0.27455 (0.005086)	2.4747	3.5561
τ_{20}	2	7.4629	2.91743 (0.121603)	2.8282	13.7671
τ_{30}	5	4.9184	0.46225 (0.007028)	4.0957	5.8955
$T = 2500$ (12,695, 42 days, 72 cores)					
τ_{01}	1	1.0019	0.04285 (0.0009227)	0.9198	1.0882
τ_{10}	1	0.9821	0.05310 (0.0009740)	0.8869	1.0968
τ_{12}	.25	0.2411	0.02347 (0.0004343)	0.2005	0.2915
τ_{02}	3	3.0110	0.18012 (0.0032739)	2.6712	3.3749
τ_{23}	3	2.9295	0.14277 (0.0026691)	2.6643	3.2199
τ_{20}	2	2.5256	0.48401 (0.0096552)	1.7842	3.6602
τ_{30}	5	5.3193	0.26249 (0.0052716)	4.8276	5.8481

Table 5.1: Validation results for a normal prior, based on $T = 100$, 500, and 2500 observations. MCMC sample size (excluding burn in), approximate total runtime, and number of processors used in parentheses. Mean, SD, and MCSE are posterior mean, standard deviation, and Monte Carlo standard error, respectively. 2.5% and 97.5% are posterior percentiles.

of observations. More precisely, as T increases, the marginal posterior distributions concentrate close to the parameter true values, and we see a progressive reduction and then a sudden stagnation of the variance; for all parameters, the distribution curves for $T = 2000$ and 2500 match closely. This suggests that although all parameters were reproduced accurately, some uncertainty remains, independently of the length of the data time series.

To test the effect of this 'sample uncertainty' on the climate model dynamics, we now verify whether the inferred values of the cloud timescale parameters do reproduce the climate features we started with. For this, we run the SMCM coupled with a toy GCM as described in Section 5.6.1, with the inferred values reported in Table 5.1 with $T = 2500$. We then compare the resulting new time series, shown in Figure 5.4, with the original ones (see Figure 5.2). In Table 5.2, we report some statistics (mean and standard deviation) for the cloud populations and main climate thermodynamic variables of interest (time series not shown), both for the original and the new (inferred) time series. From these statistics, and by inspection of the two time series, we can ascertain that we recover the climate mean and variability with high fidelity. The fact that the climate dynamics are reproduced accurately, in spite of the uncertainty in some inferred parameters such as τ_{20}, suggests that the stochastic climate model itself is not too sensitive to those parameters. This is in fact, the more meaningful test that the Bayesian methodology has to pass and it passed it very successfully.

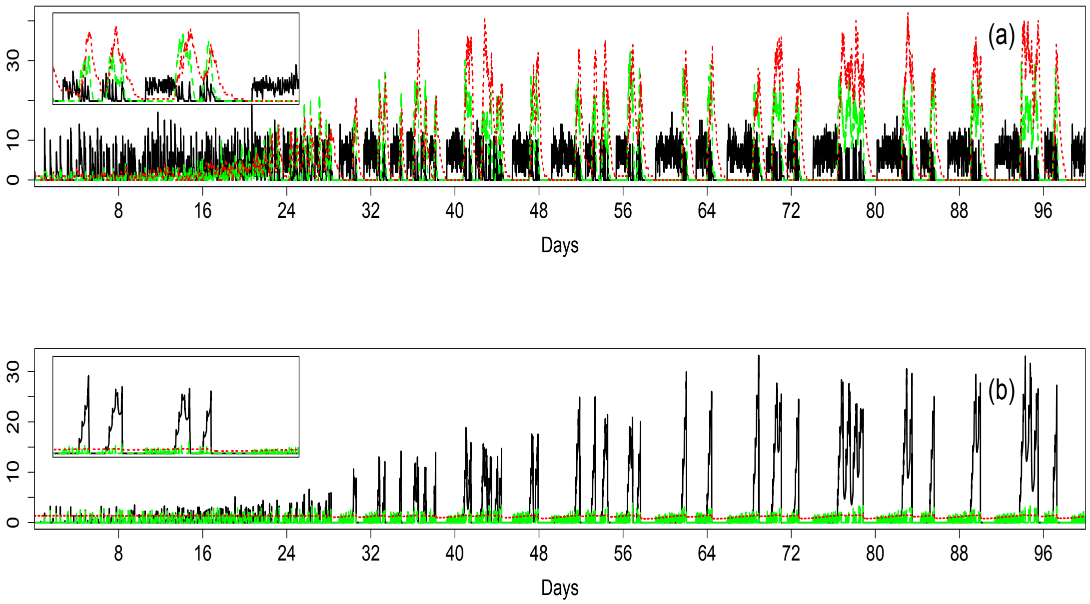

Figure 5.4: (a) *(Main)* Time series of the cloud populations of congestus N_c (*black solid*), deep N_d (*green dashed*) and stratiform N_s (*red dotted*) obtained with the GCM-multicloud model, using the inferred parameter values in Table 5.1 for T = 2500 and a normal prior. *(Inset)* Smaller interval covering day 52 through day 61. (b) Same as in (a) but for the large-scale variables C (*black solid*), C_l (*green dashed*), and D (*red dotted*).

	(1) *True* Mean (SD)	(2) *Inferred* Mean (SD)
Cloud Populations		
Congestus	3.583 (3.625)	3.267 (3.484)
Deep	3.088 (6.371)	3.456 (6.640)
Stratiform	5.214 (8.744)	6.334 (9.598)
Climate Large-Scale Variables		
θ_1	9.759e-02 (8.538e-02)	9.368e-02 (7.910e-02)
θ_2	-5.641e-02 (6.306e-02)	-5.310e-02 (5.742e-02)
θ_{eb}	-5.604e-02 (1.256e-01)	-5.196e-02 (1.158e-01)
q	4.326e-02 (4.608e-02)	4.354e-02 (4.299e-02)

Table 5.2: Mean and standard deviation (SD) for the time series of the cloud populations (shown in Figures 5.2 and 5.4) and climate large-scale variables (time series not shown), which were obtained (1) using the "true" parameter values of Table 2.4 (*true*), and (2) using the Bayes posterior mean values reported in Table 5.1, for $T = 2500$ (*inferred*). The climate thermodynamic variables shown are: θ_1 and θ_2 the potential temperatures associated with the first and second baroclinic modes, θ_{eb} the equilibrium temperature, and q the moisture.

Sensitivity to Prior Specification To investigate the sensitivity of the Bayesian model to prior belief specification, we selected a second prior, the 7-dimensional uniform distribution with large support $\mathcal{U}_7(0, 30)$. This choice of prior can represent an inference context in which there is no a priori information about the parameters. The validation results using the uniform prior were comparable to those obtained using the normal prior except, as might be expected, when only 100 data were used. In the case $T = 100$ and for a MCMC sample of size 92,000, we obtained posterior means (standard deviations) of 0.9026 (0.1641), 0.8654 (0.1418), 22.2945 (3.3827), 4.0160 (2.65), 3.7721 (3.3077), 16.327 (8.0798) and 15.381 (8.1068) for the parameters in the same order as that given in Table 5.1. We note in passing that the true value of 1 of the parameters τ_{10} and τ_{01} is recovered within one standard deviation of roughly 17%, which is consistent with the values obtained under the normal prior, and supports the evidence that the first 100 cloud observations provide information mainly about the transitions between clear sky and congestus. The posterior means for τ_{20} and τ_{30} (16.327 and 15.381, respectively) are far from their true values (2 and 5, respectively), and closer to the midpoint (15) of the large support of the uniform prior. The posterior mean of 22.2945 for τ_{12} is somewhat off, but the behaviour of the MCMC simulator may be counterintuitive on a high dimensional space in the sense that one should not expect a posterior mean somewhat between the midpoint of the uniform prior and the true value for each parameter. Also, as noted above, the first 100 observations constitute the preconditioning phase dominated by congestus activity and only very few –under sampled– intermittent deep convection events are produced. The validation results for larger T values are not reported here because they are not statistically different from those obtained under the normal prior (see Table 5.1), but the posterior marginal distributions for $T = 2500$ are shown in Figure 5.3 (red solid lines) together with the ensemble of posterior marginals obtained under the normal prior.

These results indicate that the outcome of the inference is statistically the same irrespective of the choice of the prior, provided there is sufficient data. This constitutes a formal verification of the correctness of our MCMC sampler. In particular, it verifies that our posterior simulator is robust to the choice of prior, and that it responds normally to the input data, i.e. it outputs a posterior that is dominated by the prior when the data do not provide enough information about the parameters.

5.6.3 Sequential Bayesian Inference

We end this validation study by looking at how the posterior $\pi(\boldsymbol{\theta}|\boldsymbol{x}_{1:T}, \boldsymbol{u}_{1:T})$ evolves as we sequentially update it with new data points $(\boldsymbol{x}_t, \boldsymbol{u}_t)$, $t > T$. As an illustrative case, consider a distribution of the model parameters $\boldsymbol{\theta}$ having observed a three point dataset $\boldsymbol{x}_{1:3} = (\boldsymbol{x}_1, \boldsymbol{x}_2, \boldsymbol{x}_3)$. It can be expressed as

$$\begin{aligned}
\pi(\boldsymbol{\theta}|\boldsymbol{x}_1, \boldsymbol{x}_2, \boldsymbol{x}_3) &\propto f(\boldsymbol{x}_1, \boldsymbol{x}_2, \boldsymbol{x}_3|\boldsymbol{\theta})\pi(\boldsymbol{\theta}) \\
&= f_2(\boldsymbol{x}_3|\boldsymbol{x}_2, \boldsymbol{\theta}) \times f_1(\boldsymbol{x}_2|\boldsymbol{x}_1, \boldsymbol{\theta})\pi(\boldsymbol{\theta}) \\
&= \text{Likelihood of } \{\boldsymbol{x}_3\} \times \text{posterior having observed } \{\boldsymbol{x}_2, \boldsymbol{x}_1\},
\end{aligned}$$

where the covariates $\boldsymbol{u}_{1:3}$ were dropped from the representation for simplicity. Such an incremental procedure is justified by the fact that the data are assumed to be Markovian. More generally, the posterior having observed $(\boldsymbol{x}_1, \dots, \boldsymbol{x}_K)$ can be used as a 'prior' for the remaining data $(\boldsymbol{x}_{K+1}, \dots, \boldsymbol{x}_N)$. This is a particularly useful scheme when the inference is done online with data streaming in gradually, or in cases where only time or spatially discontinuous data series are available. This sequential method is equivalent to observing the data $(\boldsymbol{x}_1, \dots, \boldsymbol{x}_N)$ all at once if a parametric form can be derived for the posterior at the update step. For the multicloud problem however, the posterior's likelihood function is numerically approximated, and we must instead rely on an *assumed* parametric form for the posterior. In this study a multivariate normal distribution is fitted to the posterior using the sample mean and sample covariance matrix. We perform the sequential Bayesian inference following the main steps below.

1. Run the Bayesian model with the first 100 observations (*Sequence 1*), using a $\mathcal{TN}_7(10, 10\,Id_7, 0, +\infty)$ prior. Obtain a posterior distribution over the model parameters. (This was done in Section 5.6.2. See validation results of Table 5.1 for $T = 100$.)

2. Use the method of moments approach to fit a multivariate normal distribution to the posterior samples.

3. Use the fitted distribution obtained in Step 2 as the prior for computing the posterior distribution from the next successive 100 observations (*Sequence 2*).

4. Iterate Steps 2 and 3 three more times until 5 sequences of 100 observations have been used for the sequential inference.

5. Compare the resulting posterior distribution with the posterior obtained by observing the 500 contiguous observations all at once.

Arguably, Step 2 can introduce a large error when the posterior samples are not close to being normally distributed. This was the case in fact when the sequential inference strategy was used with an initial $\mathcal{U}_7(0,30)$ prior: The method broke down after the first training dataset since the posterior samples' underlying distribution was still uniform (see Section 5.6.2 for the validation results under the uniform prior in the case of $T = 100$).

The method was however successful in the case of an initial $\mathcal{TN}_7(10, 10\,Id_7, 0, +\infty)$ prior, as it can be seen from the sequences of updated marginalized posteriors shown in Figure 5.5. As more and more sequences of data are observed, the posteriors shift towards and concentrate on the parameter true values. In some cases, the initial high variance reduces significantly after one or two observed sequences only. The statistics of the marginalized posteriors for Sequence 5 are summarized in Table 5.3.

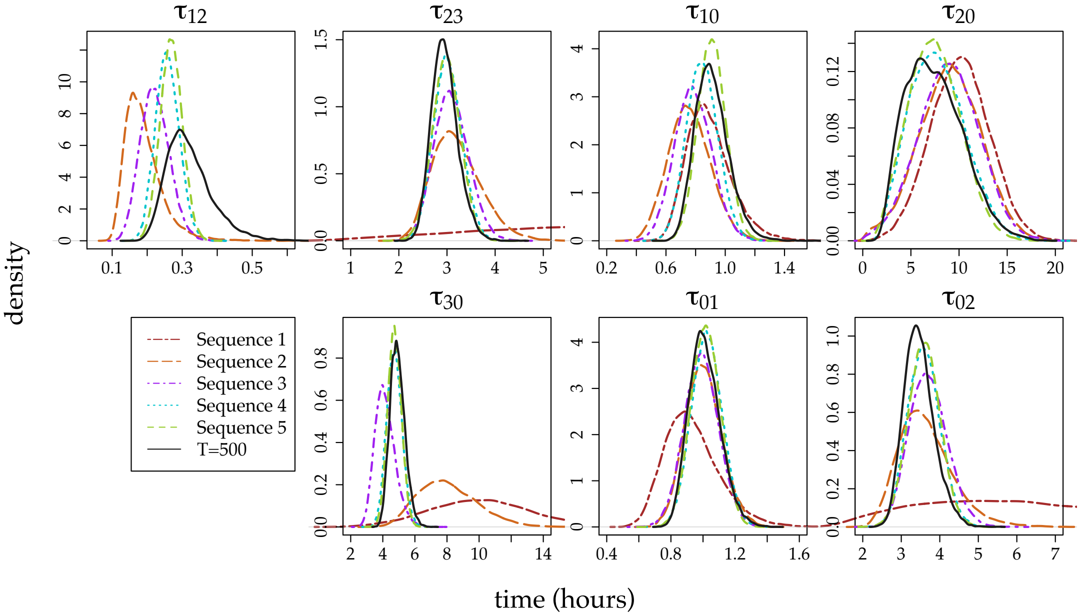

Figure 5.5: Marginal posterior densities obtained using 5 contiguous sequences of 100 observations each (Sequences 1-5), when the posterior of the previous sequence is used as the prior for the next, and for a initial $\mathcal{TN}_7(10, 10\,Id_7, 0, +\infty)$ prior. Also shown are the marginal posterior densities when 500 observations are used all at once ($T = 500$). The Sequence 1 distribution is missing for the parameter τ_{12} as it lies far from the true value.

As shown in Figure 5.5, all posterior marginals obtained after observing Sequence 5 (dashed green) match closely those obtained when all 500 data are observed at once (solid black), except in the case of the parameter τ_{12}. For that specific parameter, the posterior mean after having observed Sequence 5 (dashed green) is equal to 0.2688, which is closer to the true value of 0.25 than the posterior mean of 0.3206 obtained when all 500 data are observed at once (see Table 5.1). There is also less uncertainty about the posterior mode in the sequential case (posterior standard deviation of 0.03152 compared to 0.06582). It is interesting to see how the batch-wise technique captures the true value τ_{12} better than when the data are used all at once, which might suggest that Step 2 of the sequential learning strategy enhances the inference procedure in some way.

	True Value	Mean	SD (MCSE)	2.5%	97.5%
τ_{01}	1	1.0155	0.09064 (0.0005093)	0.8388	1.194
τ_{10}	1	0.9094	0.09471 (0.0006049)	0.6286	1.183
τ_{12}	.25	0.2688	0.03152 (0.0002034)	0.2077	0.331
τ_{02}	3	3.5928	0.40934 (0.0035545)	2.7982	4.398
τ_{23}	3	2.9869	0.29188 (0.0019786)	2.4218	3.562
τ_{20}	2	7.4548	2.68044 (0.0389249)	2.6357	12.935
τ_{30}	5	4.7373	0.42297 (0.0026518)	3.9285	5.585

Table 5.3: Sequential Bayesian inference validation results for Sequence 5, for an initial $\mathcal{TN}_7(10, 10\,Id_7, 0, +\infty)$ prior. MCMC sample size (excluding burn in) is 150,424. Mean, SD, and MCSE are posterior mean, standard deviation, and Monte Carlo standard error, respectively. 2.5% and 97.5% are posterior percentiles.

5.7 Discussion

A Bayesian method for learning the cloud transition time parameters of the SMCM (Khouider et al., 2010) is presented and validated here using synthetic data. The SMCM is in essence a three dimensional birth/death process with immigration whose population species track the time evolution of the area fractions of three cloud types, congestus, deep, and stratiform, that are observed to characterize tropical convective systems (Johnson et al., 1999; Mapes et al., 2006). The SMCM is based on a stochastic lattice model overlaid over each GCM grid box. Each lattice site is either occupied by one of the three cloud types or is a clear sky site. Lattice sites switch between the four possible states according to intuitive probability rules motivated by observations. This results in probability transition rates which depend exclusively on the large-scale variables through some prescribed functions of exogenous factors represented by the potential for convection (CAPE) and middle tropospheric humidity, modulated by timescales. While the functionals are educated guesses that take the form of

Arrhenius activation functions, the timescales are essentially free parameters whose values are very uncertain. In the past, intuitive values have been used satisfactorily in the case of idealized simulations of convectively coupled gravity waves (Frenkel et al., 2012, 2013) and rough estimates were obtained by a simple matching of the equilibrium distribution of the multicloud area fractions to radar spectrometry data (Peters et al., 2013). Yet, the accurate estimation of the parameters from observation and/or detailed cloud resolving data remains an important step forward in order to effectively use the SMCM for the parameterization of organized convection in operational climate models.

The Bayesian method formulates a complete probabilistic description of the model timescale parameters, given the cloud populations' evolution constrained by the large-scale atmospheric convection indicators CAPE, low-level CAPE, and mid-troposphere dryness. The posterior distribution is given as a consequence of two antecedents: the model likelihood function and the prior distribution. The main challenge of the Bayesian method resides in the calculation of the likelihood function which involves the computation of the birth/death process transition probability matrix for each time step of the data time series. According to the Kolmogorov backward equations, the transition probability matrix is given by the exponential of the infinitesimal generator of the Markov chain which, in this case, is of very high dimension but also very sparse. To overcome this difficulty we developed a parallel version of the Uniformization preconditioning method (Jensen, 1953; Sidje and Stewart, 1999) using the parallel numerical software library `PETSc` (Balay et al., 2015) which allows for numerically stable and fast approximations of large sparse matrix exponentials. Another layer of computational complexity is added by the fact that sampling of the high dimensional posterior distribution is done using the standard Markov Chain Monte Carlo technique, which requires the calculation of the likelihood function at each MCMC sample point.

Here the Bayesian approach is successfully tested with synthetic data generated by an idealized single column toy GCM coupled to the SMCM. At first the coupled toy GCM-SMCM model was run with prescribed parameters. The output time series of cloud area fractions and exogenous factors are then fed to the Bayesian algorithm to infer back some of the SMCM parameters, namely, the (seven) transition timescales. The Bayesian method is tested with two different choices of prior, a weakly informative normal prior centred far away from the true values and an uninformative uniform prior, and is shown to be robust to prior specification when enough observations are provided (about 500). With a moderately sized time series, around $T = 500$ observations (corresponding to 1.7 days in physical time), most of the timescales were reproduced with some accuracy–to within one standard deviation of about 21%, except for the transition of deep to clear sky parameter τ_{20} which remains highly inaccurate at this level. With the relatively higher number of observations $T = 2500$ the parameter τ_{20} is recovered within a standard deviation of 19%, while all other 6 parameters are closely recovered within one standard deviation of about 7% (see Table 4.1). Interestingly, the convergence tests reported in Figure 5.3 for the marginal distributions with $T = 500, 1000, 1500, 2000, 2500$ show a systematic convergence in the beginning and then a sudden stagnation towards a limiting posterior distribution which seems to suggest the existence of an upper bound or a maximum knowledge which can be gained from data in terms of the parameter values.

As a consistency check we rerun the coupled toy GCM-SMCM model with the newly inferred parameters (i.e. the inferred means) and compared the statistics of the resulting climate variables to their original counterparts. The results reported in Table 5.2 and Figure 5.4 demonstrate that despite the systematic errors committed by the inferred parameters, the coupled model reproduces the original climate statistics quite accurately, in terms of both the stochastic area fractions and the large-scale dynamical variables. This in essence indicates the level to which the coupled toy GCM-SMCM model is actually sensitive to these parameters. It is clearly less sensitive to some parameters such as τ_{20} than it is to others. This is in fact very good news, and explains in some sense why the SMCM is so successful in previous studies, when only rough or intuitive estimates of these parameters were used (Frenkel et al., 2012, 2013; Khouider et al., 2013a; Peters et al., 2013).

Moreover, the Bayesian methodology is tested for sequential learning, which consists of cutting the available time series into a sequence of small non-overlapping segments of 100 observations. The Bayesian algorithm is then sequentially applied on each segment, using the posterior of the previous segment as the prior for the next one. This method works on the important assumption that the posterior samples are normally distributed with sample mean and sample covariance matrix. It is found that the sequential learning performed reasonably well compared to an inference carried using the training dataset (500 observations) all at once, when an initial normal prior distribution is used. The method failed in the case of an uniform prior distribution, since the first update posterior samples still had an underlying uniform distribution and the misfit to a normal distribution was too large.

This sequential learning strategy becomes useful in the case of simulated or in-situ data which can be spatially dispersed or available in intermittent streams, for instance when multiple observation sites are used or in the case of on/off observation periods. In the next chapter, we present an inference study using LES data that applies the sequential strategy to multiple training time series obtained from nested grids on the available numerical domain.

Chapter 6

Inference Study Using the Giga-LES Dataset

The choice of observed data for the multicloud parameter estimation problem hinges on the ability of the data to capture small scale processes associated with deep convection. This inference study is based on the Giga-LES dataset (Khairoutdinov et al., 2009), a *large-eddy simulation* (LES) of deep tropical convection on a numerical domain comparable to a GCM grid cell. Traditionally, LES have been used to simulate turbulence and low clouds in the PBL, where the grid spacing of $\mathcal{O}(10 - 100\,\mathrm{m})$ is small enough to explicitly represent turbulent processes associated with large eddies occurring in the boundary layer. The "Giga-LES" is one of the very few studies that extends the technique to deep convection in the atmosphere, with a grid spacing of 100 m[1]. It is capable to simulate deep convective cloud processes and shows a tri-modal vertical distribution of deep, middle, and shallow clouds similar to that often observed in the tropics (Khairoutdinov et al., 2009).

In this chapter, the Bayesian inference procedure for the SMCM presented in

---

[1] A simulation rerun, which uses a spatial resolution of 50 m and covers a physical domain of 86 km x 86 km x 22 km, has been carried by Loh and Austin (2015; manuscript in preparation) to study entrainment and detrainment rates.

Chapter 5 is applied to the Giga-LES data. The chapter is divided as follows. Section 6.1 covers the numerical setup of the “Giga-LES” simulation, and Section 6.2 describes the partitioning of the numerical domain as nested grids used for the sequential learning strategy. The time series for the large-scale convective indicators and subgrid-scale cloud area fractions are presented in Sections 6.3.1 and 6.3.2, with a focus on the CAPE calculation and cloud identification scheme. Section 6.4 shows the results of sensitivity tests to the domain partitioning, and to other multicloud model parameters. A concluding discussion is given in Section 6.5.

6.1 The Giga-LES Dataset

The Giga-LES dataset is a 24-hr long LES of deep tropical convection over a domain of 204.8 km in both horizontal directions and about 27 km in the vertical, which uses the mean sounding and forcing observed during the GATE (GARP Atlantic Tropical Experiment) Phase III experiment over the ITCZ (Khairoutdinov et al., 2009). The atmospheric fields are available every 15 minutes at all $2048 \times 2048 \times 256$ grid points of the three dimensional space. A full description of the simulation setup, including the idealized mean GATE initial thermodynamic profiles and large–scale forcing is found in Khairoutdinov et al. (2009). This LES of deep tropical convection in the ITCZ captures a wide range of scales of motion, from turbulent eddies and low clouds in the planetary boundary layer to deep convective clouds and convective cloud systems, in a domain comparable to a typical GCM grid cell. Figure 6.1 presents a visualization of the cloud scene over the whole 205×205 km^2 domain at hour 13. The scene illustrates a complex convection activity, with individual deep clouds and cloud systems dominated by stratiform anvils, surrounded by smaller congestus and shallow clouds.

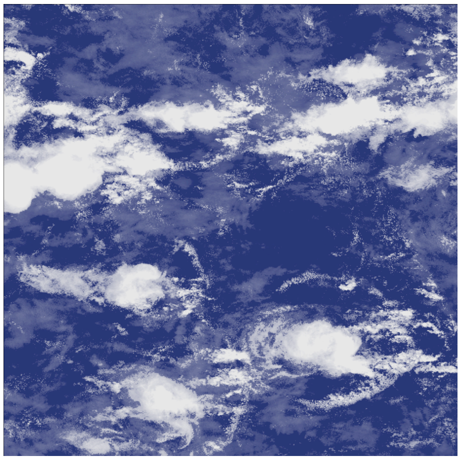

Figure 6.1: Image of simulated cloud scene over the area 205×205 km^2 corresponding to hour 13 of the Giga-LES simulation, obtained from visible albedo estimated from the liquid and ice water paths (from Khairoutdinov et al. (2009)).

The evolution of convection in the simulation is illustrated by the time series of the vertical profile of horizontally averaged non precipitating cloud liquid/ice condensate, in Figure 6.2a. Figure 6.2b presents the horizontally averaged vertical profiles of cloud water/ice and water vapor mixing ratios, and relative humidity, averaged over the last 12 hours of the simulation period. The convection activity triggers after a “spin-up” transition period of approximately 6 hours, with a shallow boundary layer appearing during that period. Figure 6.2a shows a shallow cloud layer that gradually deepens until a burst of deep cumulus convection occurs near hour 6. A nearly steady deep cumulus regime is established by hour 12, characterized by a trimodal vertical distribution of clouds with shallow and deep convective cloud maxima accompanied by a cumulus congestus maximum in the mid-troposphere near the freezing level (Khairoutdinov et al., 2009).

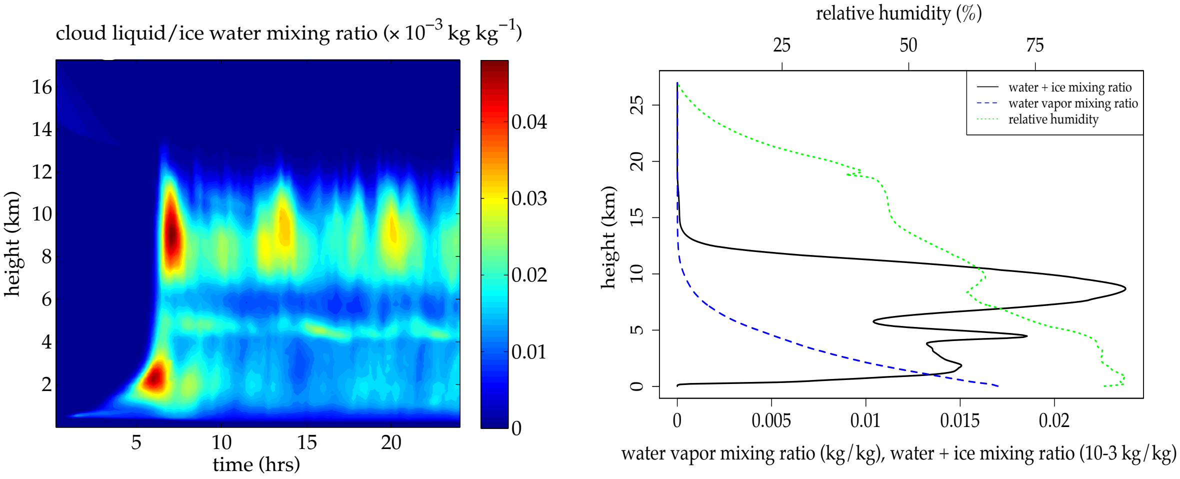

(a) (b)

Figure 6.2: (a) Evolution of horizontally averaged cloud liquid/ice water mixing ratio vertical profile. (b) Comparison of vertical profiles of horizontally averaged cloud water/ice mixing ratio (solid black), water vapor mixing ratio (dashed blue), and relative humidity (dotted green), averaged over the last 12 hours of the Giga-LES simulation run.

Figure 6.3 shows the time evolution of horizontally averaged CAPE, low level CAPE, and midtroposphere dryness $D = (\theta_{eb} - \theta_{em})/T_0$ ($T_0 = 10$ K). The CAPE and low level CAPE were computed from the domain-averaged thermodynamic profiles assuming pseudo-adiabatic ascent with the departure point at 960 mb.

During the "spin-up" transition, the CAPE value increases by about 70%, after which the onset of deep convection occurs and consumes a fraction of that CAPE. By hour 8, the simulation reaches a near equilibrium deep convection regime with an approximately steady CAPE value of 2000-2100 J/kg. The midtroposphere dryness also reaches a maximum towards the 6 hour mark, indicating a moistening of the boundary layer which sets preconditioning conditions for deep convection; It then gradually drops as the midtroposphere moisture content increases due to deep convection. The CAPE in the lower troposphere reaches a maximum of about 625 J/kg

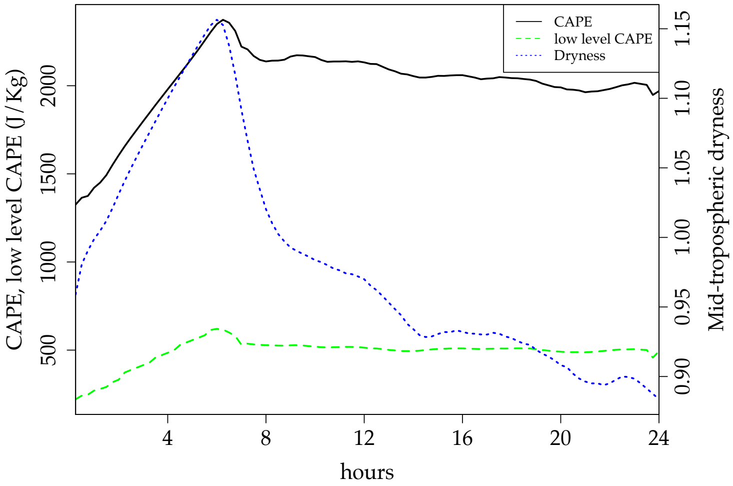

Figure 6.3: Time evolution of CAPE (J/kg), low level CAPE (J/kg), and midtroposphere dryness $D = (\theta_{eb} - \theta_{em})/T_0$, $T_0 = 10$ K, calculated from the horizontally averaged fields of the Giga-LES dataset. The midtroposphere dryness D measures the discrepancy between the boundary layer and midtroposphere equivalent potential temperatures, fixed at pressure levels 1000 mb and 500 mb, respectively.

at the onset of convection which consumes about 16% of that amount to stabilize at around 500 J/kg, indicating a sustained low level convection activity throughout the last 18 hours of simulation.

6.2 Domain Partitioning and Sequential Learning

The Giga-LES is a 24-hour long simulation, with a time resolution of 15 minutes. Excluding a transient period of approximately 4 to 5 hours, the length of the time series is between 76 to 80 data points. To increase information capacity, the full 205×205 km^2 Giga-LES domain is subdivided into N subdomains, and time series of cloud populations and large-scale convection indicators are obtained for each. The parameters are then progressively learned using the sequential learning technique described in Section 5.6.3, which in simple terms consists of a Bayesian updating scheme of the form

$$\pi_{n+1}(\theta) \propto \pi_n(\theta) \times f_{n+1}(\theta), \quad 0 \le n \le N-1,$$

where a prior $\pi_n(\theta)$ gets updated by a likelihood $f_{n+1}(\theta)$ to give a posterior $\pi_{n+1}(\theta)$. This gives the following recursive scheme: Starting on subdomain 1 and specifying an initial prior π_0, we run the Bayesian posterior simulator that outputs a posterior π_1, which in turn is used as a prior for subdomain 2, etc. At each step, a multivariate normal distribution is fitted to the posterior using the sample mean and sample covariance matrix. This method was tested in Section 5.6.3 where the inference results based on a synthetic time series of length $5a$ were compared to the sequential analysis obtained by segmenting that time series into five contiguous subsequences of length a.

Figure 6.4 illustrates the two partitions that are used in this study: a 2×2 ($N = 4$) grid and a 4×4 ($N = 16$) grid, which correspond to GCM grid box sizes of 102.4 km and 51.2 km, respectively. Time series for the cloud cover fractions σ_c, σ_d, and σ_s and large-scale convection indicators C, C_l, and D are presented next for the two partitions.

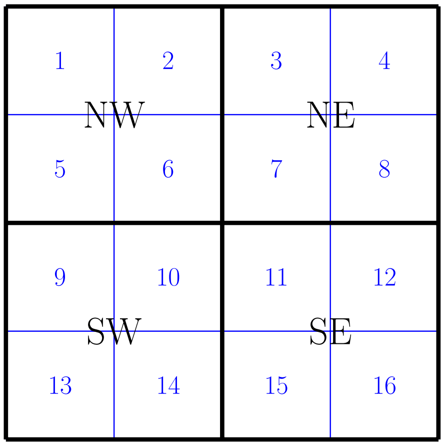

Figure 6.4: Partition of the Giga-LES domain of area 205×205 km^2 into a 2 by 2 (in black) and a 4 by 4 (in blue) grid, with GCM grid box size of 102.4 km and 51.2 km, respectively. The subdomains are referenced as NW, ..., SE and 1, ..., 16 therein.

6.3 Data Preprocessing

We have seen in Section 5.3 that the Bayesian inverse model draws its inference on the convective timescale parameters from two training sets of observations: the large-scale convection indicators

$$C = \frac{\text{CAPE}}{\text{CAPE}_0}, \quad C_l = \frac{\text{CAPE}_l}{\text{CAPE}_0}, \quad \text{and} \quad D = \frac{\theta_{eb} - \theta_{em}}{T_0}, \tag{6.3.1}$$

and the subgrid-scale area fractions σ_c, σ_d, and σ_s of congestus, deep, and stratiform clouds (or equivalently, the unnormalized cloud populations N_c, N_d, and N_s). The amount of convective available potential energy (CAPE) of the environment is determined from simple parcel theory, while the dryness D is obtained directly from the equivalent potential temperature's vertical profile. In Section 6.3.1 we outline the basic steps of the CAPE calculation (see Emanuel (1994) for an in-depth discussion) and present the time series for (6.3.1). Fractional cloud area, on the other hand, is not a well defined quantity and can only be estimated with relative accuracy, even with the most sophisticated techniques available today. Our calculation of the cloud area fractions σ_c, σ_d, and σ_s is based on a diagnosis of water and ice mixing ratios present within single vertical columns to identify clouds of the three types; See Section 6.3.2 for details and derived time series.

6.3.1 CAPE Calculation

Convection, Stability, and Buoyancy

Atmospheric convection is defined as the relatively small–scale, thermally direct circulations which result from the action of gravity upon an unstable vertical distribution of mass (Emanuel, 1994). The atmosphere is a compressible fluid with density $\rho = \rho(p, T)$, that closely obeys the perfect gas law $\rho = p/RT$ (here R is the universal gas constant). By contrast with the incompressible ocean, a blob of air slowly moving adiabatically will adjust almost instantaneously to the environment pressure. Hence an ascending (descending) parcel of dry air will finds itself in an environment of lower (higher) pressure – exerted by the weight of the column of air above it – and will expand doing work on its surrounding and thus cool (warm). So temperature is not a conserved quantity for adiabatic displacement in the atmosphere, and the negative of its rate of change in the vertical is known as the *dry adiabatic lapse rate*

$$\frac{dT}{dz} = -\frac{g}{c_p} = -\Gamma_d. \tag{6.3.2}$$

Given $c_p = 1005$ J kg^{-1} K^{-1} (see Table 2.3), we find $\Gamma_d \approx 10$ K km^{-1}. Let Γ denote the lapse rate of the environment. If Γ is larger than Γ_d, the atmosphere is *unstable*, and dry convection can be triggered to redistribute heat and restore the atmosphere to its neutral state, where Γ is close to Γ_d. Conversely, if Γ is smaller than Γ_d, then the atmosphere is stable to (dry) convection, and thus no convective heat transport takes place.

Convection and stability are directly linked to the concept of *buoyancy*. The buoyancy force per unit of mass is

$$B = g\left(\frac{\rho - \rho_p}{\rho}\right), \tag{6.3.3}$$

where ρ_p is the density of the parcel. If $\rho_p > \rho$, the parcel is negatively buoyant and sinks; if $\rho_p < \rho$ the parcel is positively buoyant and rises. In a stable atmosphere, a parcel of air displaced upwards (downwards) cools down (warms up) much faster than the environment. Since the parcel has virtually the same pressure as that of the environment, its density is higher (lower) and it becomes negatively (positively) buoyant. It will then experience a gravitational restoring force that will bring it back to its reference point, but will overshoot due to inertia, oscillating back and forth with buoyancy frequency (2.1.6). This is mechanism behind the inertio-gravity waves discussed in Chapter 2.

Conditional Instability of Moist Air and The Parcel Method

The presence of water vapor has an important impact on atmospheric stability. Adiabatic lifting of an air parcel leads to expansion and cooling, and if the temperature is cool enough to saturate the parcel (the saturation level), some water vapor condenses to form a cloud. The latent heat release due to condensation warms up the parcel and the "wet" air parcel gains extra buoyancy, which leads to moist convection.

A general method of assessing the stability of the atmosphere is to determine the buoyancy of a parcel displaced from a starting height to its level of neutral buoyancy (Emanuel, 1994). The method is based on the following assumptions; the parcel does not affect the environment and the lifting is adiabatic (and therefore exempt of mixing). We also consider that the parcel originates from the unsaturated layer, and we look at the typical situation where the displacement is stable provided the parcel remains unsaturated, but which ultimately becomes unstable if saturation occurs. These atmospheric conditions are called *conditional instability* (see Smith, 1997). In these conditions, the initially-unsaturated parcel is negatively buoyant (cooler than its environment) for small enough upward displacement. However if sufficient work is done on the parcel, it may rise up to its level of saturation, also called *lifting condensation level* (LCL). It the parcel is lifted further, excess vapor will condense, and the parcel will eventually become warmer than the environment, due to condensational heating. This height is called the *level of free convection* (LFC). The parcel is thus negatively buoyant unless displaced beyond its LFC, where it becomes unstable. The parcel will remain positively buoyant until it reaches its *level of neutral buoyancy* (LNB), where the parcel and the environmental temperatures are equal again. From this we can calculate an estimate of *convectively available potential energy* (CAPE), the maximum energy available to a parcel due to latent heat release during its convective ascent.

Concretely, the CAPE calculation consists of the following steps:

1. *Lifting Condensation Level.*

Given the pressure p_0, temperature T_0, and mixing ratio r_0 of a parcel taken at an initial height z_0, we find the *saturation temperature*, T^*, *saturation pressure* p^*, and the height z^* (or z_{LCL}) of the LCL. For this we need to define some related variables: The parcel's *mixing ratio* r and *vapor pressure* e, which are related to each other via

$$r = \epsilon \frac{e}{p - e}.$$

Here ϵ is the ratio of R_d to R_v, the gas constant for dry air and water vapor, respectively (see Table 6.2). The saturation pressure is found by finding the pressure $p = p^*$ at which the parcel's mixing ratio equals the saturation mixing ratio, that is, $r = r^*(p^*)$. During the adiabatic lifting of the unsaturated parcel from its initial level z_0, both the mixing ratio and potential temperature remain constant, but the saturation mixing ratio r^* (the air's capacity for water vapor) decreases until it becomes equal to r_0 at the LCL. Thus we need to find p^* along the *dry adiabat* such that

$$r_0 = r^*(p^*).$$

The saturation vapor pressure e^* is determined using an integration form of *Clausius-Clapeyron equation* (see Emanuel, 1994):

$$e^* = 6.017 \exp\left[\frac{L_v - (c_{pv} - c_l)T_0}{R_v}\left(\frac{1}{T_0} - \frac{1}{T}\right) + \frac{c_{pv} - c_l}{R_v}\ln\frac{T}{T_0}\right],$$

where c_l is the heat capacity of liquid water, c_{pv} is the heat capacity at constant pressure of water vapor, L_v is the latent heat of vaporization at $T_0 = 273.15$ K (see Table 2.3) and e^* is in millibars. Along the *dry adiabat*, the potential temperature

$$\theta = T\left(\frac{p_0}{p}\right)^{R_d/c_{pd}} \tag{6.3.4}$$

is conserved, and the parcel's temperature T is found by inverting that profile using the parcel's initial θ_0. The constant c_{pd} in (6.3.4) is the heat capacity at constant pressure for dry air (See Table 6.2). The LCL obtained from the Giga-LES domain averaged vertical thermodynamic profiles is reported in Table 6.1.

2. *Saturated Adiabatic Process.* When the parcel is lifted beyond the LCL it becomes saturated and excess water vapor will condense, releasing latent heat and partly compensating the cooling at the dry adiabatic rate due to expansion. Hence

its *moist* (or *saturated*) *adiabatic lapse rate* $\Gamma_m < \Gamma_d$ (a moist parcel cools less rapidly than a dry one). The condensed water vapor content r_l is approximately equal to $r_0 - r^*$. Above the LCL, a parcel undergoing convection is expected to follow the *moist adiabat* (or *pseudoadiabat*), along which the *equivalent potential temperature*

$$\theta_e = T\left(\frac{p_0}{p}\right)^{R_d/(c_{pd}+c_l r_0)} \exp\left[\frac{L_v r^*}{(c_{pd}+c_l r_0)T}\right] \tag{6.3.5}$$

is conserved. Thus, given $\theta_e(z_{LCL})$, (6.3.5) can be inverted for the parcel's temperature T along the moist adiabat.

3. *Available Energy for Convection and Convective Inhibition.* As mentioned earlier, the parcel is negatively buoyant below the LFC, after which the parcel becomes warmer than its environment and can rise freely under its own buoyancy until it reaches the LNB. Above this level the parcel becomes negatively buoyant again and decelerate. The positive buoyancy force between the LFC and the LNB is proportional to the area between the parcel curve and the sounding between these two levels, as shown in Figure 6.5. CAPE is calculated from the buoyancy as:

$$\text{CAPE} = g\int_{z_{LFC}}^{z_{LNB}} \frac{T_{vp} - T_{ve}}{T_{ve}} dz,$$

where

$$T_v = T\frac{1 + r/\epsilon}{1 + r} \tag{6.3.6}$$

is the *virtual temperature* and the subscripts p and e refer to "parcel" and "environment", respectively. CAPE is an integral of the buoyancy force (6.3.3) using the definition of the virtual temperature. CAPE$_l$ integrates the buoyancy in the lower part of the atmosphere only.

In general, work must be done on a parcel to lift it to its LFC. This amount of work is proportional to the area between the parcel curve and the environment sounding and called *convective inhibition*, or CIN:

$$\text{CIN} = -g \int_{z_{LCL}}^{z_{LFC}} \frac{T_{vp} - T_{ve}}{T_{ve}} dz.$$

The LFC and LNB obtained from the Giga-LES domain averaged vertical thermodynamic profiles are reported in Table 6.1.

Level	Approximate height
LCL	355 m
LFC	455 m
FL	4.4 km
LNB	14 km

Table 6.1: Approximate LCL, LFC, and LNB obtained from domain averaged thermodynamic fields (time averaged). FL is the *freezing level*, defined as the 273 K height.

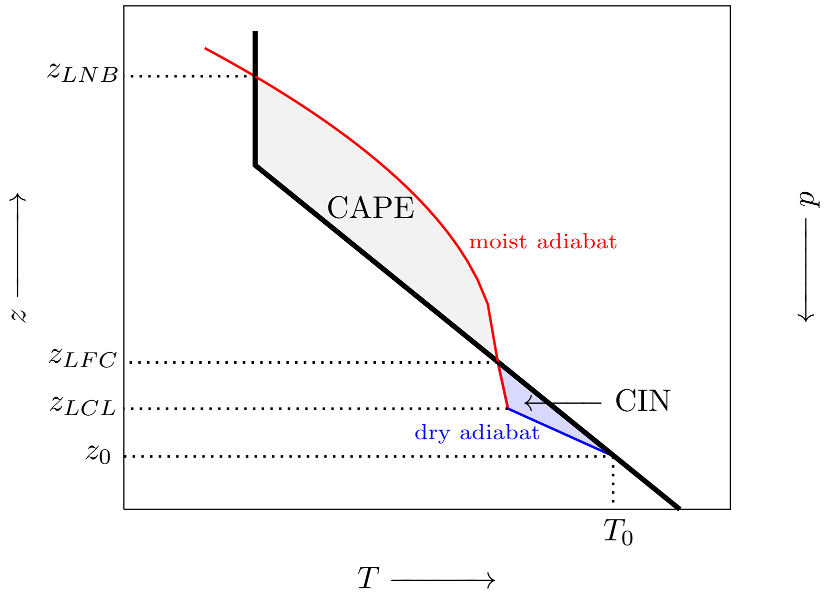

Figure 6.5: The temperature of an initially-unsaturated moist air parcel lifted in convection from a level z_0 at temperature T_0. The black solid curve is the environmental temperature. Before the LCL, the parcel remains unsaturated and follows the dry adiabat (blue curve) cooling at a constant dry adiabatic lapse rate $\Gamma_d \approx 10$ K/km. When lifted beyond the LCL, excess water vapor condenses releasing latent heat which offsets the cooling due to adiabatic expansion. The parcel then follows the moist adiabat (red curve) and cools at a moist adiabatic lapse rate that now varies with height: $\Gamma_m(T,p) < \Gamma_d$. The blue and grey shaded areas represent the regions of negative and positive buoyancy, respectively, used in the calculation of CAPE and CIN. The LFC and LNB are determined from the sign of the parcel's buoyancy.

Variable or Constant	Value	Name
R_d	287.04 J kg^{-1} K^{-1}	Gas constant of dry air
R_v	461.50 J kg^{-1} K^{-1}	Gas constant of water vapor
ϵ	0.6220	R_d/R_v
r	$\epsilon\frac{e}{p-e}$	mixing ratio (mass of water vapor per unit mass of dry air)
c_l	4190 J kg^{-1} K^{-1}	Heat capacity of liquid water
c_{pv}	1870 J kg^{-1} K^{-1}	Heat capacity at constant pressure of water vapor
c_{pd}	1006 J kg^{-1} K^{-1}	Heat capacity at constant pressure for dry air

Table 6.2: CAPE related variables and constants

Time Series

The time series of the large-scale convection indicators C, C_l, and D, defined in (2.4.19), are shown in Figure 6.6 using the two reference values $\text{CAPE}_0 = 1500$ J/kg, and $T_0 = 10$ K for both the 2 by 2 and 4 by 4 grids. The quantity D is a measure of dryness: positive when the midtroposphere is dry compared to the boundary layer, and negative when the boundary layer moisture content is smaller than that of the midtroposphere. The time series of the gridded domains are qualitatively similar to those of the full domain shown in Figure 6.3: a buildup of convective energy combined to a moistening of the boundary layer takes place until an explosive transition to deep cumulus convection occurs near hour 6, which depletes the atmosphere of CAPE and

6.3.2 Fractional Cloud Area Calculation

The cloud fractions associated with congestus, deep and stratiform clouds are derived from the prognostic cloud water/ice mixing ratio q_n. At every grid point (i, j) of the 2048×2048 horizontal gridded domain, we consider the vertical profile of q_n and binarize it using a zero threshold to obtain a 256 level binary vector $\boldsymbol{Q}_{ij}$. Each binary vertical profile is then compared to four cloud/no cloud reference profiles: congestus $\boldsymbol{\mathcal{P}_c}$, deep $\boldsymbol{\mathcal{P}_d}$, stratiform $\boldsymbol{\mathcal{P}_s}$, and clear sky $\boldsymbol{\mathcal{P}_{cs}}$. These profiles are constructed using the lifted convection level (LCL) as an estimate for congestus and deep cloud base, the freezing level (FL) as an estimated congestus cloud top and stratiform cloud base, and the level of neutral buoyancy (LNB) as an estimated deep and stratiform cloud tops, as shown in Figure 6.7.

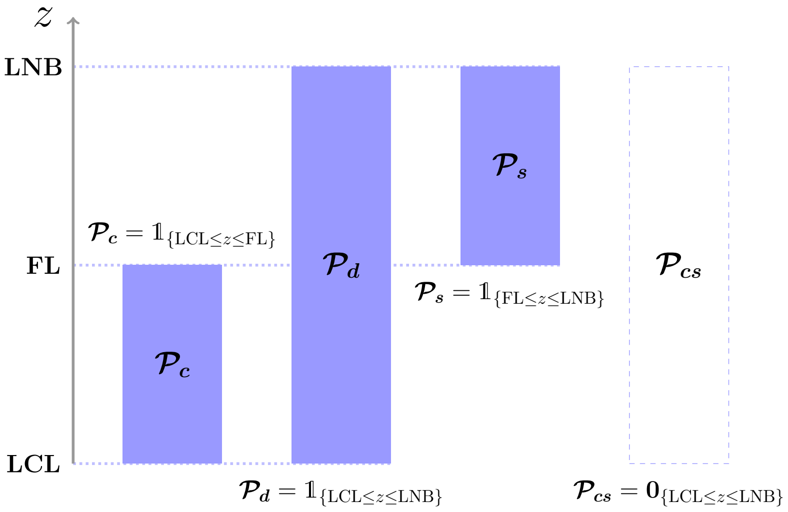

Figure 6.7: Reference profiles $\boldsymbol{\mathcal{P}_c}$, $\boldsymbol{\mathcal{P}_d}$, $\boldsymbol{\mathcal{P}_s}$, and $\boldsymbol{\mathcal{P}_{cs}}$ of congestus, deep and stratiform clouds, and clear sky. The LCL, FL, and LNB approximate heights are given in Table 6.1.

The approximate height for these reference levels are reported in Table 6.1. The reference profiles are set as

$$\boldsymbol{\mathcal{P}_c} = \mathbb{1}_{\{\mathrm{LCL} \le z \le \mathrm{FL}\}}, \quad \boldsymbol{\mathcal{P}_d} = \mathbb{1}_{\{\mathrm{LCL} \le z \le \mathrm{LNB}\}}, \quad \boldsymbol{\mathcal{P}_s} = \mathbb{1}_{\{\mathrm{FL} \le z \le \mathrm{LNB}\}}, \quad \boldsymbol{\mathcal{P}_{cs}} = \mathbf{0},$$

where z is the height, $\mathbb{1}$ is an indicator vector function, and $\mathbf{0}$ the vector of zeros. A cloud type is assigned to the LES column data $\boldsymbol{Q}_{ij}$ by minimizing some misfit measure between $\boldsymbol{Q}_{ij}$ and the set of reference profiles $\mathcal{P} = \{\boldsymbol{\mathcal{P}_c}, \boldsymbol{\mathcal{P}_d}, \boldsymbol{\mathcal{P}_s}, \boldsymbol{\mathcal{P}_{cs}}\}$. Here we minimize the 2-norm of the residual vector

$$\|\boldsymbol{Q}_{ij} - \boldsymbol{P}\|_2 = \sqrt{\sum_{k=1}^{256} \left(Q_{ij}^k - P^k\right)^2},$$

where k is the vertical level, and $\boldsymbol{P} \in \mathcal{P}$. The result is a projected two-dimensional cloud lattice whose cloud area fraction time series are shown in Figure 6.8 for both the 2 by 2 and 4 by 4 grids. The time series show an interesting pattern of intermittent cloud bursts, with frequent signatures of congestus events preceding deep and stratiform events. Larger stratiform area fractions indicate strong upper level cloud condensate.

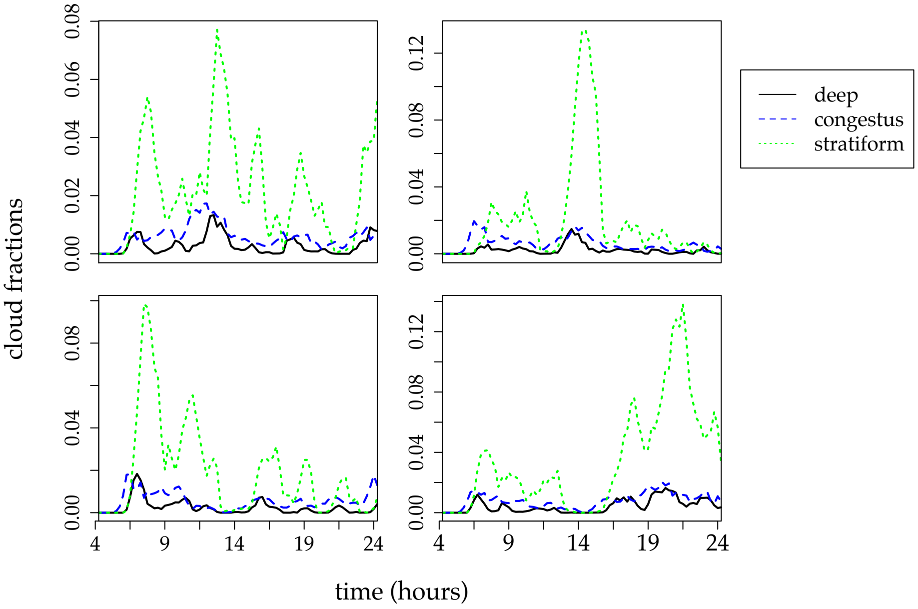

(a) 2 by 2 grid.

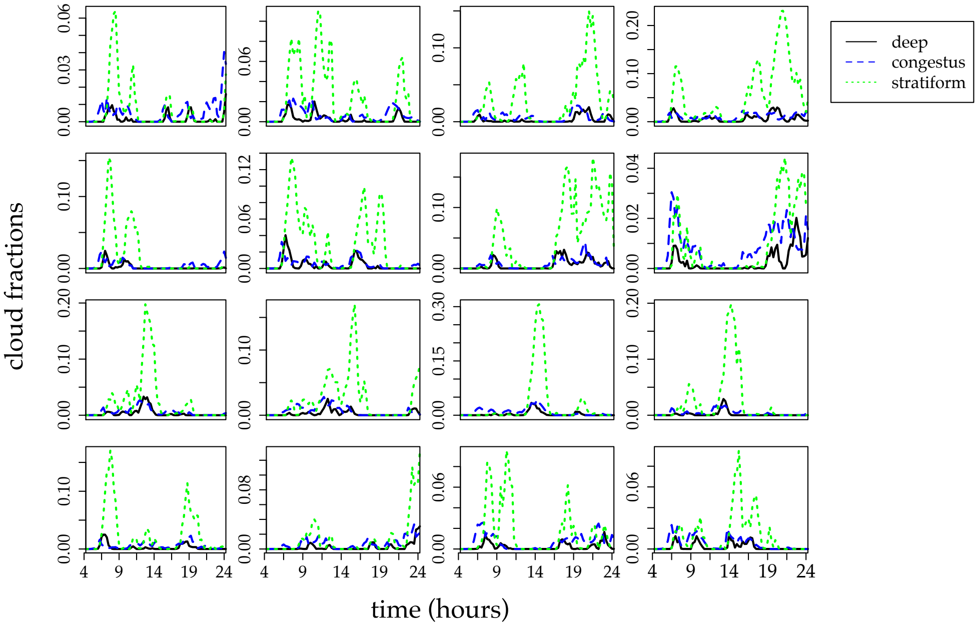

(b) 4 by 4 grid.

Figure 6.8: Time series of cloud area fractions for the (a) 2 by 2 grid and (b) 4 by 4 grid.

6.4 Results and Sensitivity Studies

The sequential learning strategy was applied to both the 2 by 2 and 4 by 4 grids of Figure 6.4 using an initial weakly informative multivariate normal prior, with the mean given by the P2013 parameter regime (see Table 6.3), and variance 50. Figures 6.9 and 6.10 show the marginal posteriors for all seven parameters for the 2 by 2 and 4 by 4 grids, respectively, using the large-scale convective indicator and cloud area fraction time series given in Figures 6.6 and 6.8.

Each posterior exploration was conducted using en ensemble of well-dispersed MCMC chains in parallel, each with a sample size of approximately 100 000. Burn in periods were removed and proposal variances were calibrated to obtain an optimal acceptance rate of 25%. Visual diagnostics were used to monitor within-chain and in between-chain mixing, and ensure that the chains have reached equilibrium. All parallel simulations were performed on the Nestor Westgrid cluster using 72 cores.

For both partition cases, the posterior densities gradually concentrate about a mean value with a progressive reduction of the variance, and appear to have reached a limiting density. The influence of the prior is negligible: The posterior is strongly dominated by the data likelihood function right after the first learning sequence.

The results for the two partitions are juxtaposed in the box plot of Figure 6.11 depicting the first, second, and third quartiles for both sets of posterior marginals. For most parameters, there are large discrepancies in the values for these two cases. The parameters are classified as “slow” and “fast” transitions, depending whether their inferred value is less than or greater than 1.5 hours.

Figure 6.12 show a sensitivity study to the other two model parameters or reference values, CAPE_0 and T_0. In is interesting to note that varying either reference values does not have a striking effect on the convective timescale inferred values. However for some parameters the discrepancy is large, notably in the case of varying CAPE_0

for the parameters τ_{01} and τ_{02}, for which there is a gap of more than 10 hours in the two sets of estimated median values. The Bayesian model does not appear to be invariant to the two reference values CAPE_0 and T_0 based on these results.

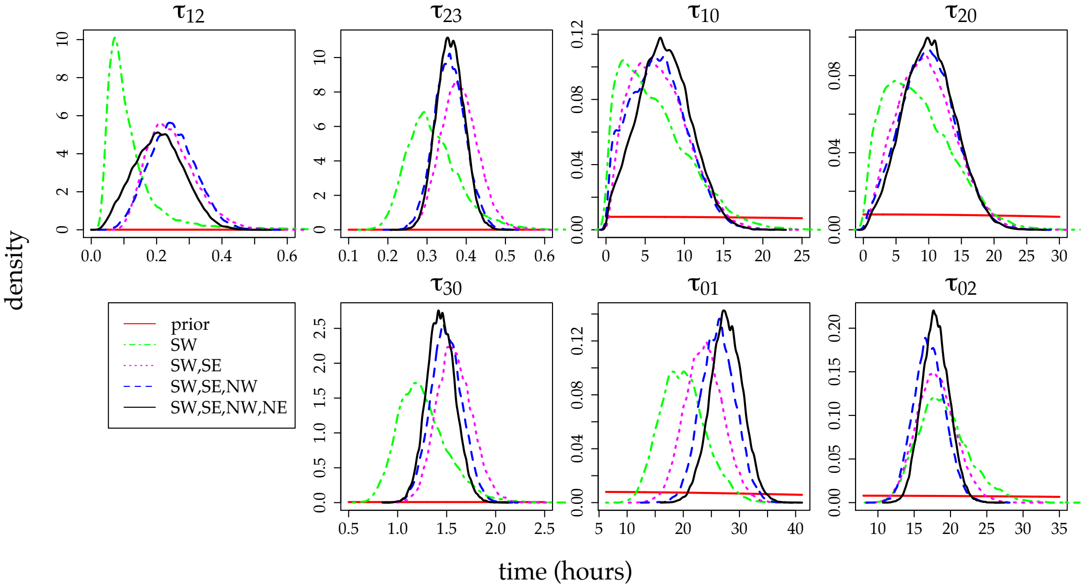

Figure 6.9: Marginal posterior densities of the seven convective timescale parameters for the 2 by 2 grid, using an initial multivariate normal prior (in red) with mean given by the P2013 values of Table 6.3 and variance 50. The parameters are sequentially learned from the SW, SE, NW, and NE subdomains, with the final inference given by the black curve.

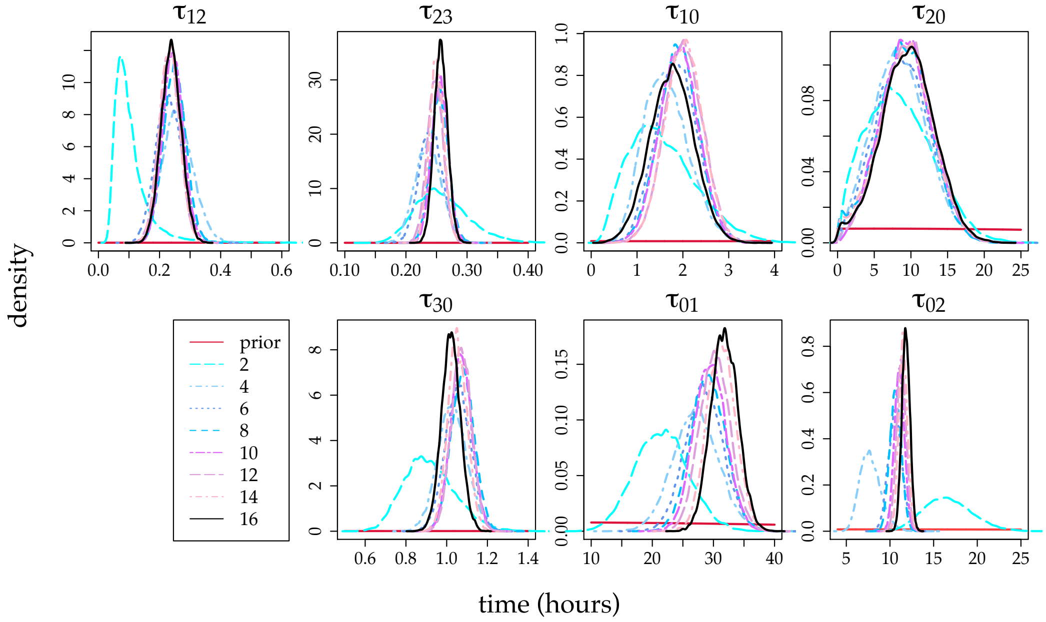

Figure 6.10: Marginal posterior densities of the seven convective timescale parameters for the 4 by 4 grid, using an initial multivariate normal prior (in red) with mean given by the P2013 values of Table 6.3 and variance 50. The parameters are sequentially learned from the subdomains 1 through 16, with the final inference given by the black curve. Only even subdomains are represented for clarity.

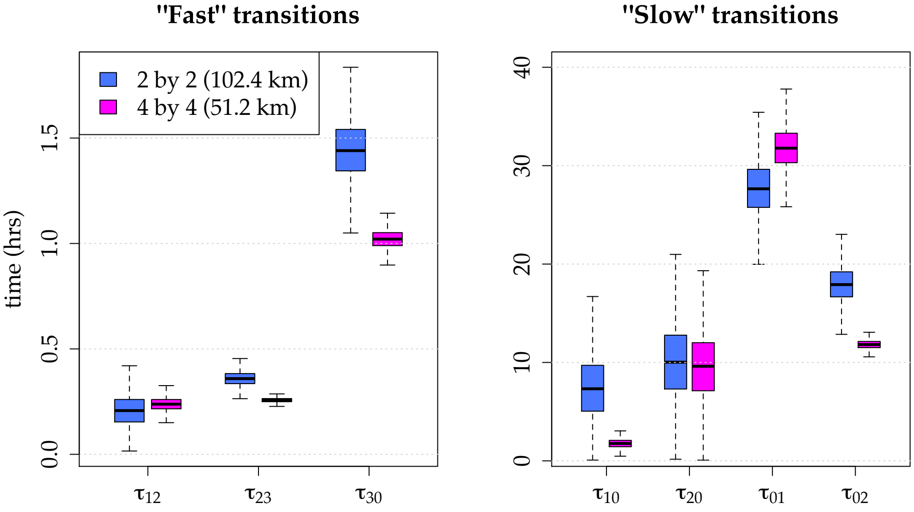

Figure 6.11: Boxplot of the marginal posteriors shown in Figure 6.9 and 6.10 for the 2 by 2 and 4 by 4 grids, respectively. The bottom and top of the boxes represent the first and third quartiles, and the band inside the box is the second quartile.

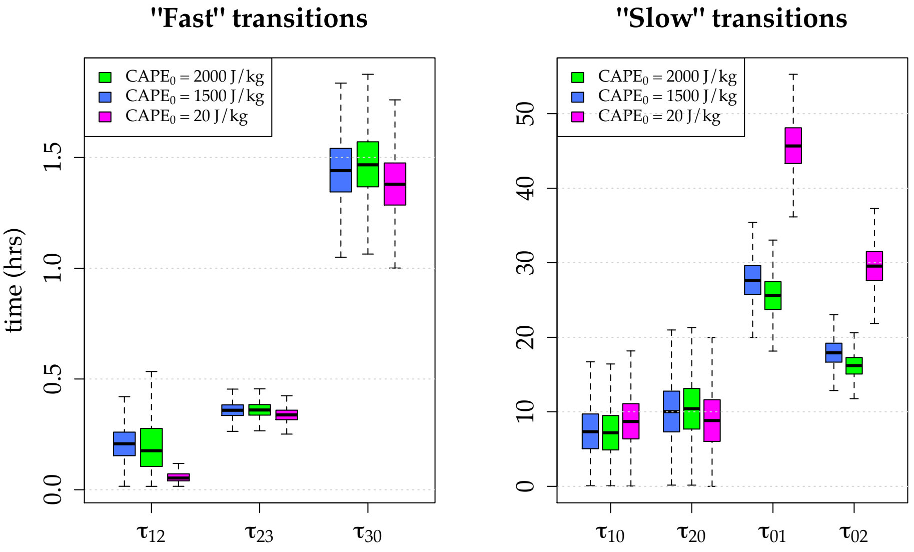

(a) $T_0 = 10$ K, varying CAPE$_0$.

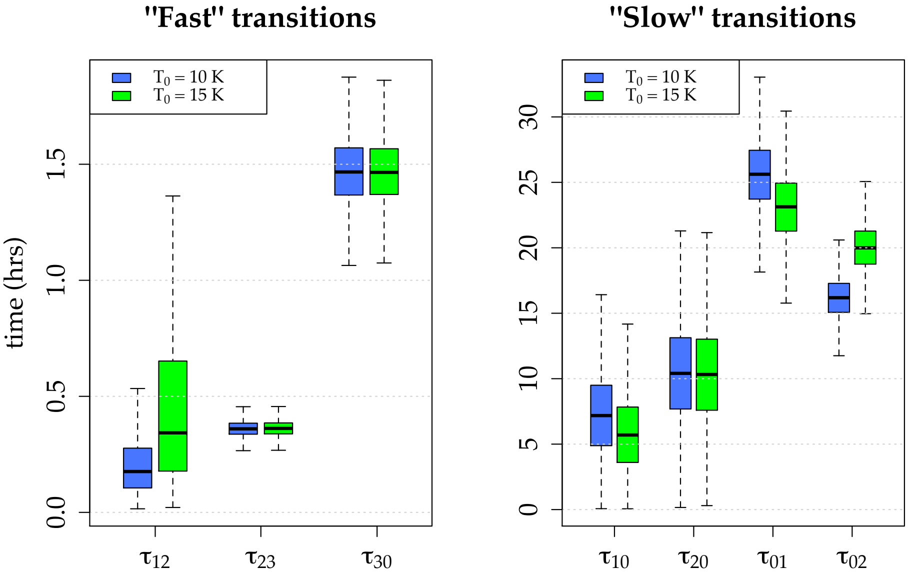

(b) CAPE$_0$ = 2000 J kg^{-1}, varying T_0.

Figure 6.12: Sensitivity studies to the reference values CAPE$_0$ and T_0.

6.5 Discussion

Here we applied the rigorous Bayesian method developed in Chapter 5 to infer the multicloud convective timescales from the Giga-LES dataset, a large-eddy simulation of deep tropical convection over a numerical domain comparable to a GCM gridbox. To maximize the potential for information, the domain is partitioned into two nested grids, and a sequential learning strategy is used on each grid.

The multicloud convective timescales are learned from large-scale convection indicator and subgrid-scale cloud area fractions data sequentially, one grid subdomain at a time. Despite a basic one-column scheme for determining fractional cloudiness from cloud condensate alone, convergence of the posterior marginals towards a limiting density is observed. All posterior densities are strongly data driven, seemingly unaffected by the priors. The estimated mean value for the 4 by 4 grid case are reported in Table 6.3, contrasted with those used in KBM10, FMK12, and P2013.

The sets of timescales obtained for the two partitions are somewhat in agreement, but large discrepancies in some parameters suggest that the subdomains of the two nested grids are not statistically self-similar. Moreover, sensitivity studies to the other multicloud model parameters CAPE_0 and T_0 indicate that the Bayesian parameter estimation model is not invariant under these parameters.

	G-LES	KBM10	FMK12	P2013
Parameter	Transition time (hrs)			
τ_{01} (Formation of congestus)	31.789	1, 3	1	1
τ_{10} (Decay of congestus)	1.761	5, 2	1	1
τ_{12} (Conversion of congestus to deep)	0.238	1, 2	1	3
τ_{02} (Formation of deep)	11.821	2, 5	3	4
τ_{23} (Conversion of deep to stratiform)	0.257	3, 0.5	3	0.13
τ_{20} (Decay of deep)	9.552	5, 5	3	5
τ_{30} (Decay of stratiform)	1.021	5, 24	5	5

Table 6.3: Cloud timescale parameter values used in Khouider et al. (2010) (KBM10, 2 cases), Frenkel et al. (2012) (FMK12), and Peters et al. (2013) (P2013; from Darwin dataset using scaled CAPE). The values obtained for the 4 by 4 partition in the study of this chapter are reported as "G-LES".

Chapter 7

Conclusions

This thesis is a study pertaining to the cumulus parameterization problem in general circulation models (GCMs), an area of intense research since its inception in the early 1960s. It focuses on the multicloud model of Khouider et al. (2010), a stochastic parameterization designed to represent the missing variability in GCMs due to unresolved features of organized tropical convection. The underlying assumption of the multicloud model is that tropical convective systems are self-similar in that they are composed a three cloud-type building block: low level congestus, deep convective, and stratiform clouds.

The multicloud parameterization is analyzed from two distinct angles: 1) from the perspective of statistical information theory, by combining observational data with the model to estimate key model parameters, and 2) from the perspective of predictive multiscale modelling, by coupling the multicloud model to an idealized GCM to study the simulated Hadley–monsoon meridional circulation.

Rigorous Parameter Estimation for the Stochastic Multicloud Model

In this study we developed a rigorous statistical method to infer parameters of the stochastic multicloud model (SMCM) from simulated or in-situ data. These parameters are the convective timescales, which determine the probability transition rates from one cloud type to another in the multicloud framework.

The statistical inference method is based on the Bayesian paradigm which derives a posterior distribution over the model parameters as a consequence of two antecedents: the model likelihood function and a prior distribution. The model likelihood function is essentially expressed as the product of large matrix exponentials, which are numerically approximated using the `PETSc` library of high-performance linear algebra routines for parallel distributed computing. The Bayesian procedure, which includes a Markov Chain Monte Carlo sampler for high dimensional posterior distributions, was successfully validated using a synthetic experiment.

The ultimate goal of this study is the application of the Bayesian procedure to the Giga-LES dataset of Khairoutdinov et al. (2009), a 24-hour large-eddy simulation of deep tropical convection over a physical domain comparable to that of a typical horizontal grid cell in a GCM. The simulation is driven by large-scale thermodynamic tendencies derived from mean conditions during the GATE Phase III field experiment, and captures the dynamics of tropical deep convection on scales ranging from large turbulent eddies to mesoscale convective systems.

The Bayesian inference procedure assimilates time series of (GCM gridbox) cloud area fractions and mean large-scale convective indicators to infer values for the cloud transition timescales. Information is maximized by partitioning the LES domain as a grid and applying the Bayesian procedure on each subdomain, sequentially. This sequential technique, despite the crude design approach (the intermediate priors are approximated by a normal distribution with the predicted posterior means and variances), converges in distribution for all seven parameters inferred. As the parameter values are progressively learned from one subdomain to the next, the marginal posterior densities gradually concentrate on the estimated values and appear to approach a limiting distribution (Figures 6.9 and 6.10).

The new inferred values for the convective timescale parameters can be used in a *calibrated* multicloud model coupled to a GCM for the purpose of predictive modeling, with the potential of producing a more realistic climate and convection features.

Zonally Symmetric Model for Hadley–Monsoon Circulation

In this study we developed a zonally symmetric model coupled to the multicloud parameterization to investigate the meridional Hadley circulation and monsoon dynamics. The zonally averaged model allows to study the Hadley–monsoon mechanisms without the effect of zonally propagating equatorial waves.

The atmospheric model includes a deep convective free troposphere, with a crude vertical truncation of the hydrostatic Boussinesq equations to the barotropic and first two baroclinic modes of vertical structure, and a dynamical boundary layer that sustains shallow convection. The free troposphere is represented by a barotropic–first two baroclinic mode system of nonlinear partial differential equations for the potential temperature and velocity, and a large-scale vertically averaged moisture equation. The multicloud parameterization is coupled to the large-scale equations through heat and precipitation forcing terms associated with the different cloud types of the multicloud framework. The dynamical boundary layer dynamics is represented by a set of equations for the potential and equivalent potential temperatures and velocity. Effects of convective downdrafts from the free troposphere into the boundary layer are included.

The full system is a nonconservative system of partial differential equations, which we solved using state-of-the-art methods for hyperbolic systems, namely the wave propagation of LeVeque (1997) and the non-oscillatory central scheme of Nessyahu and Tadmor (1990), combined using the operator splitting strategy of Strang (1968). A grid convergence error analysis confirmed the system's second-order accuracy.

We presented the results of nonlinear simulations of the meridional circulation using the dynamical core equations coupled with the stochastic multicloud model and its deterministic version. The radiative-convective equilibrium of the system was used as a background state around which large-scale waves can develop and propagate. Two different convective timescale parameter regimes were tested for the stochastic model, one using the calibrated values obtained from the Giga-LES inference study, and the other from a recent multicloud model study (Frenkel et al. 2012; FMK12 regime). The model was forced by a nonhomogeneous sea-surface temperature (SST) assuming a normal profile centered at two northward locations, 10°N and 15°N. A skew normal profile SST centered at 15°N was also tested.

The deterministic model produced a realistic mean local Hadley cell, with an ascending branch of moist air and associated first baroclinic deep heating over the warm pool (WP). Moreover, when the normal WP is located at 15°N, the deterministic simulation produces features reminiscent of the Indian and North-African monsoon trough: Easterlies over the Equator, and westerlies over 20°N, with a low pressure anomaly north of that latitude. The deterministic simulations produces regular mesoscales clouds clusters organized in a wave train like pattern.

The stochastic model using the Giga-LES parameter regime was first tested with a normal WP and $a_0 = 1$ (the contribution of the first baroclinic mode of temperature to deep convective heating anomalies). Although a mean Hadley cell was produced, it was accompanied by weak heating and higher than expected regions of mean (background) convective activity in the mid-latitudes. This was remedied by augmenting the value of a_0 from 1 to 3, which produced the benchmark Simulation 5 with a strong local Hadley cell with rising of moist air and second baroclinic heating over the WP centered 15°N. It also featured easterly-westerly surface winds over the Equator-20°N band, with turning of the winds over the WP. This surface wind pattern is accompanied with a high to low pressure anomaly across that region, which has the characteristic of a monsoon trough. The zonal winds display a baroclinic structure and the potential temperature anomaly from the background stratification shows a hot over cold stable air mass configuration. The $y - t$ contours revealed large mesoscale convective systems organized in a wave train like formation over the WP region, with intermittent localized cloud decks beyond the WP, with correlated heatings, boundary layer equivalent potential temperature and moisture contours. Overall the stochastic simulations was shown to produce more variability in the wave disturbances than the deterministic model.

The benchmark Simulation 5 was compared to 1) a skewed normal WP in Simulation 6 and 2) the FMK12 regime in Simulation 7, both resulting in suboptimal results with an unphysical Hadley cell structure. This is in fact a meaningful test for the Bayesian procedure and the Giga-LES inference study: the G-LES parameter regime produces a realistic meridional circulation unlike the FMK12 regime.

Appendix A

Gallery

A.1 Meridional Structure

A.1.1 Simulation 1: DMCM, NWP[1] at 10°N, $a_0 = 1$

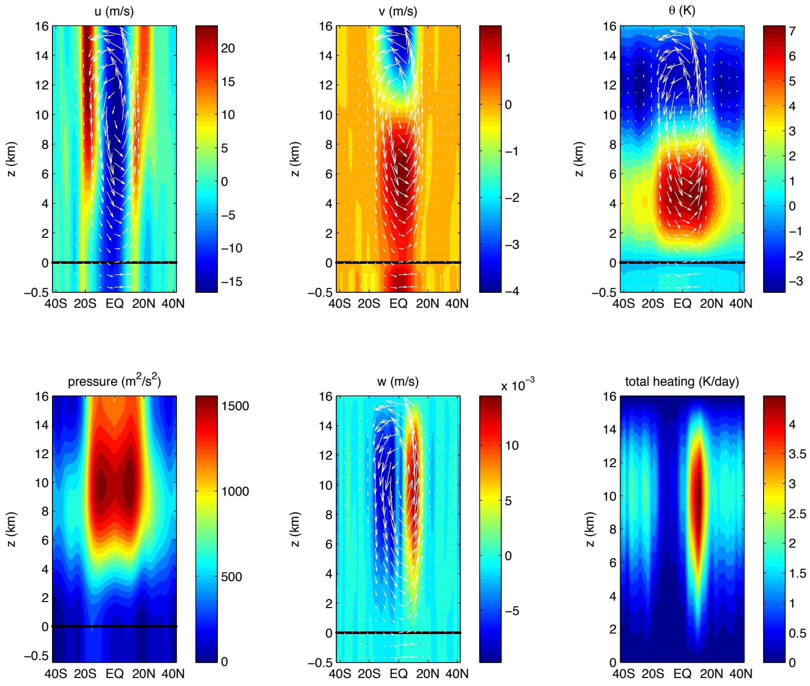

Figure A.1: *Simulation 1.* Mean meridional circulation, averaged over the last 1000 days of simulation. The top of the ABL (solid black line) is located at height 0 km. The contours represent the indicated fields, and the arrows are the velocity vector field (v, w).

---

[1] NWP: normal warm pool profile

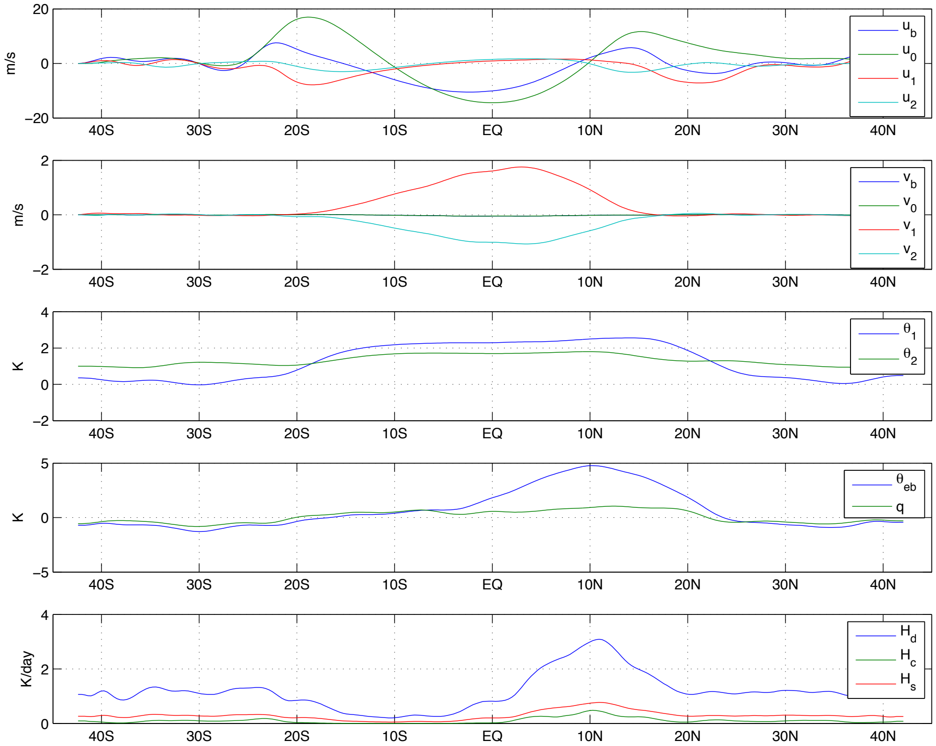

Figure A.2: *Simulation 1.* Mean meridional profiles averaged over the last 1000 days of simulation.

A.1.2 Simulation 2: DMCM, NWP at 15°N, $a_0 = 1$

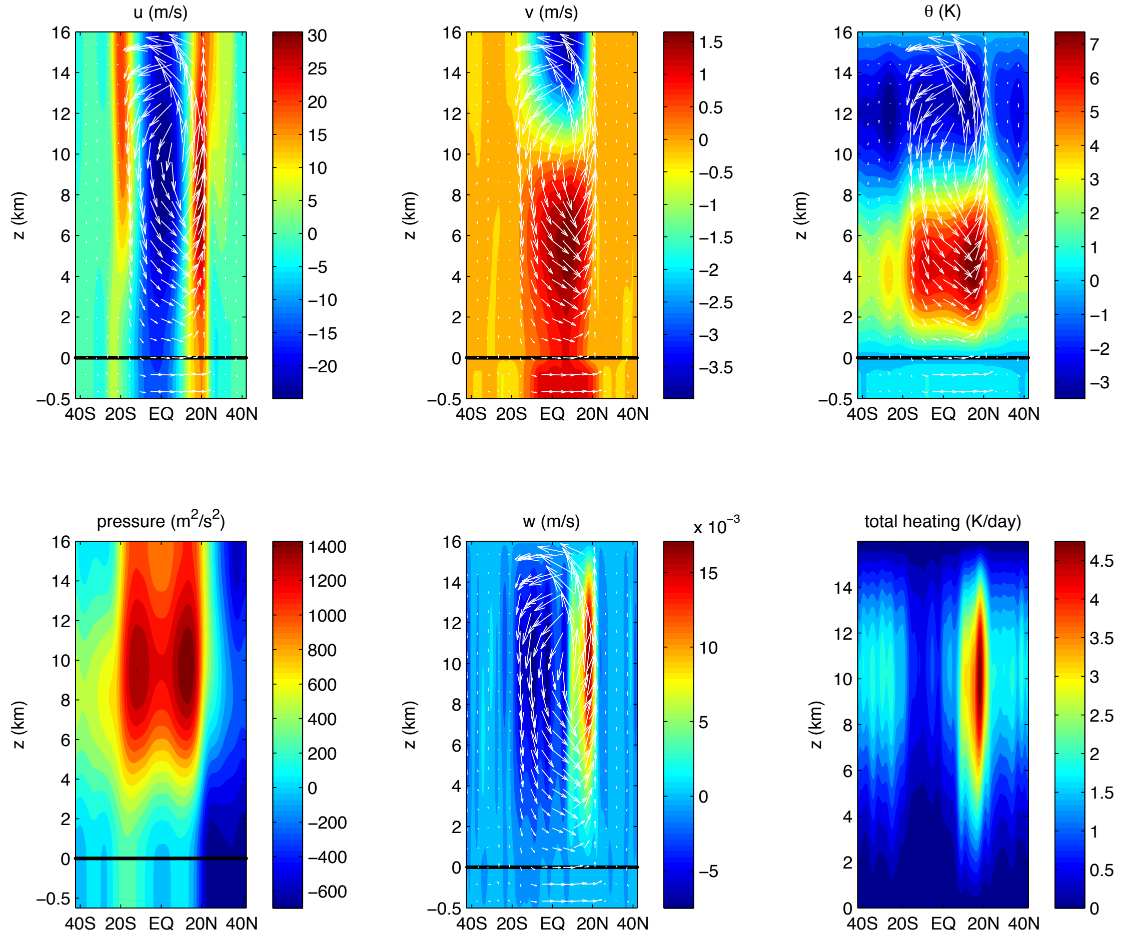

Figure A.3: *Simulation 2.* Mean meridional circulation, averaged over the last 1000 days of simulation. The top of the ABL (solid black line) is located at height 0 km. The contours represent the indicated fields, and the arrows are the velocity vector field (v, w).

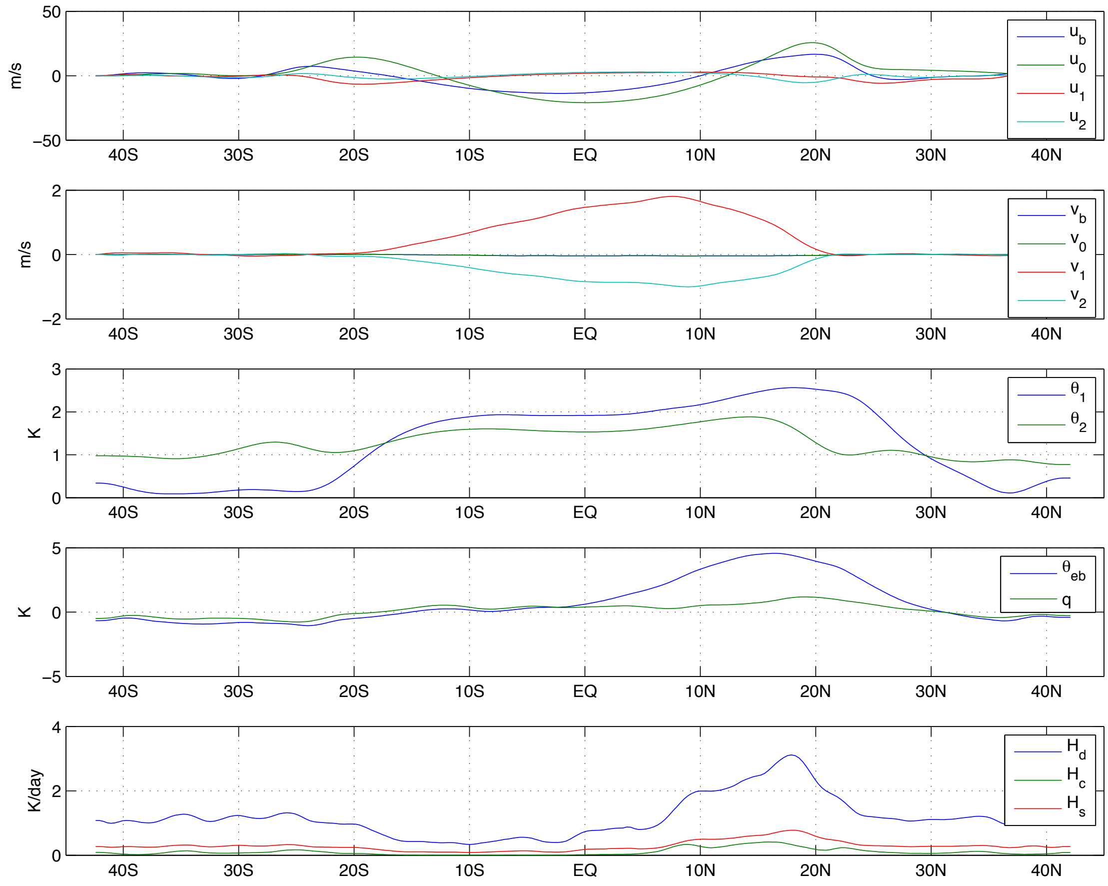

Figure A.4: *Simulation 2.* Mean meridional profiles averaged over the last 1000 days of simulation.

A.1.3 Simulation 3: SMCM, G-LES, NWP at 10°N, $a_0 = 1$

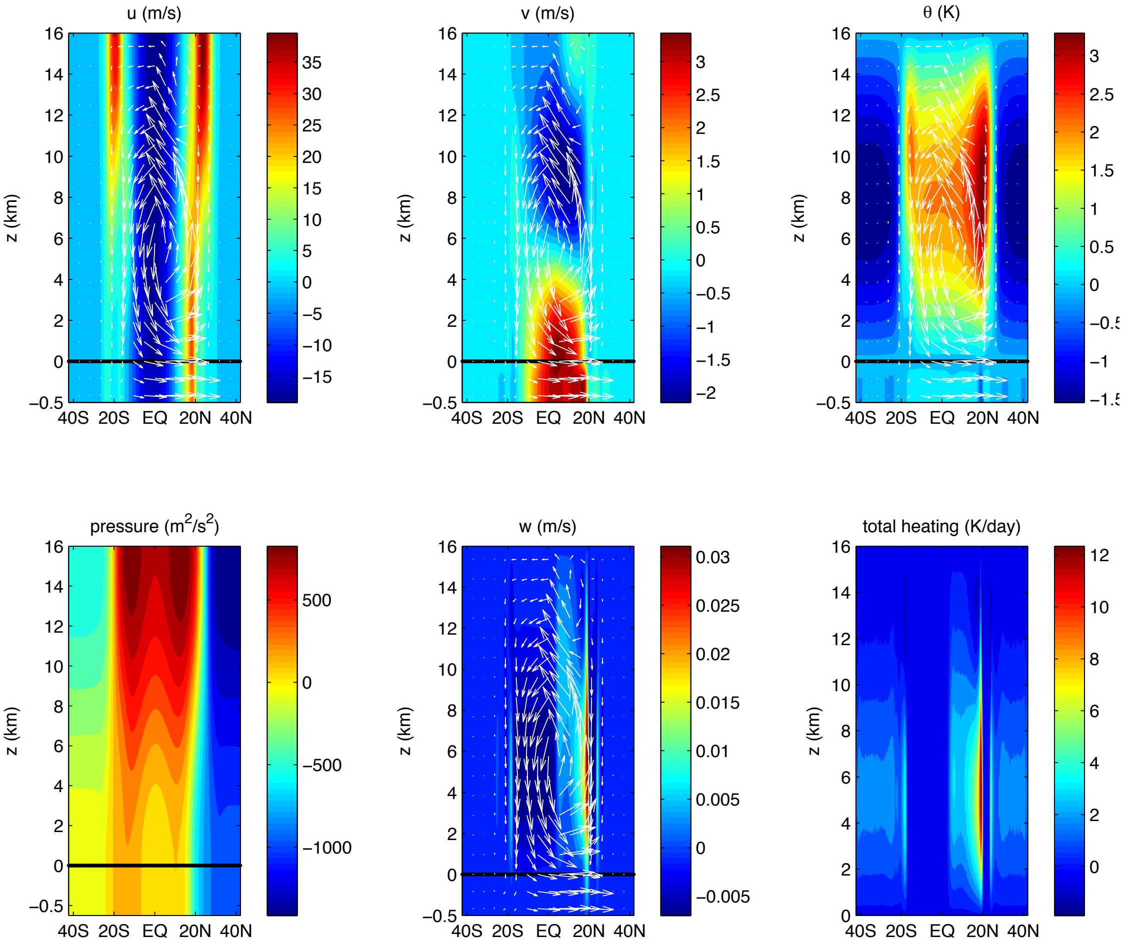

Figure A.5: *Simulation 3.* Mean meridional circulation, averaged over the last 1000 days of simulation. The top of the ABL (solid black line) is located at height 0 km. The contours represent the indicated fields, and the arrows are the velocity vector field (v, w).

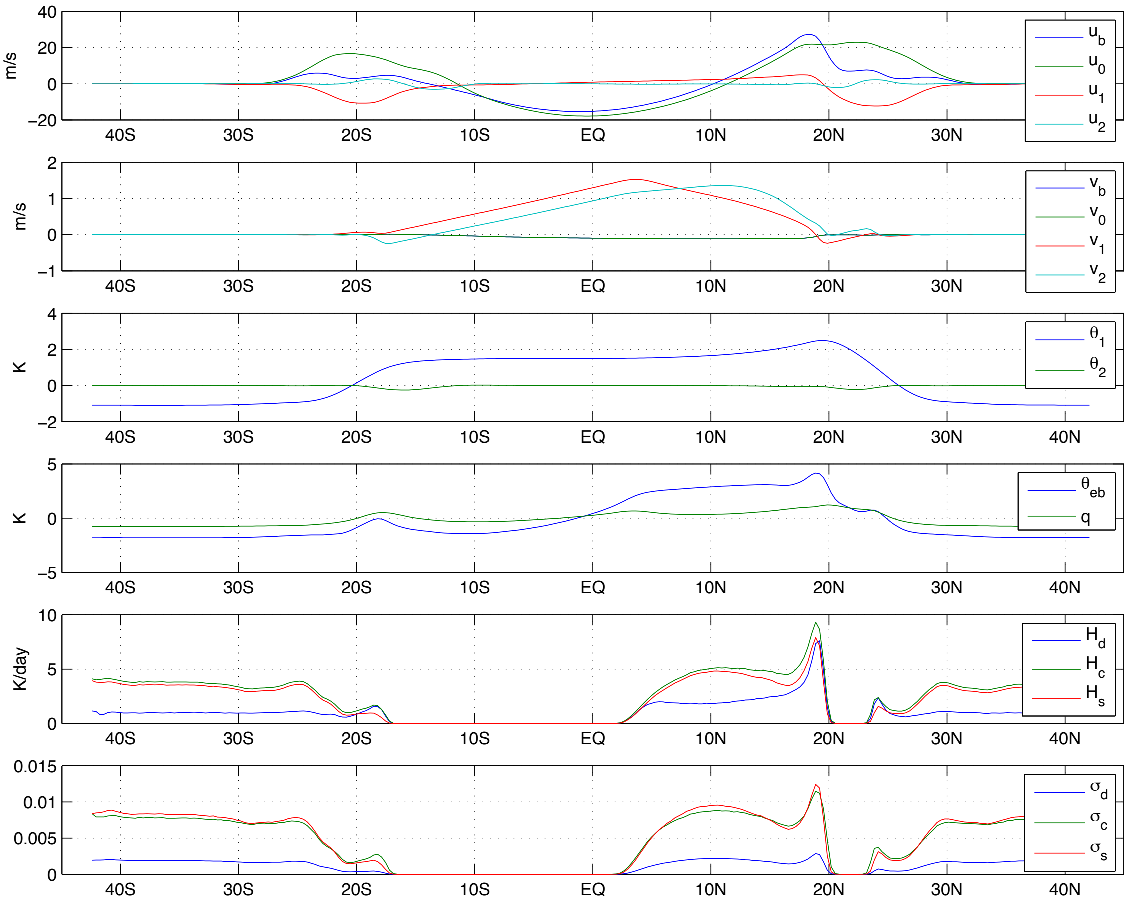

Figure A.6: *Simulation 3.* Mean meridional profiles averaged over the last 1000 days of simulation.

A.1.4 Simulation 4: SMCM, G-LES, NWP at 15°N, $a_0 = 1$

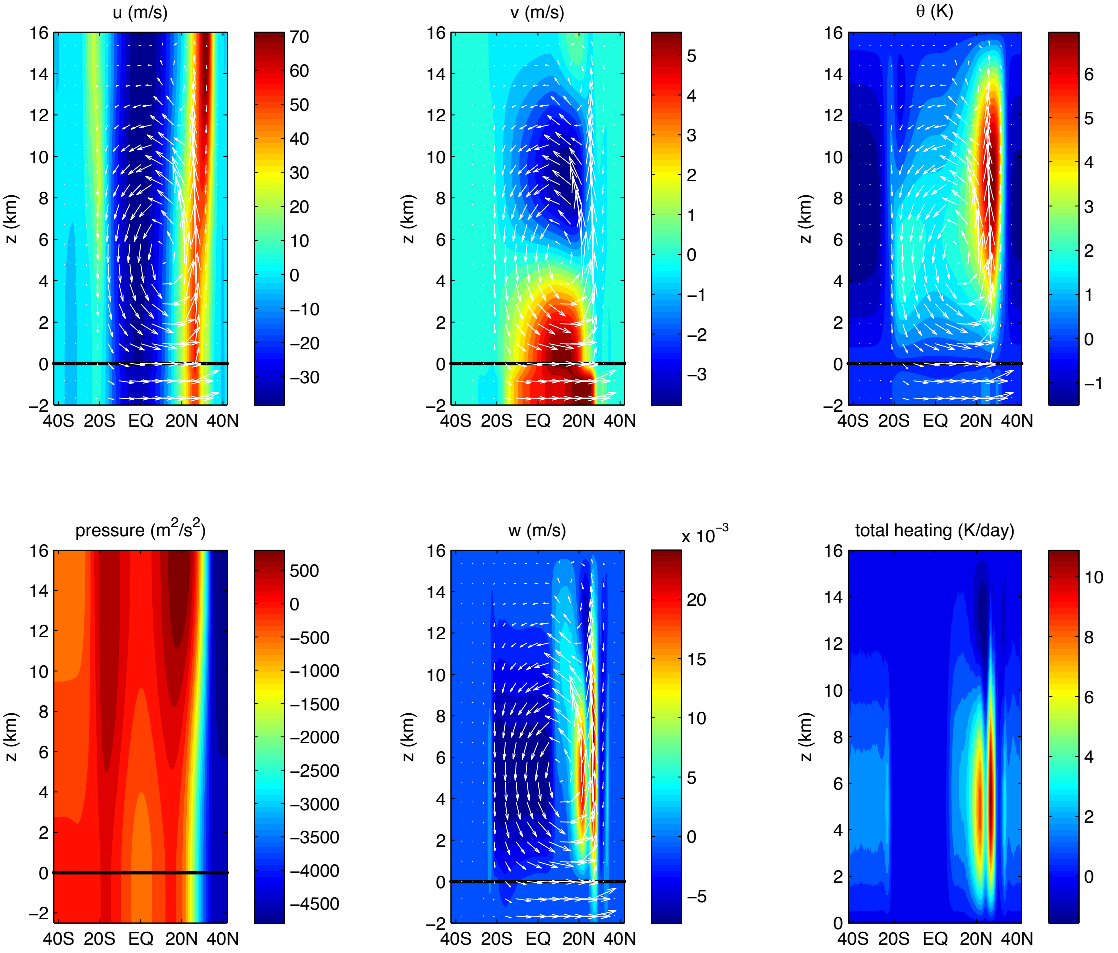

Figure A.7: *Simulation 4.* Mean meridional circulation, averaged over the last 1000 days of simulation. The top of the ABL (solid black line) is located at height 0 km. The contours represent the indicated fields, and the arrows are the velocity vector field (v, w).

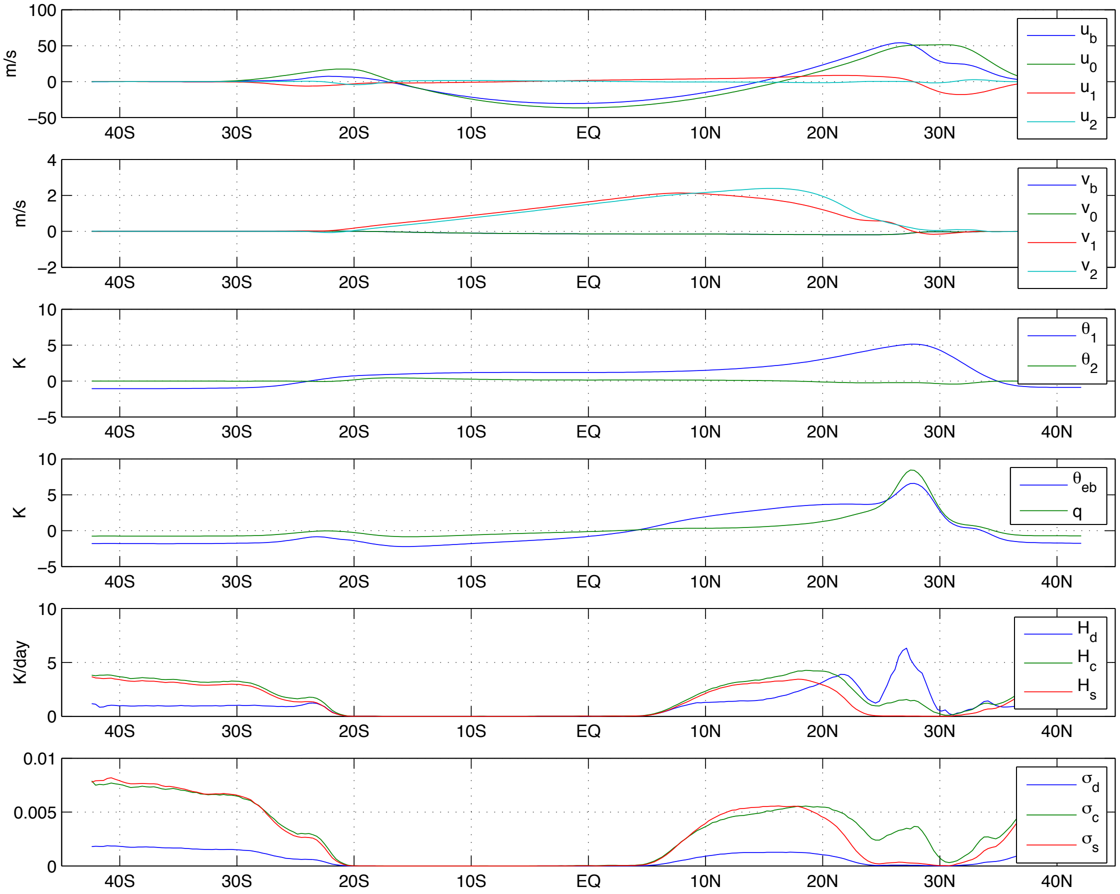

Figure A.8: *Simulation 4.* Mean meridional profiles averaged over the last 1000 days of simulation.

A.1.5 Simulation 5: SMCM, G-LES, NWP at 15°N, $a_0 = 3$

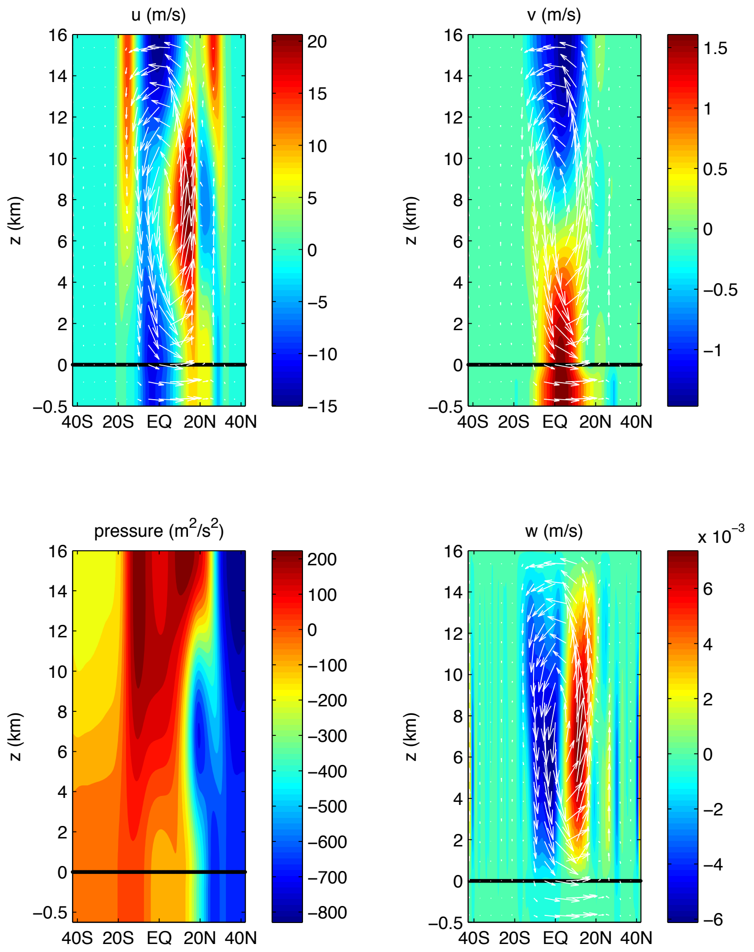

Figure A.9: *Simulation 5.* Mean meridional circulation, averaged over the last 1000 days of simulation. The top of the ABL (solid black line) is located at height 0 km. The contours represent the indicated fields, and the arrows are the velocity vector field (v, w).

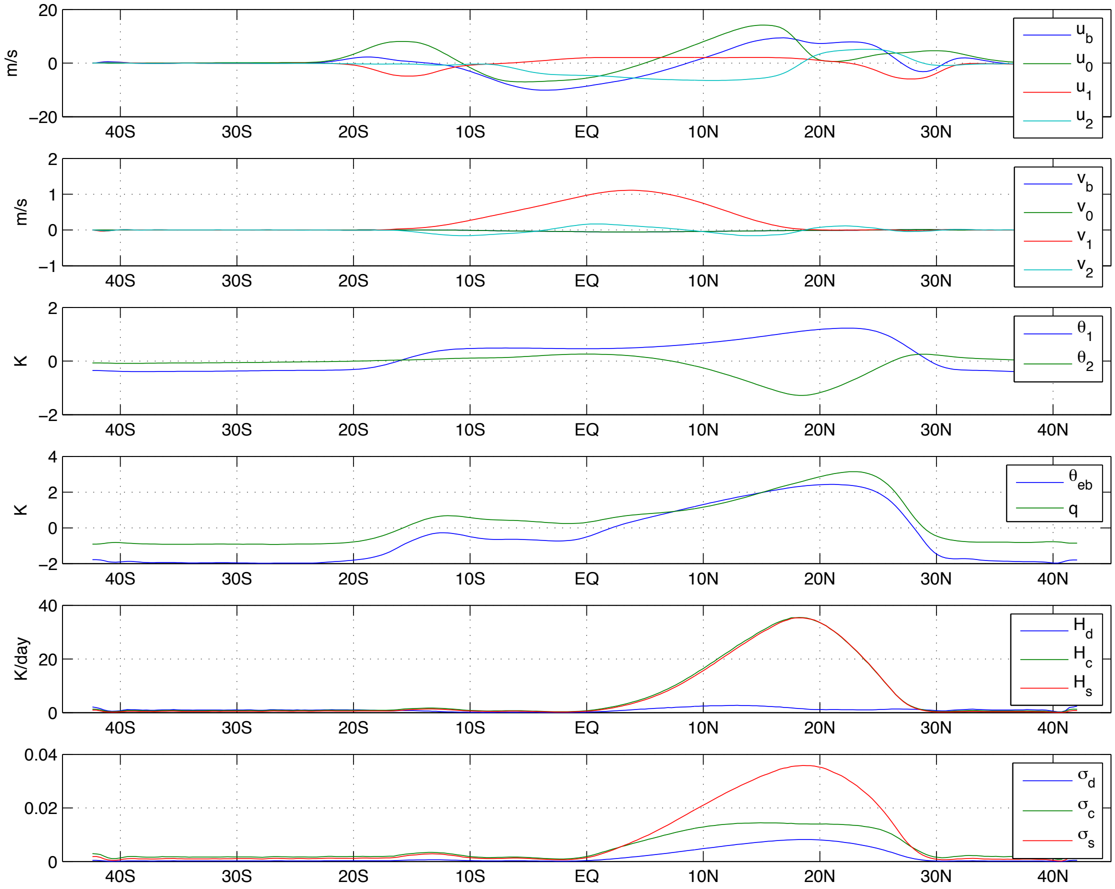

Figure A.10: *Simulation 5.* Mean meridional profiles averaged over the last 1000 days of simulation.

A.1.6 Simulation 6: SMCM, G-LES, SNWP[2] at 15°N, $a_0 = 3$

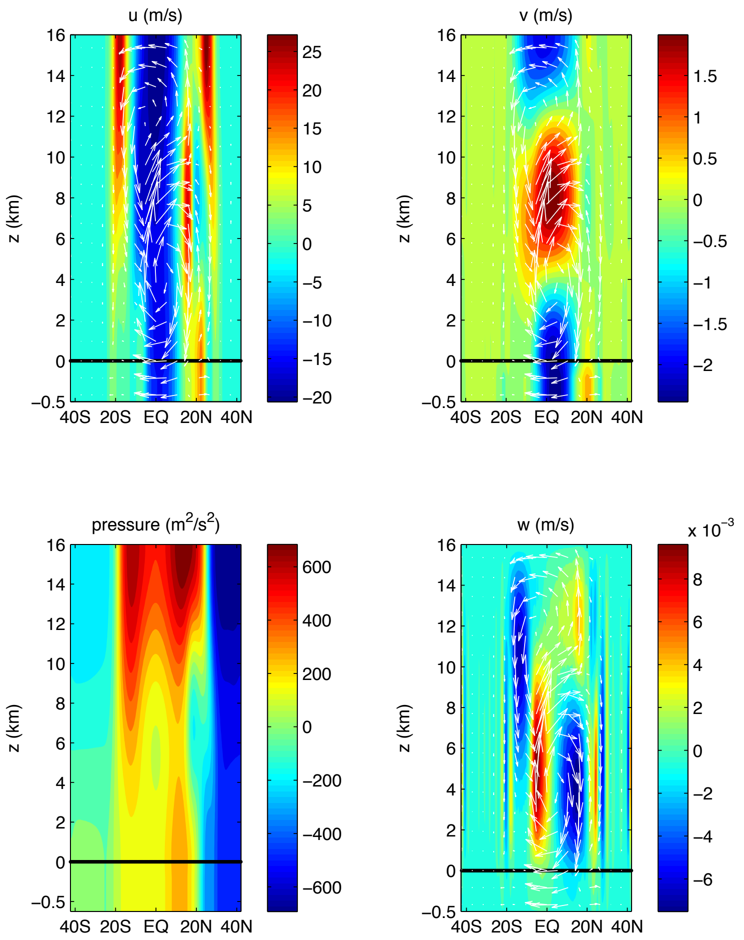

Figure A.11: *Simulation 6.* Mean meridional circulation, averaged over the last 1000 days of simulation. The top of the ABL (solid black line) is located at height 0 km. The contours represent the indicated fields, and the arrows are the velocity vector field (v, w).

---

[2] SNWP: skewed normal warm pool profile

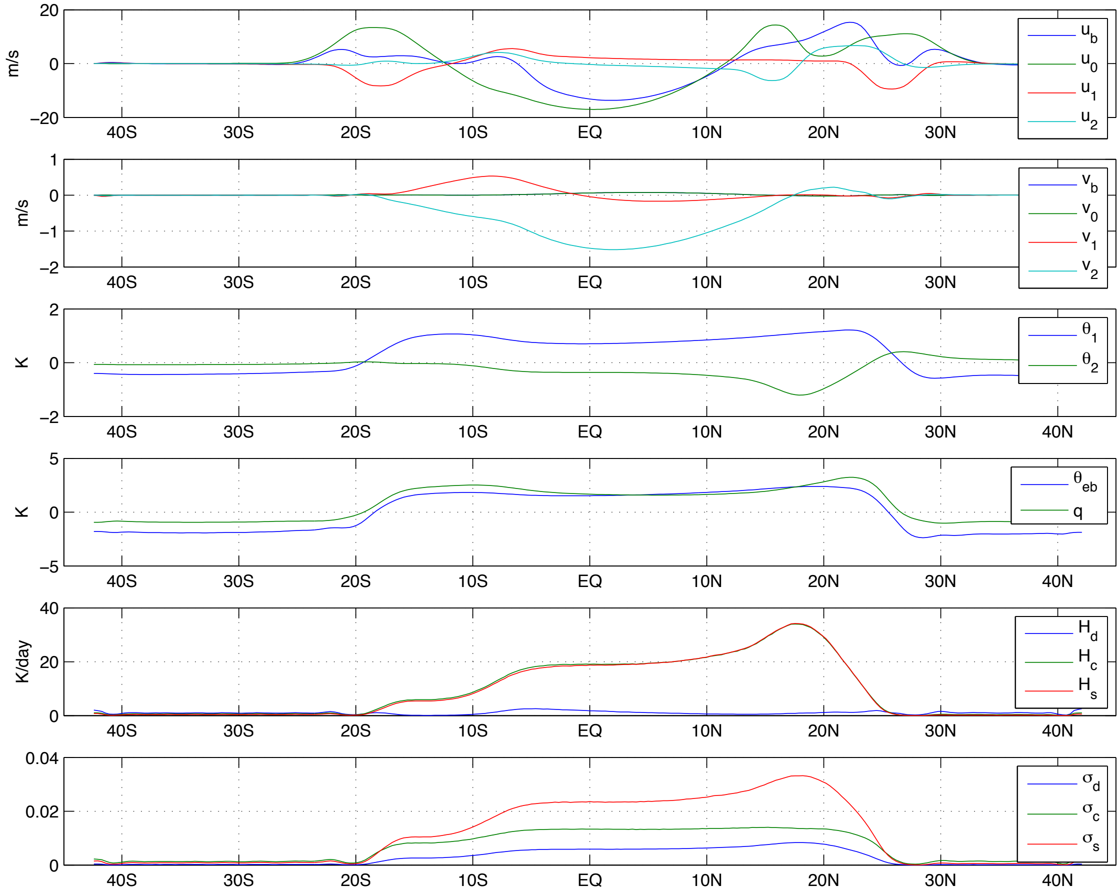

Figure A.12: *Simulation 6.* Mean meridional profiles averaged over the last 1000 days of simulation.

A.1.7 Simulation 7: SMCM, FMK12, NWP at 15°N, $a_0 = 3$

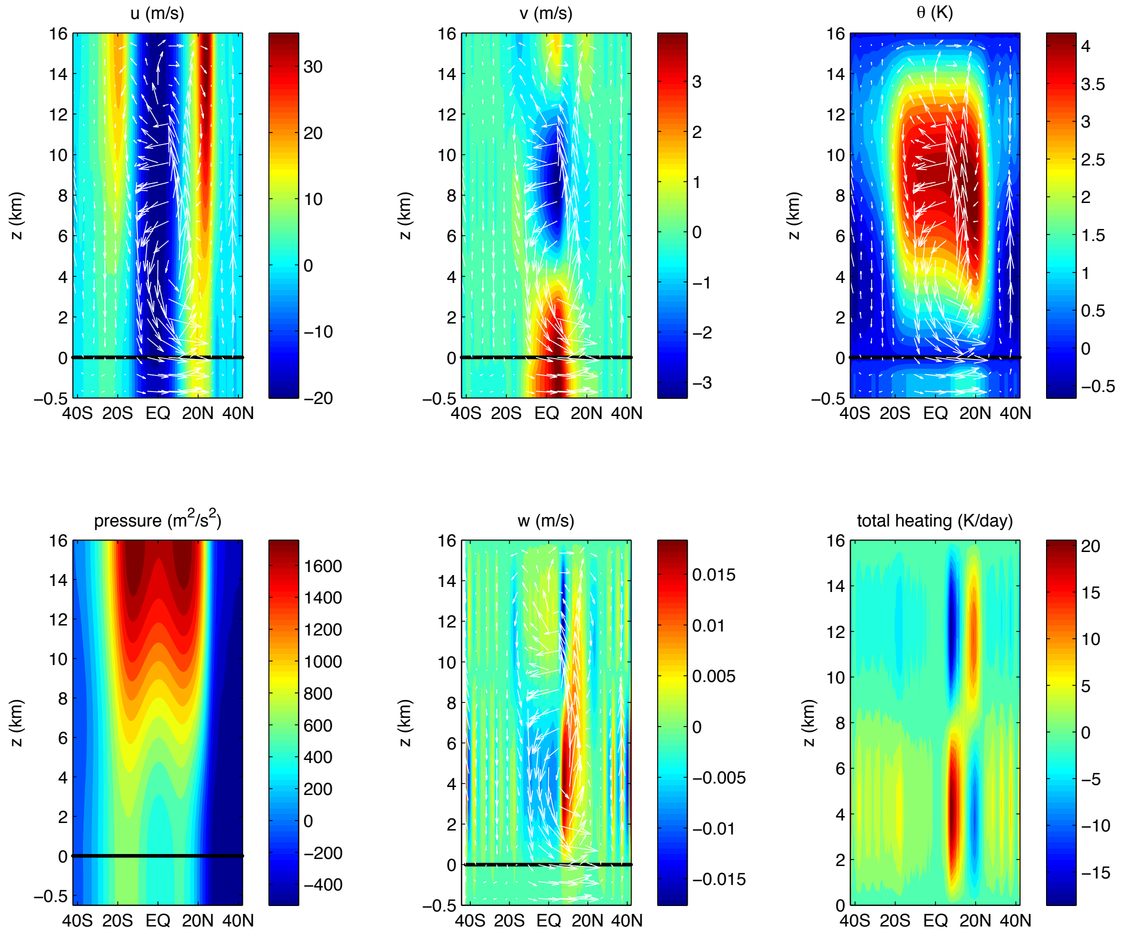

Figure A.13: *Simulation 7.* Mean meridional circulation, averaged over the last 1000 days of simulation. The top of the ABL (solid black line) is located at height 0 km. The contours represent the indicated fields, and the arrows are the velocity vector field (v, w).

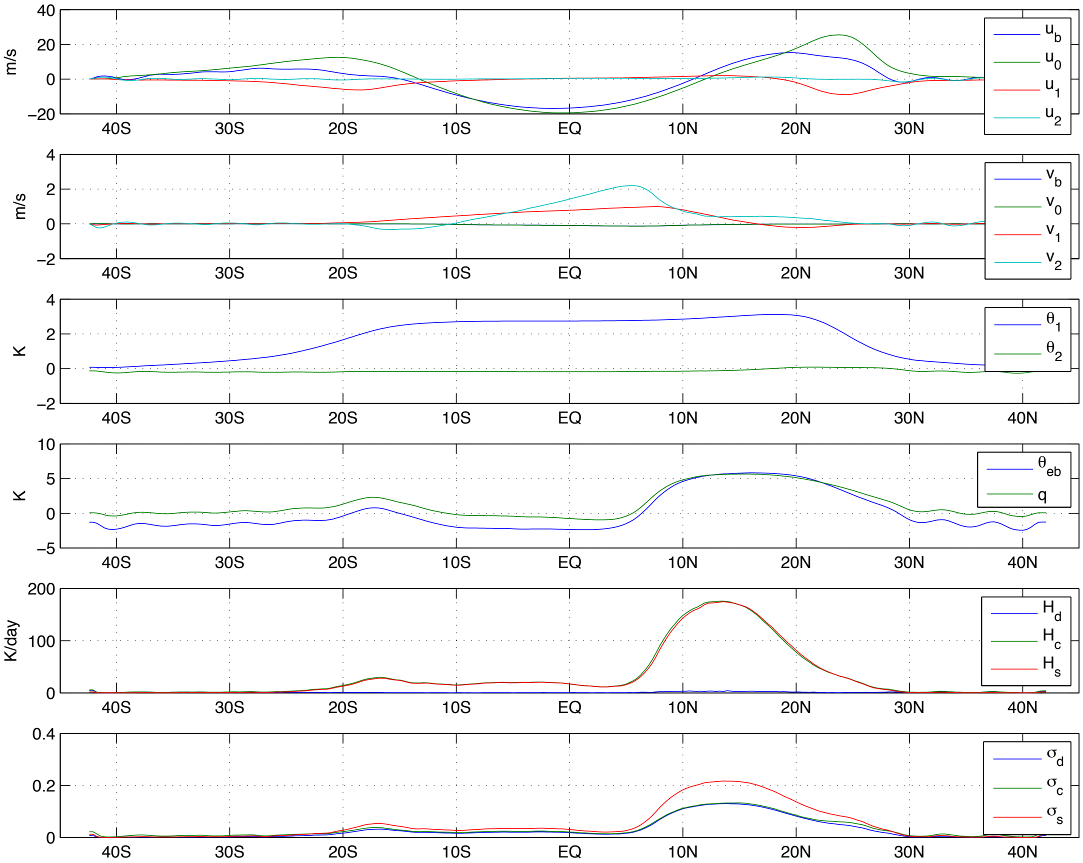

Figure A.14: *Simulation 7.* Mean meridional profiles averaged over the last 1000 days of simulation.

A.2 Hovmöller Diagrams

A.2.1 Simulation 1: DMCM, NWP[3] at 10°N, $a_0 = 1$

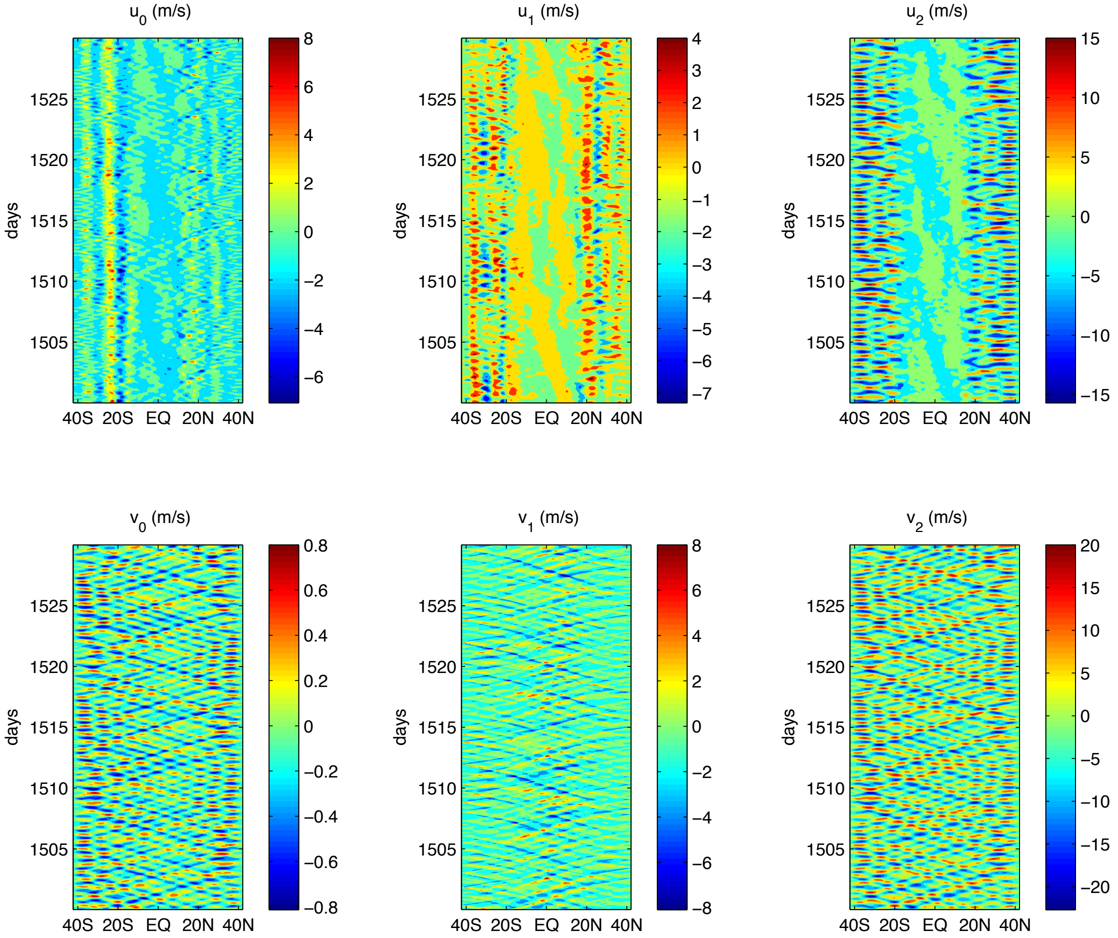

Figure A.15: *Simulation 1.* Wave disturbances of zonal and meridional velocities associated with the first three modes of vertical structure.

---

[3] NWP: normal warm pool profile

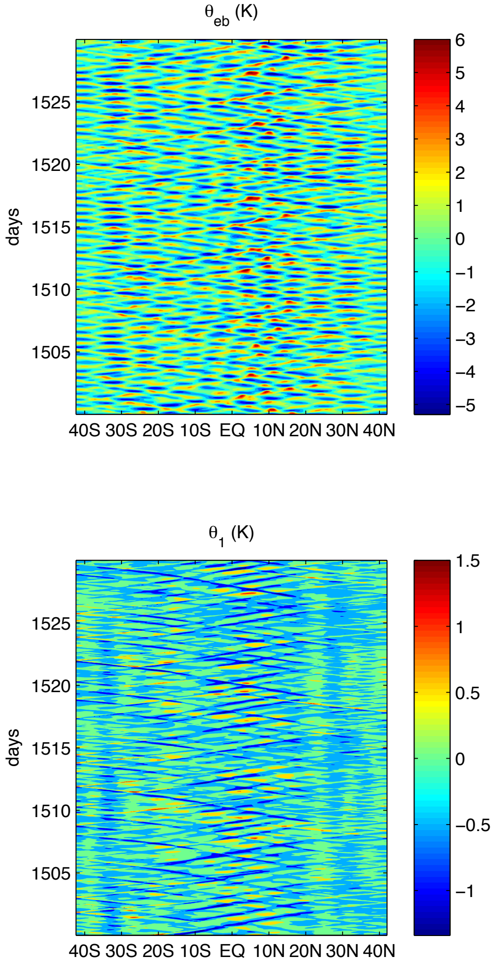

Figure A.16: *Simulation 1.* Wave disturbances of ABL equivalent potential temperature, troposphere moisture, and first two baroclinic modes of potential temperature.

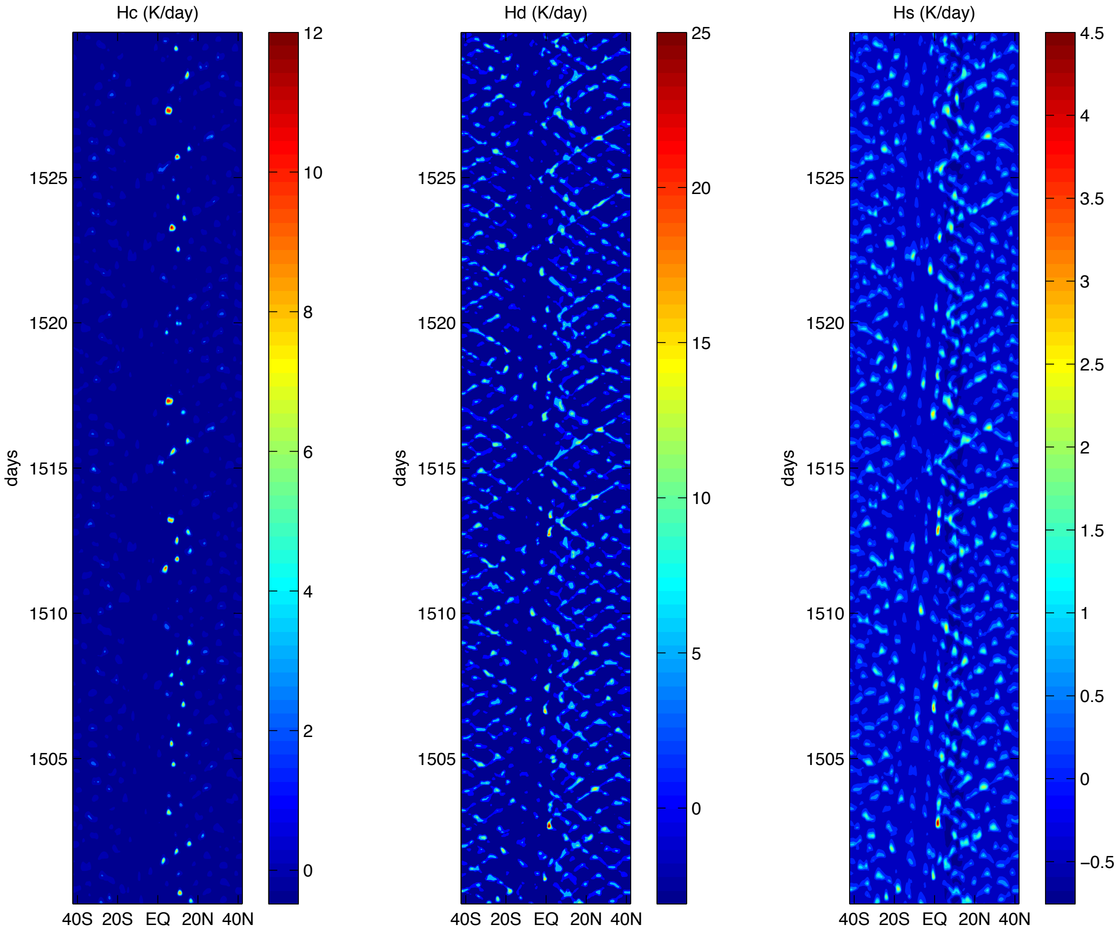

Figure A.17: *Simulation 1.* Wave disturbances of congestus, deep, and stratiform heating rates.

A.2.2 Simulation 2: DMCM, NWP at 15°N, $a_0 = 1$

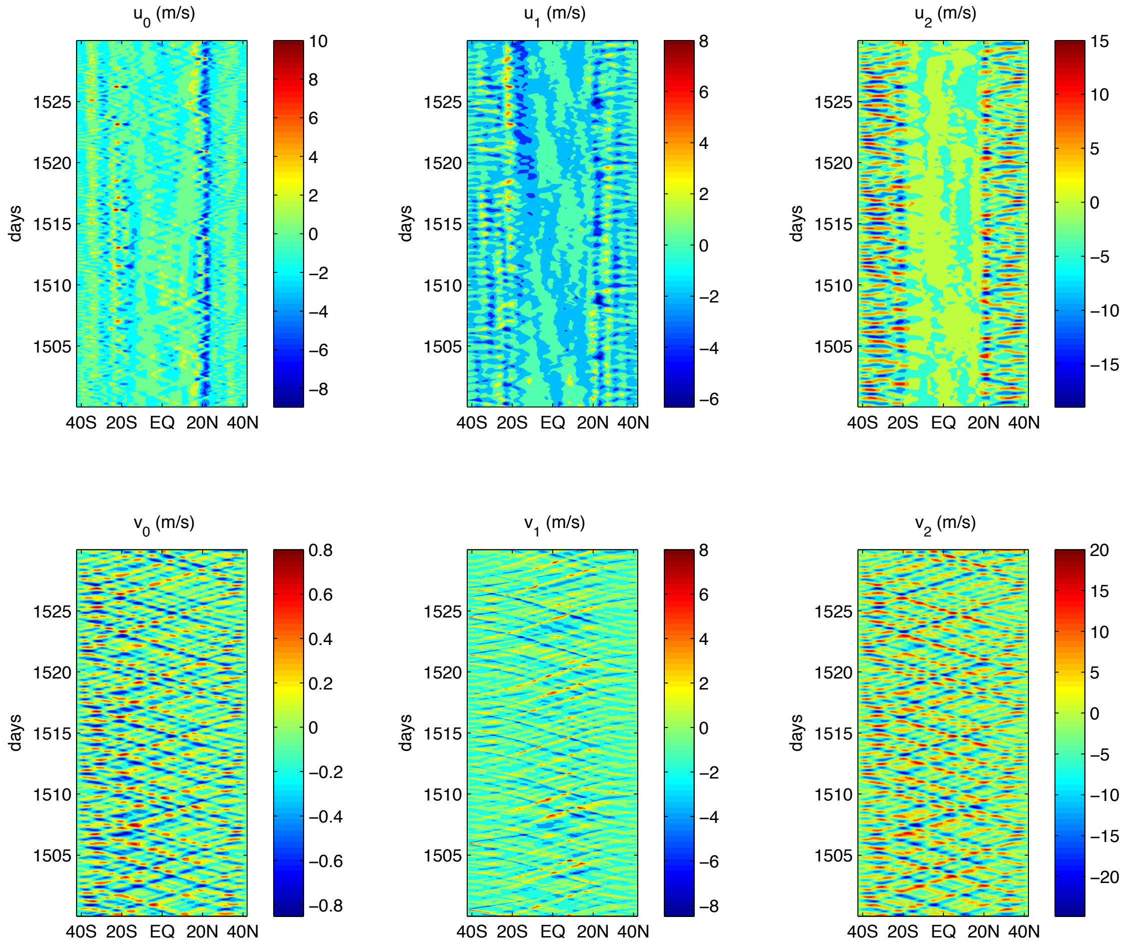

Figure A.18: *Simulation 2.* Wave disturbances of zonal and meridional velocities associated with the first three modes of vertical structure.

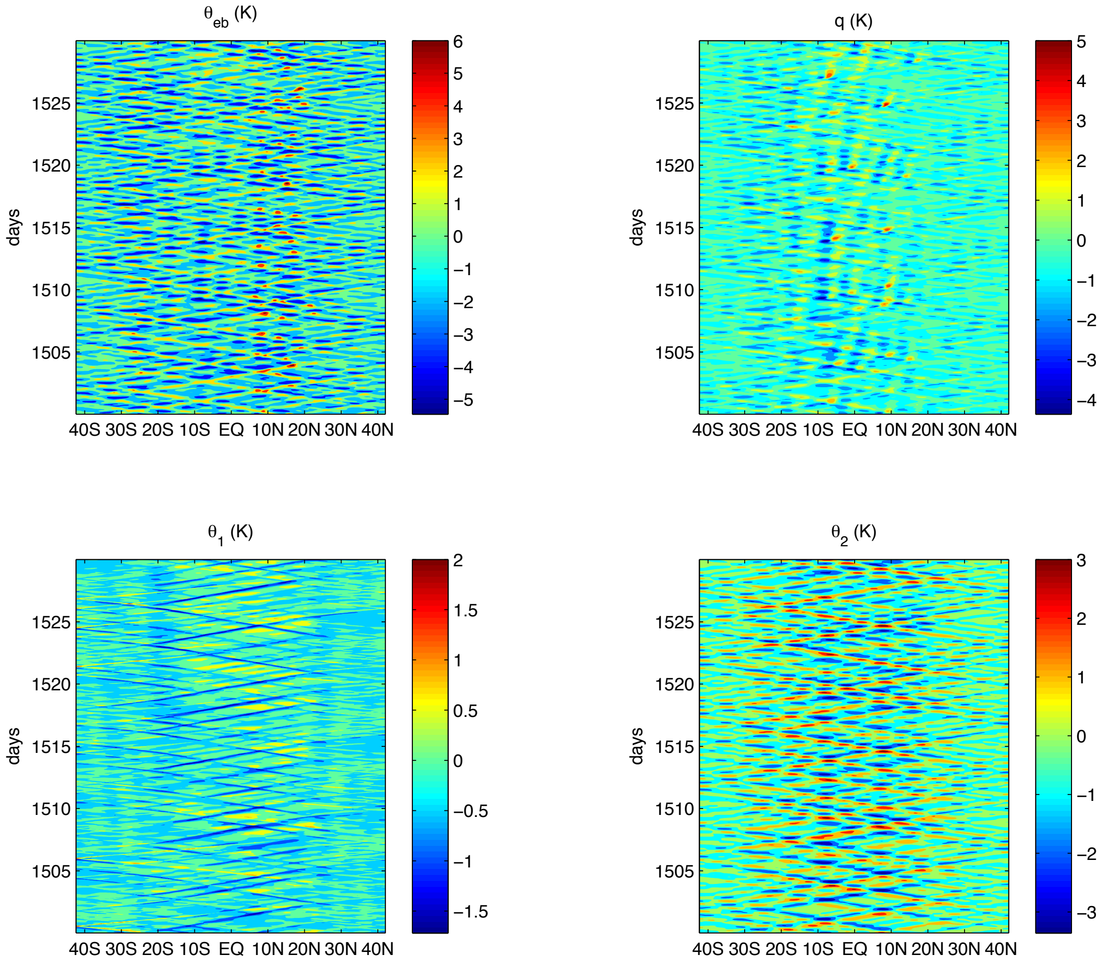

Figure A.19: *Simulation 2.* Wave disturbances of ABL equivalent potential temperature, troposphere moisture, and first two baroclinic modes of potential temperature.

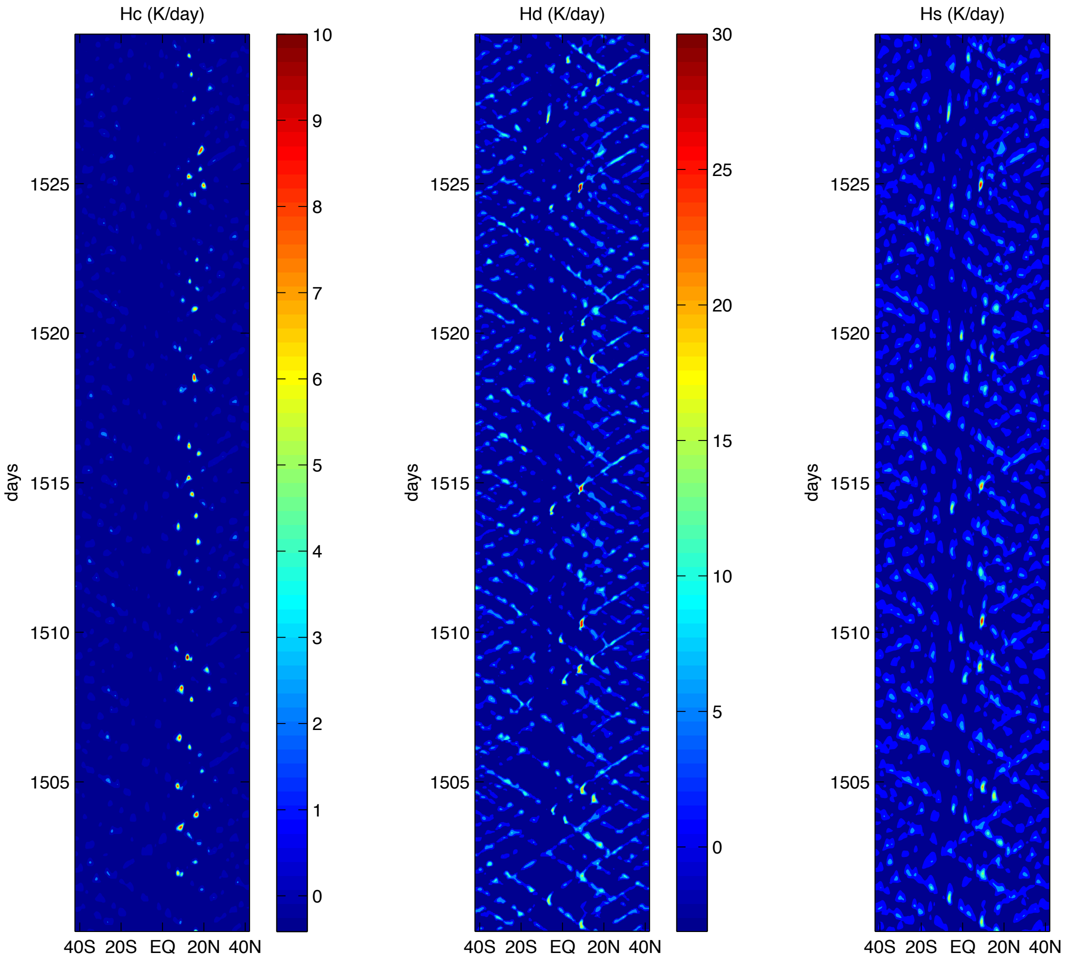

Figure A.20: *Simulation 2.* Wave disturbances of congestus, deep, and stratiform heating rates.

A.2.3 Simulation 3: SMCM, G-LES, NWP at 10°N, $a_0 = 1$

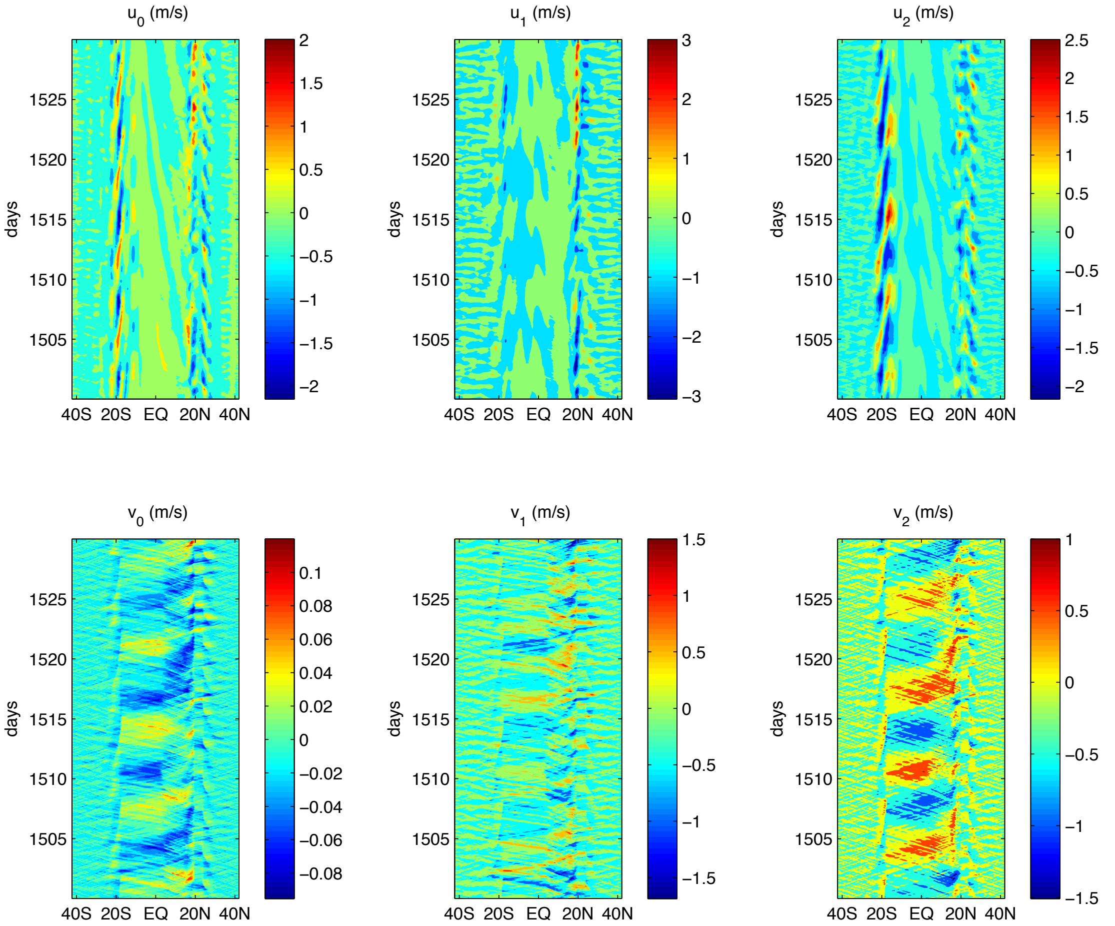

Figure A.21: *Simulation 3.* Wave disturbances of zonal and meridional velocities associated with the first three modes of vertical structure.

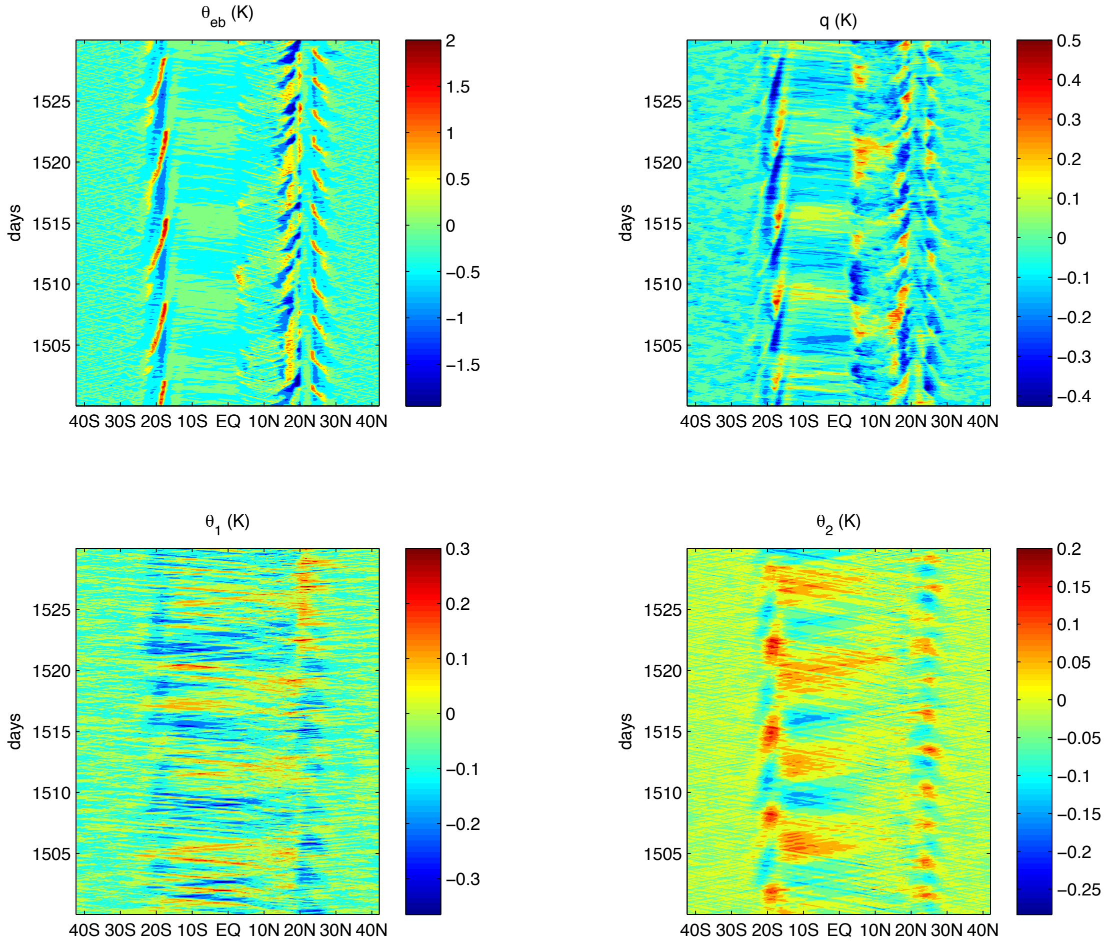

Figure A.22: *Simulation 3.* Wave disturbances of ABL equivalent potential temperature, troposphere moisture, and first two baroclinic modes of potential temperature.

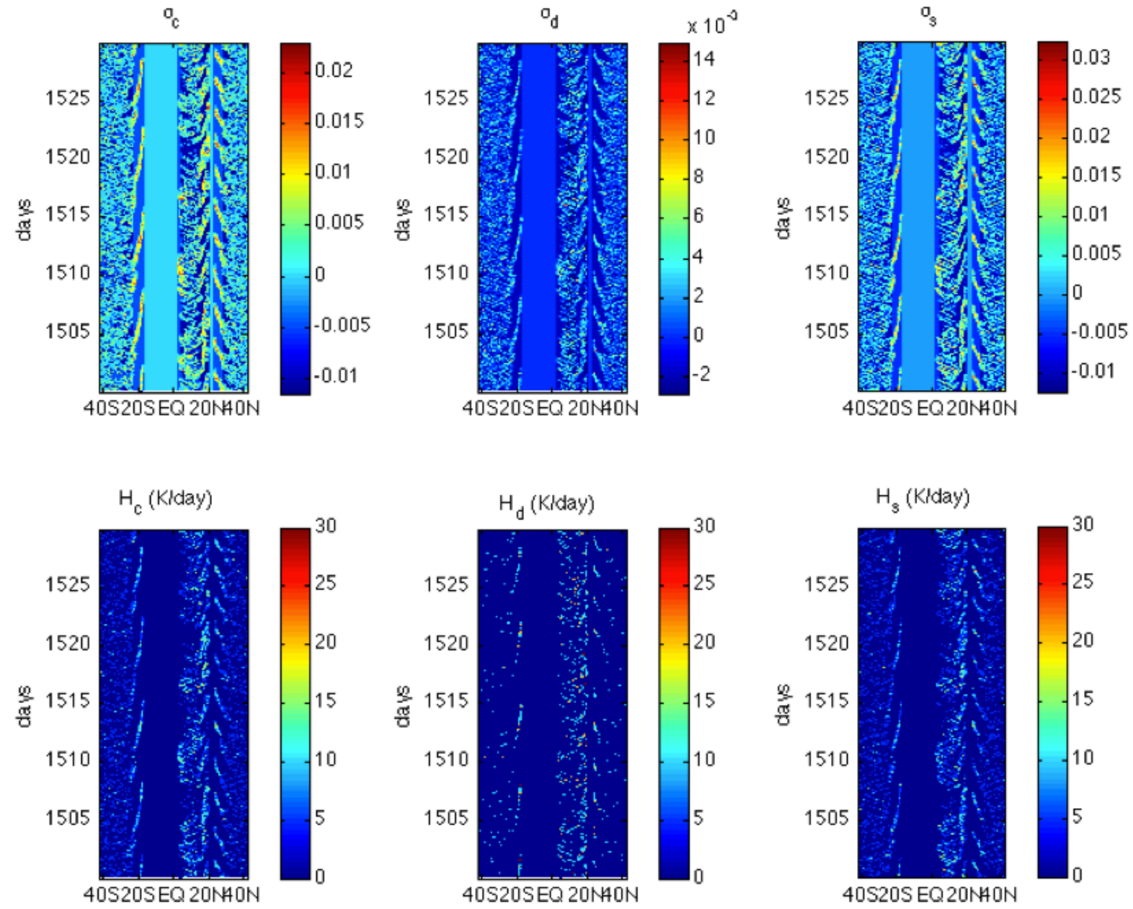

Figure A.23: *Simulation 3.* Wave disturbances of congestus, deep, and stratiform heating rates.

A.2.4 Simulation 4: SMCM, G-LES, NWP at 15°N, $a_0 = 1$

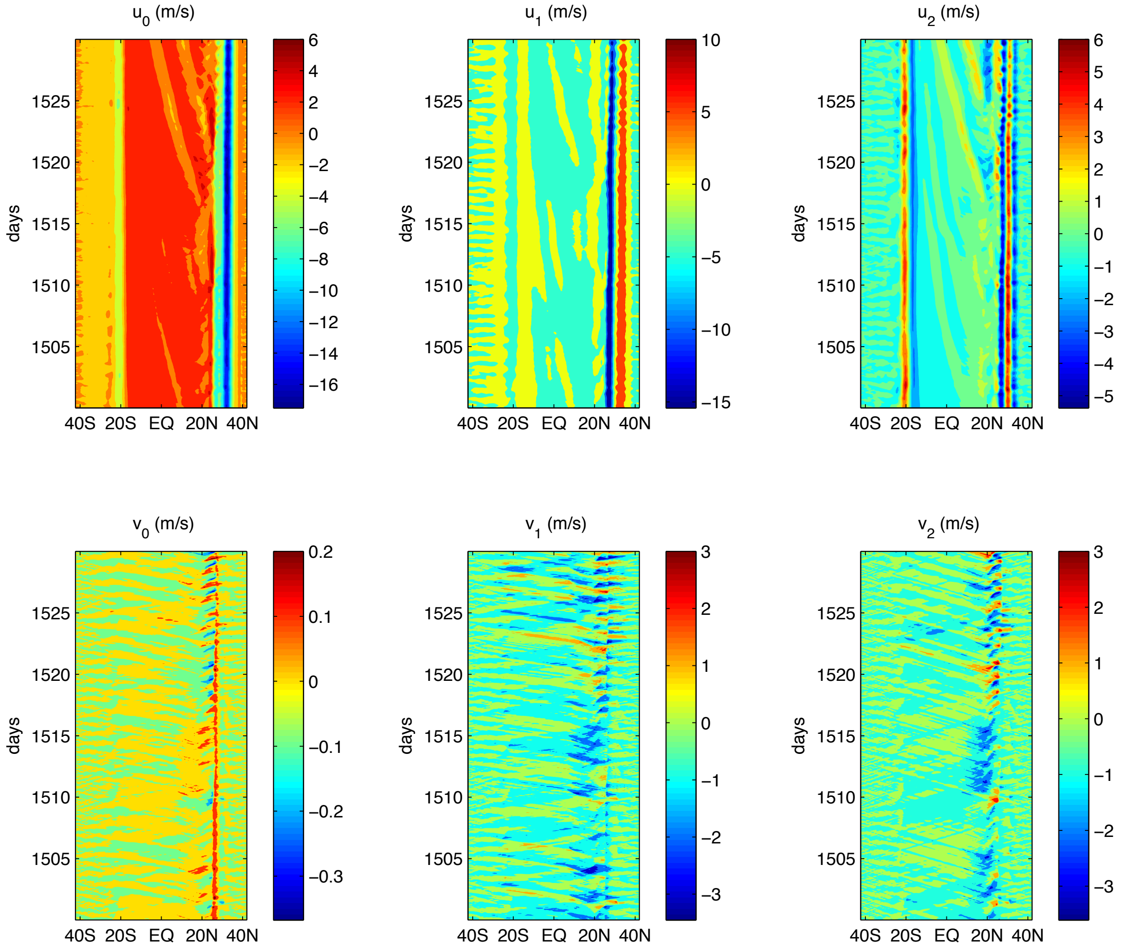

Figure A.24: *Simulation 4.* Wave disturbances of zonal and meridional velocities associated with the first three modes of vertical structure.

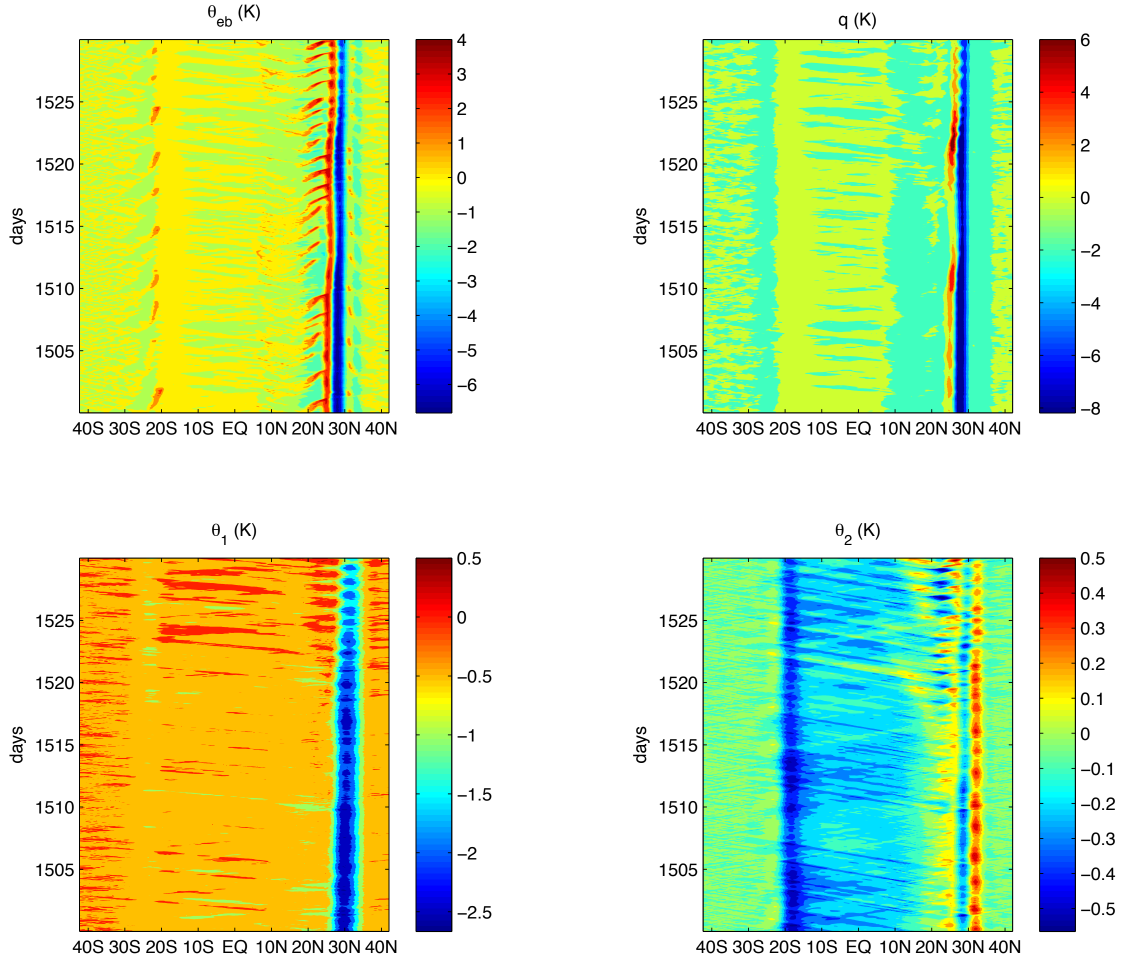

Figure A.25: *Simulation 4.* Wave disturbances of ABL equivalent potential temperature, troposphere moisture, and first two baroclinic modes of potential temperature.

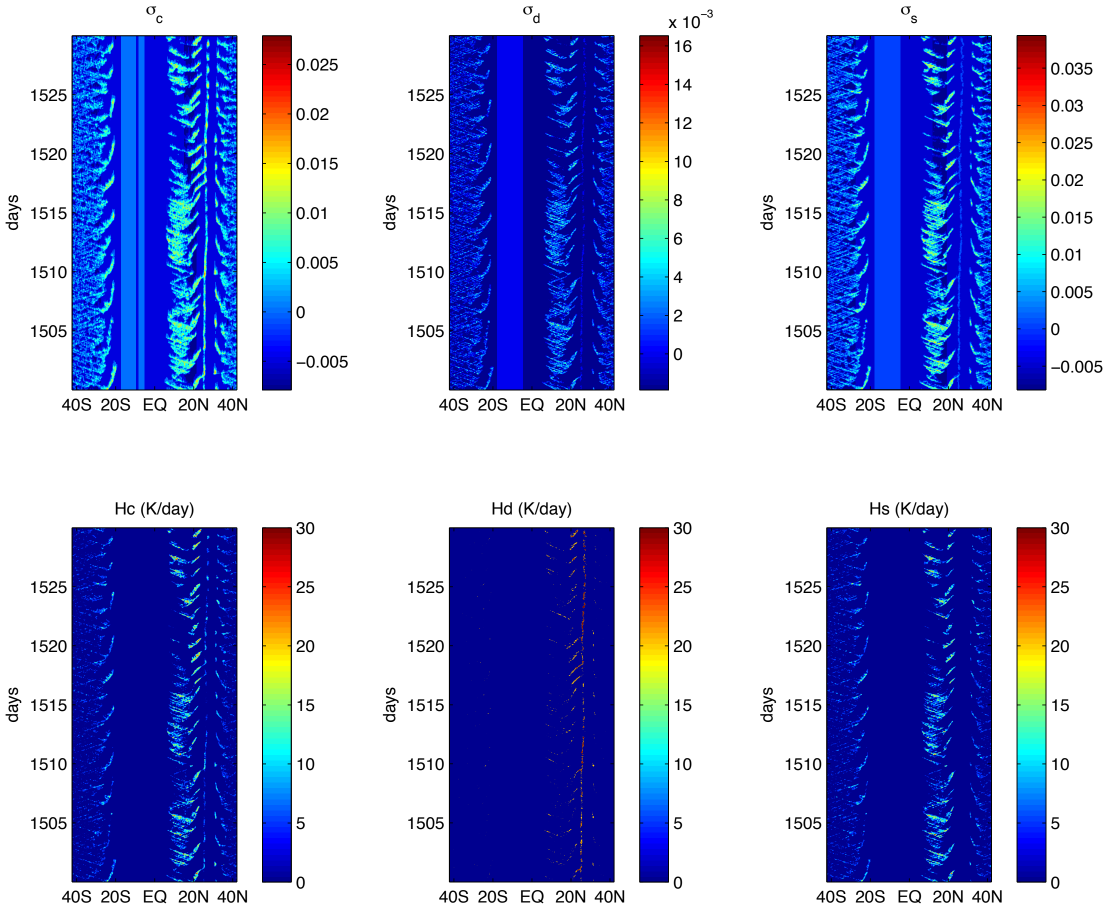

Figure A.26: *Simulation 4.* Wave disturbances of congestus, deep, and stratiform heating rates.

A.2.5 Simulation 5: SMCM, G-LES, NWP at 15°N, $a_0 = 3$

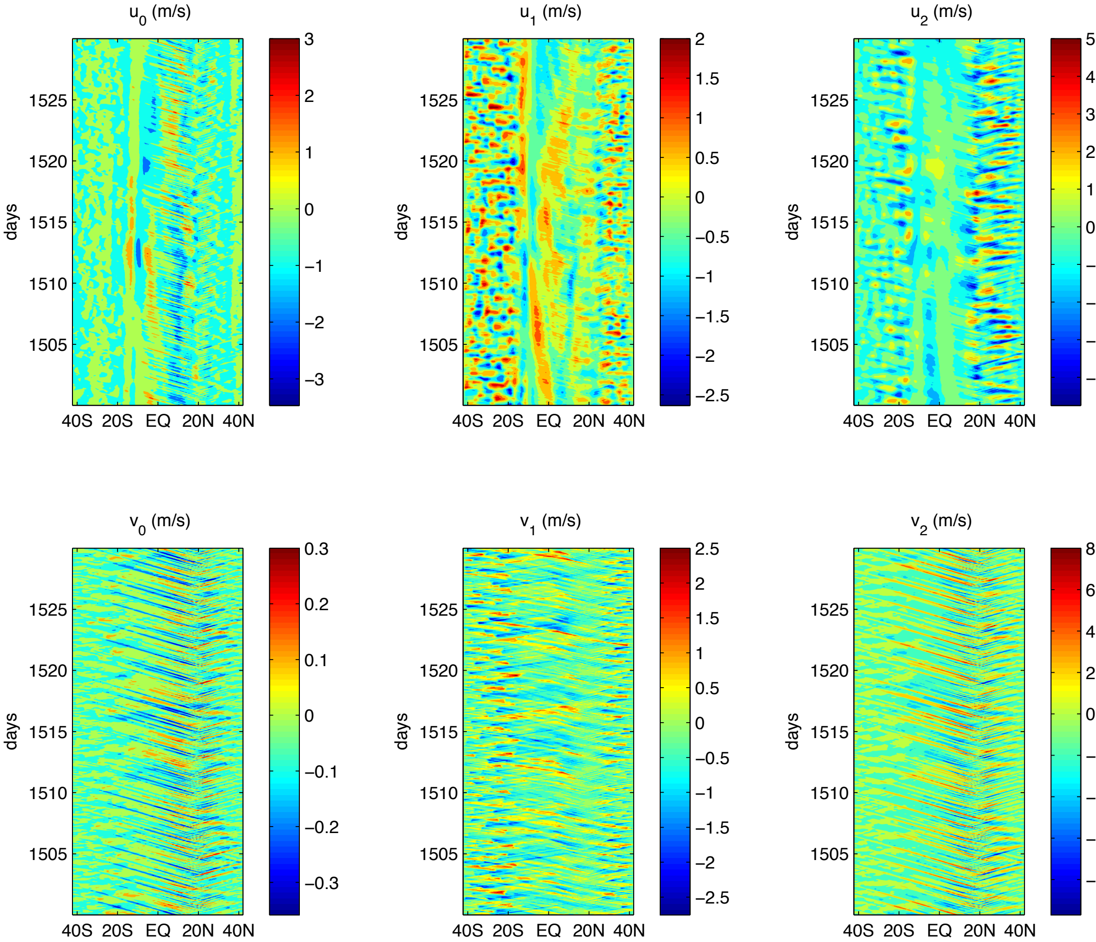

Figure A.27: *Simulation 5.* Wave disturbances of zonal and meridional velocities associated with the first three modes of vertical structure.

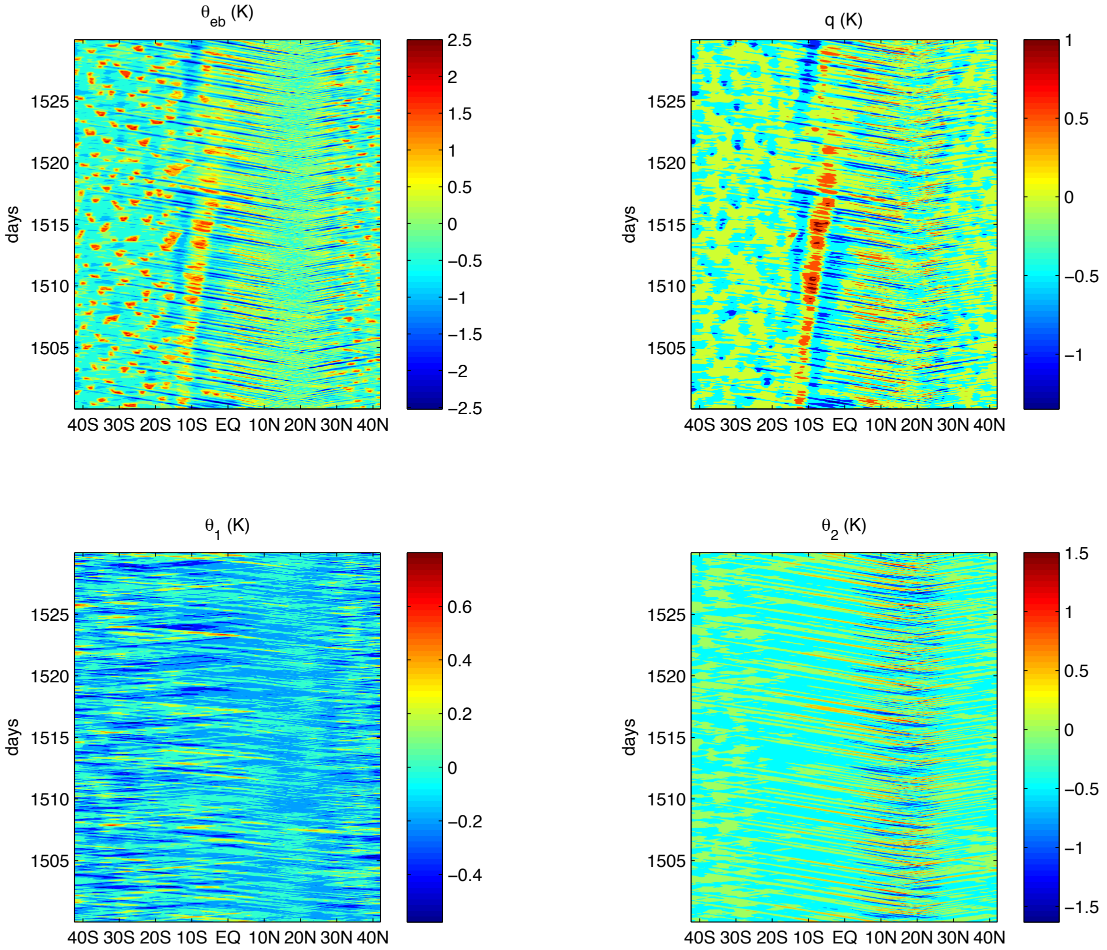

Figure A.28: *Simulation 5.* Wave disturbances of ABL equivalent potential temperature, troposphere moisture, and first two baroclinic modes of potential temperature.

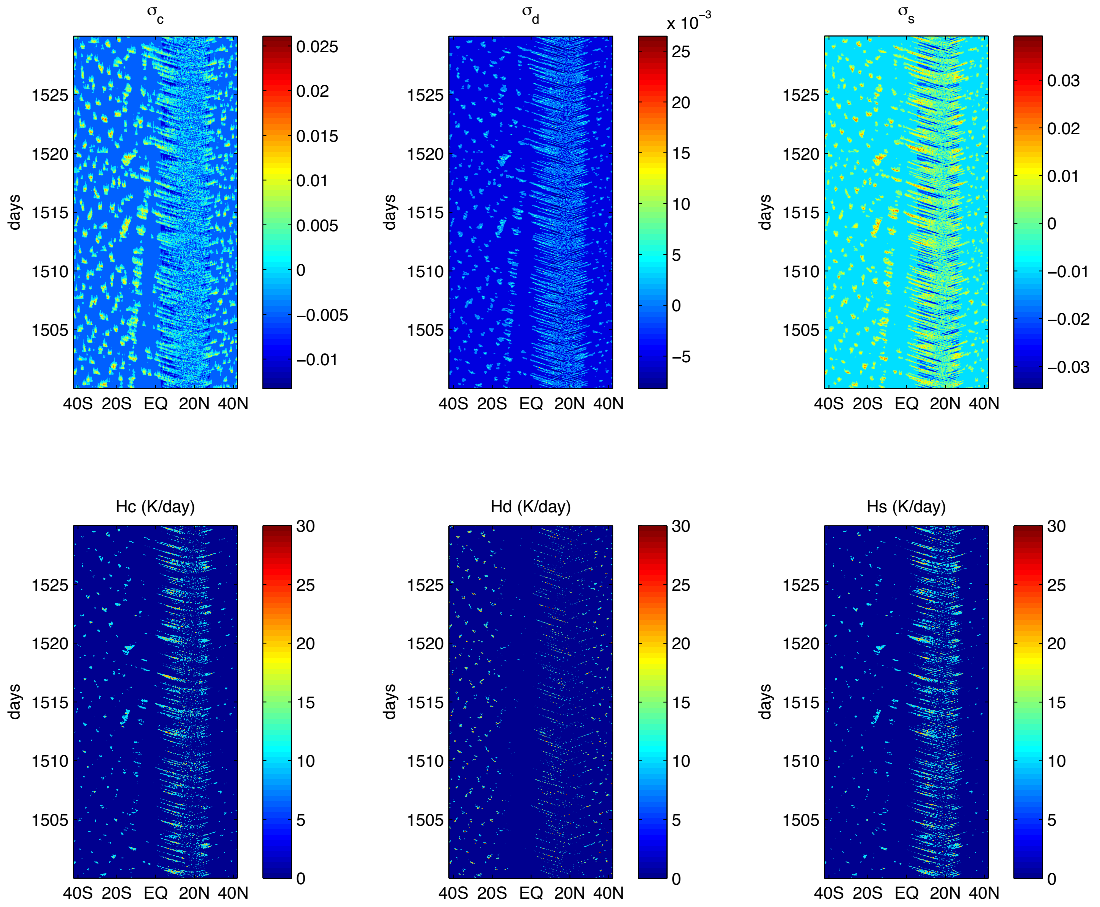

Figure A.29: *Simulation 5.* Wave disturbances of cloud area fractions and heating rates.

A.2.6 Simulation 6: SMCM, G-LES, SNWP[4] at 15°N, a_0 = 3

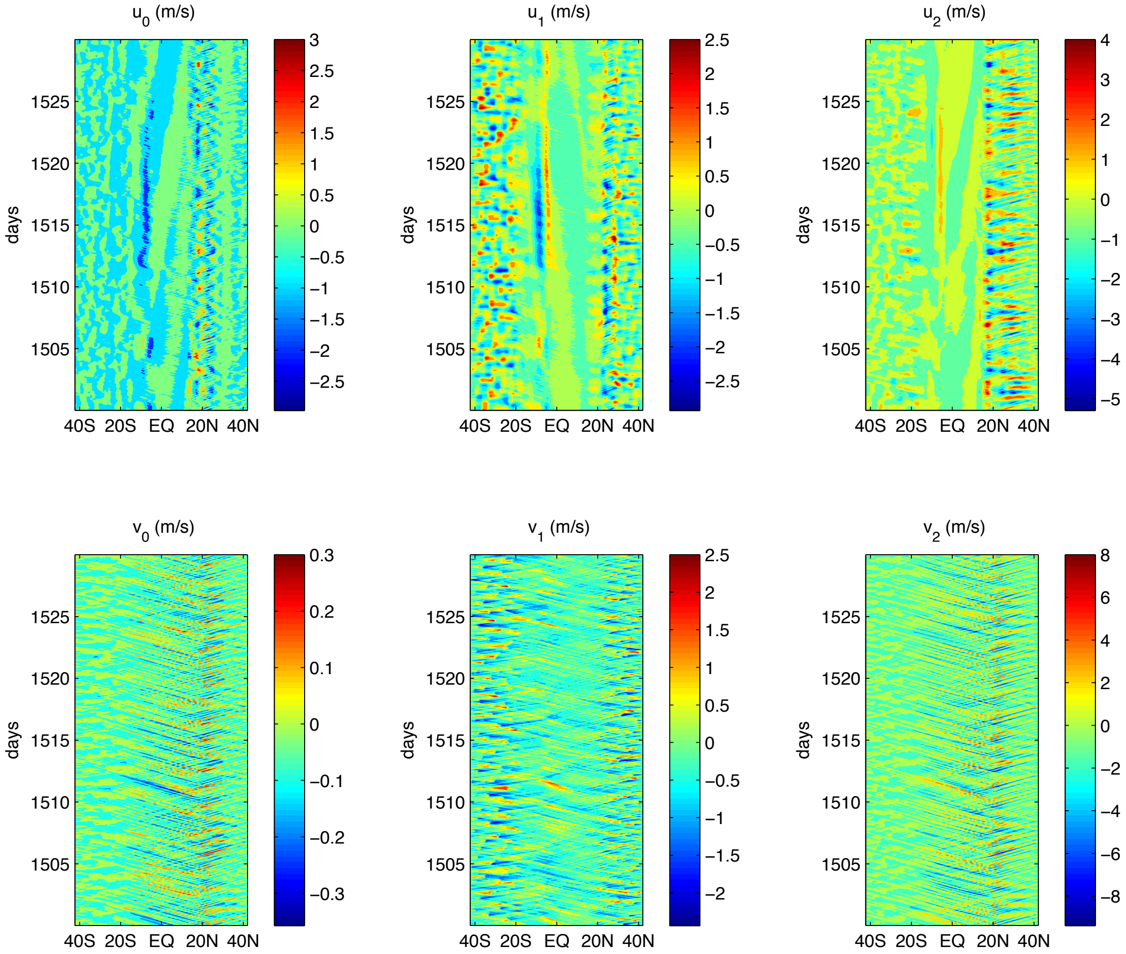

Figure A.30: *Simulation 6.* Wave disturbances of zonal and meridional velocities associated with the first three modes of vertical structure.

---

[4] SNWP: skewed normal warm pool profile

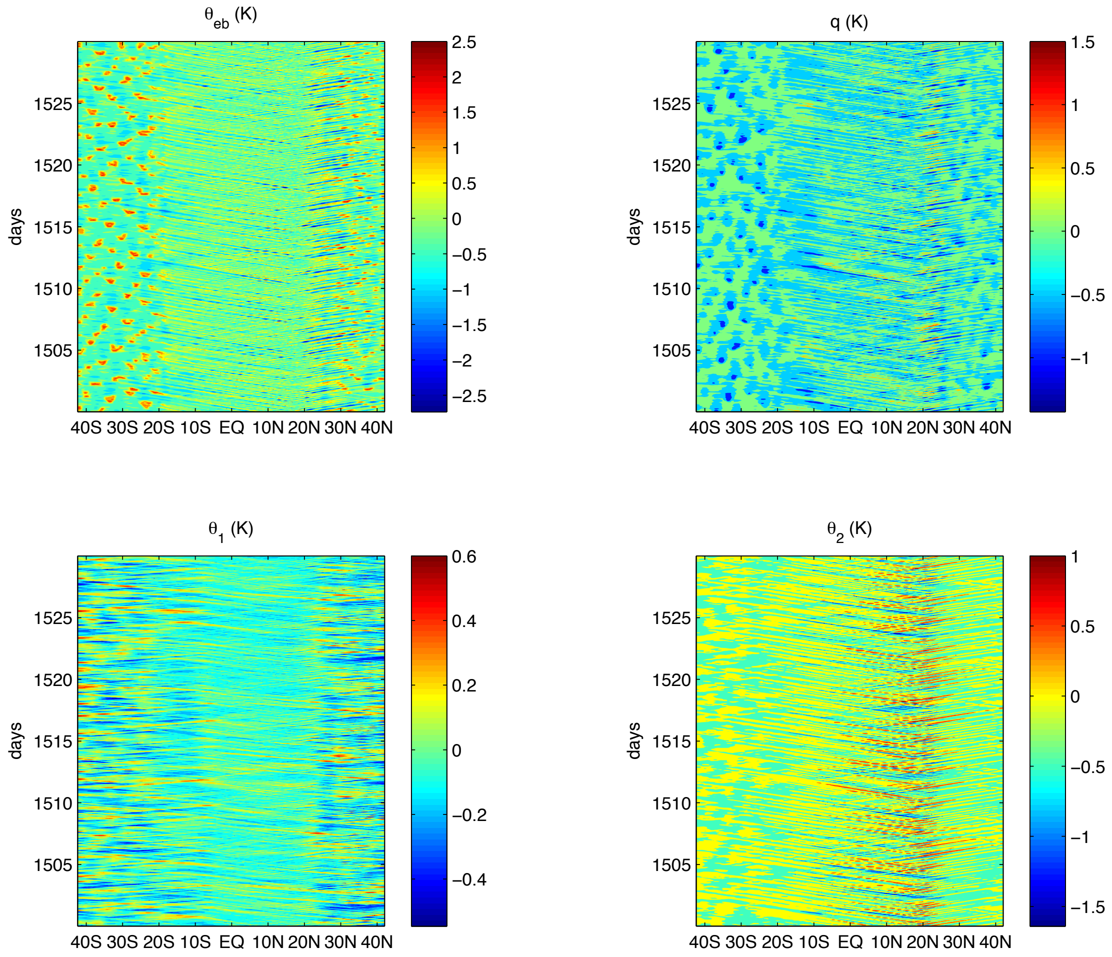

θ_{eb} (K)

q (K)

θ_1 (K)

θ_2 (K)

Figure A.31: *Simulation 6.* Wave disturbances of ABL equivalent potential temperature, troposphere moisture, and first two baroclinic modes of potential temperature.

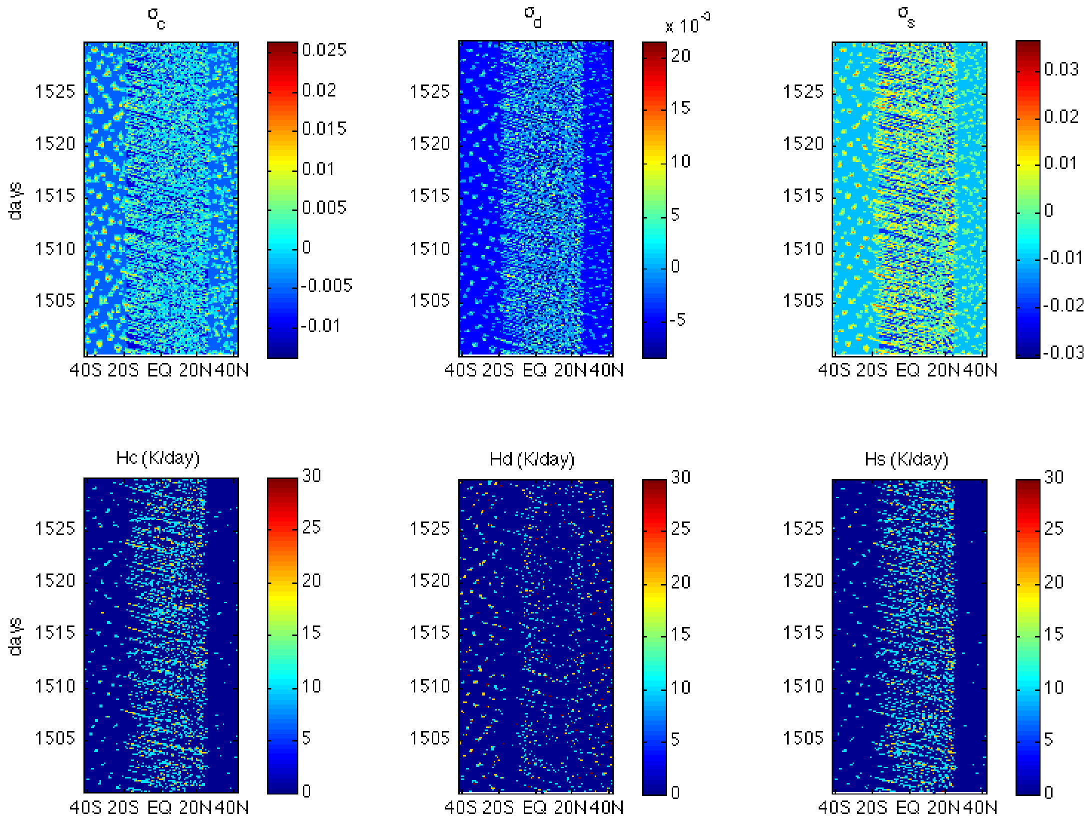

Figure A.32: *Simulation 6.* Wave disturbances of cloud area fractions and heating rates.

A.2.7 Simulation 7: SMCM, FMK12, NWP at 15°N, $a_0 = 3$

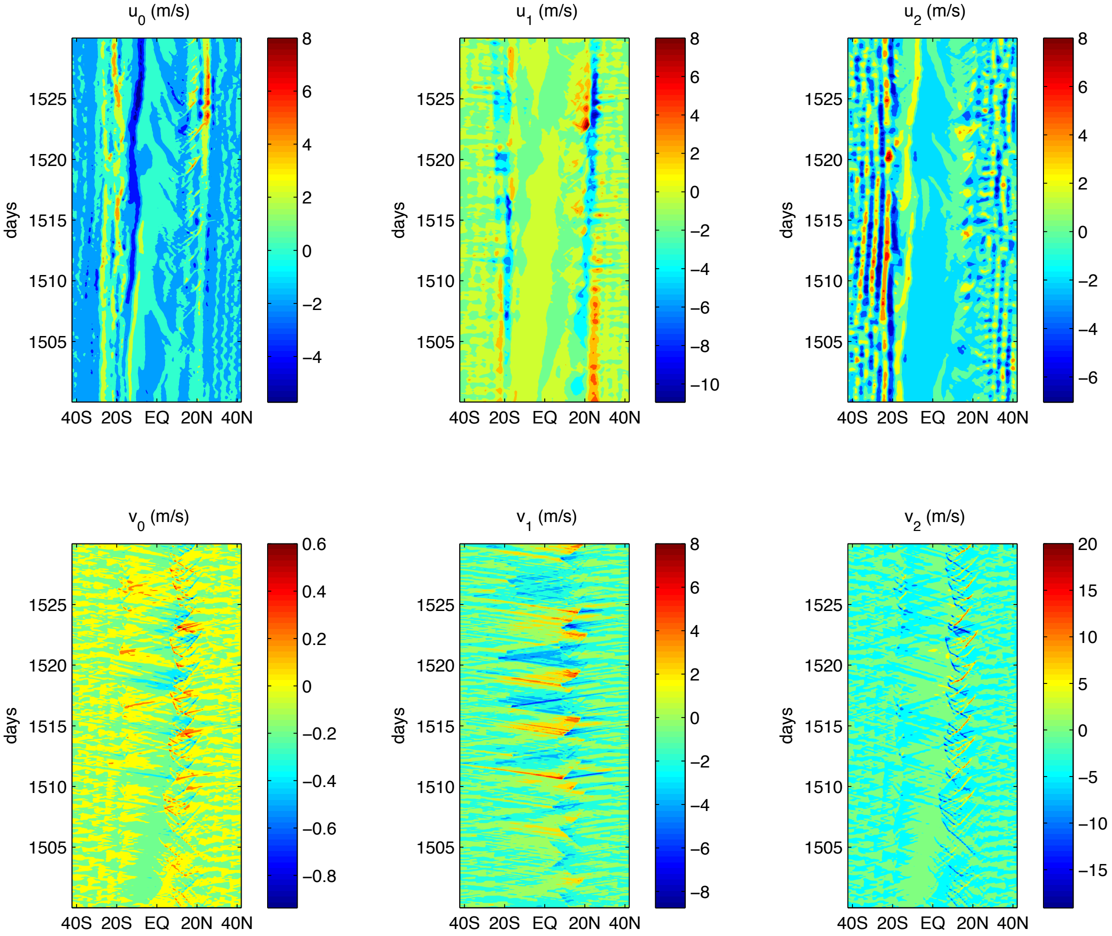

Figure A.33: *Simulation 7.* Wave disturbances of zonal and meridional velocities associated with the first three modes of vertical structure.

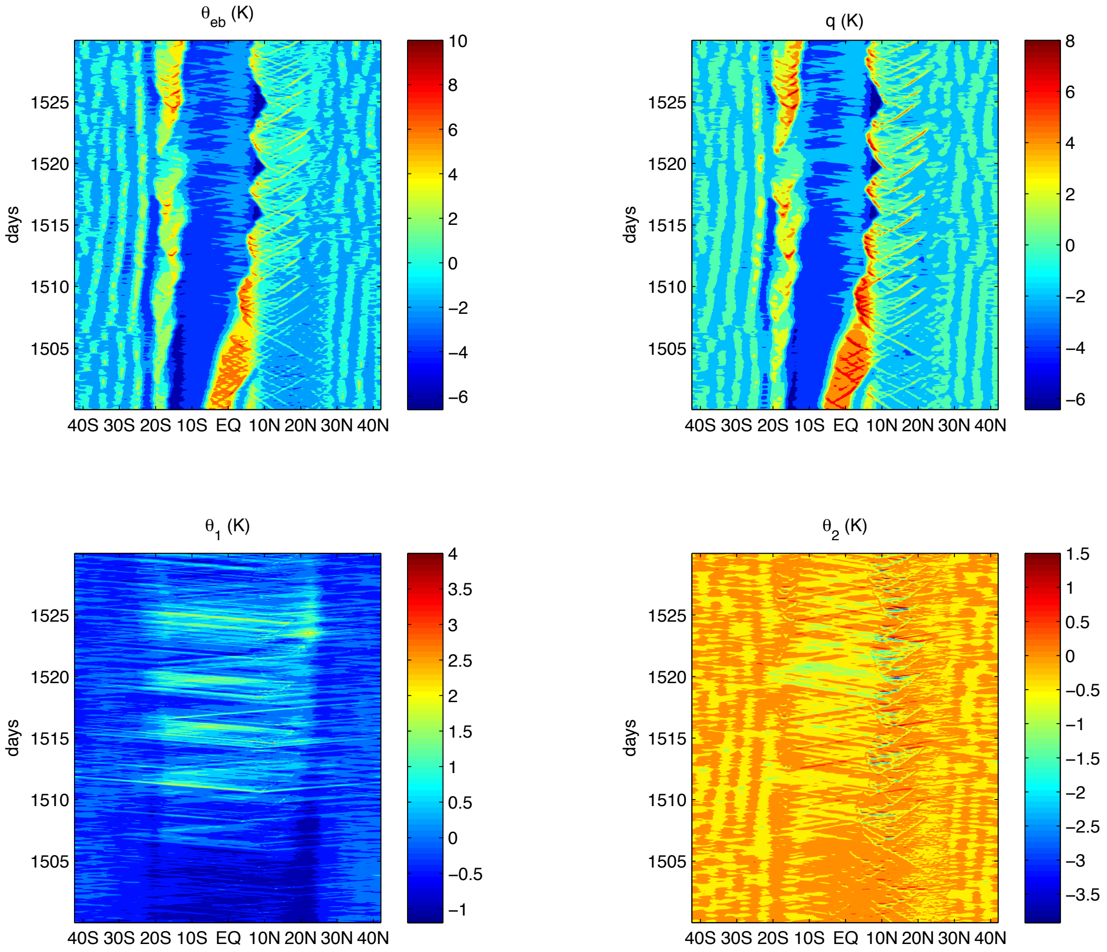

Figure A.34: *Simulation 7.* Wave disturbances of ABL equivalent potential temperature, troposphere moisture, and first two baroclinic modes of potential temperature.

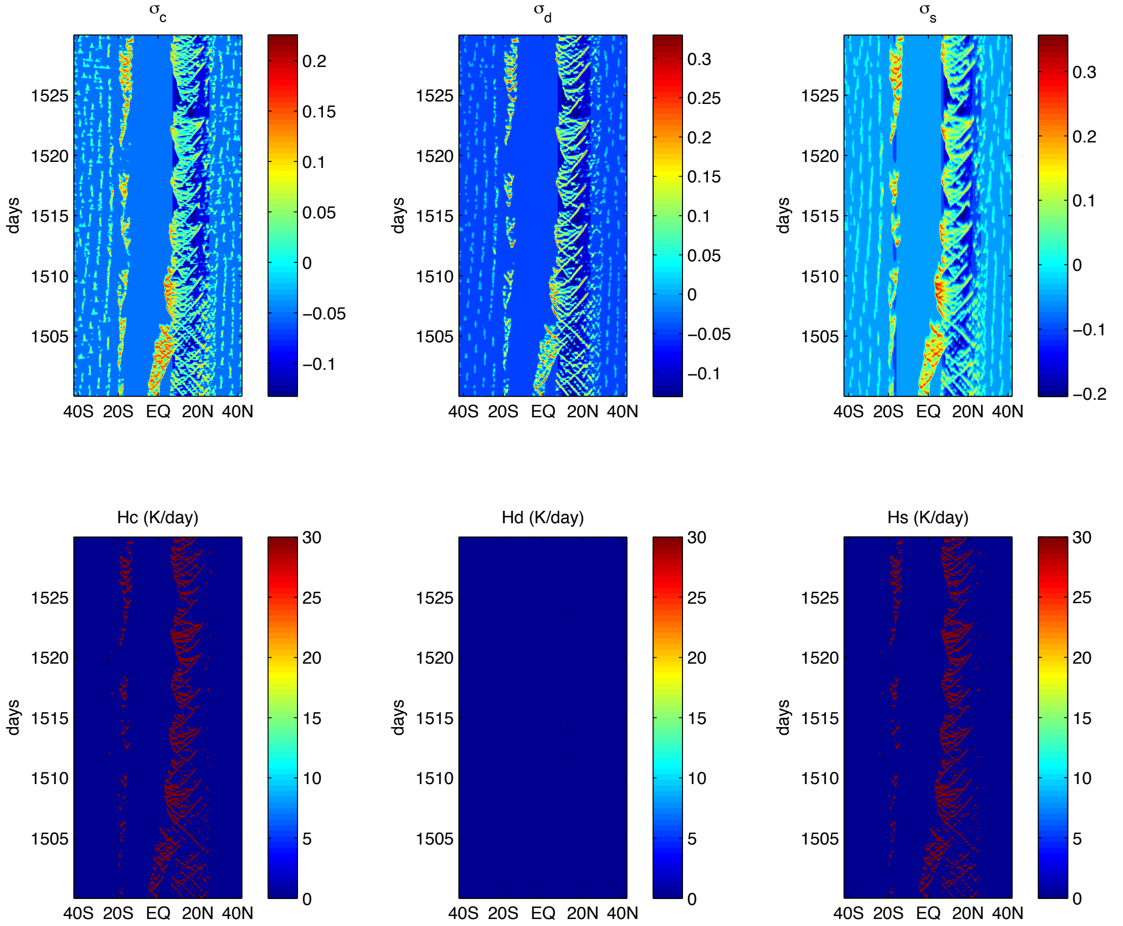

Figure A.35: *Simulation 7.* Wave disturbances of cloud area fractions and heating rates.

Appendix B

List of Symbols and Acronyms

H_T	Tropopause height
θ_{ref}	Reference potential temperature
g	Gravitational acceleration
θ_0	Background potential temperature, in K
N_v	Brent-Väisälä buoyancy frequency
c	Horizontal velocity scale
β	Variation of Coriolis parameter f at the Equator
L	Equatorial Rossby deformation radius/Horizontal reference length scale
T	Reference timescale
α	Potential temperature scale
ν	Free troposphere vertical velocity scale
h_b	ABL depth
q_v	Ratio of density of water vapor to density of dry air
τ_e	Surface evaporation timescale
U	Strength of turbulent velocity
C_d	Surface drag coefficient
τ_T	Momentum entrainment timescale

M_u	Updraft velocity
M_d	Downdraft velocity
Q_{R_b}	ABL radiative cooling rate
α_m	Ratio of D_c to M_u
δ	Ratio of boundary layer depth to height of the troposphere
L_v	Latent heat of vaporization at 0°C
c_p	Heat capacity at constant pressure
q_0	Constant reference background value of moisture at the top of the ABL
q_{v0}	Water vapor mixing ratio estimated at 500 m
H_q	e-folding distance of moisture background
κ	Top of ABL moisture to vertically averaged free tropospheric moisture ratio
η_q	Ratio of H_T over H_q
$\tilde{Q}_0$	Background contribution to barotropic vertical moisture advection
$\tilde{Q}_1$	Background contribution to first baroclinic vertical moisture advection
$\tilde{Q}_2$	Background contribution to second baroclinic vertical moisture advection
$\tilde{\alpha}_1$	First baroclinic relative contribution to the moisture convergence associated with the moisture anomalies
$\tilde{\alpha}_2$	Second baroclinic relative contribution to the moisture convergence associated with the moisture anomalies
H_m	Average height of the middle troposphere
R	CAPE constant
Q_{R1}	Longwave first baroclinic radiative cooling rate
Q_{R2}	Longwave second baroclinic radiative cooling rate
$\overline{Q}$	Heating potential at RCE
m_0	Large-scale background downdraft velocity
τ_c^0	Reference convective timescale

α_c, α_s	Contribution of CAPE to congestus, stratiform heating
a_0	Contribution of θ_1 to deep convective heating anomalies
a_1	Contribution of θ_{eb} to deep convective heating anomalies
a_2	Contribution of q to deep convective heating anomalies
a_0'	Contribution of θ_1 to CAPE anomalies
γ_2	Relative contribution of θ_2 to deep convective anomalies
γ_2'	Relative contribution of θ_2 to low level CAPE anomalies
CAPE_0	Reference value of CAPE
T_0	Reference value of CAPE
α_2	Relative contribution of θ_2 to θ_{em}
μ	Contribution of convective downdrafts to M_d
τ_c, τ_s	Congestus, stratiform adjustment timescales
τ_{conv}	Convective timescale
θ^-, θ^+	Moisture switch threshold values
τ_D	Newtonian cooling timescale
τ_R	Rayleigh drag timescale
τ_T	Momentum entrainment timescale
τ_{01}/r_{01}	Clear sky to congestus cloud transition timescale/probability rate
τ_{10}/r_{10}	Congestus cloud to clear sky transition timescale/probability rate
τ_{12}/r_{12}	Congestus to deep cloud transition timescale/probability rate
τ_{02}/r_{02}	Clear sky to deep cloud transition timescale/probability rate
τ_{23}/r_{23}	Deep to stratiform cloud transition timescale/probability rate
τ_{20}/r_{20}	Deep cloud to clear sky transition timescale/probability rate
τ_{30}/r_{30}	Stratiform cloud to clear sky transition timescale/probability rate
σ_c	Congestus cloud area fraction
σ_s	Stratiform cloud area fraction

σ_d	Deep cloud area fraction
N	Total number of sites of stochastic lattice
n	Size of stochastic lattice
N_c	Congestus cloud population
N_d	Deep cloud population
N_s	Stratiform cloud population
ρ	Density of the environment
Γ_d	Dry adiabatic lapse rate
Γ_m	Moist adiabatic lapse rate
Γ	Lapse rate of the environment
ρ_p	Density of the parcel
B	Buoyancy
z_0	Initial height in the parcel method
p_0	Initial pressure in the parcel method
T_0	Initial temperature in the parcel method
r_0	Initial mixing ratio in the parcel method
T^*	Saturation temperature
p^*	Saturation pressure
z^*	Saturation height
r	Parcel mixing ratio
e	Parcel vapor pressure
R_d	Gas constant for dry air
R_v	Gas constant for water vapor
ϵ	Ratio of R_d to R_v
L_v	Latent heat of vaporization
c_{pv}	Heat capacity at constant pressure of water vapor
c_l	Heat capacity of liquid water

c_{pd}	Heat capacity at constant pressure for dry air
T_{vp}	Virtual temperature of the parcel
T_{ve}	Virtual temperature of the environment
z_{LNB}	Height of the LNB level
z_{LFC}	Height of the LFC level
z_{LCL}	Height of the LCL level (corresponds to z^*)
GCM	General circulation model
LES	Large-eddy-simulation
ENSO	El Ninõ Southern oscillation
MCA	Moist convective adjustment
SMCM	Stochastic multicloud model
DMCM	Deterministic multicloud model
ABL	Atmospheric boundary layer
MCMC	Markov Chain Monte Carlo
3MoFTM	3-mode free troposphere model
CAPE	Convective available potential energy
RCE	Radiative convective equilibrium
MOSNE	Hadley-Monsoon equations
NT	Nessyahu and Tadmor central scheme
SST	Sea-surface temperature
WP	Warm pool
NWP/SNWP	Normal/skewed normal warm pool profile
ITCZ	Atlantic inter-tropical convergence zone
GATE	GARP Atlantic Tropical Experiment
LCL	Lifting condensation level
LFC	Level of free convection
LNB	Level of neutral buoyancy
CIN	Convective inhibition

Bibliography

A. Arakawa. Modelling clouds and cloud processes for use in climate models. *WMO The Phys. Basis of Climate and Climate Modelling*, pages 183–197, 1975.

A. Arakawa and W. H. Schubert. Interaction of a cumulus cloud ensemble with the large-scale environment, Part I. *Journal of the Atmospheric Sciences*, 31 (3):674–701, 1974.

Satish Balay, Shrirang Abhyankar, Mark F. Adams, Jed Brown, Peter Brune, Kris Buschelman, Lisandro Dalcin, Victor Eijkhout, William D. Gropp, Dinesh Kaushik, Matthew G. Knepley, Lois Curfman McInnes, Karl Rupp, Barry F. Smith, Stefano Zampini, and Hong Zhang. PETSc users manual. Technical Report ANL-95/11 - Revision 3.6, Argonne National Laboratory, 2015. URL `http://www.mcs.anl.gov/petsc`.

G. K. Batchelor. *An introduction to fluid dynamics*. Cambridge University Press, 2000.

G. Bellon and B. Stevens. On bulk models of shallow cumulus convection. *Journal of the atmospheric sciences*, 62(9):3286–3302, 2005.

A. K. Betts. Modeling subcloud layer structure and interaction with a shallow cumulus layer. *Journal of the Atmospheric Sciences*, 33(12):2363–2382, 1976.

M. A. Botchev. A short guide to exponential Krylov subspace time integration for Maxwell's equations. *Internal Report, Department of Applied Mathematics, University of Twente*, 2012.

S. Brooks, A. Gelman, G. Jones, and X.-L. Meng. *Handbook of Markov Chain Monte Carlo*. Taylor & Francis US, 2011.

Z. Chen. Bayesian filtering: From kalman filters to particle filters, and beyond. *Statistics*, 182(1):1–69, 2003.

M. De La Chevrotière, B. Khouider, and A. J. Majda. Calibration of the stochastic multicloud model using bayesian inference. *SIAM Journal on Scientific Computing*, 36(3):B538–B560, 2014.

Q. Deng, B. Khouider, and A. J. Majda. The mjo in a coarse-resolution gcm with a stochastic multicloud parameterization. *Journal of the Atmospheric Sciences*, 72(1):55–74, 2015.

H.-K. L. Drbohlav and B. Wang. Mechanism of the northward-propagating intraseasonal oscillation: Insights from a zonally symmetric model. *Journal of Climate*, 18(7):952–972, 2005.

D. Drikakis and W. Rider. *High-resolution methods for incompressible and low-speed flows*. Springer Science & Business Media, 2006.

F. Dulat, J.-P. Katoen, and V. Y. Nguyen. Model checking markov chains using krylov subspace methods: an experience report. In *Computer Performance Engineering*, pages 115–130. Springer, 2010.

K. A. Emanuel. *Atmospheric convection*. Oxford University Press, 1994.

L. Evans. *Partial differential equations.* American Mathematical Society, 1998.

W. Feller. On the theory of stochastic processes, with particular reference to applications. In *Proceedings of the First Berkeley Symposium on Mathematical Statistics and Probability. August 13-18, 1945 and January 27-29, 1946. Statistical Laboratory of the University of California, Berkeley. Berkeley, Calif.: University of California Press, 1949. 501 pp. Editor: Jerzy Neyman, p. 403-432*, volume 1, pages 403–432, 1949.

Y. Frenkel, A. J. Majda, and B. Khouider. Using the stochastic multicloud model to improve tropical convective parameterization: A paradigm example. *Journal of the Atmospheric Sciences*, 69(3):1080–1105, 2012.

Y. Frenkel, A. J. Majda, and B. Khouider. Stochastic and deterministic multicloud parameterizations for tropical convection. *Climate Dynamics*, 41(5-6): 1527–1551, 2013.

D. M. W. Frierson, A. J. Majda, O. M. Pauluis, et al. Large scale dynamics of precipitation fronts in the tropical atmosphere: A novel relaxation limit. *Communications in Mathematical Sciences*, 2(4):591–626, 2004.

D. T. Gillespie. An exact method for numerically simulating the stochastic coalescence process in a cloud. *Journal of the Atmospheric Sciences*, 32(10):1977–1989, 1975.

P. T. Haertel and G. N. Kiladis. Dynamics of 2-day equatorial waves. *Journal of the Atmospheric Sciences*, 61(22):2707–2721, 2004.

J. R. Holton and G. J. Hakim. *An introduction to dynamic meteorology.* Academic Press, 2012.

A. Jensen. Markoff chains as an aid in the study of Markoff processes. *Scandinavian Actuarial Journal*, 1953(sup1):87–91, 1953.

G.-S. Jiang and E. Tadmor. Nonoscillatory central schemes for multidimensional hyperbolic conservation laws. *SIAM Journal on Scientific Computing*, 19(6): 1892–1917, 1998.

R. H. Johnson, T. M. Rickenbach, S. A. Rutledge, P. E. Ciesielski, and W. H. Schubert. Trimodal characteristics of tropical convection. *Journal of Climate*, 12 (8):2397–2418, 1999.

M. A. Katsoulakis, A. J. Majda, and D. G. Vlachos. Coarse-grained stochastic processes for microscopic lattice systems. *Proceedings of the National Academy of Sciences*, 100(3):782–787, 2003.

M. F. Khairoutdinov, S. K. Krueger, C.-H. Moeng, P. A. Bogenschutz, and D. A. Randall. Large-eddy simulation of maritime deep tropical convection. *Journal of Advances in Modeling Earth Systems*, 1(15):1–13, 2009.

B. Khouider and A. J. Majda. A non-oscillatory balanced scheme for an idealized tropical climate model. *Theoretical and Computational Fluid Dynamics*, 19(5):331–354, 2005.

B. Khouider and A. J. Majda. Model multicloud parameterizations for convectively coupled waves: Detailed nonlinear wave evolution. *Dynamics of Atmospheres and Oceans*, 42(1):59–80, 2006a.

B. Khouider and A. J. Majda. Multicloud convective parameterizations with crude vertical structure. *Theoretical and Computational Fluid Dynamics*, 20(5-6): 351–375, 2006b.

B. Khouider and A. J. Majda. A simple multicloud parameterization for convectively coupled tropical waves. Part I: Linear analysis. *Journal of the Atmospheric Sciences*, 63(4):1308–1323, 2006c.

B. Khouider and A. J. Majda. A simple multicloud parameterization for convectively coupled tropical waves. part ii: Nonlinear simulations. *Journal of the Atmospheric Sciences*, 64(2):381–400, 2007.

B. Khouider and A. J. Majda. Equatorial convectively coupled waves in a simple multicloud model. *Journal of the Atmospheric Sciences*, 65(11):3376–3397, 2008.

B. Khouider, A. J. Majda, and M. A. Katsoulakis. Coarse-grained stochastic models for tropical convection and climate. *Proceedings of the National Academy of Sciences*, 100(21):11941–11946, 2003.

B. Khouider, J. Biello, and A. J. Majda. A stochastic multicloud model for tropical convection. *Communications in Mathematical Sciences*, 8(1):187–216, 2010.

B. Khouider, A. J. Majda, and Y. Frenkel. Effects of rotation and mid-troposphere moisture on organized convection and convectively coupled waves. In *AGU Fall Meeting Abstracts*, volume 1, page 0098, 2013a.

B. Khouider, A. J. Majda, and S. N. Stechmann. Climate science in the tropics: waves, vortices and pdes. *Nonlinearity*, 26(1):R1–R68, 2013b.

G. N. Kiladis, K. H. Straub, and P. T. Haertel. Zonal and vertical structure of the madden-julian oscillation. *Journal of the Atmospheric Sciences*, 62(8):2790–2809, 2005.

G. N. Kiladis, M. C. Wheeler, P. T. Haertel, K. H. Straub, and P. E. Roundy. Convectively coupled equatorial waves. *Reviews of Geophysics*, 47(2):274–399, 2009.

H.-L. Kuo. Further studies of the parameterization of the influence of cumulus convection on large-scale flow. *Journal of the Atmospheric Sciences*, 31(5):1232–1240, 1974.

R. J. LeVeque. Wave propagation algorithms for multidimensional hyperbolic systems. *Journal of Computational Physics*, 131(2):327–353, 1997.

R. J. LeVeque. *Finite volume methods for hyperbolic problems*, volume 31. Cambridge University Press, 2002.

R. J. LeVeque. *Finite difference methods for ordinary and partial differential equations: steady-state and time-dependent problems*, volume 98. SIAM, 2007.

J.-L. Lin, G. N. Kiladis, B. E. Mapes, K. M. Weickmann, K. R. Sperber, W. Lin, M. C. Wheeler, S. D. Schubert, A. Del Genio, L. J. Donner, et al. Tropical intraseasonal variability in 14 ipcc ar4 climate models. part i: Convective signals. *Journal of Climate*, 19(12):2665–2690, 2006.

J. W.-B. Lin and J. D. Neelin. Toward stochastic deep convective parameterization in general circulation models. *Geophysical Research Letters*, 30(4):1–4, 2003.

X. Lin and R. H. Johnson. Kinematic and thermodynamic characteristics of the flow over the western pacific warm pool during toga coare. *Journal of the Atmospheric Sciences*, 53(5):695–715, 1996.

R. A. Madden and P. R. Julian. Description of global-scale circulation cells in the tropics with a 40-50 day period. *Journal of the Atmospheric Sciences*, 29(6): 1109–1123, 1972.

A. J. Majda. *Introduction to PDEs and Waves for the Atmosphere and Ocean*, volume 9. AMS Bookstore, 2003.

A. J. Majda. New multiscale models and self-similarity in tropical convection. *Journal of the Atmospheric Sciences*, 64(4):1393–1404, 2007.

A. J. Majda and B. Khouider. Stochastic and mesoscopic models for tropical convection. *Proceedings of the National Academy of Sciences*, 99(3):1123–1128, 2002.

A. J. Majda, S. N. Stechmann, and B. Khouider. Madden–julian oscillation analog and intraseasonal variability in a multicloud model above the equator. *Proceedings of the National Academy of Sciences*, 104(24):9919–9924, 2007.

S. Manabe and J. Smagorinsky. Simulated climatology of a general circulation model with a hydrologic cycle. *Monthly Weather Review*, 95(4):155–169, 1967.

S. Manabe and R. T. Wetherald. Thermal equilibrium of the atmosphere with a given distribution of relative humidity. *Journal of the Atmospheric Sciences*, 24 (3):241–259, 1967.

B. E. Mapes. Convective inhibition, subgrid-scale triggering energy, and stratiform instability in a toy tropical wave model. *Journal of the Atmospheric Sciences*, 57(10):1515–1535, 2000.

B. E. Mapes and R. A. Houze. Diabatic divergence profiles in western pacific mesoscale convective systems. *Journal of the Atmospheric Sciences*, 52(10):1807–1828, 1995.

B. E. Mapes, S. Tulich, J. Lin, and P. Zuidema. The mesoscale convection life cycle: Building block or prototype for large-scale tropical waves? *Dynamics of Atmospheres and Oceans*, 42(1):3–29, 2006.

A. D. Martin, K. M. Quinn, and J. H. Park. Mcmcpack: Markov Chain Monte Carlo in R. *Journal of Statistical Software*, 42(9):1–21, 2011.

C. Moler and C. Van Loan. Nineteen dubious ways to compute the exponential of a matrix. *SIAM review*, 20(4):801–836, 1978.

M. W. Moncrieff. Organized convective systems: Archetypal dynamical models, mass and momentum flux theory, and parametrization. *Quarterly Journal of the Royal Meteorological Society*, 118(507):819–850, 1992.

J. D. Neelin and N. Zeng. A quasi-equilibrium tropical circulation model-formulation. *Journal of the Atmospheric Sciences*, 57(11):1741–1766, 2000.

H. Nessyahu and E. Tadmor. Non-oscillatory central differencing for hyperbolic conservation laws. *Journal of Computational Physics*, 87(2):408–463, 1990.

O. Pauluis. Boundary layer dynamics and cross-equatorial hadley circulation. *Journal of the Atmospheric Sciences*, 61(10):1161–1173, 2004.

K. Peters, C. Jakob, L. Davies, B. Khouider, and A. J. Majda. Stochastic behavior of tropical convection in observations and a multicloud model. *Journal of the Atmospheric Sciences*, 70(11):3556–3575, 2013.

A. S. Ravindran, B. Khouider, and A. J. Majda. Realistic madden-julian oscillation initiation and dynamics in a coarse resolution general circulation model. In *AGU Fall Meeting Abstracts*, volume 1, page 0094, 2013.

A. S. Ravindran, B. Khouider, and A. J. Majda. Simulation of monsoon intraseasonal oscillations in a coarse-resolution aquaplanet gcm. *Geophysical Research Letters*, 41(15):5662–5669, 2014.

A. S. Ravindran, B. Khouider, A. J. Majda, and D. Qiang. Role of stratiform heating on the organization of convection over the monsoon trough. *Manuscript submitted*, 2015.

D. J. Raymond. Regulation of moist convection over the west pacific warm pool. *Journal of the Atmospheric Sciences*, 52(22):3945–3959, 1995.

P. J. Roache. Quantification of uncertainty in computational fluid dynamics. *Annual Review of Fluid Mechanics*, 29(1):123–160, 1997.

C. P. Robert. *The Bayesian choice: from decision-theoretic foundations to computational implementation*. Springer, 2007.

C. P. Robert and G. Casella. *Monte Carlo statistical methods*, volume 319. Citeseer, 2004.

C. P. Robert and G. Casella. *Introducing Monte Carlo Methods with R*. Springer, 2010.

Y. Saad. Analysis of some Krylov subspace approximations to the matrix exponential operator. *SIAM Journal on Numerical Analysis*, 29(1):209–228, 1992.

J. F. Scinocca and N. A. McFarlane. The variability of modeled tropical precipitation. *Journal of the Atmospheric Sciences*, 61(16):1993–2015, 2004.

R. B. Sidje. Expokit: a software package for computing matrix exponentials. *ACM Transactions on Mathematical Software (TOMS)*, 24(1):130–156, 1998.

R. B. Sidje and W. J. Stewart. A numerical study of large sparse matrix exponentials arising in Markov chains. *Computational Statistics & Data Analysis*, 29(3):345–368, 1999.

R. K. Smith. *The physics and parameterization of moist atmospheric convection*, volume 505. Springer Science & Business Media, 1997.

S. N. Stechmann. *Models of convectively coupled waves in the tropical atmosphere*. ProQuest, 2008.

S. N. Stechmann, A. J. Majda, and B. Khouider. Nonlinear dynamics of hydrostatic internal gravity waves. *Theoretical and Computational Fluid Dynamics*, 22(6):407–432, 2008.

D. J. Stensrud. *Parameterization schemes: keys to understanding numerical weather prediction models*. Cambridge University Press, 2007.

B. Stevens. Bulk boundary-layer concepts for simplified models of tropical dynamics. *Theoretical and Computational Fluid Dynamics*, 20(5-6):279–304, 2006.

G. Strang. On the construction and comparison of difference schemes. *SIAM Journal on Numerical Analysis*, 5(3):506–517, 1968.

R. B. Stull. *An introduction to boundary layer meteorology*, volume 13. Springer Science & Business Media, 1988.

E. Tadmor. *Approximate solutions of nonlinear conservation laws*. Springer, 1998.

G. K. Vallis. *Atmospheric and oceanic fluid dynamics: fundamentals and large-scale circulation*. Cambridge University Press, 2006.

M. L. Waite and B. Khouider. Boundary layer dynamics in a simple model for convectively coupled gravity waves. *Journal of the Atmospheric Sciences*, 66 (9):2780–2795, 2009.